The Dynamics of Circulations Within the Stratiform Regions of Squall Lines

by
William A. Gallus Jr.

Department of Atmospheric Science
Colorado State University
Fort Collins, Colorado

Colorado
State
University

Department of
Atmospheric Science

Paper No. 537

ABSTRACT

THE DYNAMICS OF CIRCULATIONS WITHIN THE STRATIFORM REGIONS OF SQUALL LINES

A dynamic version of the two dimensional kinematic cloud model of Rutledge and Houze (1987) has been developed to investigate the effect of microphysics on circulations within the stratiform region associated with mesoscale convective systems. The design of the model allows for specified inputs of hydrometeors, water vapor and heat from the convective region. While there are some disadvantages to this approach, there are also distinct advantages: (1) the complexities of initialization and simulation of a realistic convective line are avoided and (2) many simulations (over 100) were conducted to examine the sensitivity of the results to many physical processes and assumptions. The 10-11 June 1985 PRE-STORM squall line is simulated first, with initialization based upon appropriate soundings, heat budgets and 1-D cumulonimbus model results. A 5 km mesh size is used, a value between those typically used in cloud models and in mesoscale models.

The model accurately simulates the evolution of the stratiform rain area with a transition zone broadening over time, especially late in the simulation after leading convective elements weaken. Significant ascent is simulated with peak intensities agreeing with observations. In-situ condensate production within the updraft contributes increasingly to the surface rainfall, and the ratio of condensate produced within the mesoscale updraft to that advected from the convective line generally agrees with previous water budgets of squall lines. Simulated horizontal flows agree qualitatively with observations, and include a sloping rear-inflow jet that develops with peak magnitudes approaching those observed.

Surface rainfall is underestimated as in previous 2D models, possibly implying the importance of 3D convergent forcing of strong ascent in the anvil cloud. Although peak

upward motion is as strong as observed, ascent is underestimated near cloud top, perhaps indicating the importance of radiative effects. Strong rear-inflow is restricted to within 100 km of the convective line; rear-inflow at high levels far from the convective line may require large-scale baroclinicity.

Convective heating alone generates significant ascent and condensate in the anvil; however, surface rainfall is scarce without the advection of hydrometeors from the convective line. Hydrometeor advection alone does not lead to strong ascent in the anvil cloud, implying the important interaction of both heat and hydrometeor advection in generating broad regions of significant stratiform rainfall. Evaporative cooling is the primary mechanism for driving the circulations in the lower portion of the stratiform region; when all other processes are neglected, evaporation induces a rear inflow jet and mesoscale downdraft nearly as strong as in the full microphysical simulation. Vertical motion in the stratiform region depends strongly on stability. Increasing instability greatly increases in situ production of condensate, surface rainfall, and low-level drying within the mesoscale downdraft. Some three-dimensional variations observed in stratiform regions may be due to variations in stability. The intensity of hydrometeor advection from convective elements also significantly influences the amount of stratiform surface rainfall.

Finer resolution simulations of the rear of the stratiform region for the 3-4 June PRE-STORM case find a delicate balance between microphysical cooling and adiabatic warming so that small changes in temperature and moisture, or in precipitation rates, greatly affect the intensity of a surface wake low. Enhanced precipitation near the rear of the stratiform region produces 3-5 m s^{-1} descent, but adiabatic warming is generally opposed by microphysical cooling. Warming only occurs in the subsidence above the melting level and near the surface. Pressure falls are significant in a small region under the strongest descent. The wake low is more intense when precipitation rates in the region are rapidly decreasing, and pressure falls in that case are nearly as large as observed. This implies that microphysical processes alone may be sufficient to explain intense descent and the formation of strong wake lows near the back of the stratiform region.

A GATE squall line is simulated in a moister environment with significantly different hydrometeor contents in the convective line. Realistic circulations are again produced.

Although more moist conditions reduce evaporation from individual hydrometeors, greater hydrometeor input from the tropical convective line is sufficient to produce similarly large net evaporation rates as in midlatitude cases.

TABLE OF CONTENTS

ACKNOWLEDGEMENTS

LIST OF FIGURES

LIST OF TABLES

Chapter 1

INTRODUCTION

Observational studies have long shown that convective cells can organize into long lines extending over distances of several hundred kilometers, with large regions of stratiform precipitation trailing the intense convection (e.g. Newton, 1950). These systems are known as squall lines, and they produce extensive anvil clouds at high levels which can cover over 100,000 square kilometers. Broad and rather intense mesoscale circulations develop which play a role in maintaining the large systems over time periods that can exceed 12 hours (LaFore and Moncrieff, 1989; Rasmussen and Rutledge, 1993). The broad effects of the squall line can alter the synoptic scale environment.

Strong ascending front-to-rear flow is generally observed in these systems at middle and high levels. The ascent is associated with the rearward transport of heat from the intense convective line at middle and upper levels. Detrainment from anvils of active and dissipating convection can horizontally distribute high θ_e air which is slightly positively buoyant (Knupp and Cotton, 1987). In a storm-relative sense, dissipating convective towers move rearward from the convective line region, and these dying towers contribute to some of the vertical motion observed in the anvil cloud. The strong front-to-rear flow can also transport large amounts of hydrometeors rearward (e.g. Houze, 1981). This transport is believed to play a major role in the establishment of the extensive anvil cloud and the development of precipitation over broad regions behind the leading convective line (Rutledge, 1986; Rutledge and Houze, 1987). In addition, the microphysics resulting from the presence of these hydrometeors can initiate circulations due to the diabatic heat released when water changes phase. Ascent in the anvil cloud leads to the production of additional condensate which can be deposited on the hydrometeors advected from the

convective line. Some studies have shown that the majority of surface rainfall in the stratiform region is due to this in situ production mechanism (e.g. Rutledge and Houze, 1987). However, the same studies have indicated that this condensate would not reach the surface were it not for the advected hydrometeors which initiate a seeder-feeder type process.

Within the stratiform region, a strong current of rear-to-front flow typically develops and often descends toward the surface. This current is known as the rear-inflow jet (Smull and Houze, 1985). Although this jet is known to transport air with low equivalent potential temperatures into the line, allowing for large evaporative cooling rates which maintain the cold pool and prolong the life of the squall line, the mechanisms for its development remain unclear. Brown (1979) has shown that a mesoscale area of low pressure can develop in midlevels, the hydrostatic result of condensational heating aloft over evaporational and melting-induced cooling below. LeMone (1983) has also found a midlevel hydrostatically-induced mesolow just behind the convective towers in the leading line. The midlevel mesolows produce pressure gradient accelerations consistent with the observed rear-inflow jet at the back of the system and the enhanced front-to-rear flow near the convective line. Schmidt and Cotton (1990) argue that the blocking of the ambient flow enhanced by interacting gravity wave circulations forces air to descend and move from rear to front at middle and high levels to the rear of the intense convection. In some cases, the rear-inflow jet may be enhanced by large-scale baroclinicity and may exist prior to formation of the squall line, as argued by Zhang and Gao (1989).

Because questions about the origin and evolution of ascent in the anvil cloud and intensification and maintenance of the rear-inflow jet may require data on spatial scales smaller and time scales longer than those available by conventional observational means, numerical simulations of squall lines have become increasingly popular. Several meso-α (200-2000 km) and meso-β (20-200 km) scale models have successfully reproduced the evolution of a squall line with extensive trailing anvil precipitation. In general, however, these models have not concentrated on the differing roles of separate microphysical processes, or distinguished between convective line processes and those taking place within

the stratiform region. The object of this study has been to develop a two-dimensional model with a rather fine resolution and parameterized microphysical scheme to concentrate on the role of microphysics developing and sustaining mesoscale circulations within the stratiform region. In particular, several questions are investigated:

- Does the advection of hydrometeors alone from the convective line produce significant upward motion in the anvil cloud as heat is released in the processes of vapor deposition, fusion and condensation?

- Is the ensuing cooling from sublimation, melting and evaporation of these hydrometeors sufficient to induce a rear-inflow jet of significant magnitude?

- What is the role of advection of heat from the convective line in the establishment of circulations in the stratiform region?

- Can the microphysical processes explain the differences in behavior of the rear-inflow jet among cases?

- What differences might occur between the microphysically-induced circulations in a moist tropical squall line and those of a drier midlatitude system?

Chapter 2

BACKGROUND

2.1 Observational overview of mesoscale convective systems

Observational studies over the last few decades have shown that individual thunderstorms with horizontal dimensions of less than 50 km often exist in conglomerates covering meso-alpha and meso-beta scale regions in both the tropics and midlatitudes (e.g. Newton, 1950; Fujita, 1955). These systems can be collectively called mesoscale convective systems (MCSs), and are known to account for a large part of the atmospheric vertical heat, moisture and momentum transport (Riehl and Malkus, 1958). Within MCSs, individual cumulonimbus cells are often interspersed among large areas of lighter stratiform precipitation (Houze et al., 1990). The cold upper-level cirroform cloud shield that develops can cover horizontal distances approaching 1000 km. Although larger-scale processes generally influence the initiation, development, and dissipation of MCSs, MCSs in turn can alter the larger-scale synoptic environment (e.g. Ninomiya, 1971; Houze and Betts, 1981; Fritsch and Maddox, 1981a; Perkey and Maddox, 1985) as intense diabatic heating influences the pressure fields, resulting in extensive circulations and often significant production or redistribution of vorticity (e.g. Johnston, 1982; Bartels and Maddox, 1991; Biggerstaff and Houze, 1991b).

MCSs have been further classified based upon the size and shape characteristics of their cloud shields. Large, rather circular convective systems whose eccentricity (ratio of minor axis to major axis) is greater than 0.7 are known as mesoscale convective complexes (MCCs). The criteria used to classify a system as an MCC were developed by Maddox (1980), who found that these large systems were responsible for a significant amount of the heavy rain and severe weather reports in the central United States. Fritsch et al.

(1986) discuss the importance of the rainfall from these MCCs on agriculture across this region. Non-squall cloud clusters are a common form of MCS in tropical oceanic regions (e.g. Houze and Betts, 1981; Esbensen et al., 1988) and often meet the size criteria for MCC classification. Squall lines are a frequently highly organized type of MCS observed in both the tropics and midlatitudes. Although the radar echo associated with squall lines may be linear, the cirroform cloud shield may meet the eccentricity criteria for MCC classification.

Many studies have shown that in these squall lines, a leading line of intense convective cells is frequently followed by a much larger region, 50-100 km and more, of stratiform rain (e.g. Newton, 1950; Fujita, 1955; Pedgley, 1962; Gamache and Houze, 1982, 1983, 1985, Rutledge et al., 1988). Squall lines with this structure are often rather two-dimensional (e.g. Kessinger et al., 1987; Houze et al., 1989). Occasionally the stratiform cloud can lie ahead of the line of convective cells or straddle it, depending on the upper level winds relative to the system (Newton, 1966; Houze and Rappaport, 1984; Roux 1988). Some squall lines may not include any significant stratiform precipitation, particularly if the shear vector is parallel to the line (Heymsfield and Schotz, 1985).

Some squall lines do have significant variations in the along-line direction, and much less two-dimensionality (e.g. Brandes, 1990; Stumpf et al., 1991, Smull and Augustine, 1993). Frequently in these cases, intense convective cells form at the south or southwestern end of the system, and the stratiform rain and extensive anvil cloud lie to the north or northeast (Newton and Fankhauser, 1964; Houze et al., 1989). In a study of Oklahoma rain systems, squall lines with trailing stratiform regions were classified into one of two types based on the relation of the precipitation pattern to an axis normal to the squall line (Houze et al., 1990). Squall lines like those studied by Ogura and Liou (1980) and Gamache and Houze (1982) where the precipitation structure is relatively symmetric with respect to an axis normal to and passing through the midpoint of the line were referred to as *symmetric*. The less two-dimensional lines that had stronger, more discrete convective elements at the upwind end and extensive stratiform precipitation at the downwind end of the line were referred to as *asymmetric*. That study also found that some convective

systems had little relation between the stratiform rain regions and convective elements within them, and were unclassifiable.

Quasi-two-dimensional squall lines with trailing anvil cloud have been the subject of numerous studies based upon data from several large research projects. These include the tropical GATE (GARP Atlantic Tropical Experiment) and COPT (COnvection Profonde Tropicale) programs and the midlatitude PRE-STORM (Preliminary Regional Experiment for STORM-Central) and SESAME (Severe Environmental Storms and Mesoscale Experiment) projects and NSSL (National Severe Storms Laboratory) Spring Programs (e.g. Houze, 1977; Zipser, 1977; Gamache and Houze, 1982, 1983, 1985; Kuo and Anthes, 1984; Roux et al., 1984; Kalb, 1985: Chong et al., 1987; Ogura and Liou, 1980; Smull and Houze 1985, 1987; Rutledge, 1986; Johnson and Hamilton, 1988; Hemler et al., 1991, and many others). These squall lines typically contain a 10-50 km wide band of intense convective cells, a trailing 100-300 km wide region of lighter steady stratiform precipitation and a transition zone separating the two regions (Smull and Houze, 1985). The transition zone is a region of little or no rainfall and weak radar reflectivity, and was first identified by Sommeria and Testud in 1984 as a "reflectivity trough".

The convective line contains the most intense vertical motions within the squall line, and appears to drive many of the other features observed throughout both the transition zone and stratiform region of the system. A schematic depicting features within the different regions of a typical squall line with trailing stratiform cloud can be seen in Fig. 2.1 (from Houze et al., 1989). Intense convection within the leading line typically occurs during the first few hours of the lifetime of a squall line, and it is during this time that the stratiform region will often develop just behind the convection. Vertical velocities within the convective line are on the order of tens of meters per second, and rainfall rates can exceed 100 mm h^{-1}.

The movement of the convective line is dependent upon both the environmental shear and the orientation of the line to the shear vector. Some squall lines form in such a way so that they are aligned to maximize the vertical shear parallel to them. These lines generally move at relatively slow speeds, on the order of 5 m s^{-1} (LeMone et al., 1984). More
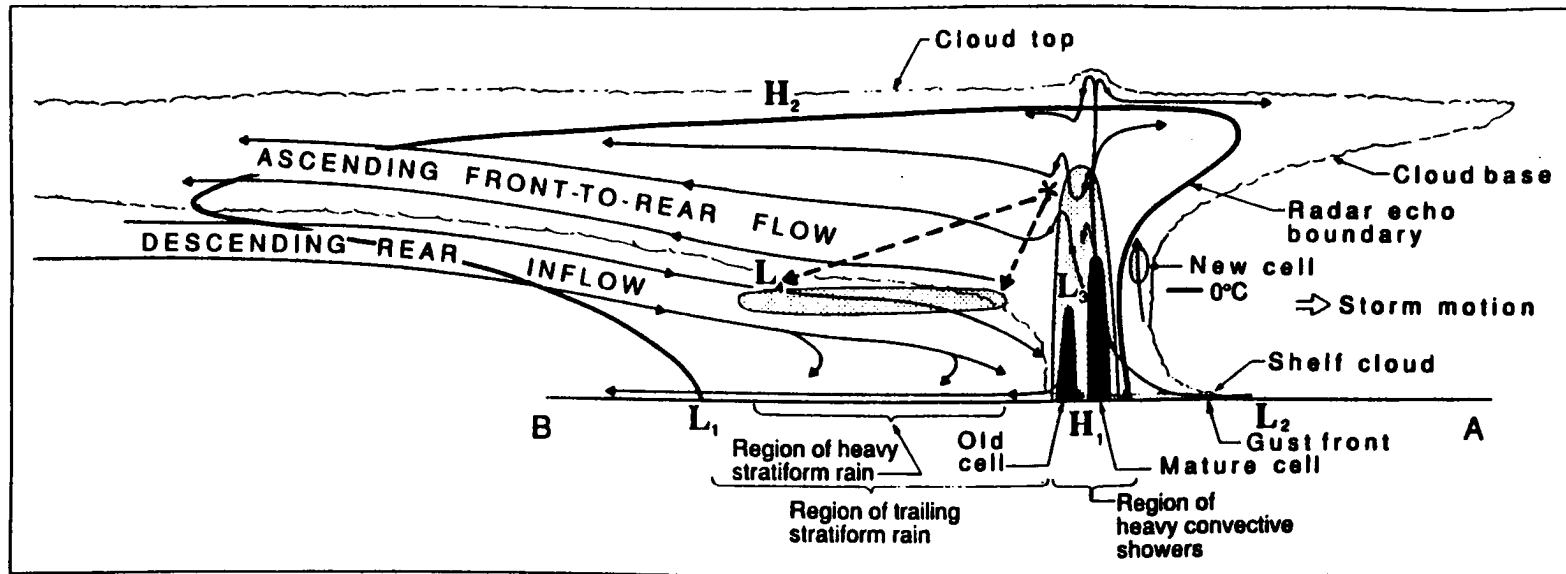
Figure 2.1: Conceptual model of a squall line with a trailing stratiform area viewed in a vertical cross section oriented perpendicular to the convective line (i.e., parallel to its motion). From Houze et al. (1989).

typically, squall lines are oriented so that shear is maximized in the line-normal direction. These lines often move at relatively fast speeds, sometimes exceeding 15 m s^{-1}. The faster moving squall lines move into the wind at all levels and can be called "propagating" lines (e.g. Moncrieff and Miller, 1976; Moncrieff, 1981), since the line appears to move by discrete propagation of its cells. As new cells develop out in front, moisture is cut off and the existing convective cells weaken (Fovell and Ogura, 1988). These older, dissipating cells are often precipitation laden and they move rearward relative to the gust front and blend into the anvil, and may be responsible for some of the upward motion occurring in the anvil cloud (Houze, 1977; Kessinger et al., 1987). Smull and Houze (1987a) found this rearward motion to be 9 m s^{-1} in an Oklahoma line. The older cells become nearly indistinguishable from the anvil as implied in Kessler's cloud model (1969) which showed that cloud bases rise rapidly upon cessation of a strong updraft, as cloud droplets at low levels are collected by precipitation-sized particles. Srivastava et al. (1986) showed that up to 75 % of the forward motion of the convective line in an Illinois squall line system was due to the formation of new convective elements up to 25 km ahead of the existing line. Individual cores only had lifetimes of 30-40 minutes.

The convective line appears to initiate front-to-rear flow at mid and high levels, or intensify existing front-to-rear flow (Smull and Houze, 1987a) by the convergence of horizontal momentum transported vertically by convective motions. Small-scale pressure perturbations induced at midlevels in the convective line assist in the momentum transport (LeMone, 1983; Flatau and Stevens, 1987). The front-to-rear flow is believed to transport significant amounts of hydrometeors rearward, into the stratiform region (Houze, 1981; Chen and Zipser, 1982; Smull and Houze, 1985; Hauser and Amayenc, 1986; Rutledge, 1986). Atlas et al. (1963) suggested a similar mechanism to explain the breadth of stratiform rain bands in hurricanes. Downward sloping reflectivity contours at middle and upper levels near the rear of one convective region has been shown to imply the importance of the upper portions of convective cells as sources of ice transported into the stratiform region (Gamache and Houze, 1983). Rearward advected hydrometeors then fall to the surface, accounting for at least a portion of the observed rainfall in the stratiform

region. Gamache and Houze (1983) found that 60-75% of the stratiform precipitation in one tropical squall line was due to horizontal advection of condensate from the convective line. Gallus and Johnson (1991) found a similarly large percentage (roughly 50%) of the stratiform rain may have been due to horizontal advection in a midlatitude case. Hauser and Amayenc (1986) used radar data supplemented with a two-dimensional model and found large cloud water amounts relatively far rearward from the convective cells in the 6-10 km layer. This implied a moderate 50 % precipitation efficiency in the convective region, and indicated the importance of transfer of condensate into the stratiform region above 4 km. In the 28 June GATE squall line studied by Houze and Rappaport (1984), relative flow was parallel to the line, and some flow extended out ahead of the line at high levels. The resulting echo overhang and stratiform region ahead of the line imply the importance of hydrometeor advection on the development of stratiform regions.

With time, the stratiform region grows in size, and rainfall on the order of several mm h^{-1} gradually extends farther rearward (e.g. Sanders and Paine, 1975; Sanders and Emanuel, 1977). In the case studied by Srivastava et al. (1986) the stratiform region expanded over 100 km in less than 2 hours, although the stratiform radar echo in the case studied by Ogura and Liou (1980) expanded at a rate closer to 20 km per hour.

After a period of a few hours, convective elements within the leading edge of the system typically begin to weaken, but the stratiform region continues to grow for a few more hours, and the most intense stratiform rainfall can occur significantly after the convective line has reached its peak intensity (e.g. Ogura and Liou, 1980; Gallus and Johnson, 1991). Light stratiform precipitation can occur hours after the convective line has completely dissipated (e.g. Srivastava et al., 1986; Johnson and Hamilton, 1988).

A transition zone generally develops several hours after the convective line has formed, and it widens with time. It may therefore not be present during the early stages of the development of the stratiform region; in some cases it may not form at all. In those cases that do exhibit a transition zone, the leading line of cumulus towers may move faster than the stratiform region (Matejka and Schurr, 1991) and become separated from it (Zipser, 1969) late in the lifetime of the system, usually during a period of rapid dissipation.

The transition zone with its small values of radar reflectivity and surface rainfall has been theorized to be a result of one or both of the following processes:

1. fallspeed sorting with heavier ice particles falling out quickly within the convective line region and lighter ice particles being carried significantly farther rearward (Smull and Houze, 1987a; Rutledge and Houze, 1987), and

2. enhanced downward motion and increased sublimation and evaporation over a larger depth of the troposphere just to the rear of the intense convection (Smull and Houze, 1985).

Smull and Houze (1987a) found using Doppler radar data particularly intense subsidence in the transition zone of the 22 May 1976 squall line. They theorized that the convergence of upper level outflow from the leading line convective cells with the ambient flow or other cells was responsible for high-level downdrafts present just behind the cells. Similar descent from the tropopause down to 3.5 km just behind convective cells was found by Heymsfield and Schotz (1985). Doppler radar data in the 10-11 June squall line found that deep mid- to upper-level subsidence coincided with the reflectivity minima (Rutledge et al., 1988, Biggerstaff and Houze, 1991a). Biggerstaff and Houze also found using EVAD analyses, however, that fallspeed sorting must also have been active. Increased upper level descent is implied by the streamlines in the Houze et al. schematic shown in Fig. 2.1. An increased depth of downward motion was detected by Doppler radar near the transition zone studied by Srivastava et al. (1986). Doppler data indicated downward motion throughout the depth of the troposphere in the transition zone of a COPT African squall line (Roux, 1988), and this descent reached 6 m s^{-1}. Houze and Rappaport (1984) found that the strongest low-level divergence existed in the transition region of a GATE tropical oceanic squall line. A tropical continental squall line studied by Chong et al. (1987) exhibited low-level descent as high up as 6 km in the transition zone, but only to cloud base, 4 km, in the stratiform region. In many cases the transition zone exhibits an orientation similar to that of the leading convection (e.g. Leary and Rappaport, 1987), implying that the convection influences the region significantly.

Behind the transition zone, stratiform rainfall rates generally peak in the range of 5-10 mm h^{-1}, often within an enhanced radar reflectivity band that may exceed 35 dBZ (Ogura and Liou, 1980). This band frequently is oriented similar to the leading convective line. Biggerstaff and Houze (1991a) found that the enhanced band in the 10-11 June PRE-STORM squall line was downwind of the most intense portions of the convective line. Because of the large size of the stratiform region, a significant portion of the total precipitation produced by a squall line can be attributed to its stratiform portion. In a tropical system, the amount may equal or exceed 40% (Cheng and Houze, 1979; Churchill and Houze, 1984), and in a midlatitude case, 30% (Johnson and Hamilton, 1988). Gamache and Houze (1983) and Rutledge (1986) show that this percentage must include some contribution from horizontal advection of condensate.

Although some of the precipitation reaching the surface in the stratiform region is due to the condensate advected rearward from the convective line, a significant amount is created within the stratiform region. Large-scale ascent with magnitudes on the order of several tens of cm s^{-1} occurs within the middle and upper portions of the troposphere in the stratiform anvil cloud (see Fig. 2.1). The upward motion has been attributed to fusion and condensation in the anvil cloud (Houze, 1982; Johnson and Young, 1983), although vapor deposition must certainly play a role (Churchill and Houze, 1984; Rutledge and Houze, 1987). Strong midlevel convergence in the stratiform region is associated with the upward motion. Roux (1988) suggests that the increase in the effective buoyancy due to the fallout of precipitation can maintain the mesoscale updraft. Longwave radiative transfer can also enhance ascent by destabilizing the stratiform cloud layer (Webster and Stephens, 1980; Tao et al., 1991). Knupp and Cotton (1987) found that the peak upward motion occurred around the midpoint of a stable layer, suggesting that the mesoscale updraft may be sensitive to the stability of the environment.

The upward motion in the anvil cloud allows nearly saturated conditions to exist which permit the growth of the rearward-moving hydrometeors through a seeder-feeder type process (Bergeron, 1950) and the initiation of additional snow and ice (Rutledge, 1986; Rutledge and Houze, 1987). At levels above 5 km, vapor deposition can dominate

(Smull and Houze, 1987a). Rutledge and Houze (1987) found that a mesoscale updraft allowed substantial vapor deposition to occur so that up to 80% of the observed rainfall would be due to condensate produced within the anvil cloud. Houze (1977) also argues that the large amount of surface rainfall from the stratiform portion of tropical squall lines cannot be explained by the advection of ice alone. Rutledge (1986) used a kinematic cloud model to study a GATE squall line and determined that ice could not be advected far enough rearward to account for moderate reflectivities at the rear of the system. In a study of a GATE squall line having both trailing and preceding stratiform regions, Houze and Rappaport (1984) found that the trailing stratiform region outlived the other portions of the system because the hydrometeor advection from the south was accompanied by a mesoscale updraft. The pre-line stratiform region existed only because of the temporary advection of hydrometeors in the 400-240 mb layer. A strong mesoscale updraft was absent and thus the region dissipated rapidly. This implies that a mesoscale updraft may not be the automatic consequence of hydrometeor and heat advection.

Localized stronger ascent in portions of the anvil cloud may explain the band of enhanced rainfall within the larger stratiform region. Because the orientation of this band is often similar to that of the leading convective line (e.g. Leary and Rappaport, 1987), it has been hypothesized that this region of increased rain rates is merely a product of an enhanced mesoscale swath of "seed" ice particles from the convective line, which "feed" on the condensate present in the anvil cloud (Rutledge and Houze, 1987; Smull and Houze, 1987a). In other words, the enhanced band is the preferred fallout region of hydrometeors, especially low-density graupel or aggregates of snow, detrained from the convective line at levels of 4-9 km. In the 22 May 1976 case, Smull and Houze (1987a) found that maximum radar reflectivities overlapped with maximum rearward flow at several location, implying the importance of the rearward advection of condensate. Matejka and Schuur (1991) argue that an enhanced swath of hydrometeors from the convective line is not necessary to explain the precipitation band, if a relative maximum in upward motion exists near the leading edge of the stratiform region as was observed in the 10-11 June PRE-STORM squall line case. However, there may be a link between enhanced regions of hydrometeor

and heat transport from the convective line and relatively strong ascent in the front portion of the stratiform region. This is implied in the modeling study of a GATE case by Tao and Simpson (1989) who found that most of the condensation and deposition in the stratiform region took place within 40-50 km of the convective line. Knupp and Cotton (1987) found that mesoscale ascent within a small MCS was strongly tied to the location of convective cores.

The large amounts of condensate advected into the domain and produced in situ within the anvil cloud generally move rearward as they fall, encountering subsaturated air. The resulting cooling from the microphysical processes of sublimation, evaporation, and melting generates a mesoscale downdraft (see Fig. 2.1), first discussed by Hamilton and Archibold (1945). This downdraft generally has a similar magnitude to the updraft in the anvil cloud. Typically the melting level is the separation between the upward and downward motion (Gamache and Houze, 1982; Johnson and Kriete, 1982; Srivastava et al., 1986), although some studies have shown that descent may extend a few kilometers above this level, especially toward the rear of the region (Rutldege et al., 1988; Gallus and Johnson, 1991). The downward motion is believed to be primarily caused by the evaporation of falling rain, with melting and sublimation playing a lesser role (Zipser, 1969; Zipser, 1977; Brown, 1979; Gamache and Houze, 1982; Johnson, 1982). This is supported by Knupp and Cotton (1987) who found that within a small isolated MCS in the Colorado mountains, although the mesoscale updraft formed within two hours of the first appearance of cloud, the mesoscale downdraft did not form until three hours after precipitation. Although the mesoscale updraft may occur on the larger scale of the anvil cloud, the mesoscale downdraft may be limited to the scale of the precipitation region itself (Biggerstaff and Houze, 1991a). The mesoscale downdraft can occupy a 100-500 km wide region, as opposed to the narrower convective downdrafts which are generally restricted to 10-20 km areas (Zipser, 1969; Moncrieff and Miller, 1976; Houze, 1977).

In some trailing anvil squall line systems, the mesoscale downdraft may include a small region of much stronger descent. Downward motion as large as 6 m s^{-1} has been found near the back of the stratiform region in one PRE-STORM MCS case (Stumpf et

al., 1991). Similarly strong descent was found in a similar position within the stratiform region of a different PRE-STORM case by Johnson and Bartels (1992). The 6 m s^{-1} descent occurred within a narrow 10 km wide region. In these cases, the strong downward motion is associated with a rapidly descending rear-inflow jet.

The rear-inflow jet has been well-studied in recent years (Smull and Houze, 1985, 1987a, 1987b; Chong et al., 1987; Biggerstaff and Houze, 1991a, b; Johnson and Hamilton, 1988). The intensity of the jet is generally measured in a storm-relative reference frame. The rear-inflow jet often enters the stratiform region at mid-levels at its rear, and usually descends gradually toward the surface as it approaches the leading convective line (see Fig. 2.1). The rear-to-front flow can extend to relatively high levels (8-9 km) at the rear of the squall line (Rutledge et al., 1988; Gallus and Johnson, 1991). Stensrud et al. (1991) have shown that evaporation and sublimation of precipitation can cause an initially high rear-inflow jet to descend in only a few hours. Many of these jets descend gradually and reach the surface well behind the convective line (Gallus and Johnson, 1991; Rutledge et al., 1988), although others remain elevated (e.g. Hjelmfelt, 1992), sometimes descending abruptly to the ground far behind the convective line near the back edge of the stratiform rain region (Stumpf et al., 1991). As stated earlier, this sudden descent can exceed several m s^{-1}. Such strong descent can lead to a very large gradient in the subsidence heating and an extreme pressure gradient at the surface. In the case studied by Stumpf et al., the rear-inflow jet appeared to be blocked. Though uncommon, the rear-inflow jet has been observed *to ascend* toward the convective line at a rate of 5-10 cm s^{-1} in at least one case (Carbone et al., 1990). That case was somewhat unique in that the system failed to produce appreciable stratiform precipitation, and was a secondary squall line that formed downshear from a dissipating primary system.

Rear inflow jets can become rather strong, usually within extratropical systems, with system-relative speeds of 10-15 m s^{-1} or more (Smull and Houze, 1987b; Rutledge et al., 1988), but more typically are weaker, on the order of a few m s^{-1}. In some cases, only a stagnation zone exists, or very weak rear-inflow at the back edge of the system with stronger flow near the leading-edge convection (Chong et al., 1987). Both strong and

weak rear-inflow cases all have a zone of sloping negative vorticity associated with them (Rasmussen and Rutledge, 1993). Smull and Houze (1987b) observed that squall lines with little or no rear-inflow jet typically were associated with weaker front-to-rear flow aloft than the cases with stronger rear-inflow. In addition, the stagnation zone tended to lie around the 650-700 mb layer, somewhat lower than the 550 mb layer where strong rear inflow tended to be maximized in the three cases studied. Kessinger et al. (1987) found in one case with a very weak rear-inflow jet that flow parallel to the squall line was stronger than that perpendicular to it. The rear-inflow jets appear crucial in maintaining the MCSs, as they supply potentially cold and dry midlevel air to aid in the production of both the convective and mesoscale downdrafts. It is theorized that these jets can be responsible for keeping the MCSs active for many hours (Lafore and Moncrieff, 1989).

Lafore and Moncrieff (1989) and Weisman (1992) have shown that the strength of the buoyancy gradient at the back of the convective line determines to a large extent the strength and behavior of the rear-inflow jet. Some studies have indicated that a rear-inflow jet may exist prior to the formation of convection (Zhang and Gao, 1989). Zhang and Gao argue that the baroclinicity associated with a short wave trough can make an important contribution to the rear-inflow jet, and often such short waves are present near MCSs, having acted as a trigger to release the convective available potential energy. Other authors have argued that microphysical feedbacks within the MCS lead to the response of strong rear-inflow rather than large scale anomalies in the wind field (Smull and Houze, 1987b). The intense convective line itself definitely alters the ambient flow, and can by itself lead to a circulation where air is moved toward the system at mid-levels from its rear, possibly under the influence of the hydrostatically-induced mesolow at midlevels beneath the sloping convective towers (LeMone, 1983). Cases like the one studied by Chong et al. (1987), where the strongest rear-inflow exists close to the convective line, imply that the convective system itself may play the primary role, although the authors in that study attributed 60% of the deep rear inflow to mesoscale downdrafts. Klimowski (1993) also found using detailed Doppler radar data from a North Dakota MCS that the rear-to-front perturbation first forms at the back of the convective line region, and later expands

rearward. Smull and Houze (1987b) have suggested that hydrostatically-induced pressure perturbations immediately under upshear-tilted warm convective updrafts are responsible for the increasing magnitude of rear-inflow toward convective regions of squall lines.

Additionally, the microphysical processes that occur in the stratiform region, most notably evaporation, sublimation and melting, lead to cooling that enhances the buoyancy gradients in the system, and may play some role in strengthening or maintaining a rear-inflow jet. The midlevel mesolow that forms between the mesoscale saturated ascent and the evaporative and melting-induced cooling may work in tandem with the convective mesolow to create a continuous flow of air from rear to front (Smull and Houze, 1987b). In some squall lines the rear-inflow jet actually develops at midlevels within the interior of the stratiform region (Smull and Houze, 1987b), indicating the importance of physical processes within an MCS (Chong et al., 1987; Leary and Rappaport, 1987). In many of the stagnation zone cases studied by Smull and Houze (1987b) no rear inflow was present at the back edge of the systems, yet some rear inflow did exist in the middle and front portions of the systems. The 22 May 1976 case studied by Smull and Houze (1985) and Ogura and Liou (1980), along with the 10-11 June PRE-STORM case studied by Smull and Houze (1987b) and Rutledge et al. (1988) among many others, exhibited the appearance of intense rear-inflow about the same time the active convective zone weakened. Gallus and Johnson (1991) found that the rear-inflow, at least on the scale of the rawinsonde network, actually continued to strengthen for several hours after the convection had begun weakening, and the jet maintained its intensity even when the convection nearly dissipated.

Schmidt and Cotton (1990) suggest that blocking of ambient air moving toward the squall line from the rear could cause a channeling of the flow beneath the rear anvil outflow. The blocking is initiated by high pressure which forms where convective updrafts meet the tropopause (Fritsch and Maddox, 1981b). The channeling would be enhanced through the presence of a stable boundary layer and the coupling of low and high-level gravity wave circulations that could increase the magnitude of the flow toward the front of the line through a Bernoulli-like effect. The simulations of Seitter and Kuo (1983) supported this theory as subsidence was found upshear of the updraft, implying the descent was not

the result of evaporation or water loading. In general, the lack of observations on a fine scale has prevented definitive conclusions being drawn regarding the cause or mechanisms of strengthening of the rear-inflow jet.

Frequently within the stratiform region of these systems, a third air current exists, at low levels beneath the rear-inflow jet and upper-level front-to-rear flow (Srivastava et al., 1986, Smull et al., 1987b). This front-to-rear flow often appears as the overturning of the rear-inflow jet (see Fig. 2.1). Wind speeds in this lower current can be nearly as large as those found in the other two jets (e.g. Gallus and Johnson, 1991).

The condensational heating occurring at high levels, along with deposition, in addition to the cooling processes of evaporation, melting and sublimation at lower levels, leads to a hydrostatically induced mesolow around the melting level in the stratiform region, with a mesohigh at the surface (Brown, 1979; LeMone, 1983). In addition, just behind the back edge of surface rainfall, a wake low (Johnson and Hamilton, 1988) sometimes forms, where the cooling microphysical processes do not outweigh the warming from adiabatic descent where the rear-inflow enters the precipitating portion of the MCS. Intense pressure changes, sometimes over 3 mb h^{-1}, may exist near the wake low, along with heat bursts (Johnson, 1983; Johnson et al., 1989). The midlevel mesolow may be associated with a cyclonic vortex which can influence the advection of hydrometeors (Johnson and Bartels, 1992) , and when long-lived, also result in the redevelopment of convection on subsequent days (Menard et al., 1988). Additionally, the surface wake low can also outlive the initial MCS and possibly contribute to redevelopment of convection (Zhang and Fritsch, 1988b). The pressure perturbations within an MCS contribute to circulations that develop and may extend well outside of the precipitating portion of the system. Gallus and Johnson (1992) found using rawinsonde data that the pressure gradient can cause accelerations of several meters per second per hour from rear to front within the stratiform region. Similar accelerations were obtained in a numerical simulation of the same case by Zhang and Gao (1989).

From the many observational studies of the leading line - trailing stratiform region squall lines, a rather general picture has emerged regarding typical circulation features in

the near-squall environment. Although much information about the "broad" impacts of these squall lines has been obtained from the large field programs in the past two decades, many smaller-scale aspects of the systems are still unclear. The dense rawinsonde networks used in projects like PRE-STORM provided data with a resolution of approximately 100 km. This is still too coarse to investigate smaller features within the stratiform region (McAnelly and Cotton, 1986) such as individual dissipating convective cores, and it causes aliasing of data between the distinct convective and stratiform regions, adding uncertainty to budget studies that attempt to separate these components (e.g. Johnson, 1982; Gamache and Houze, 1982; Houze, 1982; Johnson and Young, 1983; Johnson, 1984; Gallus and Johnson, 1991). Doppler-radar data with its much finer resolution help to alleviate some of these problems, but it typically is restricted to relatively small portions of the squall line systems. Because accurate parameterization of the effects of MCSs on large scale fields of heat, moisture and momentum in large-scale models continues to be a problem in numerical weather prediction, a better understanding of these systems requires supplementing the observational data with information from smaller-scale numerical models.

2.2 Overview of modeling methods

Numerical models have been used increasingly often to simulate some of the observed squall lines and mesoscale convective systems, in both two and three dimensions. The resolution of these models has varied considerably based on the purpose of the simulations. Squall lines have been investigated using numerical models that vary from the "cloud" or "cumulus" scale with horizontal meshes of under 1 km (e.g. Thorpe et al., 1982; Yoshizaki, 1986; Seitter and Kuo, 1983; Nicholls and Weissbluth, 1988) to meso-alpha and regional scale models with meshes on the order of 50 km or more (e.g. Perkey and Maddox, 1985; Zhang and Fritsch, 1988b). Mesoscale convective systems, including squall lines, are especially difficult to simulate because they generally contain convective cores with intense motions on the meso-gamma scale (0.1-1 km), and yet also contain regions of broader circulation and precipitation which may cover several hundred kilometers. A model that has

a resolution fine enough to accurately resolve the convective motions becomes computationally expensive when designed to adequately simulate the entire squall line system and its effects on the larger scale environment. Fine resolution models are typically nonhydrostatic, and usually require the restrictions of two dimensionality, simplified microphysics, or simulation of only a portion of the event (Weisman et al., 1988; Redelsberger and Lafore, 1988). Similarly a model well-designed to capture an entire MCS within its synoptic environment will generally be unable to resolve convective-scale features (e.g. Zhang and Fritsch, 1986). One solution that has been used to capture the convective portions of these systems with significant detail and yet also simulate the entire system is the nesting of grids (e.g. Fovell and Ogura, 1989). Care must be taken in such a model so as to not introduce spurious numerical effects due to the nesting of grids of finer resolution within larger coarser domains.

The resolution of a model has a significant impact on the type of moist physics that are used to represent convective and mesoscale processes. Linear studies of the growth of disturbances in a saturated convectively unstable atmosphere (e.g. Lilly, 1960) found that the dominant growth rate occurred at the smallest scale. This implied uncontrolled growth would occur at the smallest resolvable scale of a numerical model if saturation were allowed to develop under convectively unstable conditions. This problem appeared in Kasahara (1961) when localized rapid growth occurred, obscuring any larger scale features. To avoid this difficulty, most early models used an implicit cumulus parameterization. Any approach to diabatic heating where grid scale properties and cloud properties are synonymous is referred to as explicit (Molinari and Dudek, 1986). The implicit approaches differ in that the cloud properties are specified in terms of grid scale counterparts, and the convective effects are calculated in the absence of grid-scale saturation. In general, the larger the mesh size, the more likely it is that convective processes will have to be parameterized (the implicit approach). The higher the resolution, the more likely the model will be able to accurately resolve the effects of small-scale convective elements at each grid point (explicit approach). Zhang, Hsie and Moncrieff (1988) have discussed the question of which approach– implicit, explicit, or semi-implicit (the use of both an implicit

convective scheme and diagnostic formulation to compute resolvable scale condensation)–produces the most realistic results.

It is generally acknowledged that individual convective clouds are explicitly resolvable by meso- gamma scale cloud models (Zhang, Hsie and Moncrieff, 1988). These high resolution models have been used with some success by Moncrieff and Miller (1976), Tripoli and Cotton (1978), Klemp and Wilhelmson (1978) and Clark (1977, 1979). However, models that are used to simulate the response of convection on the surrounding environment are often forced by computational requirements to use much larger meshes. These models treat convective elements as subgrid scale processes and parameterize their collective effects (e.g. Anthes and Warner, 1978). Among the most commonly used cumulus parameterizations are the Kuo scheme (1974) and the Arakawa and Schubert (1974) scheme. Frank (1983) discusses some of the fundamental principles, goals and restraints applying to cumulus parameterization. At scales between these extremes, the meso-alpha and meso-beta, the treatment of convective activity is varied. Within these spatial scales lie most of the current squall line modeling efforts, and often these models use the semi-implicit approach.

Meso-alpha scale models that rely totally on the explicit approach, calculating resolvable scale condensation have been used to successfully simulate frontogenesis (Ross and Orlanski, 1982; Hsie et al., 1984). However, Molinari and Dudek (1986) found that the explicit approach with a similar resolution, was unable to simulate an MCS without localized regions of excessive rainfall that were due to a runaway positive feedback of latent heat release, large scale moisture convergence and surface pressure falls. Similar "blow-ups" of precipitation occurred in the simulation of Phillips (1979) and Kalb (1987). Zhang, Hsie and Moncrieff (1988) describe this particular problem of the explicit approach in meso-alpha models as the unrealistic development of conditional instability of the second kind (a CISK-like instability) resulting from the neglect of certain resolvable and subgrid-scale retarding factors. This instability has been referred to as gravitational instability (Kasahara, 1961), explicit instability (Molinari and Dudek, 1986), and grid-point instability. The explicit approach also resulted in an unrealistic delay in the resolvable

scale condensation due to the long duration required for grid-box saturation in the squall line simulations (Molinari and Dudek, 1986). The long delay allowed excessive convective instability to build, and the neglect of eddy fluxes prevented this instability from being released in a realistic manner. In the real world, convective rainfall does not necessarily require meso-beta scale saturation.

Meso-beta models, those using grid meshes on the order of 10-50 km, generally have more success with the explicit approach than meso-alpha models. Rosenthal (1979) found that in hurricane simulations with a hydrostatic model, the development of the systems was highly sensitive to the cumulus parameterization. Therefore, the explicit approach of moist physics was better, having the advantage of allowing a broad spectrum of interaction between resolved mesoscale convergence and the larger scale environment (Rosenthal, 1978). Orographically-induced clouds were successfully simulated with the explicit approach on a 10 km mesh in the hydrostatic model used by Nickerson et al. (1986). All of the hydrostatic model simulations using explicit methods required the use of idealized initial conditions. The finer resolution of the meso-beta scale models diminished the problem of a resolvable-scale saturation time delay. However, in some cases, the runaway CISK-like instability was aggravated by the increased resolution of small-scale convergence. Zhang, Hsie and Moncrieff (1988) found that the explicit convective scheme failed to reproduce the convective precipitation related to the squall line and MCC in the 1977 Johnstown flood case, and overpredicted the stratiform rainfall in the region of the mesovortex. The runaway CISK problem was present, although it was mitigated somewhat by the inclusion of liquid water evaporation and water loading. The authors argue that a grid size of at most 4-5 km is necessary for adequate resolution of downdraft dynamics. Molinari and Dudek (1986) investigated the performance of the explicit approach for models having mesh sizes between 20-200 km. They found that meso-beta models had considerably reduced saturation delay problems, and the updraft and downdraft magnitudes were more realistic than in meso-alpha scale models. However, they were forced to conclude that the issue of implicit versus explicit treatment of cumulus convection is still unresolved for the meso-beta scale. They hypothesized that unless grid sizes are reduced to the point

where the saturation delay problem is minimized, more complex microphysics will not substantially improve these models.

Problems with time delays and unrealistic precipitation blow-ups were avoided by several investigators who have successfully simulated convective systems using hydrostatic meso-beta scale models with some form of cumulus parameterization. Zhang, Hsie and Moncrieff (1988) found that the implicit convective scheme reproduced well the convective rainfall in the Johnstown flood case but failed to produce the stratiform region associated with the mesovortex. Zhang and Fritsch (1988a) found in similar simulations that resolvable-scale condensation was directly responsible for the development of a warm-core mesovortex and indirectly responsible for the MCC. With convective parameterization only, the model reproduced just the squall line associated with the MCC. Fritsch and Chappell (1980) and Frank and Cohen (1985) used the implicit approach with grid resolutions as fine as 20-30 km. A large MCS that produced the 1977 Johnstown flood was realistically simulated using the semi-implicit approach on a 25 km grid (Zhang and Fritsch, 1986). Even on these relatively small scales, an implicit approach may be necessary since convective elements often coexist within the stratiform portions of convective systems. Leary and Rappaport (1987) have shown that the "stratiform" region of some systems is actually marginally convective. Zhang, Hsie and Moncrieff (1988) found that with a 12.5 km resolution, the semi-implicit approach worked best, with the cumulus parameterization aiding in the accurate representation of the convective precipitation, and the full explicit physics reproducing the stratiform region. They argue that in hydrostatic models with resolutions on the order of 10 km, both implicit and prognostic explicit schemes should be incorporated.

Most of the convective simulations that have been done with even finer grid meshes used nonhydrostatic models. These models often contain sophisticated microphysics that allow in conjunction with the fine resolutions, the explicit resolving of convective elements. Because the fine resolution often limits the domain size, many of these works have concentrated on smaller tropical cyclone convection (Yamasaki, 1977; Lord et al., 1984; Rotunno and Emanuel, 1987), or have been restricted to simulate only portions of squall line systems (Weisman and Klemp, 1982; Weisman et al., 1988; Redelsberger and Lafore, 1988).

Many features of squall line systems have been successfully reproduced in recent simulations that use a meshing of the fine resolution domain within a coarser one (e.g. Fovell and Ogura, 1988, 1989; Weisman, 1992). These nested models generally use the same dynamic equations in each nest, with the only changes being in the resolution. A SESAME squall line in Texas was successfully simulated by Hemler et al. (1991) using a different approach with nested grids. In that study, a nonhydrostatic cloud model with a 5 km horizontal resolution was nested within a hydrostatic mesoscale model having a 20 km horizontal mesh. The authors concluded that 5 km was sufficiently small to adequately represent the important features within a squall line, including the movement and location of convective cells, even though these cells might not be fully resolved. The most serious problem was a 2-3 hour time delay in the development of the squall line. In spite of this success in modeling convective systems, it is still argued that even a 5 km mesh may be too large to explicitly resolve the internal structure of convective elements (Pointin, 1985). It may be necessary even with meshes of a few km, to include a parameterized convective scheme in non-hydrostatic models. The choice of an explicit or implicit approach to convection may depend on the type of system being simulated. Zhang, Hsie and Moncrieff (1988) argue that the precipitating mode (convective or stratiform), the forcing type (quasi-stationary or propagating) and the baroclinicity (weak or strong) will determine the success or failure of simulations using either approach.

Not only do variations exist among the mesoscale numerical models on the explicit or implicit treatment of convective processes, but also on the treatment of microphysics. Although many models are considered to include explicit heating, a wide range of microphysical parameterizations may be used (Hsie and Anthes, 1984) within these explicit methods. Some of the simpler treatments of microphysics have included the instantaneous falling out as rain of any condensed water. In this treatment no cloud water or evaporation is permitted. Other forms of explicit heating include a predictive equation for cloud water (e.g. Ross and Orlanski, 1982; Hsie et al., 1984; Dudhia and Moncrieff, 1989). In this type of model, cloud water is assumed to become rain when the mixing ratio exceeds a critical value (Takeda, 1965), and in some simple parameterizations, may fall out instantaneously

at the critical value. This critical value has varied from 0.5 to 1.5 g kg^{-1}. This method of microphysical representation allows for hydrostatic water loading. In a hydrostatic model, however, actual rain drag cannot be included.

More complex microphysical parameterizations that include frozen particles are restricted to meso-beta and smaller scale models. McCumber et al. (1991), among others, have shown that the inclusion of ice in microphysical schemes significantly improves the results of MCS simulations. Ice effects have been modeled in different ways, with the most elaborate approach being the use of spectral ice schemes that explicitly predict size spectra, sometimes using more than 20 size and mass categories for ice (Takahashi, 1976; Hall, 1980; Farley and Orville, 1986). Most existing cloud models use either two or three ice classes.

The vast majority of simulations have used a microphysical treatment that parameterizes particle size distributions of various hydrometeor fields using theoretical or empirical relationships (e.g. Kessler, 1969; Orville and Kopp, 1977; Lin et al., 1983; Rutledge and Hobbs, 1983, 1984). One dimensional dynamic models using parameterized microphysics include those developed by Simpson and Wiggert (1969), Cotton (1972), Wisner et al. (1972), and Cheng (1981), among others. Two dimensional versions have been developed by Orville and Kopp (1977). Three-dimensional cloud models that have often been used to simulate convection include those of Klemp and Wilhelmson (1978), Clark (1979), Bennetts and Rawlings (1981), Tripoli and Cotton (1982) and Cotton et al. (1982). Within these models, only the overall size distribution of particles is known, and continuity equations are integrated to provide information on the total (bulk) mixing ratios of different water substances. These bulk microphysical equations make assumptions on the size distributions, the slopes and the slope intercepts of the hydrometeor fields. It has been most common to maintain a constant slope intercept, and diagnose the slope at any point based on the predicted mixing ratio (e.g. Rutledge and Hobbs, 1983, 1984). Cotton and Anthes (1989) argue that this assumption may not be valid, especially in regions where turbulence can significantly alter the size distribution. The assumptions on the size distributions allow simplified diagnostic equations that determine conversions between the water classes,

and in cases of phase change, the diabatic heating. In general, most of the dynamic models used to simulate squall lines have concentrated on liquid water and vapor (Weisman, 1992), and have at best included only crude representations of ice phase processes (e.g. Hemler et al., 1991). Elaborate bulk microphysics including multiple ice classes have been used extensively in some kinematic models (Rutledge and Hobbs, 1983, 1984; Rutledge, 1986; Rutledge and Houze, 1987).

The other approach to microphysics is the explicit calculation of particle size distributions. One dimensional explicit microphysical models have been used by Danielsen et al. (1972), Ogura and Takahashi (1973), Young (1974), Scott and Hobbs (1977) and Yau and Austin (1979). The explicit formulation has been expanded to two dimensions by Takahashi (1976), Soong (1974), and Hall (1980), and to three dimensions in Takehashi (1981). With the explicit treatment, discrete particle size distributions of various hydrometeor fields are specified, and interactions between individual particles are then simulated (e.g. Szeto et al., 1988a). A simplification of this method is to divide hydrometeor classes into bins based on size. This approach is discussed in Cotton and Anthes (1989) and will likely be used more often in upcoming years. These models with explicit treatment of microphysics are the most detailed ones available, and the explicit approach greatly adds to computational costs which unfortunately may result in other restrictions within the models in which they are used.

2.3 Squall line modeling results

The simulation of squall line systems has generally been successful in reproducing long-lived systems, upshear tilts, updraft-downdraft mesoscale couplets, and three-tiered sloping flow arrangements. Simulations in both two and three dimensions have accurately reproduced many observed squall lines features. In addition, numerical models have offered insights into some processes that may not be easily seen from real data.

Squall line simulations have shown that the environmental wind profile is critically important to the dynamical structure and longevity of MCSs (Thorpe et al., 1982; Dudhia et al., 1987) Many numerical simulations in the 1970s that were done in two dimensions failed to produce long-lived squall lines (Rotunno et al., 1988). In fact, Moncrieff

(1978) found that it was impossible to achieve steady overturning in constant shear with a deep downdraft, and this implied that three-dimensional effects were probably important. Takeda (1971) was one of the first to show the importance of shear in simulating a long-lived storm. Hane (1973) simulated a long lasting storm, achieving this result in an environment of low-level shear with constant middle and upper level winds. Strong shear throughout the troposphere caused a problem in 2D simulations since the air was forced to flow through, and not around the convective towers. This led to a downshear tilt in the updraft in the upper troposphere, causing the system to dissipate. Low-level and upper level shears are particularly important in the evolution of squall line systems. Barnes and Sieckman (1984) found, as discussed earlier, that the speed of movement of GATE squall lines was a function of the low-level shear. Fast movers occurred in environments of strong low-level shear with the principle component of the shear perpendicular to the lines. Slow movers occurred when shear was negligible and the atmosphere was more moist above the boundary layer.

The two-dimensional simulations of Seitter and Kuo (1983) with a very fine resolution nonhydrostatic cloud model showed that precipitation loading contributed strongly to the buoyancy gradients that tilt a system upshear. Although liquid water loading alone was not sufficient to drive a downdraft when evaporation was ignored, the large amounts of liquid water present did cause a continual erosion of the downdraft side of the updraft. Part of the updraft mass flux was diverted into downdraft. Because more liquid water is present at lower levels, the erosion is most severe there, so that an upshear tilt is induced. After the upshear slope is established the entire length of the updraft, the liquid water distribution tends to become more uniform along the interface, so that the slope is maintained. This theory was supported by the finding that squall lines were more vertically oriented in cooler cases where less moisture was available. It should be noted, however, that their simulation was brief, lasting less than an hour, and the effects could be transient. Dudhia et al. (1987) remark that rainwater loading was most significant several kilometers behind the gust front in a simulated long-lived multicell squall line and not in close proximity to it as it was in the transient Seitter and Kuo case.

Dudhia et al. (1987) successfully simulated both multicellular and unicellular squall lines using a two-dimensional model. Rain drag was shown to have an important contribution to the density current. The simulation used a rather fine mesh, 1 km × 500 m, and the authors noted that higher horizontal and vertical resolutions did not cause appreciable changes in the simulation. The authors noted a 30-40 minute periodicity in the generation of convective cells that they proposed might be due to gravity wave response, or microphysical aspects regarding rain production. A cellular structure was also noted in the stratiform region. Cyclic cells were also a feature of the 2D simulation of Rutunno et al. (1988). The 2D model used by Dudhia et al. (1987) underestimated precipitation, possibly because it could not account for lateral convergence that occurs within 3D anvil clouds. The simulation also determined that the slight thermal instability present after squall line passage was not likely to be buoyant due to the stabilizing effects of liquid water and virtual temperature. However, cellular structure has been found within some stratiform anvil clouds, and further investigation is needed.

Many simulations of squall lines have been successful at reproducing an evolving rear-inflow jet (Fovell and Ogura, 1989; LaFore and Moncrieff, 1989; Weisman et al., 1988). The rear inflow appears to develop as the convective system changes from a narrow band of intense convective cells to a broader band of more gradual ascent and stratiform precipitation. Weisman (1992) states that a convective cell developing in a vertically-sheared environmental flow will initially tilt downshear, as it responds to the ambient shear. As a cold pool develops beneath it, horizontal buoyancy gradients along the downshear edge of the pool produce a circulation that is the opposite sense as the inherent circulation of the ambient shear. If the circulations are balanced, deep lifting occurs and the system is typically strong with little tilt. Eventually, as the cold pool continues to strengthen, its circulation overwhelms that of the ambient shear and the convection tilts rearward over the cold air, or upshear. LaFore and Moncrieff (1989) point out that the rear inflow jet is typically generated when horizontal buoyancy gradients at the rear edge of the plume aloft and cold pool near the surface generate horizontal vorticity, accelerating the flow from rear to front at midlevels.

The 2D simulations of Lafore and Moncrieff (1989) were successful at reproducing a rear-inflow jet and its temporal behavior in a West-African COPT case. In this case, the rear-inflow jet had a peak speed of 8 m s^{-1} and was restricted to the inner portion of the system below 4 km (Chong et al., 1987). Ascent in the stratiform anvil cloud, however, was consistently underestimated. The inclusion of ice microphysics increased vertical velocities in the anvil cloud over what they were without ice physics, but ascent was still too localized and weak in comparison with observations. Simulated rainfalls were never more than 70% of observed values.

Nicholls and Weissbluth (1988) found that the choice of two or three dimensions played some role in the strength of the accelerations when simulating tropical squall lines. In general, the three-dimensional simulation produced less front-to-rear acceleration of updraft air and rear-to-front acceleration of downdraft air. In addition, vertical motions were somewhat stronger in the 3D simulation. The mesoscale downdraft was weaker in two dimensions at low levels, possibly because the cold pool could not spread out as well as in three dimensions. In general, however, Nicholls et al. (1988) concluded that the similarities of the simulations indicate that for some cases, two-dimensional models are an appropriate economical way to model convection. Rotunno et al. (1988) agree, finding that two and three dimensional simulations compare very well until stronger, deeper shears are present. The 2D simulation of a GATE squall line by Nicholls (1987) successfully reproduced many of the observed features of the system including a rear-inflow jet.

Numerical models, like observations, show differing behaviors of the rear inflow jets among different cases. LaFore and Moncrieff (1989) proposed that a rear inflow current that descends to the surface could increase convergence at the gust front, enhancing the convective system through the generation of new convective cells. Fovell and Ogura (1989) and Fovell (1991) both hypothesized that a strong rear inflow could advect more dry air into the mesoscale downdraft region, enhancing evaporation and increasing the strength of the cold pool. In contrast to the theory of LaFore and Moncrieff, the cases studied in these papers showed that the strongest systems had elevated rear-inflow jets which did not descend to the surface at some distance behind the leading edge.

The work of Weisman (1992) investigated possible causes for the differing behaviors of the jets using vorticity forcing arguments (see Fig. 2.2, taken from Weisman, 1992). Negative forcing occurs along the leading edge of the cold pool, weak positive forcing along the back edge of the deeper portion of the rearward-spreading cold pool, and weak negative forcing aloft at the back edge of the warm plume. The forcing regions advect rearward and coincide with the main generation zone for the jet. Mixing in the parcels as they ascend the slope lowers buoyancy. With stronger shear and increased vertical updrafts, less mixing occurs and more of the buoyancy gradient is realized. The upshear-tilting phase of squall lines, generally in the first 2-3 hours of the system's lifetime, was when significant rear-inflow jets were usually generated. The strongest convective systems were associated with elevated rear-inflow jets. He found that only in cases of strong shear did the processes leading to vertical circulations become three-dimensional. This was the result of vortex development at both ends of the system which contributed to the strength of the rear inflow.

Modelling studies have also revealed the importance of ice phase processes in the convective systems. Houghton (1968) found that typical ice crystal concentrations within midlatitude stratiform cloud can often remove all condensate present, resulting in high precipitation efficiencies. Lafore and Moncrieff (1989) showed that even very simple representations of ice physics modulate the intensity of the rear inflow in simulated squall lines.

Willoughby et al. (1984) used an axisymmetric nonhydrostatic model to study a hurricane and found that ice was necessary to produce realistic concentric rings of convection. McCumber et al. (1991) found that the inclusion of ice in model physics enhances the agreement of both modeled tropical squall lines and non-squall systems to observations. In particular, the inclusion of ice resulted in more realistic simulation of the proportion of surface rainfall falling under the anvil, and intensity and structure of the bright band observed on radar near the melting level. McCumber et al. also found that the use of three ice classes was superior to two, or none. For tropical simulations, the best three ice class microphysical scheme included graupel, snow and cloud ice. Their study indicated

a) Cold Pool Balanced by Shear
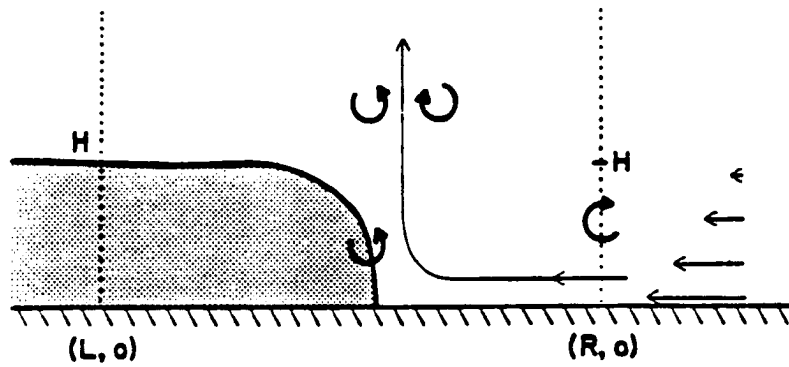
b) Cold Pool with Shear and Elevated Jet
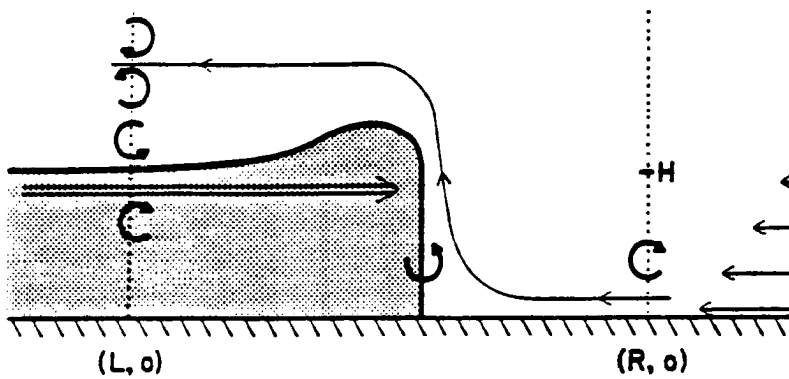
c) Cold Pool with Shear and Surface Jet
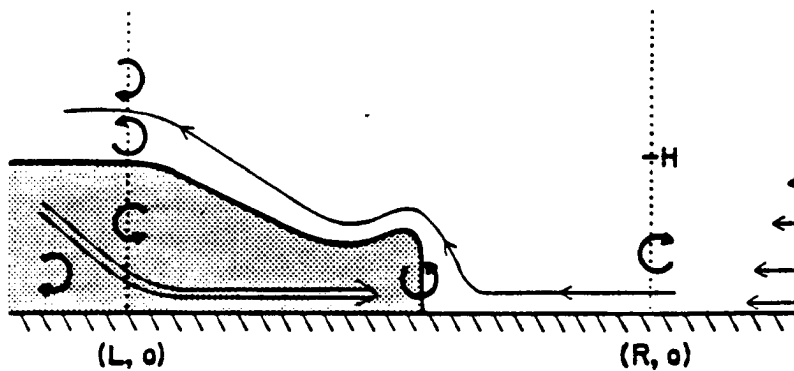
Figure 2.2: Schematic depiction of (a) a cold pool spreading in an environment having sufficient vertical wind shear to balance the cold-pool-generated circulation, (b) a cold pool balanced by the ambient vertical wind shear and an elevated rear inflow jet, and (c) a cold pool in the presence of a surface rear-inflow jet. The shading denotes the region of negatively buoyant air. The thick arrows depict the sense of the vorticity that is generated at the leading edge of the cold pool or that is advected through the boundaries. From Weisman (1992).

that the application of bulk ice microphysics may be case specific, and a generalization of ice processes might require even more ice categories, or the prediction of hydrometeor concentrations and particle-size spectra. In particular, because of the different dynamics between the convective and stratiform portions of MCSs, an improved approach is suggested whereby the number density of hydrometeors is predicted along with the mass. Fovell and Ogura (1989) found that simulated squall line precipitation efficiencies were far more sensitive to alterations in microphysical "knobs" like autoconversion rate and activation thresholds and particle distribution parameters than to the intensity of low-level wind shear.

McCumber et al. (1991) simulated a tropical GATE squall line (Houze, 1977; Houze and Betts, 1981) and found that although the inclusion of ice microphysics improved the model toward the 32-49 % anvil precipitation observed, the simulated percentage was still less than observations. The anvil area increased significantly with the inclusion of ice. The amount of rainfall in the anvil region was highest when graupel was used as the densest ice hydrometeor, not hail. Similarly, graupel was the primary source of anvil rain in these simulations, while snow was the main source in the hail simulations.

McCumber et al. (1991) also concluded that the type of large precipitating ice particles had more effect on simulations than differences in the microphysical processes. The terminal velocity of graupel and hail was the most influential characteristic. In non-squall systems, the model overpredicted the rainfall, but again the three ice class scheme using graupel worked best. Lord et al. (1984) also concluded that a third ice class was necessary to successfully simulate a tropical cyclone.

Chen and Cotton (1988) used the RAMS (Regional Analysis and Modeling System) to study a midwestern squall line. As in the previously mentioned studies, they found that the inclusion of ice greatly increased the strength of circulations in the system. In fact, if no ice was present, a significant rear-inflow jet did not form. This modeling work also found that melting by itself had little effect on the stratiform circulations, although it did cool the cloud layer by 2 K. It should be added that the 2D modeling work of an African squall line done by Lafore and Moncrieff (1989) found that although the inclusion of ice

enhanced subsidence, it did not enhance warming, because the subsidence warming was more than compensated by the cooling effects of melting, and therefore midlevel pressure gradients and the resulting circulations weakened due to ice. The ice physics in the Lafore and Moncrieff work were said to be inexact, and they stated that this difference indicates that ice phase microphysics must be detailed.

The RAMS simulation also found that radiative effects were significant and seemed to increase the intensity of both convection and upward motion in the trailing stratiform anvil cloud. Without radiative effects, upward motion in the anvil cloud decreased over 30%. In addition, the rear-inflow jet was discontinuous and weak when radiation was not included in the model. Webster and Stephens (1980) found the magnitude of radiative heating or cooling due to shortwave and longwave radiation compared to the diabatic heating from microphysics is relatively more important when rainfall is small in tropical stratiform regions. Stephens (1983) suggests that longwave radiation can enhance the growth rate of individual ice crystals in the ice cloud.

Radiative effects were also studied by Tao et al. (1991) in a 2D simulation of a subtropical squall line that occurred during TAMEX (Taiwan Area Mesoscale Experiment). Longwave radiative effects were shown to increase the amount of surface precipitation by around 16%, with the greatest changes late in the model simulation. Dudhia (1990) also found that most of the changes in surface rainfall between runs with and without radiation occurred rather late in the lifetime of a WMONEX (Winter MONsoon EXperiment) case. Tao et al. (1993) found a similar time-dependence of the effects of radiative heating and cooling for simulated squall lines from both the midlatitude PRE-STORM and tropical EMEX (Eastern Monsoon EXperiment) projects. Longwave radiative effects increased surface precipitation by 14% in the PRE-STORM case, and 31% in the EMEX case. The greater increase for the EMEX case was attributed to a faster formation of the stratiform region in the moist, tropical environment. Although radiation changed the magnitudes of terms in the heat and moisture budgets, the profiles were qualitatively similar.

Tao et al. (1993) also found that longwave radiative effects reduced the ratio of advected condensate to condensate produced within the anvil cloud by 7.5-15%, implying

that radiative cooling near cloud top and heating near cloud base significantly increases the generation of hydrometeors within the stratiform region. Tao et al. (1991) found that deposition was enhanced in the anvil cloud by longwave radiative effects, and more ice particles were generated in the anvil. The increased amounts of hydrometeors led to increased evaporation and melting so that the mesoscale circulation and structure of the stratiform region were enhanced. Total radiative cooling rates were as large as 20-30 K day^{-1} near cloud top, with heating of 9-15 K day^{-1} near cloud base, agreeing with case studies by Cox and Griffith (1979) and Webster and Stephens (1980). The radiative heating and cooling destabilized the stratiform cloud layer. Tao et al. concluded that longwave radiative transfer had the greatest impact on surface rainfall after microphysical processes. The effects of radiation were more important than surface heat and moisture fluxes, even though the system was over the ocean. Pre-storm mesoscale convergence lifting had the least impact of the four processes on the surface rainfall.

Although most of the simulations that investigated the role of radiative transfer found that it did measurably increase the strength of circulations and surface precipitation in the stratiform region, especially after time periods of at least 4-8 hours, at least one study found far less of an effect. Churchill and Houze (1991) found in a cloud model simulation that solar and infrared radiation did not substantially change the hydrometeor fields and water budget of a WMONEX case. It appears as though the effects of radiation may be highly dependent upon other factors, possibly including time of day, and duration of the event. Overall, most of the impact of radiative effects seems to be quantitative and not qualitative.

Among the more detailed simulations of squall lines is the work of Fovell and Ogura (1988; 1989). The fine-mesh 2D anelastic cloud model of Soong and Ogura (1980) was used to simulate the Oklahoma squall line studied by Ogura and Liou (1980) and Smull and Houze (1987a). Stretched vertical coordinates were used with nested grids down to 1 km resolution over a 115 km domain. The larger domain was quite extensive, covering 4500 km. The microphysical scheme of Lin et al. (1983) was used with hail as the third ice class.

In simulations without ice, convection first experienced an upshear tilt at 100 minutes, and was totally organized at 225 minutes. A trailing stratiform region of appreciable size failed to develop, although a rear-inflow current developed slowly during the organizational stage. The rear-inflow first developed near the back edge of the convection and then spread rearward with time (Fovell and Ogura, 1989). The convective cells pulsed with a 33 minute interval between bursts. The mesoscale and convective downdrafts shared a common origin and were difficult to separate.

When ice was included in the simulation, the storm was much bigger and a larger fine-mesh domain was used. The period of the cells decreased to 28 minutes. Fovell and Ogura (1988) found that most of the cloud water was present in the new and mature updrafts, while the rest of the cloud was glaciated. The horizontal winds were much stronger in this case. A warm dry subsidence area developed at the rear of the system where the rearward precipitation flux was small. The simulation also showed that convective elements decayed very quickly due to heavy snow loading, so that the upward motion in the anvil was separate from the leading edge upward motion. Convergence in the decelerating front-to-rear airflow contributed to its presence. The rear-inflow jet was confined below the melting level in the simulations. Neither the no-ice nor full ice simulations produced a good transition zone. The model also failed to produce significant amounts of condensate in the high-level updraft at the rear of the system. The maximum condensation rate was just enough to cancel fallout and allow horizontal homogeneity. The rearward advection of condensate appeared to be the primary factor in creating the light rainfall in the trailing stratiform region.

Fovell and Ogura (1989) also noted that in simulations with a very large domain, the squall lines did not dissipate, even after time periods of many hours. This raises the possibility that the demise of many squall lines in numerical simulations may be a spurious effect created by insufficiently large domains.

Fovell (1991) also investigated the role of the Coriolis force in squall line simulations with this model and found that rotation exerted a "braking" effect on the circulations. The Coriolis effect created a component of the wind that eventually opposed that which

caused it in the first place. The rear-inflow jet was weakened with time and the simulated system decayed. Additionally, rotation effectively traps the storm's exhaust, the air that has undergone subsidence warming, and allows it to accumulate in the region near the storm where it will later be ingested. The exhaust air entering the storm is another mechanism for dissipation. Fovell found that in no way the addition of rotation to a 2D model increased the strength of the system or its longevity. However, Schubert et al. (1989) proposed that the Coriolis force could lead to a destabilization in the upper troposphere of the trailing region of the system,

Because some squall line systems include three-dimensional supercell behavior in their convective lines, 3D models may occasionally be required for their accurate simulation. One such case was the 7 May 1985 PRE-STORM system, which was reasonably simulated using a 2×2 km horizontal mesh 3D nonhydrostatic model lacking ice physics by Dudhia and Moncrieff (1989). This system contained a pronounced midlevel mesovortex which was discussed by Brandes (1990). Although 2D models are generally sufficient to accurately simulate most squall lines, some systems that develop extensive stratiform regions lasting for many hours do develop midlevel rotation (e.g. Houze, 1977; Bosart and Sanders, 1981; Johnston, 1982; Johnson et al., 1989) and may require a 3D model for meaningful simulation.

Weisman et al. (1988) used the Klemp-Wilhelmson (1978) 3D cloud model to study the effects of three-dimensional wind shear on squall line structure and evolution. When no low-level shear was present, convection was short-lived. Convection occurring within moderate, line-normal shear (10 m s^{-1} over the lowest 2.5 km) developed a 140 km anvil cloud within 4 hours, with light rain falling in a 60 km band. When the line-normal shear over the layer was increased to 17.5 m s^{-1}, the convection had more downshear anvil at earlier times, but later evolved into a typical trailing-anvil squall line with even stronger rear-to-front flow than the weaker shear case. When shear reached 25 m s^{-1}, the system leaned downshear most of the time. The rear inflow expanded outward from the intense convective core. If the wind shear was oriented parallel to the line, convection was short-lived.

The 10-11 June PRE-STORM squall line to be discussed in great detail in this paper has been simulated extensively with a 3D mesoscale model by Zhang et al. (1989), Zhang and Gao (1989), Gao et al. (1990), Zhang and Cho (1992), Zhang (1992), and Grell (1993). The Penn State model was used with a 25 km horizontal resolution in the nested grid for these simulations. In general, these modeling studies reproduced the observed event exceptionally well with well-defined three-tiered circulations and midlevel and surface mesolows, along with well-reproduced time evolution of all features. The simulated rear-inflow jet lowered with time, descending from around 500 mb to 650 mb in two hours. Five hours after initiation of the convection, the rear inflow strengthened as the rearward portion of the jet connected with a lower portion ahead of the surface mesohigh. The surface wake low was said to be the end product of a chain of complicated dynamic reactions including the convective generation of condensate, latent cooling, water loading, development of the surface mesohigh, generation of a midlevel low which enhanced the descending rear-inflow jet which in turn increased the adiabatic warming and drying. The interface between the rear-inflow jet and the front-to-rear current extended up to 300 mb. The model indicated significant cooling above 600 mb, which implies the importance of sublimation of ice crystals. Zhang and Gao (1989) hypothesized that the transition zone could be the result of the rearward movement of the upper-level mesohigh within the front-to-rear updrafts. The system dissipated rapidly after 06 UTC, agreeing with observations. The rear-inflow jet maintained its eastward propagation with little change in speed, so that the forward updraft was quickly elevated into a convectively unfavorable environment. This resulted in a decrease of water loading, melting and evaporation which weakened the mesohigh, mesolow and downdraft. The rear-inflow jet became almost entirely elevated by the end of the simulation. In spite of the dissipation of these features within the squall line, the surface wake low experienced little change in intensity.

Sensitivity tests with the Penn State model (Zhang and Gao, 1989) showed that resolvable scale evaporation was necessary to bring the rear-inflow jet to the surface. Without this evaporation, the model failed to generate a strong surface mesohigh. A strong midlevel mesolow did develop, implying that this feature alone cannot explain the

generation of a descending rear-inflow jet (Smull and Houze, 1987b). The neglect of ice in the model weakened every circulation and pressure feature, and prevented the rear-inflow jet from descending to the surface. Water loading was also necessary to simulate strong circulations.

Contrary to many of the squall line studies, Zhang and Gao (1989) found that large scale baroclinicity contributed strongly to a rear-to-front flow component. Using simulations without diabatic heating, they determined that the squall line was responsible for at most, 50 % of the intensity of the trailing rear inflow. The rear inflow jet could be thought of as existing on three different scales. At high levels, rear-inflow existed due to large-scale baroclinicity. The mesoscale response allowed rear inflow to descend over a roughly 300 km region which could be thought of as the convectively controlled part of the jet. Moist downdrafts nearest the convective line were responsible for the final descent of the jet.

This particular squall line had an extensive stratiform region which influenced the development of a midlevel cyclonic vortex which was successfully simulated with the model (Zhang et al., 1989; Zhang and Cho, 1992; Zhang 1992). The mesovortex was found to be cooling-induced instead of the more typical warming-induced. Zhang (1992) argues that the vortex originated from pre-existing cyclonic vorticity within a traveling meso-α scale short wave. The vortex was intensified in the descending rear-to-front flow as a result of continued sublimative melting and evaporative cooling. Early in its development, tilting of horizontal vorticity played the major role in spin-up, but at later stages, stretching became dominant. Verlinde and Cotton (1990) also found that tilting was most important in spinning up a much smaller-scaled vortex in a PRE-STORM MCS, although stretching, especially around the 5 km level, intensified the vortex at later times. Zhang and Fritsch (1987, 1988b) had previously hypothesized that thermodynamically induced convergence near the melting level had an important effect on spinup. The mesovortex was most intense just above the melting level. Because planetary vorticity is not required for cooling-induced vortex development, Zhang (1992) proposed that this process may explain tropical mesovortices existing in convective systems trailed by stratiform precipitation (Zipser, 1969; Houze, 1977; Gamache and Houze, 1982).

In general, the many numerical simulations of squall lines have shown that for rather two-dimensional systems, the lack of a third model dimension does not significantly harm the modeling results. The most significant limitation of a 2D model may be in the overestimation of horizontal winds, and underestimation of vertical motions and therefore surface precipitation. Microphysical schemes should include ice, as the failure to do so causes a gross underestimation of the dynamics of the stratiform portions of these systems. If possible, ice parameterizations should be complex and allow for at least two or three different ice classes. Convective initiation and the structure and evolution of resulting systems are markedly sensitive to the wind shear used in a two-dimensional model. Long-lived systems form in environments with significant low-level shear and relatively weak shear at middle and high levels. Although often ignored in two dimensional modeling, both radiative effects and the Coriolis force may play a noticeable role in the evolution of squall line systems. It is possible, however, that their contributions act in opposition, and this may explain the significant number of successful simulations neglecting these processes.

Although successful 2D simulations of convective systems have yielded valuable information about the physical processes influencing the behavior of MCSs, some gaps still exist in the understanding of how certain features evolve within the systems. Large models have often simplified the microphysics that occur in the atmosphere so that specific roles of different processes cannot be isolated. Models generally rely on some artificial method to initiate convection, so that the evolution of the stratiform region may be somewhat far removed from actual data. In addition, the dynamics within the stratiform region that influence circulations there have generally been looked at only from a broad perspective, with emphasis on the convective line region. This may partially explain why there is no consensus on the mechanisms for the initiation, behavior and maintenance of the rear-inflow jet. Some studies that have drawn conclusions about the behavior of the jet have neglected ice physics which can play an important role. The simulations that are done in this study assist in filling the gaps in understanding by concentrating on the stratiform region alone with emphasis placed on the use of real data, where possible, and the use of a sophisticated microphysical scheme that does include three ice classes.

Chapter 3

DESCRIPTION OF THE NUMERICAL MODEL

For this study, the primary goal is to determine the impact of processes within the stratiform region of an MCS on the circulations that occur there, and therefore, a model which can explore these processes in great detail is necessary. Primitive equation models typically do not provide exceptional detail in the stratiform region, and they are generally more elaborate over a larger scale than is necessary to meet the goals of this study. By restricting the model domain to only the stratiform portion of a system, the simulations in this study can be done without having to take into account the significantly more dynamic and complicated processes occurring within intense convective cells. A longer time step and somewhat coarser mesh can be used than if the intense cells were to be simulated, and the complicated issue of whether a form of cumulus parameterization is needed with the still relatively small horizontal mesh could be reasonably avoided. In addition, artificial initiation of convection is not necessary, and several hours of simulation can be neglected, saving additional computational costs. These savings, along with the restriction of the model to two dimensions, allow the inclusion of a detailed microphysical scheme, which is felt to be important in understanding the ability of a stratiform anvil cloud to generate or intensify circulations. In essence, the model developed is a dynamic version of the detailed kinematic microphysical model used by Rutledge (1986) and Rutledge and Houze (1987). The microphysical parameterization of that model is discussed in Rutledge and Hobbs (1983; 1984). The choice of model domain to neglect the convective line also allows more real observational data to influence the stratiform region simulations than would be the case if a convective line were first simulated and allowed to produce a stratiform region. The model in some ways elaborates on the stratiform simulations of Szeto et al. (1988b) and Stensrud et al. (1991) by using an expanded microphysical scheme.

3.1 Model equations

As stated above, the model used in this study is designed for specific application to the stratiform region of rather linear squall line systems, and therefore to save on computational resources, is chosen to be two-dimensional. Redelsperger and Lefore (1988), Weisman et al. (1988) and Nicholls et al. (1988) all found that there was little difference between the 2D and 3D physics of most linear squall lines, and the use of a 2D model was an acceptable economical way to model convection. This model uses the "deep anelastic" equations formulated by Ogura and Phillips (1962), and ignores variations in the predicted variables in the y-direction, or along the squall line. The equations governing the dynamics are therefore very similar to those expressed in Orlanski and Ross (1977) and Szeto et al. (1988a), with flat terrain, radiation excluded, and the Coriolis parameter f assumed to be a constant. The systems studied occurred over relatively flat terrain so that a lack of model orography should not adversely affect results. Longwave radiative effects have been shown to increase surface rainfall and the strength of circulations by roughly 15% in the stratiform region (e.g. Tao et al., 1993), but the exclusion of radiation does not seem to change simulations qualitatively. Because the primary effect of radiative transfer is a reasonably small quantitative change, and radiative parameterizations are generally very computationally expensive, the exclusion of radiation is felt to be an acceptable simplification in the model. For most of the simulations performed, the Coriolis parameter is set to zero, so that the model is truly two-dimensional. Fovell (1991) suggested that the lack of Coriolis force has no significant impact for simulations of 4 hours or less. It may be important after six hours, and seems to produce a braking affect on circulations after ten hours. The simulations discussed in this study were only integrated to 7 hours or less. Surface sources and sinks of heat are neglected; for the PRE-STORM simulations which occurred at night over land, the exclusion should be acceptable. Even in oceanic cases, surface terms may not play a strong role in influencing the stratiform region (Tao et al., 1991). Moist processes are permitted in the model, however, and precipitation drag is included.

The diabatic heating term Q^* is computed using the bulk water parameterized micro-physical equations of Rutledge and Hobbs (1983; 1984) which were based upon the work of Lin et al. (1983). This microphysical scheme, or modifications of it, have found acceptance as reliable and accurate (Potter, 1991) in a wide range of kinematic and dynamic models (e.g. Ziegler, 1985; Proctor, 1988). The model allows for six classes of water substance, including three ice-phase classes. The details of the microphysical equations are discussed in Appendix A. No initial variation of potential temperature in the along-line direction is assumed. The model equations are formulated using the streamfunction ψ and y-component vorticity η for motion in the x-z plane. The resulting equation set is:

$$\frac{\partial \eta}{\partial t} = J(\psi, \alpha_0 \eta) + f\frac{\partial v}{\partial z} - \frac{g}{\theta_0}\frac{\partial \theta}{\partial x} + \frac{\partial}{\partial x}\left(\nu_H \frac{\partial \eta}{\partial x}\right) + \frac{\partial}{\partial z}\left(\nu_Z \frac{\partial \eta}{\partial z}\right) - gE\frac{\partial q_v}{\partial x} + g\frac{\partial q_T}{\partial x} \quad (3.1)$$

$$\frac{\partial v}{\partial t} = \alpha_0 J(\psi, v) - f(\frac{\alpha_0 \partial \psi}{\partial z} - U) + \frac{\partial}{\partial x}\left(\nu_H \frac{\partial v}{\partial x}\right) + \frac{\partial}{\partial z}\left(\nu_Z \frac{\partial v}{\partial z}\right) \quad (3.2)$$

$$\frac{\partial \theta}{\partial t} = \alpha_0 J(\psi, \theta) - v\frac{\partial \theta_g}{\partial y} + \frac{\partial}{\partial x}\left(K_H \frac{\partial \theta}{\partial x}\right) + \frac{\partial}{\partial z}\left(K_Z \frac{\partial \theta}{\partial z}\right) + \frac{\theta_0}{C_p}\frac{Q^*}{T_0} \quad (3.3)$$

$$\eta = \frac{\partial}{\partial x}(\alpha_0 \frac{\partial \psi}{\partial x}) + \frac{\partial}{\partial z}(\alpha_0 \frac{\partial \psi}{\partial z}) \quad (3.4)$$

$$u = \alpha_0 \frac{\partial \psi}{\partial z} \quad (3.5)$$

$$w = -\alpha_0 \frac{\partial \psi}{\partial x} \quad (3.6)$$

where ν_H and ν_Z are the horizontal and vertical eddy viscosity, K_H and K_Z are the horizontal and vertical eddy diffusivity, E is the constant 0.61, q_T is the total hydrometeor mixing ratio, q_v the water vapor mixing ratio, α_0 the initial horizontally averaged value of specific volume, θ_g the initial geostrophic potential temperature which can vary in the y-direction, and C_p the heat capacity of dry air. Equation (3.2) is not used in the simulations discussed in this study since the Coriolis parameter is assumed to be zero. The

notation in the equations is generally conventional, and a full list of all symbols appears in the Appendix. The term Q^* represents all diabatic heating sources. In total, there are 18 phase changes that contribute to this term, and these are expressed in (A46) and (A47). The advective effects in these equations are represented in Jacobian form with the Jacobian $J(a,b)$ defined as

$$J(A,B) = (\frac{\partial A}{\partial x})(\frac{\partial B}{\partial z}) - (\frac{\partial A}{\partial z})(\frac{\partial B}{\partial x}).$$

3.2 Numerical Aspects

The system of partial differential equations (3.1-3.3) is solved using the leapfrog finite differencing scheme. Spatial derivatives are represented with centered differences except at the boundaries where one-sided differences must be used. The diffusion terms are lagged by one time step (as in Szeto et al., 1988a). Finite differencing of the Jacobian terms is done using the Arakawa (1966) formulation to minimize computational instability. The presence of the Laplacian on the right hand side of the vorticity equation means that an elliptic equation must be solved to advance the equation set in time. The model uses the MUDPACK partial differential equation elliptic equation solver from NCARgraphics (John Adams, personal communication) to do so. The time step used in the model is typically 15 seconds which fulfills the Courant- Friedrich-Levy (CFL) criterion, but is adjusted downward in simulations where larger concentrations of hydrometeors lead to greater terminal fallspeeds so as to insure numerical stability. To suppress the time mode splitting associated with the leapfrog scheme, a Robert frequency filter (Asselin, 1972) of 0.18 is applied at every time step. Simulations are typically integrated for 7 hours.

The model domain is resolved by a non-staggered grid system uniformly spaced in both x and z. The horizontal grid length is 5 km, and the vertical, 400 meters, unless otherwise specified. For most of the simulations, the grid network consists of 65 points in the x-direction and 41 in y, with a lower boundary assumed to be at 500 meters elevation [the approximate average surface elevation of the PRE-STORM project domain (Johnson and Hamilton, 1988)], and an upper boundary at 16.5 km (roughly 3 km above the height

of the tropopause for most PRE-STORM cases). For GATE simulations a sea-level lower boundary is used, with an upper boundary at 16 km. It will be shown later that the model results are apparently not particularly sensitive to the domain size and grid spacing, a not uncommon feature in mesoscale convective simulations (e.g. Dudhia et al., 1987; Hsie et al., 1984; Schmidt and Cotton, 1990). The insensitivity to domain size is probably due in part to the open radiative lateral boundary conditions (Orlanski, 1976), and also to the rather smooth motions that were taking place within the domain. A finite difference filter, the horizontal smoother-desmoother used by Kreitzburg and Perkey (1977) was tested in the stratiform region simulations, but since gradients in velocity and temperature were rather gradual, the filter appeared to be unnecessary, and in fact, detrimental to the results. (In experimental simulations of developing convection that were done with a much finer resolution to test the response of the diabatic heating on circulations tens of kilometers ahead of and behind the intense convection, the smoother-desmoother was found to be necessary. These results are not shown.)

3.3 Parameterizations

3.3.1 Microphysical equations

Because earlier works (e.g. Heymsfield and Hjelmfelt, 1984; Rutledge, 1986) have shown that ice, snow and graupel are all present within convective cores and can all be distinguished advecting to the rear of a convective line, and all phase changes involving vapor, ice and liquid within the stratiform anvil are believed to be important in generating circulations, a sophisticated microphysical parameterization is important to successfully simulate the stratiform region. Dudhia and Moncrieff (1989) have shown that even a simple representation of ice is beneficial for accurately simulating the rear-inflow jet in squall lines. McCumber et al. (1991) have shown that in general, the more ice classes used in the scheme, the better the simulations obtained. Recent studies have often examined the role of only a few microphysical processes in great detail. Szeto et al. (1988b), for instance, studied the role of melting and evaporation on generating circulations in an idealized stratiform region. Stensrud et al. (1991) concentrated on the role of sublimation

in the anvil region. This study uses a microphysical scheme that includes nearly all water phase changes, and allows interaction between six different water classes.

In general, the same bulk microphysical parameterized model used by Rutledge and Hobbs (1983; 1984) is used to compute the diabatic heating effects, with some minor changes. As in that work, the particles comprising the cloud water and cloud ice fields are assumed to be monodisperse. The sizes of rain, snow, and graupel are assumed to be distributed continuously according to an inverse exponential distribution, shown in Appendix A. The rain, snow and graupel distributions of Rutledge and Hobbs (1983; 1984) are used to represent these fields in this model.

The Rutledge and Hobbs parameters for graupel are actually more representative of aggregates than graupel, and these parameters are appropriate for this model since graupel are relatively rare rearward of the transition zone in actual squall line systems (McCumber et al., 1991). The graupel is assumed to be quasi-spherical with a density of 0.4 g cm^{-3}. The slope intercept values N_{0x} are held constant, and the slope factors therefore vary according to the mixing ratios of the hydrometeors present. Cotton and Anthes (1989) have shown that the assumption of a constant slope intercept value, though commonly used, may not be valid, particularly in regions where the size distributions may change significantly due to breakup; however, since this model is applied to the rather tranquil conditions of the stratiform rain regions of squall lines, where vertical velocities generally remain small, it was felt that a constant intercept value was a better assumption than a constant slope value.

The slope factors, as in Rutledge and Hobbs (1983; 1984) but with modifications to agree with Locatelli and Hobbs (1974) as presented in Potter (1991) are

$$\lambda_R = \left(\frac{\alpha\pi\rho_L N_{0R}}{q_r}\right) \tag{3.7a}$$

$$\lambda_S = \left(\frac{\alpha\pi\rho_L N_{0S}}{q_s}\right) \tag{3.7b}$$

$$\lambda_G = \left(\frac{\alpha\pi\rho_L N_{0G}}{q_g}\right), \tag{3.7c}$$

where α is the specific volume. These factors differ from those of Rutledge and Hobbs (1983, 1984) and Lin et al. (1983) in that the density of liquid water is used for all three slopes, instead of the densities of the corresponding water class. Potter (1991) showed that the slope factors were incorrectly derived from Locatelli and Hobbs (1974) in the work of Lin et al. (1983) and Rutledge and Hobbs (1983; 1984), and the correct derivation results in a dependence for all three factors on the liquid water density, not the density of the specific hydrometeor. The errors in the Lin et al. (1983) scheme were present in other modeling studies (e.g. Lord et al., 1984) and because the calculated hydrometeor fallspeeds are a function of the slope factor, the errors often necessitated a downward adjustment to the diagnosed fallspeeds of snow or graupel (e.g. Zhang et al., 1989). The graupel fallspeeds also were roughly a factor of two too large in this model study before the Potter (1991) corrections were made.

Six different continuity equations are solved using the leapfrog finite differencing scheme. The equations for water vapor, ice and cloud water are of the form

$$\frac{\partial q}{\partial t} = -u\frac{\partial q}{\partial x} - w\frac{\partial q}{\partial z} + \alpha S_0 \qquad (3.8)$$

while the precipitating fields of snow, rain and graupel are represented as

$$\frac{\partial q}{\partial t} = -u\frac{\partial q}{\partial x} - w\frac{\partial q}{\partial z} + \alpha S_0 - V\frac{\partial q}{\partial z} + \frac{q}{\rho}\frac{\partial(\rho V)}{\partial z} \qquad (3.9)$$

with V being the corresponding hydrometeor fallspeed, calculated from the relations shown in Appendix A. Note that the last term in equation (3.9) is preceded by a plus sign. This corrects the error that appears in Rutledge and Hobbs (1983; 1984). The source or sink term in each equation (S_0), in addition to the total diabatic heating rate, used in equation (3.3) are also described in detail in Appendix A. The advection terms are computed using the positive definite scheme of Bott (1989) which produces only small numerical diffusion, and avoids the problem of negative hydrometeor values that can arise when using schemes like the second order Crowley. The Bott scheme suppresses negative values of a transported quantity by nonlinearly limiting the normalized fluxes. This advective scheme seemed to best handle the advections taking place with the grid size used in this model. McCumber

et al. (1991) has shown that graupel is a more realistic third ice-class for simulations of tropical convection, but hail, as used in Lin et al. (1983) may be more representative of midlatitude convection. In some runs of this model in which a warm bubble was used with a smaller mesh to investigate convective initiation, the replacing of graupel with hail was also found to produce more realistic results. However, because hail has a much greater fall speed than graupel, it would entirely fall out before reaching the stratiform region, and would not advect into the domain used in this study. In addition, the upward motions in the stratiform anvil cloud are typically not large enough to support the development of hail, so that hail can be neglected in this model. Therefore, low-density graupel (or aggregates) is used, as in Rutledge and Hobbs (1984).

3.3.2 Subgrid-scale turbulence parameterization

A first order closure is used for the Reynolds stress terms. Turbulent fluxes of momentum and heat are parameterized using an eddy viscosity scheme that accounts for increased turbulence production in regions of convective instability. The eddy diffusivity in this scheme (from Orlanski and Ross, 1973) takes the form:

$$\nu_z = K_z = \begin{cases} K_{z0}\left[1 + c\left(\frac{g\Delta\theta(\Delta z)^3}{\theta K_{z0}\nu_{z0}}\right)^{1/3}\right], & \Delta\theta < 0 \\ K_{z0}, & \Delta\theta \geq 0 \end{cases} \tag{3.10}$$

where K_{z0} and ν_{z0} are the constant background values of vertical eddy diffusivity and viscosity, respectively; $\Delta\theta$ and Δz are local values of the vertical potential temperature difference across a grid box, and the vertical grid spacing, respectively; and c is a constant. In a study of the effects of melting on circulations, Szeto et al. (1988a) set c equal to 0.1. In the cold frontal simulations of Orlanski and Ross (1977), c was set to 0.75. For this study, c was set to 0.5 since the horizontal grid spacing lies between the spacings used in those two studies. When tested, the model showed little change due to variations of c within the range of 0.1 to 0.75 for the stratiform region simulations. In the experimental simulations of convective development from a buoyant plume, the larger values of c worked best. Horizontal diffusion is included in the model as an additional source of numerical smoothing. The horizontal exchange coefficients are related to the vertical values as in Szeto et al. (1988a):

$$\nu_H = K_H = D \left(\frac{\delta x}{\delta z}\right)^2 K_z \qquad (3.11)$$

with D a constant set at 5.0. K_{z0} is set at 0.6 m^2s^{-1} for all stratiform domain simulations, which is slightly larger than the 0.3 m^2s^{-1} value used in Szeto et al. (1988a), but significantly less than the 5.0 m^2s^{-1} value used in Orlanski and Ross (1977). In general, the stratiform simulations were rather insensitive to variations of K_{z0} from 0.3 to 4.0. (More significant improvements were noted using larger values in the experimental simulations of convective development with a finer mesh).

3.4 Boundary conditions

Because of computational constraints, the domain size chosen is not large enough to fully include a large MCS (the horizontal domain covered roughly 300 km) so open radiative, or wave-permeable, boundary conditions are used, following Orlanski (1976). These boundary conditions, or derivatives from them, have been used extensively in the modeling of convection (e.g. Clark, 1977; Fovell and Ogura, 1988). Sensitivity tests showed that the model is not adversely affected by the limited horizontal domain. The domain is assumed to travel with a convective system so that one lateral boundary always stays at the "interface" between a convective line region, and a stratiform region. The model is driven by the rearward transport of hydrometeors from this convective line region, so that inflow conditions occur within the cloud layer on this boundary. Any transition zone must develop within the model domain, and hydrometeors are assumed to move rearward as they fall through high levels of this zone. A schematic depicting the organization of the model domain and fundamental processes within it is shown in Figure 3.1. Because rain has a large fallspeed, it reaches the surface within the convective region and does not advect into the stratiform region. (Specialized simulations with only a portion of the stratiform domain are discussed in Chapter 8. The organization of the domain is changed somewhat for these runs.)

Similar to Orlanski (1976), a pure outflow gravity wave speed is assumed at both lateral boundaries for certain variables. The use of this outflow speed for all dynamic
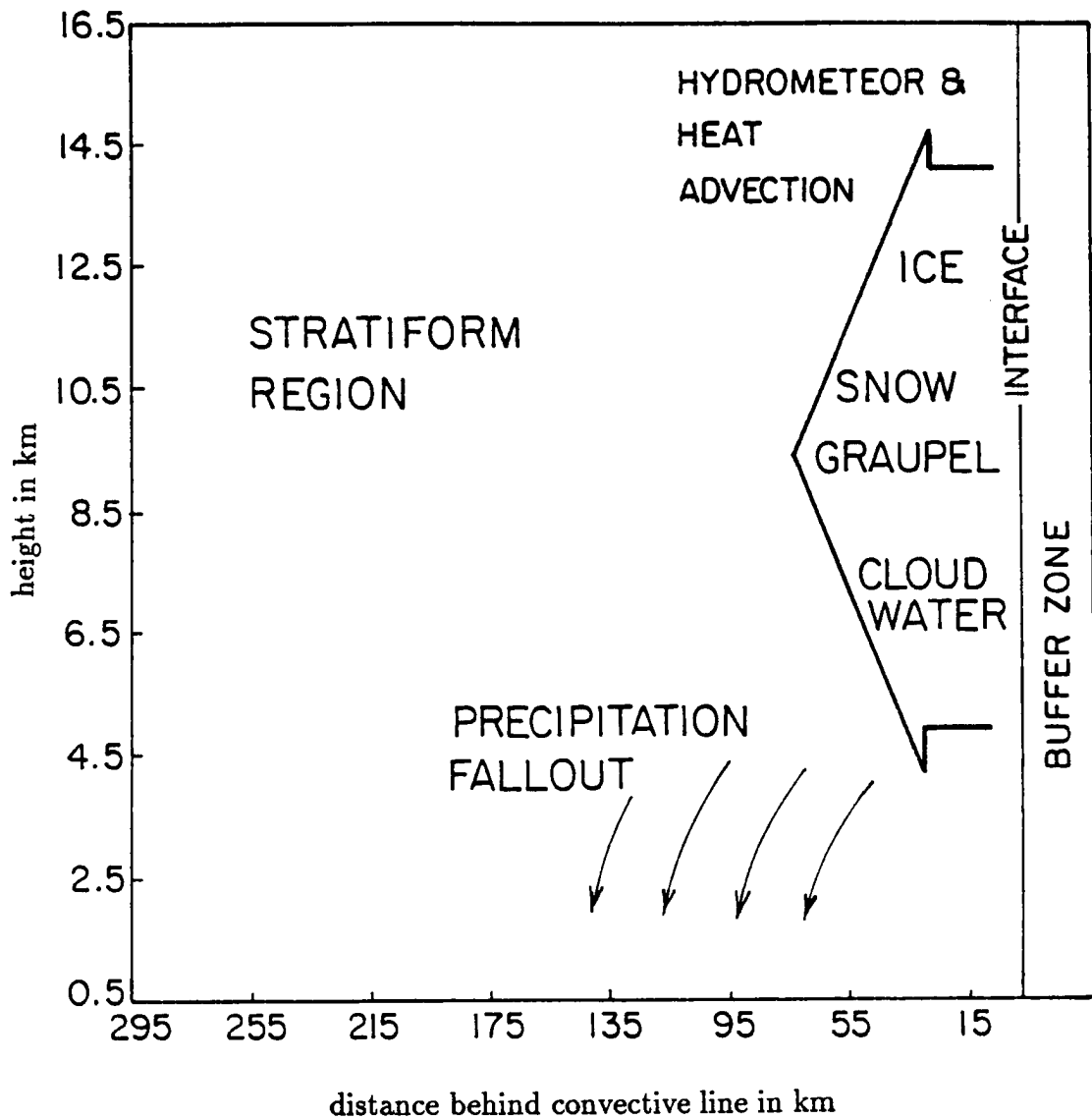
Figure 3.1: Schematic of the model domain depicting important driving processes to the circulations that may develop. Convective line is assumed to lie at the right boundary.

variables results in more realistic model output, and is supported by Durran et al. (1993). The more sophisticated two- dimensional radiative condition of Raymond and Kuo (1981) which was used by Seitter and Kuo (1983) to study a squall line thunderstorm was tested, but it decreased the quality of the results with this model, and is not used. Again as in Durran et al. (1993), it appears a fixed outflow phase speed for most variables works better than any method of calculating the phase speed.

Hydrometeor contents on the inflow boundary are prescribed according to a set pulsing rate, usually 30 minutes. As will be discussed later, this pulsing rate was necessary so that the amount of water mass entering the stratiform region agreed with the water budget of this case by Gallus and Johnson (1991). In addition, modeling studies of Dudhia et al. (1987), LaFore and Moncrieff (1989) and Fovell and Ogura (1988) showed that convection within the simulated MCSs typically pulsed with a frequency of roughly 15-30 minutes. Observations also imply this pulsing of the cumulus towers, which are believed to be left behind, and drift in a relative sense into the stratiform region of these large systems. Therefore, the hydrometeor advection into the stratiform region will realistically not be continuous, but vary over time. A sinusoidal variation is assumed for simplicity in this model. The model is insensitive to changes in the pulsing from 30 minutes to 15 minutes. A sensitivity test in which no pulsing occurred will be discussed in Chapter 6.

Radiative conditions are used for the opposite (left) boundary. A "buffer zone" is used at the inflow boundary so that the effects of the microphysical processes can be smoothed slightly in that region (see Fig. 3.1). The buffer zone consists of 5 grid points where the microphysical rates can be simply assumed to decrease linearly toward the right boundary from the calculated value 5 grid points from the boundary. This region is therefore "transparent" to the hydrometeors passing through it, and these hydrometeors are not permitted to fall. The buffer zone helps slightly to smooth the circulation at the inflow boundary. Because it is not a region where the full model equations are used, it is neglected on most figures to be shown.

This buffer zone also permits a crude convective heating parameterization to be used in some simulations, which represents the additional effects of the nearby convective line

region and transport of convective heating along with the hydrometeors into the domain. Weisman (1992) has found that the strength of the buoyancy gradient at the back edge of the convective line determines to a large extent the behavior of the rear-inflow within the stratiform region. Some of this gradient is due to processes which may be occurring within the front portion of the stratiform region, but it is unrealistic to ignore the effects of the intense diabatic heating in the convective line region. The buffer zone heating is prescribed as an attempt to consider effects the convective line would have on stratiform circulations without introducing complications to the model necessary to fully resolve convective cores. Thermodynamic conditions at the right boundary are relaxed toward initial conditions after the convective influence of heating and hydrometeor advection diminishes. Momentum transport from the convective line to the stratiform region is neglected in this study. Vertical momentum transport within the convective line has been shown to be significant in several squall line systems (Moncrieff, 1981; LeMone, 1983; Gallus and Johnson, 1992), and is often countergradient, resulting in accelerations of the flows. Momentum transport from the convective line to the stratiform region may be important, especially in generating mesoscale ascent; therefore, this momentum transport will be studied in future work. Preliminary work with this model in which additional momentum, based on the momentum budget of the 11 June system by Gallus and Johnson (1992), is transported from the convective region into the model domain has shown that this transport does not significantly affect model results.

A free-slip rigid lid is used for the upper boundary, and the lapse rate is held at its initial value. Newtonian damping (a spongey layer) similar to Kreitzburg and Perkey (1977) is applied to the upper three layers (1.2 km) to absorb vertically propagating gravity waves. The lower boundary is also rigid and free-slip, and its lapse rate is also held at the initial value. Rain is assumed to fall through the surface, and rain content is adjusted in the lowest layer based upon evaporation at the first grid point away from the boundary. A spongey layer is also used at the surface for water vapor.

In addition, water vapor is adjusted at the left boundary for inflow conditions to allow drier air to enter the domain. Initially, as will be discussed in the next section, flow is

assumed to be from front to rear throughout the domain. However, as the stratiform region matures, a rear-to-front current may develop. The vapor adjustment is accomplished by assuming that a similar gradient in vapor exists outside the domain as that initially within it. It is believed that this minimizes errors that can occur due to the limited domain. Squall lines can have large circulations extending for several hundred kilometers beyond the size of the model domain. Without the vapor adjustment, vapor can advect rapidly across the domain and reach the left boundary before significant rear-inflow develops. After that time, the radiative boundary condition would prohibit the amount of vapor from decreasing, even though rear-to-front flow is from an environment that is most likely still dry and somewhat undisturbed. A comparison of relative humidities within a smaller 200 km domain with those in the normal 300 km domain showed that this vapor adjustment resulted in humidities near the rear of the 200 km domain that were similar to those at the same relative position in the 300 km domain. This implies that the gradual vapor gradient assumed for the vapor adjustment is realistic. The adjustment generally changes the humidities at the rear points by less than 5%, since the rear boundary is rather far removed from the more intense circulations in the stratiform region.

3.5   Initial conditions

One goal of this modeling study is to rely heavily upon the dense network of observing sites available during projects like PRE-STORM, so that the model can be initialized with real data, and the simulation of the initial convective development can be bypassed. Although a significant amount of valuable data was available for initialization of the model runs, it became apparent that the precise data needed, a sounding from just behind a newly formed convective line prior to the development of any stratiform rain region, would be difficult to obtain. Therefore, some interpolation was necessary to determine the most accurate initial wind and thermodynamics for the model simulations. Pre-squall soundings were available, along with soundings taken within the established stratiform regions of the MCSs simulated, and occasionally within the convective line regions. The vertical cross-sections of Gallus and Johnson (1991) and Johnson and Hamilton (1988) were taken into

account for the initial conditions of the 11 June PRE-STORM case. In addition, the modeling study of Zhang and Gao (1989) was also consulted to determine the initial wind profile based upon model results for the time period prior to the formation of an extensive stratiform region. These model results were supplemented with some experimental runs of this model on a much finer scale grid to explicitly resolve convective development. In Chapter 8, simulations will be discussed that used a finer 2 km horizontal mesh to look at only the rear portion of the stratiform region. Initialization of that smaller domain was partially based on soundings from Russell, KS at 00 and 0130 UTC during the 4 June PRE-STORM MCS (Stumpf et al., 1991). For the GATE case discussed in Chapter 9, raw rawinsonde data were studied, along with the observational studies of Gamache and Houze (1983; 1985) and the modeling study of the same case by Nicholls (1987), Nicholls and Weissbluth (1988) and Nicholls et al. (1988). Details about the initialization of the stratiform subset domain and the GATE case are presented in Chapter 9.

For all simulations, no initial horizontal variation of the wind is permitted, and the vertical motion is assumed to be zero. In other words, it is assumed that the convective line has not had a significant impact on the region extending 300 km to its rear, other than to lead to a uniform flow field which can advect hydrometeors rearward. The explicit simulations of convection by Weisman (1992) imply that this assumption may be rather accurate. It does not appear that a rear-inflow jet had developed prior to the formation of a stratiform region in his simulations. The results of Zhang et al. (1989) imply that some rear-to-front flow may already be entering the convective line region shortly after initiation of convection. The rather idealized wind profile with its lack of initial vertical motion is used in all of the simulations so as to better understand basic physical processes.

In general, for the 11 June PRE-STORM case, the model assumes a relative wind directed from front-to-rear at all levels, with one maximum near the surface, and a stronger one at high levels (Fig. 3.2). A minimum in front-to-rear flow exists near the melting level (roughly 4 km). This wind profile resembles a mix between that of the pre-squall environment and the developing convective line region (see Fig. 10; Gallus and Johnson, 1992). Lapse rates are stable within 1 km or so of the surface, but rather unstable above

this level through 700 mb. Lapse rates then become increasingly stable with height. The temperature field is horizontally homogeneous above the melting level, but a cold pool is initialized below that level in the 75 km nearest the right boundary, peaking at roughly 3 K near the surface, to represent the region that would have been influenced by cold downdrafts from the newly developed convective line. Initial soundings near both lateral boundaries are shown in Figure 3.2. Model sensitivity to these initial conditions is discussed in Chapter 6.

The initial humidity profile with respect to water across the domain is shown in Figure 3.3. Horizontal variations in the initial relative humidity field are negligible below 3 km. Humidities are greatest below 2 km and then decrease with height up to just below the melting level. A significant horizontal variation in humidity is initialized above the melting level, with the greatest gradient within 70 km of the right boundary. Saturated conditions with respect to water exist at the right boundary within the layer in which cloud water advects into the domain from the convective line (4-9 km). Humidities decrease toward the left boundary with a constant value of just under 40% at the left boundary in the 3.7-10.5 km layer. This establishes a vapor gradient of up to 3 g kg^{-1} over a 100 km region. Humidities above 10.5 km decrease with height everywhere in the domain, with values ranging from under 30% to around 55%. The initial vapor gradient creates a buoyancy gradient that is able to produce a weak circulation, in the absence of any other processes. It was found that a horizontally homogeneous initialization of the vapor field using the rather dry values found at the left of the domain eventually produced similar model results as the horizontally varying method used, with the main difference being a short time lag. The initial variation was determined to be realistic and non-detrimental to the simulations.

Hydrometeor mixing ratio data to be used as input on the right boundary were not readily available for the 10-11 June case. Rutledge (1986) and Rutledge and Houze (1987) have determined that simulations of the microphysics within the stratiform anvil cloud are very sensitive to the hydrometeor mixing ratios chosen as input from the intense convective cores into the anvil cloud. Empirical relationships for mixing ratios based upon radar reflectivity data can be used only if one is not interested in distinguishing between
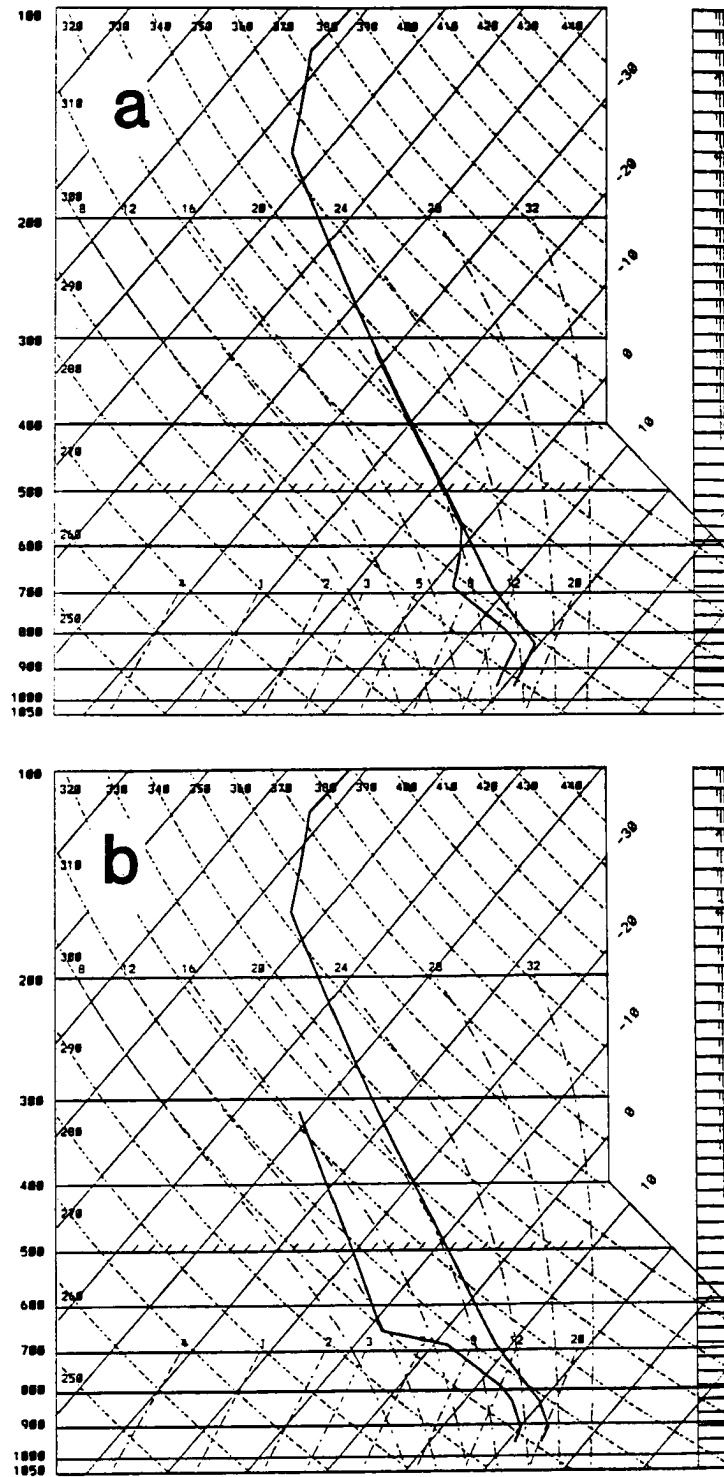
Figure 3.2: Initial thermodynamic profiles at (a) the right boundary and (b) left boundary of the domain. Ambient wind is horizontally homogeneous and can be seen at the right of each skew-T.
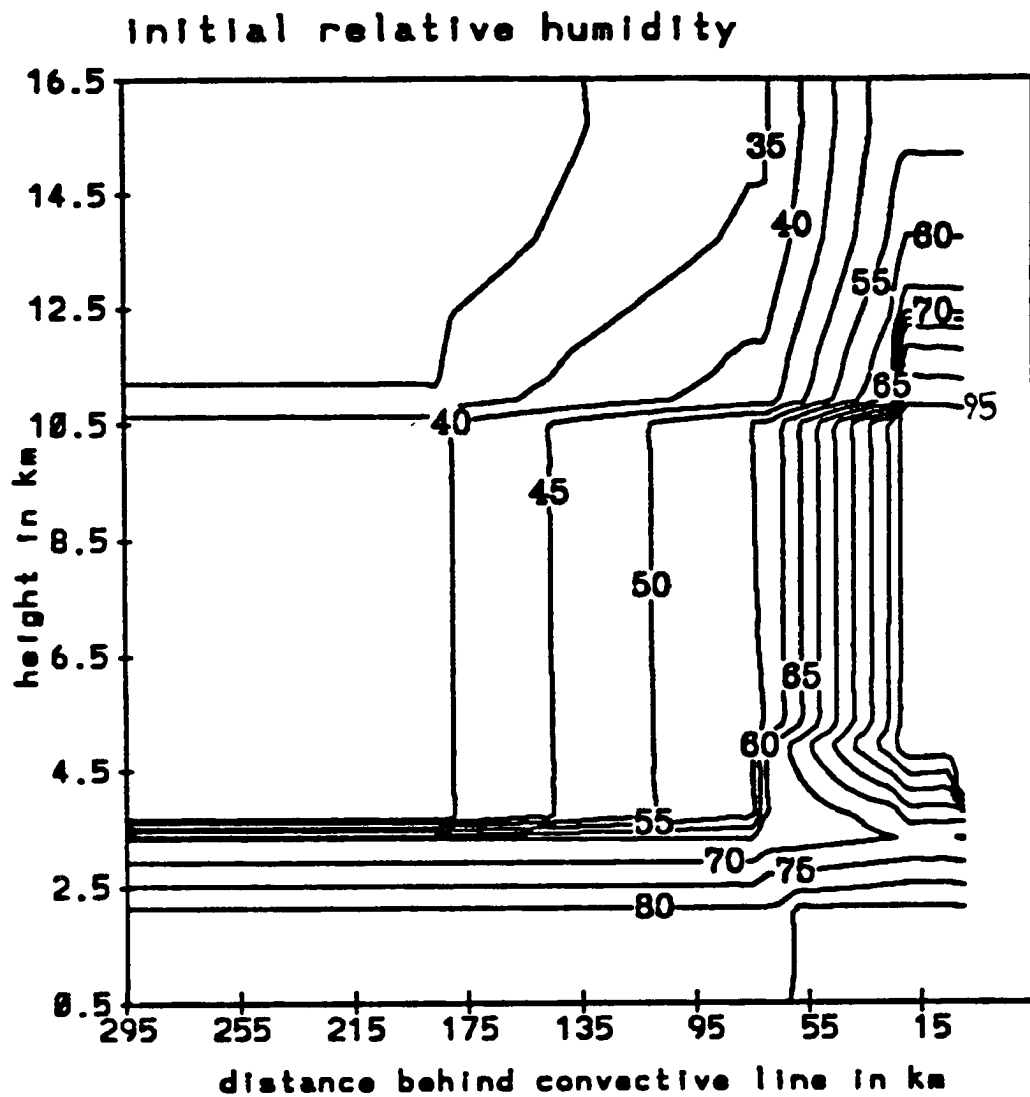
Figure 3.3: Initial relative humidity field with respect to water in the model domain. Contour interval is 5%.

different types of hydrometeors. Because snow, ice, graupel, rain and cloud water do exist together in some convective cores, these relationships could not be used for this case. Therefore, the most accurate method of estimating the hydrometeor contents in the 10-11 June squall line appeared to be the use of a detailed cumulonimbus model.

Ferrier and Houze (1989) developed a one-dimensional, time dependent, Eulerian cumulonimbus model with a primary goal being the accurate estimation of hydrometeor quantities above the melting level for input into stratiform anvil simulations. The model incorporated an ice-phase parameterization similar to that used in Rutledge and Hobbs (1984) and this model. The cumulonimbus model calculates cloud top heights, vertical velocities and water contents from a pre-squall sounding, and these quantities have been shown to be reasonably consistent with observations that are available from convective cores. The success of the model is due in part to the accurate representation of several important physical processes. Vertical mixing occurs through the inclusion of an overturning thermal circulation near the cloud top. Lateral entrainment is accurately estimated by allowing variations in the shape of the cloud with height. The simulated convection is initiated with sustained boundary layer forcing that resembles the lift caused by gust fronts associated with convection. The model also determines pressure perturbations internally consistent with the horizontal distribution of vertical velocities in the cloud.

Rickenbach (1990) applied this model to the June 10-11 PRE-STORM case, initializing it with the Enid, Oklahoma 2330 UTC sounding. Model predicted vertical profiles of reflectivity were compared with observed profiles over a three hour period corresponding to the mature phase of the convective line when the stratiform region was undergoing its development. The model profile of reflectivity most closely matching the observed reflectivity was used at several times to provide an accurate estimate of the hydrometeor contents within the squall line convection. Radar observations showed a slight decrease in reflectivity at upper levels over time implying a temporal decrease in ice hydrometeor mixing ratios. In general, vertical profiles of snow and graupel content were rather constant over the three hour period. An average value of the vertical distribution of mixing ratios of snow, graupel and ice diagnosed by Rickenbach over the three hour period is used as input for the PRE-STORM simulation in this study.

The vertical profiles of ice, snow and graupel used in this study are shown in Figure 3.4. Maximum snow and graupel mixing ratios are similar to those used in the midlatitude squall line study of Rutledge and Houze (1987), which were based upon the aircraft measurements of Heymsfeld and Hjelmfelt (1984) within Oklahoma convection. Maximum ice mixing ratios are significantly larger (2 or 3 times greater) than in the Rutledge and Houze case, and all three ice-phase hydrometeors are found extending to higher levels, with ice present up to 15 km. This may be too high for midlatitude convection, although the convection on 11 June was vigorous with reflectivities exceeding 50 dBZ. Any errors introduced by overestimating the height to which ice extended should be small since the ice contents were rather small in the highest 1 or 2 km. Houze (1977) found that in a tropical oceanic GATE squall line, line elements did extend to 16 or 17 km at the time of peak convection. Decaying line elements drifting rearward into the anvil cloud generally had their tops at 13-14 km. The 15 km height of the highest ice particles for the 11 June case is supported by Biggerstaff and Houze (1991a) who found that the ice which melted in the main precipitation band came from the 150 mb level ($\approx$ 14 km) in the convective line.

Because vertical profiles of cloud water at the back of the convective cores were not available in the Rickenbach (1990) study, values from Rutledge and Houze (1987) are used to initialize the current simulation. Cloud water is generally confined to a relatively shallow layer. The cloud water contents may be underestimated, as Heymsfield and Hjelmfelt (1984) found peak values as large as 6 g kg^{-1} in six days of penetrations into mature Oklahoma convective clouds.

As stated earlier, a pulsing rate is used for the influx of hydrometeors. The use of pulsing is not only supported by the results of other numerical simulations, but it led to better agreement with the hydrometeor advection estimated for this case in the water budget of Gallus and Johnson (1991). The diagnosed values described above, if permitted to enter the domain at a constant rate, allowed too much hydrometeor mass to enter the stratiform region over a given time period. Gallus and Johnson showed that roughly 2 mm hr^{-1} (over 50% of the average stratiform rain rates) was probably added to the observed
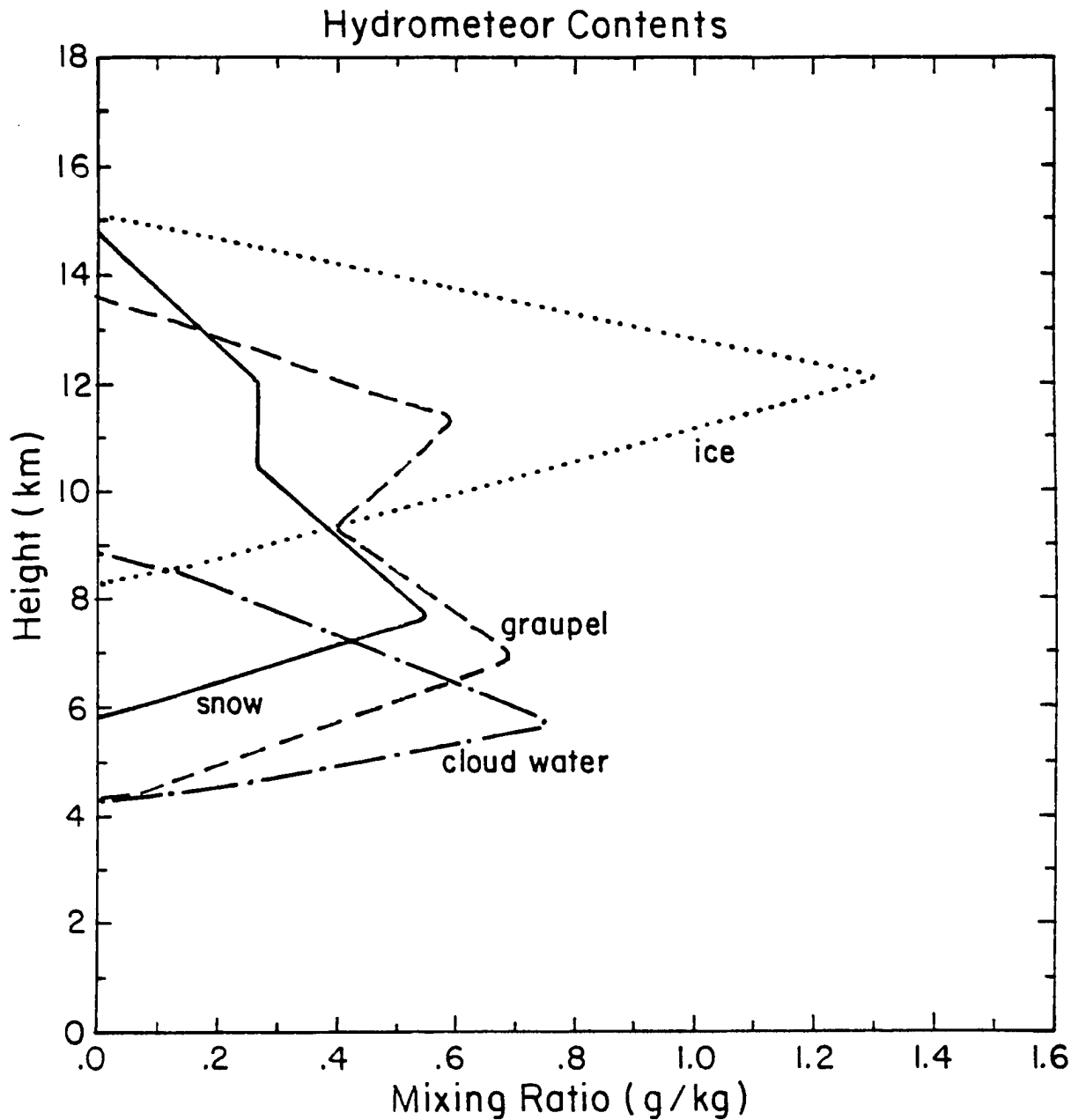
Figure 3.4: Peak hydrometeor contents within convective line cells. Profiles of snow (solid), graupel (dashed) and ice (dotted) are averages taken from Rickenbach (1990). Cloud water (dash-dotted) is taken from Rutledge and Houze (1987).

rainfall rates in the stratiform region of the 11 June system by rearward transport of hydrometeors. That water budget was based upon the Doppler reflectivity and velocity measurements of Rutledge et al. (1988), and the diagnosed rainfall rates from integrated Q_1 and Q_2 budgets (Gallus and Johnson, 1991). Sensitivity tests to be discussed in Chapter 6 found that a constant influx of hydrometeors with quantities decreased to also agree with the Gallus and Johnson water budget yields results that differ quantitatively but not qualitatively. Peak values of ascent, descent and surface rainfall are significantly diminished, but the overall evolution of the circulations is similar.

For the GATE case, values for the hydrometeor content at the inflow boundary are taken from the study of Rutledge (1986) of this same case. A similar pulsing is used, and the three-dimensional cores are averaged over the length of that study's model domain to determine values to be advected in the current model.

A crude convective parameterization is used in many simulations to test whether or not the convective line region might impact the stratiform region in additional ways beyond the rearward transport of hydrometeors. It is theorized that a significant amount of heat can be transported vertically and rearward by intense convection. In addition, circulations produced by the intense diabatic heating may interact with the circulations developing from microphysics in the anvil cloud. To investigate these effects, diabatic heating rates are prescribed over a 15 km wide portion of the buffer zone based upon the heat and moisture budget of the 10-11 June squall line performed by Gallus and Johnson (1991). In this parameterization, heating and low-level cooling pulse with the same frequency as the hydrometeors. Heating is maximized at around 6.5 km with values briefly reaching 12 K h^{-1}. The heating profile is assumed to be sinusoidal with an additional sinusoidal enhancement in the 5.5-7.5 km layer. As will be discussed in Chapter 6, the model was rather insensitive to the magnitude of the peak heating within this profile. Cooling, presumably from evaporation of falling rain and cold downdrafts, is restricted to the lowest km of the buffer zone. This cooling has a peak value of 3 K h^{-1}. It is acknowledged that this representation of the convective line is highly simplified; however, a recent evaluation of closure assumptions used in cumulus parameterizations (Grell, 1993) found that a very

simplified parameterization can do as well as a very sophisticated one. This gives some support to results obtained with the crude prescribed heating in this model.

3.6   Description of simulations

The "simplicity" of the model permitted over 100 simulations to be run as part of this research and approximately 30 will be discussed in varying degrees in Chapters 5-9. Table 3.1 provides a brief listing of the purpose of each simulation along with the chapter in which it is discussed. The many variations in the simulations were designed to yield insights into the roles of convective heating, hydrometeor advection, and specific microphysical processes, the sensitivity of the model to initial conditions and environmental variables, and internal model parameters, and the application of the model to different cases or regions. Simulations labeled with a C are those runs most closely linked with the control run. These simulations do not vary initial conditions but instead examine the physical processes of heat and hydrometeor advection, along with individual microphysical processes within the control case. Simulations labeled with an S examine sensitivity to initial environmental conditions, and assumptions relating to the convective line inputs. Simulations labeled with an I involve changes to internal model parameters such as domain and mesh size, and "knobs" of the microphysical parameterization. Simulations of the intense wake low within the 3-4 June PRE-STORM case using a specialized 2 km mesh are labeled with SP. Simulations of the tropical GATE case are labeled with GATE.

Table 3.1: Listing of simulations discussed in this paper. A brief description of the purpose of each run, along with the chapter in which it is discussed is shown. The control run includes full microphysics, convective heating, and hydrometeor advection from convective cells.

Chapter	Simulation	Description
5	CTL	Control run for 11 June
	C2	Convective heating neglected from CTL
	C3	Hydrometeor advection from convective cells neglected from CTL
	C4	Melting only with no convective heating
	C5	Melting+Evaporation with no convective heating
	C6	Deposition and Sublimation excluded with no convective heating
	C7	Condensation excluded with no convective heating
	C8	Sublimation only with no convective heating
	C6'	Deposition excluded with convective heating included
	C7'	Condensation excluded with convective heating included
	C9'	Evaporation excluded with convective heating included
6	S1	Uniformly dry initialization
	S2	Moister initialization
	S3	Increased instability for initialization
	S4	Decreased instability for initialization
	S5	Weaker front-to-rear ambient flow
	S6	Altered vertical profile of ambient front-to-rear flow
	S7	50% reduction in convective hydrometeor input
	S8	50% increase in convective hydrometeor input
	S9	Increased convective heating
	S10	Altered vertical profile of convective heating
	S11	Pulsing neglected
7	I1	Smaller domain version of CTL
	I2	Expanded domain version of CTL
	I3	Adjustments in the ice activation scheme
	I4	Adjustments in the raindrop size distribution
	I5	Adjustments in the snowflake size distribution
	I6	Smaller horizontal mesh version of CTL
8	SP	Finer resolution domain of rear portion of stratiform region with steady precipitation
	SP1	Finer resolution domain of rear portion of stratiform region with diminishing precipitation
9	GATE	Control run for 12 September GATE case
	GATE1	Convective heating neglected from GATE

Chapter 4

OBSERVATIONS OF THE 11 JUNE SQUALL LINE

The 10-11 June PRE-STORM squall line is a classic example of a quasi-two dimensional squall line with an intense leading convective line trailed by a region of stratiform rainfall. Because the system grew to maximum intensity while nearly centered within the dense data array of the PRE-STORM project, it has been studied extensively using both observations and numerical models (e.g. Augustine and Zipser, 1987; Rutledge et al., 1988; Johnson and Hamilton, 1988; Vasiloff and Bluestein, 1988; Rutledge and MacGorman, 1988; Zhang and Gao, 1989; Gao et al., 1989; Johnson et al., 1990; Gallus and Johnson, 1991, 1992; Biggerstaff and Houze, 1991a, 1991b, Grell, 1993). Because these studies give detailed descriptions of the synoptic setting, internal airflow, reflectivity structure and heat, moisture, momentum, and vorticity budgets, this chapter will provide only a brief background of the system, concentrating on aspects that can be compared with the numerical simulations to follow.

The 10-11 June squall line began as broken line convection (Bluestein and Jain, 1985) over southwestern Kansas and the Oklahoma panhandle ahead of a cold front prior to 2100 UTC 10 June. The environment was moderately unstable with a CAPE of 1660 J kg^{-1} (Biggerstaff and Houze, 1991a). Convective inhibition was small, only 77 J kg^{-1}. The low-level shear was $\approx$ 10 m s^{-1} over the lowest 2.5 km, which would be classified as intermediate based upon the modeling work of Weisman et al. (1988). The system later grew to include a transition zone and broad stratiform region as it passed through the PRE-STORM domain. The evolution of the low-level reflectivity field is shown in Figure 4.1 (from Rutledge et al., 1988). Reflectivities in the convective line peaked between 0100 and 0300 UTC (Figs. 4.1b, c), during which time the stratiform region was growing
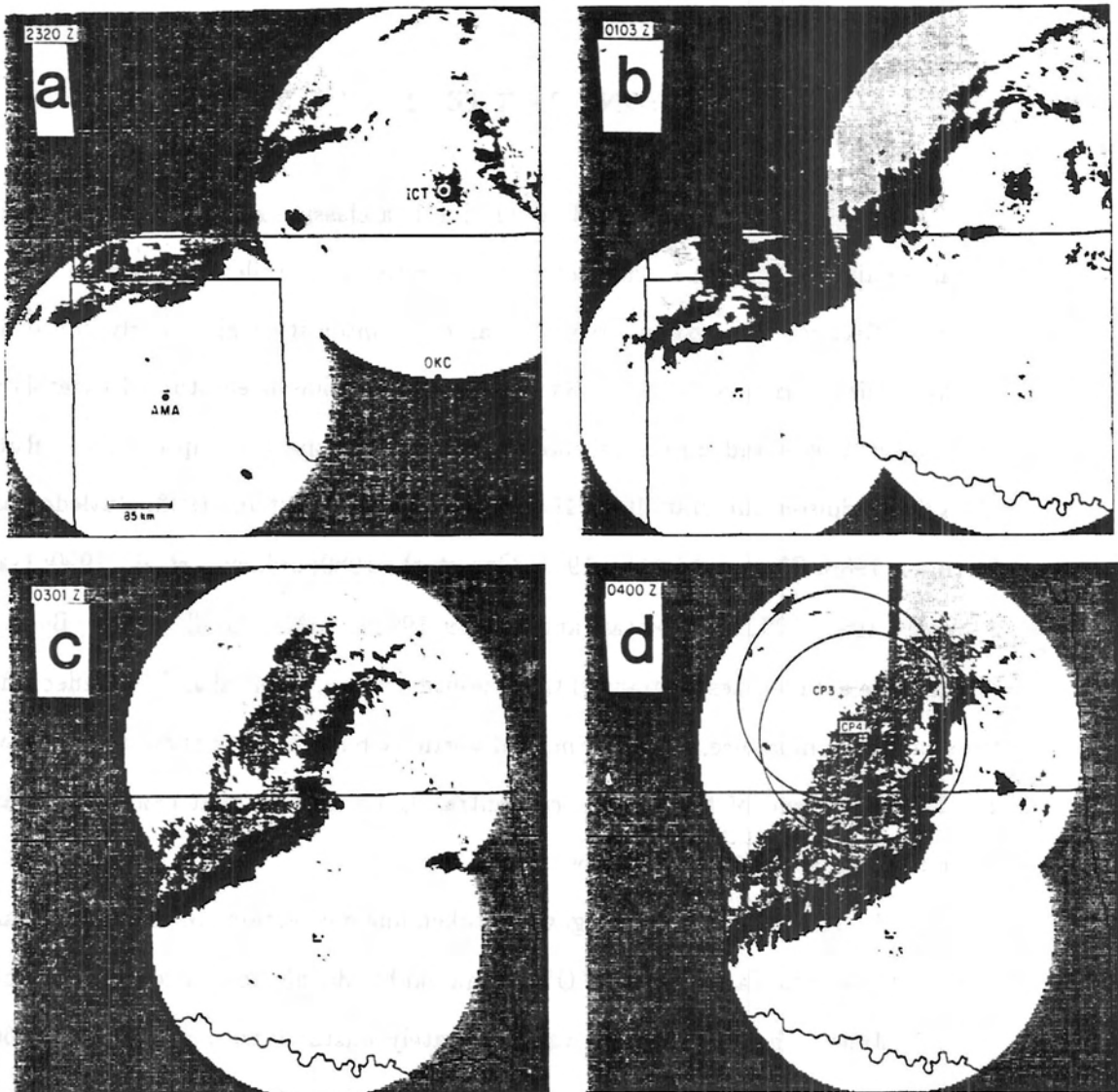
Figure 4.1: Composite low-level echo patterns from the AMA, ICT and OKC WSR-57 10 cm radars for (a) 2320 UTC, (b) 0103 UTC, (c) 0301 UTC, (d) 0400 UTC, (e) 0600 UTC, and (f) 0700 UTC (taken from Rutledge et al., 1988). Reflectivity of 15-25 dBZ shown with light stippling; 25-35 dBZ, heavy stippling; 35-50 dBZ, hatching; and $\geq$ 50 dBZ, solid. Circles at 0400 UTC show the coverage of CP-3 and CP-4 radars.
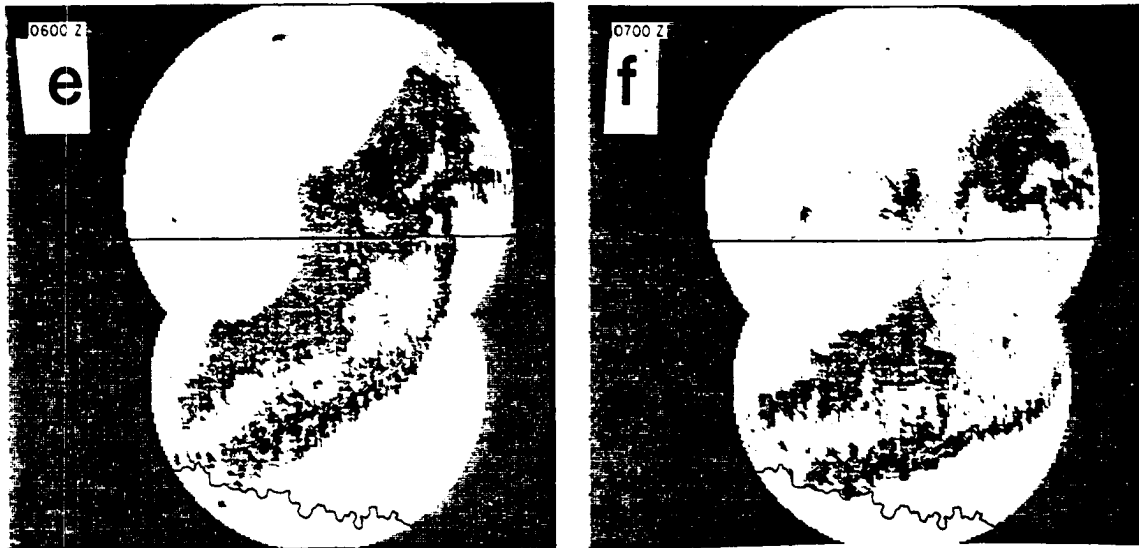
Figure 4.1: continued

significantly in area and intensity. The initial development of a stratiform region appeared to occur just prior to 0000 UTC. The stratiform region appeared to reach its maximum intensity between 0400 and 0600 UTC (Figs. 4.1d,e) with surface rainfall rates as high as 6 mm h^{-1} in areas with reflectivity exceeding 35 dBZ.

Average rainfall rates in the stratiform region at these times were around 3 mm h^{-1} (Gallus and Johnson, 1991). Although these rates are significantly less than those within the convective line, the large area covered by stratiform rainfall allowed the region to provide 29% of the total precipitation falling from the convective system (Johnson and Hamilton, 1988). During this time, and later when the stratiform region began dissipating (Fig. 4.1f), the transition zone broadened markedly, as the convective line moved with a much faster speed (over 15 m s^{-1}) than the stratiform region (roughly 8 m s^{-1}).

The cloud shield associated with the 10-11 June squall line was extensive, covering between 100,000 and 150,000 km^2 during much of its lifetime (Fig. 4.2, from Rutledge et al., 1988). At 0200 and 0300 UTC (Figs. 4.2a, b), intense convective cells in the leading line had cloud top temperatures of nearly -80° C. As the convective line weakened after this time, minimum cloud top temperatures warmed, implying that less hydrometeor advection would have occurred at high levels after 0300 UTC (Figs 4.2c, d). By 0600 UTC (Fig. 4.2d), the cloud shield had begun to weaken noticeably, with erosion of the cloud shield enhanced in western Kansas where the rear-inflow jet was most pronounced.

The squall line developed in an environment with small line-normal wind shear through much of the depth of the troposphere (Johnson and Hamilton, 1988; Gallus and Johnson, 1992). Storm-relative winds were generally directed from front to rear (FTR) during the initiation of convection. A significant along-line component of the wind existed at high levels. Within a few hours of initiation, the near-squall line normal winds had changed significantly, with three distinct currents present. High θ_e air entered the system from low-levels at the front, and quickly ascended through the convective line, exiting toward the rear at middle and high levels. Doppler and rawinsonde data (Rutledge et al., 1988; Gallus and Johnson, 1991) showed this current to be strongest over the stratiform region prior to and around 0300 UTC with peak values exceeding 25 m s^{-1} at around
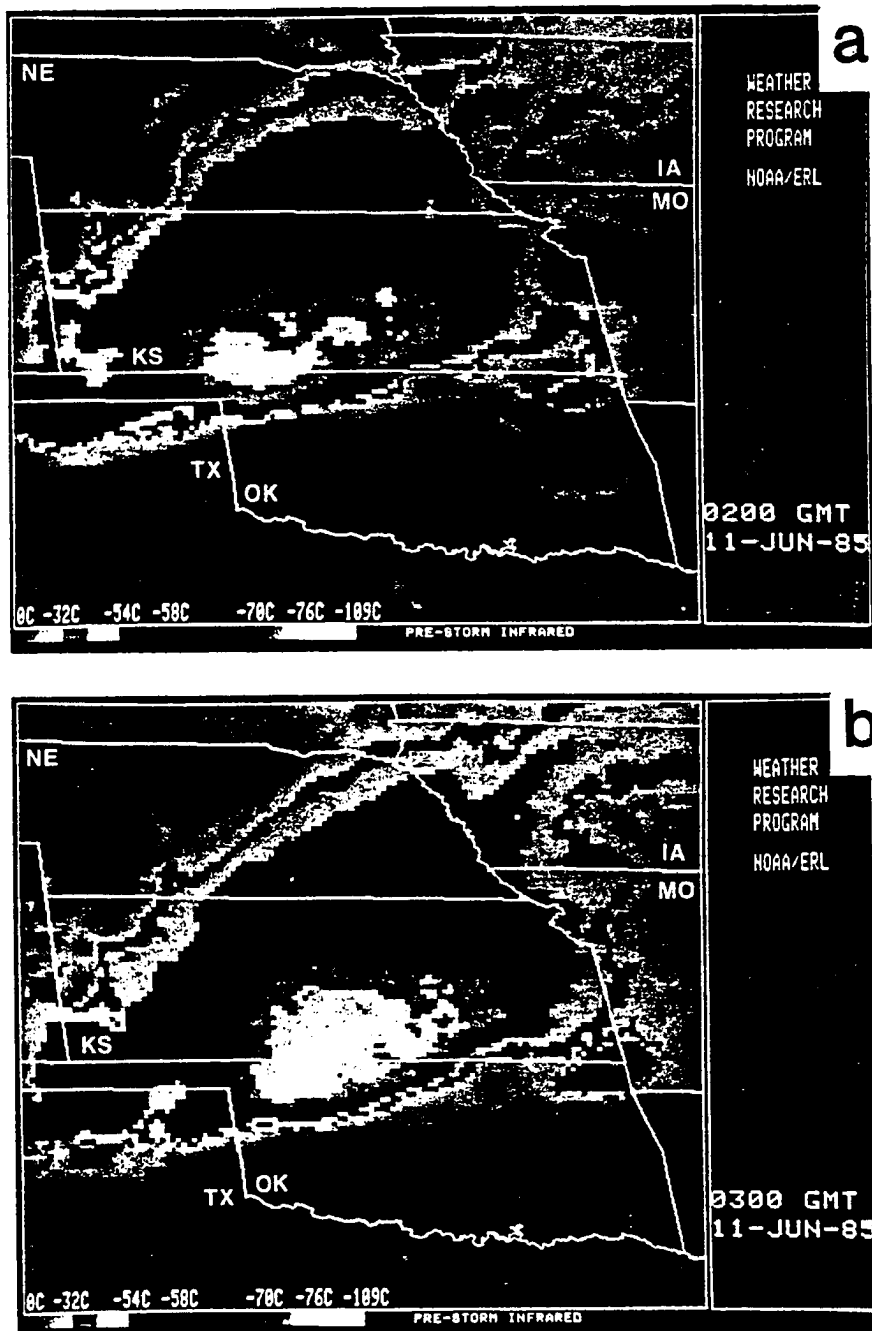
Figure 4.2: Infrared satellite images for the 11 June squall line at (a) 0200 UTC, (b) 0300 UTC, (c) 0400 UTC, and (d) 0600 UTC (taken from Rutledge et al., 1988). Temperature scale is shown at the lower left of each figure.
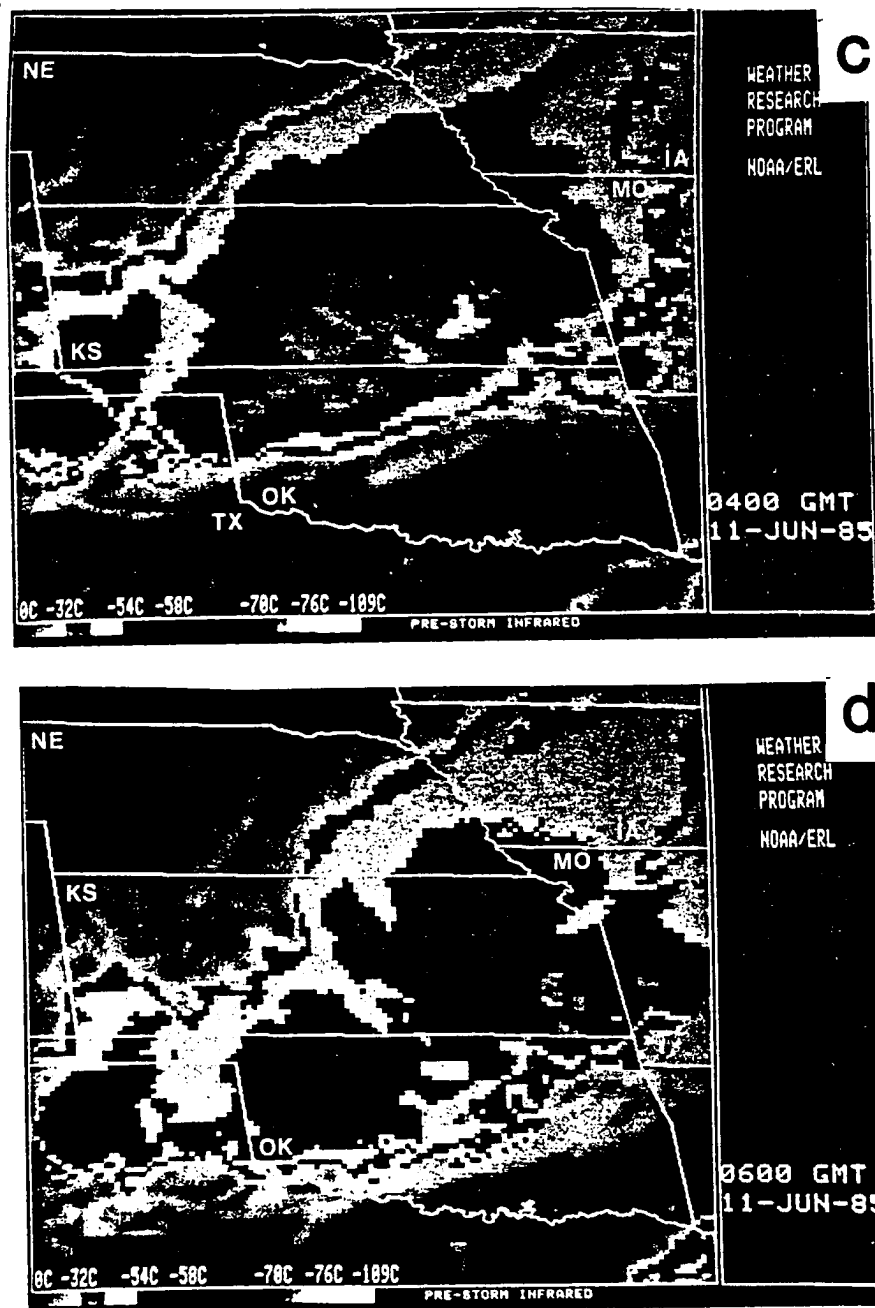
Figure 4.2: continued

the 10-12 km level. A sample of the horizontal winds as measured by Doppler radar and rawinsondes is shown in Figure 4.3. Doppler data from the CP3 (Fig. 4.3a) and CP4 (Fig. 4.3b) radars at 0414 UTC, around the time of maximum intensity of the stratiform region, is taken from Rutledge et al. (1988). Objectively analyzed rawinsonde data at 0300 UTC (Fig. 4.3c), 0600 UTC (Fig. 4.3d) and 0730 UTC (Fig. 4.3e) is taken from Gallus and Johnson (1991).

The data from the Doppler radars show that variations existed in the wind field between CP3 and CP4 (Fig. 4.3a, b), implying that the system was not strictly two dimensional. In both of these figures, the strongest rear-to-front (RTF) flow was found at the back edge or just behind the region of surface precipitation, which extended to about 30 km behind both radars. The peak speeds were just over 15 m s^{-1} at both radars. Through most of the stratiform rain region, the rear-inflow jet was located below the melting level with a gradual descent to below 2-3 km in the convective line region (around 100 km ahead of the radar sites). Rear-inflow extended to as high as at least 8 km farther toward the back of the anvil cloud, and remained strong in this region. The axis of the FTR jet aloft extended from around 5-7 km at the back of the convective line region to 9-10 km at the back of the region of surface stratiform rain, to as high as 11 or 12 km at the rear of the cloud. Peak magnitudes were generally near 20 m s^{-1} at this time. Beneath the rear inflow jet, another FTR current existed near the surface, the result of an overturning downdraft beneath the stratiform anvil cloud. The Doppler data show peak values of this flow of around 20 m s^{-1}.

The rawinsonde data lack the resolution of the Doppler data, since the objective analysis was done using composited data with an average station spacing of roughly 80 km, and the values shown in the figures are averages over the 3D system at given distances behind the convective line. However, temporal trends in the flow fields can be seen over this 4.5 hr period. The location of the squall line system with its stratiform region, transition zone, and convective line is shown as a bar beneath each rawinsonde-derived figure (Figs. 4.3c, d, e). At 0300 UTC (Fig. 4.3c) when the stratiform region was still growing in intensity, the rear-inflow jet appeared to be weaker than at later times, and
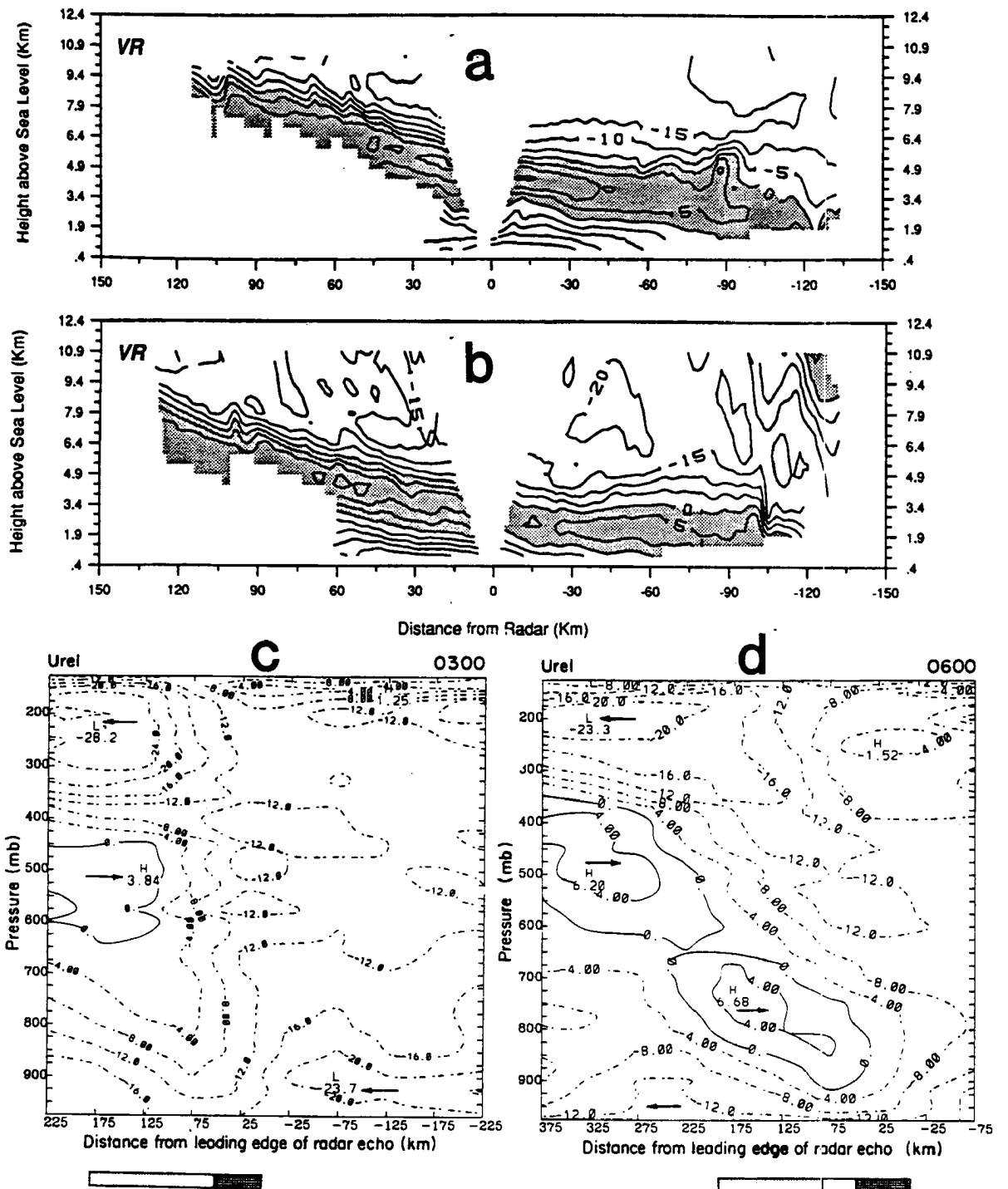
Figure 4.3: Horizontal storm-relative velocities for the 11 June squall line from the (a) CP-3, and (b) CP-4 Doppler radars at 0414 UTC (from Rutledge et al, 1988), and from the rawinsonde-based study of Gallus and Johnson (1991) at (c) 0300 UTC, (d) 0600 UTC, and (e) 0730 UTC. Rawinsonde-derived values are taken from 3-hourly composites centered at each time. Contour interval for the Doppler results is 5 m s^{-1}; 4 m s^{-1} for the rawinsonde results. Shading in (a) and (b) represents rear-to-front flow. Bar below (c), (d) and (e) represents position of the squall line with convective line darkest shading, stratiform region lighter shading, and transition zone between them.
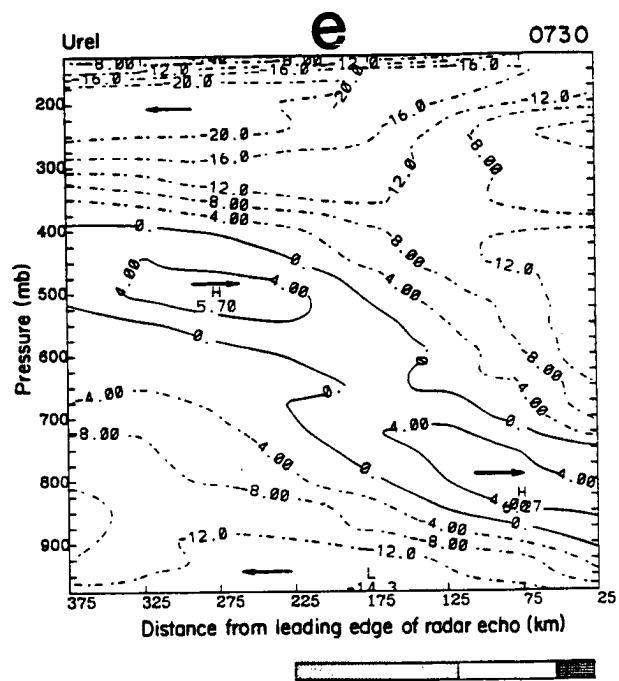
Figure 4.3: continued

did not descend as far toward the surface and convective line region. The jet seemed to advance with time, eventually outrunning the convective line. Some of the weakness in the jet at 0300 UTC may be due to data deficiencies, since the system had just entered the main sounding network at this time. Peak averaged RTF flow is over 6 m s^{-1}, but individual rawinsonde sites did record 15 m s^{-1} flow. The rear-inflow jet appeared to remain strong with little indication of weakening, even at 0730 UTC when the system itself was dissipating rapidly. The FTR jet slowly decreased in intensity after the convective line had reached its peak intensity, with peak values of nearly 30 m s^{-1} at 03 UTC weakening to slightly more than 20 m s^{-1} by 0730 UTC. The strongest FTR flow existed at high levels (10-13 km) at the rear of the stratiform region. The FTR flow near the surface maintained a peak intensity of around 15 m s^{-1} through the life of the system.

The opposing jets in this system were associated with strong midlevel convergence in the stratiform region, which fed a mesoscale updraft at middle and high levels, and a downdraft below. Observational data for the strength of the small-scale convective updrafts are not available, but modeling work with a 25 km grid (Zhang and Gao, 1989) showed peak intensities of several meters per second, centered around 5 km. Peak ascent was probably as large as 20-30 m s^{-1} in very small convective cores. Surface rainfall rates in the convective line were as large as 50-100 mm h^{-1}, supporting the presence of strong ascent. The broader stratiform region was sampled by observational methods and some values of vertical motion are shown in Fig. 4.4. EVAD-derived vertical motion from both the CP3 and CP4 Doppler radars over a roughly 90 minute period is shown in Figs. 4.4a and b (from Rutledge et al., 1988). These figures show the transition from low-level descent to ascent aloft occurs between the melting level, 4.1km, and 6.5 km. The depth of the mesoscale downdraft varies significantly between the CP3 and CP4 sites. Peak descent at CP3 is often close to the melting level, while at CP4, the peak descent occurs around 2.5 or 3 km. The greatest values of subsidence are between 60-75 cm s^{-1}. Strongest ascent aloft is generally between 50-60 cm s^{-1}. The level of peak ascent varies between the radars and at different times, between 8 km at 03 UTC at CP3, to as high as 12 km at CP4 at 0430 UTC.
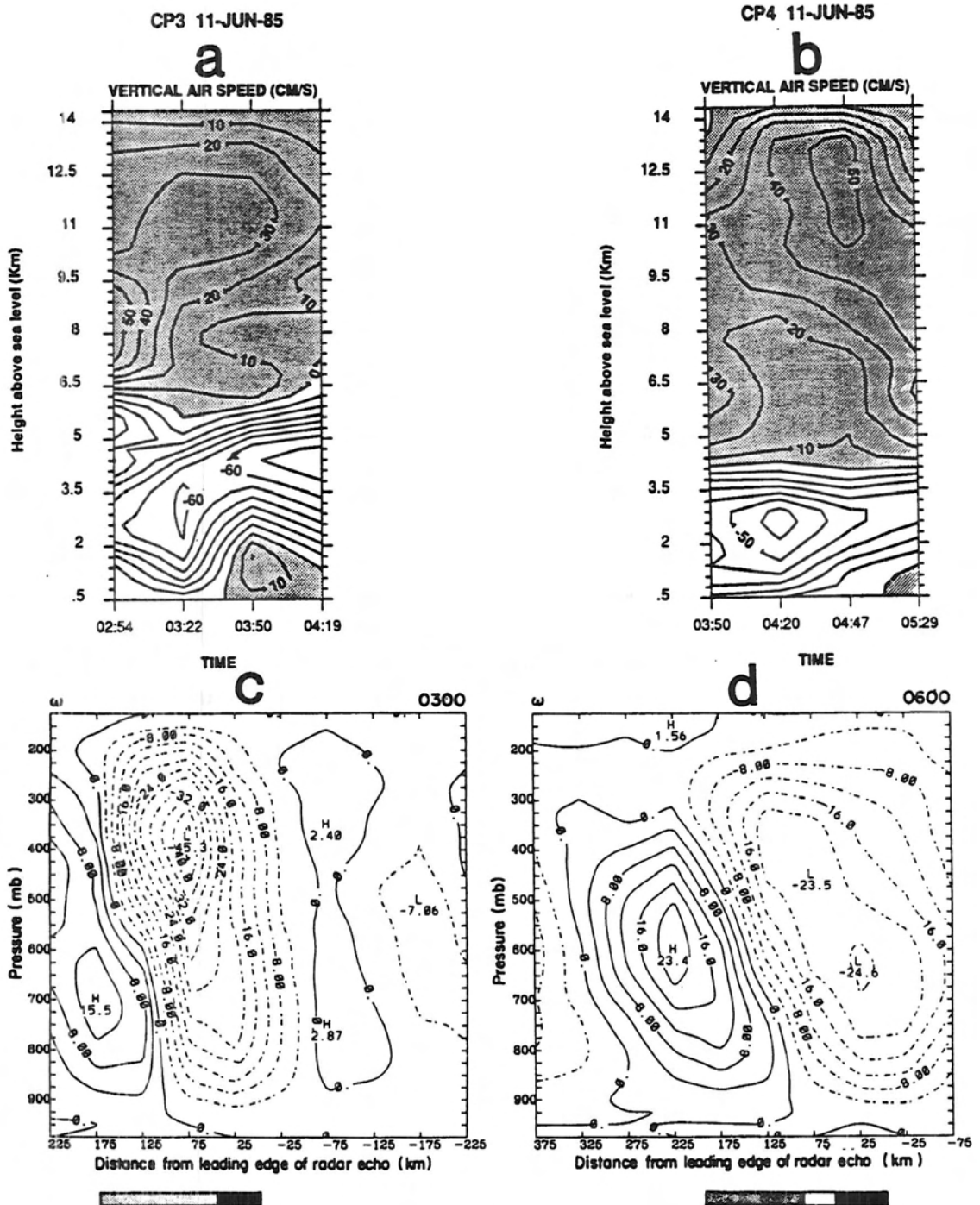
Figure 4.4: Vertical velocities for the 11 June system from EVAD Doppler analyses at (a) CP-3 between 02:54 and 04:19 UTC, and (b) CP-4 between 03:50 and 05:29 UTC (from Rutledge et al., 1988), and from kinematic method applied to rawinsonde data at (c) 0300 UTC, (d) 0600 UTC and (e) 0730 UTC (from Gallus and Johnson, 1991). Contour interval for Doppler data is 10 cm s^{-1}, and for rawinsonde data, 4 μb s^{-1}. Shading in (a) and (b) represents upward motion. Bar below (c), (d) and (e) is same as in Fig. 4.3. In (c)-(e), 1 μb s^{-1} is roughly 1 cm s^{-1} below 700 mb, roughly 2 cm s^{-1} at 400 mb, and 4 cm s^{-1} at 200 mb.
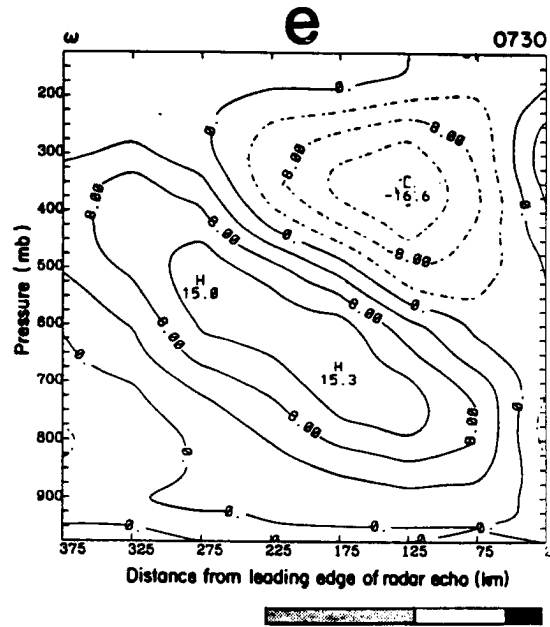
Figure 4.4: continued

The evolution of vertical motions can be seen in the rawinsonde-derived ω field at 0300 (Fig. 4.4c), 0600 (Fig. 4.4d) and 0730 UTC (Fig. 4.4e). Aliasing of data between the convective line and stratiform regions is a significant problem, particularly in the 0300 and 0600 UTC data. The peak ascent in the stratiform region at 0730 UTC, when aliasing was less of a problem, was around 30 cm s^{-1}. The strongest stratiform region ascent generally occurs around the 300 mb level, or 9 km. This level is significantly lower than the peak level diagnosed by the Doppler radars, but it agrees well with many other squall line cases (e.g. Gamache and Houze, 1982). Doppler-derived vertical motions are susceptible to error at high levels due to approximations that must be made about cloud top height. Although aliasing of data also affects the diagnosed mesoscale downdraft, the rawinsonde data do indicate peak descent of between 15 and 25 cm s^{-1} over broad regions, with the strongest descent at around the same general levels as found by the Doppler radars, generally near or just above the melting level. The rawinsonde data imply that the mesoscale downdraft may have extended to higher levels when the system was rapidly dissipating (Fig. 4.4e). Descent of at least several cm s^{-1} occurs over a 200 km wide region after 0600 UTC.

The broad regions of ascent and descent, along with the associated microphysical processes in the large region of stratiform rainfall resulted in temperature perturbations that induced mesoscale pressure features. The 10-11 June squall line was associated with both surface pressure perturbations including a surface mesohigh, pre-squall mesolow and wake low (Johnson and Hamilton, 1988), and midlevel mesolows (Biggerstaff and Houze, 1991a; Gallus and Johnson, 1992). The wake low just behind the back edge of surface precipitation had local pressure perturbations as low as 2 mb below the region average around 0300 UTC, with about a 6 mb gradient over a 200 km distance between the wake low and the mesohigh at the back of the convective line region (Johnson and Hamilton, 1988). The average pressure at the back of the stratiform rain region was similar to or only a few tenths of a millibar below the pressure 100 km behind the system, but about 2.5-3.0 mb lower than the average pressure in the front portion of the stratiform region.

The detailed data available for this case depicting variations in the circulations, rainfall, and pressure fields enable relatively thorough validation of model results. As implied

above, however, even this data must be interpreted in light of the area over which the data were sampled, the location of the data relative to the system, and possible errors that can affect observations. Detailed comparisons of the model simulations in this paper with observations from the 11 June case follow in Chapters 5 through 7.

Chapter 5

NUMERICAL SIMULATIONS OF THE 11 JUNE SQUALL LINE

A series of simulations were done with the 2D model to investigate the effects of both hydrometeor advection and heat advection from the convective line on circulations that develop in the stratiform region. The purpose of this chapter is to discuss the ability of the model to reproduce realistic features observed in the stratiform region of the 10-11 June squall line, and to also discuss the processes which play important roles in the development and evolution of the circulations. This chapter will explore interactions between heat and hydrometeor advection, and the corresponding roles of both in situ production (within the mesoscale updraft) of condensate, and the advected condensate from the convective line. The individual roles of certain microphysical processes are also examined. In the next chapter, model sensitivity to initial conditions and other environmental variables is investigated. Model sensitivity to domain and grid sizes, time step, and alterations in the microphysical and turbulence parameterizations will be discussed in Chapter 7.

5.1 Control run

In the first simulation to be discussed (labeled CTL for control run) hydrometeors advect into the domain from the right boundary, with the peak mixing ratio profiles shown earlier in Fig. 3.4. Heat also advects into the domain, and the heating profiles discussed in chapter 3 are used within a 15 km wide region in the buffer zone at the right boundary. The intense heating representing the convective line may also play a role in generating gravity waves that influence the circulations within the domain. The heating and advection of hydrometeors are time dependent, and the pulses have a period of 30 minutes. The hydrometeor mixing ratios advecting into the domain are prescribed to begin a slow decrease at 300 minutes, and cease at 405 minutes. The intense "convective"

heating in the buffer zone increases during the first 15 minutes and the maximum pulse values remain at the established rate until 190 minutes, when they are permitted to slowly decrease and cease at 300 minutes. In effect, the time variations represent active convection with intense condensational heating for approximately 3 hours, with a gradual weakening thereafter. Hydrometeors are assumed to be present in the dissipating convection, even during the time period where convective heating is becoming rather small. By 405 minutes, all influences from the convective line have stopped.

The pulsing and finite time periods for heating and hydrometeor input approximate the observed squall line conditions reasonably well. The stratiform region of the 10-11 June squall line began to form shortly before 0000 UTC, and this time can be considered the start of the model simulations. Convective elements in the leading line were most intense around 0200 UTC, and began to noticeably weaken after 0300 UTC, or roughly 180 minutes in the simulation. Highest radar reflectivities over broad areas of the stratiform region occurred during the period 0430-0530 UTC, or 270-330 minutes, with the stratiform region remaining well-developed through about 0600 UTC, or 360 minutes. After this time, rapid dissipation was observed.

The ambient wind field which permits the advection in this simulation has been discussed in chapter 3. Winds are from front-to-rear at all levels, although speed shear is present. Initial humidity and temperature gradients do exist in the domain, as explained earlier in chapter 3. All microphysical processes are permitted in CTL.

5.1.1 Hydrometeor fields

In CTL, snow advects into the domain and moves rearward, gradually experiencing increasing upward motion in the anvil cloud (Fig. 5.1a, b). Even though the maximum mixing ratios exiting the convective towers are no larger than 0.6 g kg^{-1}, snow quantities more than double that amount occur by 180 minutes (Fig. 5.1a). Through this time, vertical motions are weak in the domain (shown later), but the terminal fallspeeds of the snow are small enough, generally 1 -1.5 m s^{-1}, that vapor deposition adds to the snow mass. Riming and collection of cloud ice also add to the snow mass but play a much less important role. The majority of the increase in the snow mixing ratios is due to
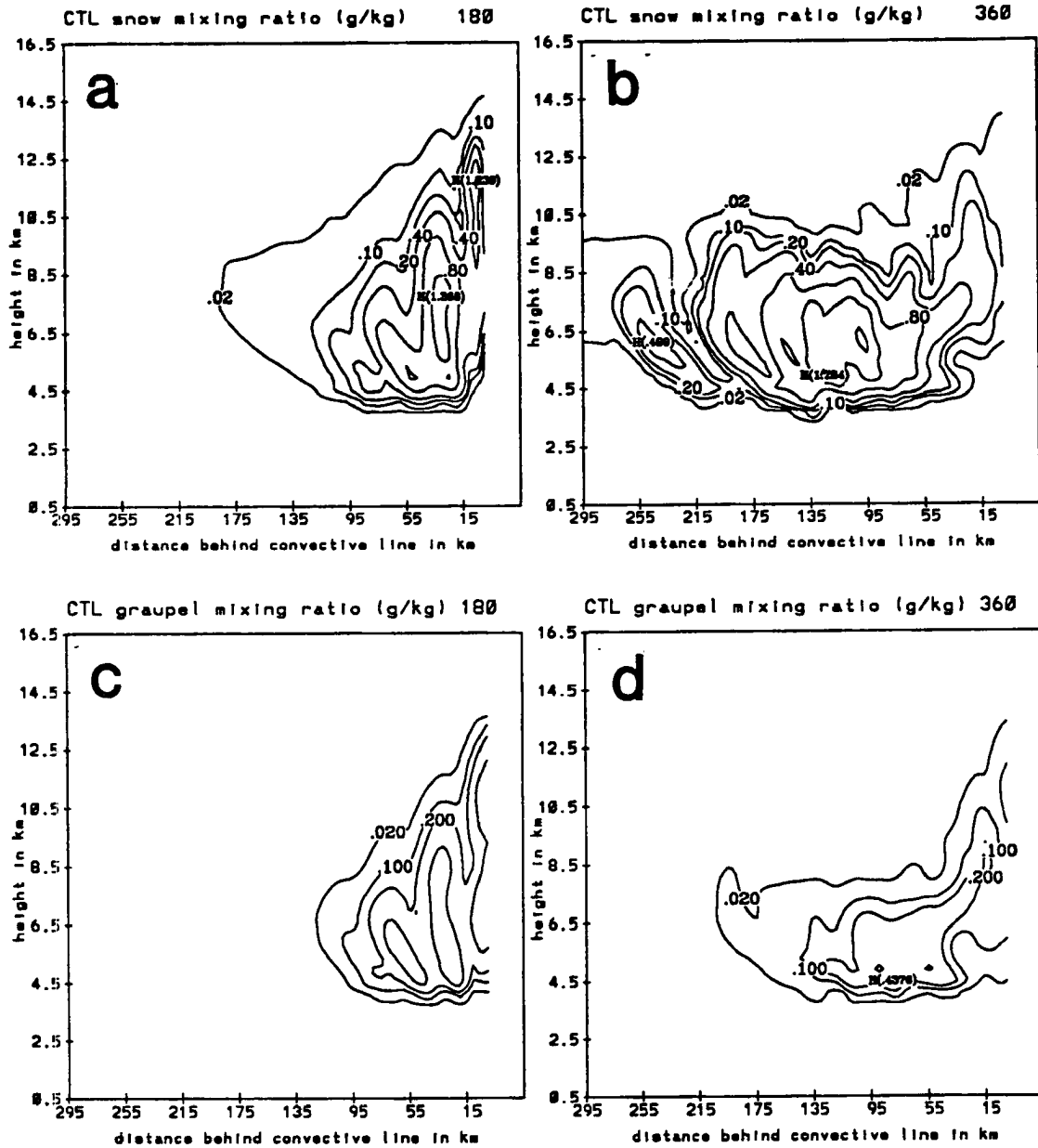
Figure 5.1: Mixing ratios (g kg^{-1}) in the control model simulation of snow at (a) 180 minutes, and (b) 360 minutes, and graupel at (c) 180 minutes and (d) 360 minutes. Contours at .02, .1, .2, .4, .8, 1.2, and 1.6 g kg^{-1}.

the autoconversion of ice to snow, since ice mixing ratios exiting the convective line are significantly greater than the 0.4 g kg^{-1} conversion threshold used in the microphysical parameterization. In addition, as will be shown later, vertical motions are strongest in a region just behind the convective line. The enhanced upward motion at the front of the anvil cloud has been observed by Doppler radar in this case (Matejka and Schurr, 1991), and helps to enhance the vapor deposition onto snow that has entered the domain from the convective line. By 270 minutes, broad areas of significant upward motion are developing within the anvil cloud, and this increases the production of snow. From 270 minutes through 360 minutes (Fig. 5.1b), snow quantities are as large as 1.8 g kg^{-1}. The contours of mixing ratio are relatively horizontal at 360 minutes, the result of a well-developed mesoscale updraft. After 300 minutes, hydrometeor advection into the domain decreases, becoming negligible by 405 minutes. Even though snow contents decrease at the end of the simulation, upward motions are sufficient to allow significant generation of snow within the anvil cloud so that peak snow contents are still around 1.6 g kg^{-1} at 405 minutes (figure not shown).

Low-density graupel, or more accurately aggregates of snow, also advect across the domain (Fig. 5.1c, d). Unlike snow, the peak graupel contents at both 180 and 360 minutes are not significantly different from those entering the domain. The slightly faster fallspeed of the graupel decreases the amount of vapor deposition that occurs, and does not allow for as much collection of the ice. Graupel does not grow by autoconversion from ice, as snow does. Additionally, the microphysical parameterization first allows snow to grow if excess vapor is present, and then later graupel if the same conditions are still met. In this regard it favors the growth of snow. Significant amounts of graupel are generally restricted to within 100 km or so of the convective line, even at 360 minutes (Fig. 5.1d). The peak graupel fallspeeds are around 2 m s^{-1}.

The fallspeeds of the snow and graupel generally agree with those determined from Doppler radar data for this case (Rutledge and MacGorman, 1988; Rutledge et al., 1988), although the CP3 radar did find a small region in the 2 km layer just above the melting level where fallspeeds were as large as 3 m s^{-1}. The CP4 radar did not measure fallspeeds this

large. The failure of the model to produce graupel with fallspeeds of this magnitude may be due to several factors. The size distribution of the graupel may be slightly in error, and the parameters used in the equations for fallspeed may need adjustment. Isolated regions of particularly strong ascent may not be diagnosed in the 2D model, so that graupel mixing ratios are underestimated at certain points. In addition, the low-density graupel used as the third ice-class in the microphysical parameterization would more accurately be called aggregates of snowflakes. The measured 3 m s^{-1} fallspeeds may indeed reflect the presence of true higher-density graupel in certain regions of the anvil cloud, as stated by Rutledge and MacGorman (1988). In general, the fallspeeds calculated by the model agree well with observations through a deep layer over a large region, and deficiencies in the parameterization itself appear to be minor.

Large amounts of ice are converted to snow, or collected by snow and graupel, upon entering the domain and this can easily be seen in the mixing ratio field at 180 minutes (Fig. 5.2a), which shows a sharp dropoff in the ice contents at the right boundary. Significant ice is initiated in the 10-11 km layer after approximately 270 minutes, where vapor is present in sufficient quantities. This is evidenced by a secondary peak in ice mixing ratios around the 10.5 km level at 360 minutes (Fig. 5.2b). Ice rapidly advects across the domain, reaching the rear boundary by 225 minutes. Ice is assumed to have a small fallspeed, 10 cm s^{-1}, independent of mixing ratio. This differs slightly from the work of Rutledge and colleagues where ice was assumed to have a negligible fallspeed.

Although cloud water advects into the domain from the convective line, it is quickly collected by snow and graupel, and sizeable amounts also evaporate in subsaturated air (Figs. 5.2c,d). Cloud water is very sensitive to changes in the humidity within 1 % of saturation. Through 180 minutes, significant cloud water is restricted to points near the convective line (Fig. 5.2c) After this time, upward motion is stronger and condensation produces over 0.1 g kg^{-1} of cloud water in a few regions at 360 minutes (Fig. 5.2d). Although advection of cloud water from the convective line is negligible by the end of the simulation at 405 minutes, extensive upward motion continues to produce large areas of significant cloud water content. Because cloud water contents remain less than a few tenths of 1 g kg^{-1}, no conversion to rain occurs since the threshold used was 1 g kg^{-1}.
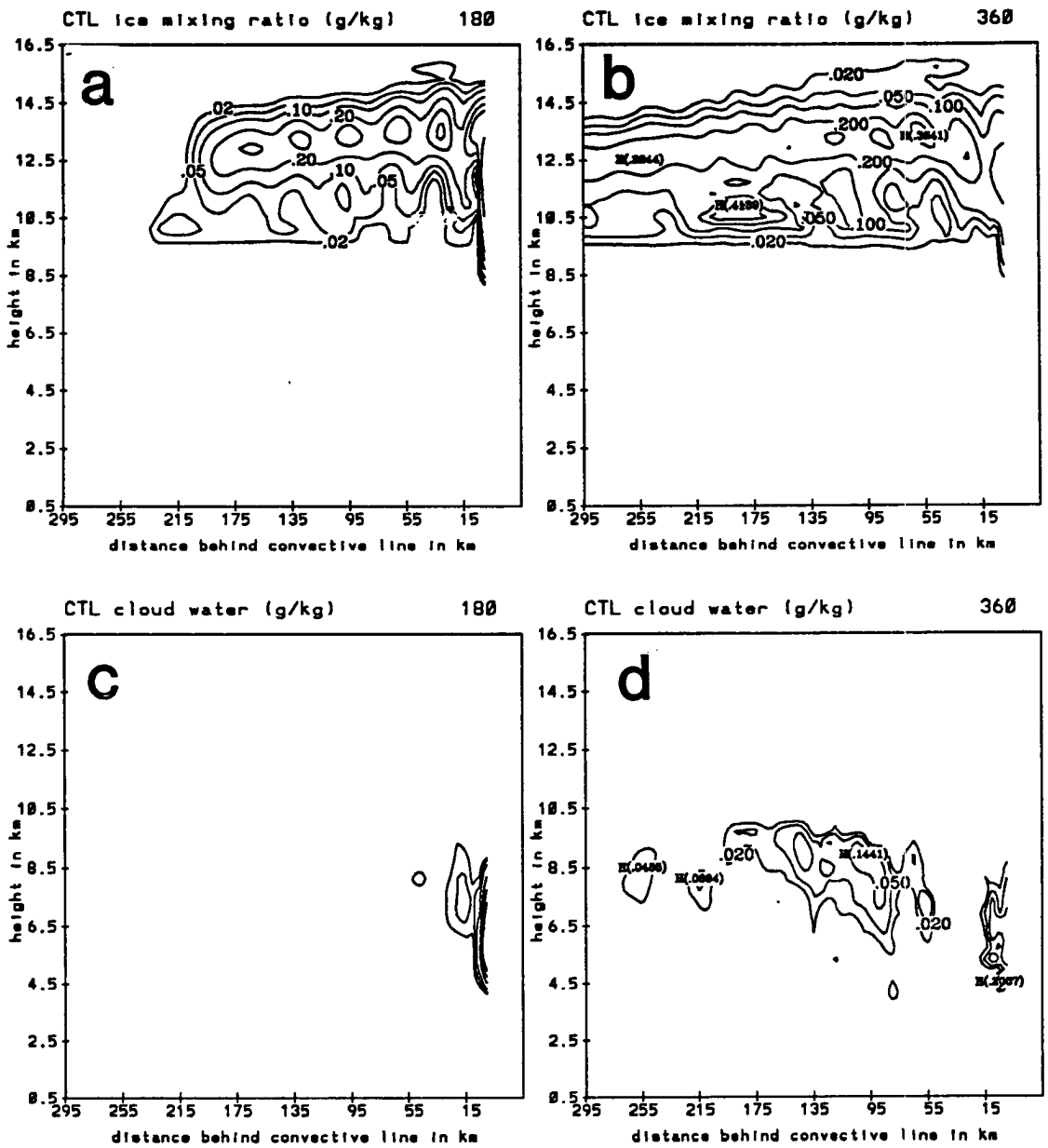
Figure 5.2: As in Fig. 5.1 except for ice, (a) and (b), and cloud water, (c) and (d). Contours for both fields are .02 and .05 g kg^{-1}, with an interval of .1 g kg^{-1} above these values.

These small amounts of cloud water are supported by aircraft observations of lightly rimed aggregates in the stratiform region of the system (Rutledge and MacGorman, 1988). In addition, significant lightning activity was observed in the stratiform region of this case, at least suggesting the possible presence of cloud water (Ziegler et al., 1986; Rutledge and MacGorman, 1988). Laboratory data suggest that interactions between small ice crystals and rimed ice particles in the presence of supercooled water can produce charge, even if the liquid water contents are only 0.1 g m^{-3} at temperatures of -5 to -15 °C. The cloud water at 360 minutes (Fig. 5.2d) is located in regions where the temperature is not far from -15 °C. Rutledge and MacGorman (1988) also found that the greatest frequency of positive cloud-to-ground lightning strokes occurred around the time of maximum stratiform rain intensity, or 0430 UTC. This may imply that cloud water quantities were largest around this time, a result also indicated by the model. Rutledge et al. (1988) indicate that although cloud water in small amounts probably existed in the anvil cloud, it must not have been extensive in the system, since airborne measurements were unable to detect any above the 0° C level. The kinematic modeling work of Rutledge and Houze (1987) also found some cloud water in the stratiform region of an Oklahoma squall line.

Both snow and graupel fall and reach the melting level, around 4.1 km, producing rain (Fig. 5.3). Rain rates in mm h^{-1} at six different times are shown in the figure. Only that portion of the domain within 200 km of the convective line is shown, since rain did not occur at the surface rearward of 200 km. Rain reaches the surface shortly after 45 minutes, and by 90 minutes, rainfall exceeding 0.5 mm h^{-1} is occurring in a 40 km region just behind the back edge of the convective line (Fig. 5.3a). The peak surface rainfall is around 1.5 mm h^{-1}. Rain quantities increase with time during the period that advection from the convective line occurs, and the peak amount, equivalent to a rain rate of 7 mm h^{-1} occurs at 360 minutes (Fig. 5.3e), or an hour after convective heating has ceased, and hydrometeor advection has significantly weakened.

The region experiencing surface rainfall in the model agrees reasonably well with observations. Table 5.1 shows the regions, in distance behind the convective line, experiencing surface rainfall greater than 0.1 mm h^{-1}, both in the model and observed. The
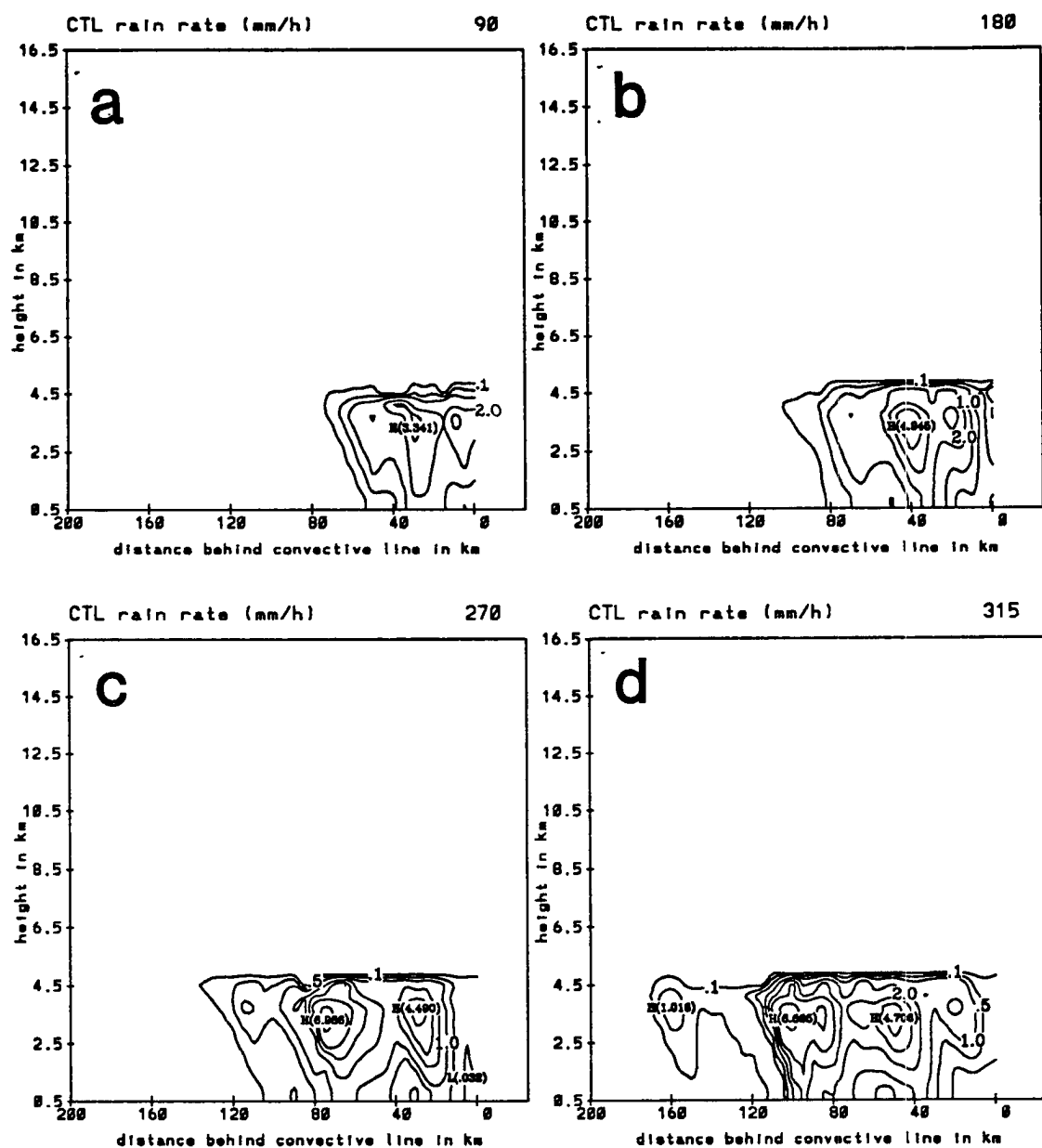
Figure 5.3: Rain rates (in mm h^{-1}) for (a) 90 minutes, (b) 180 minutes, (c) 270 minutes, (d) 315 minutes, (e) 360 minutes, and (f) 405 minutes of model simulation. Contours are shown for .1, .5, 1, 2, 3, 4, 6 and 8 mm h^{-1} rain rates. Rightmost 200 km of the domain is shown in each figure.

84
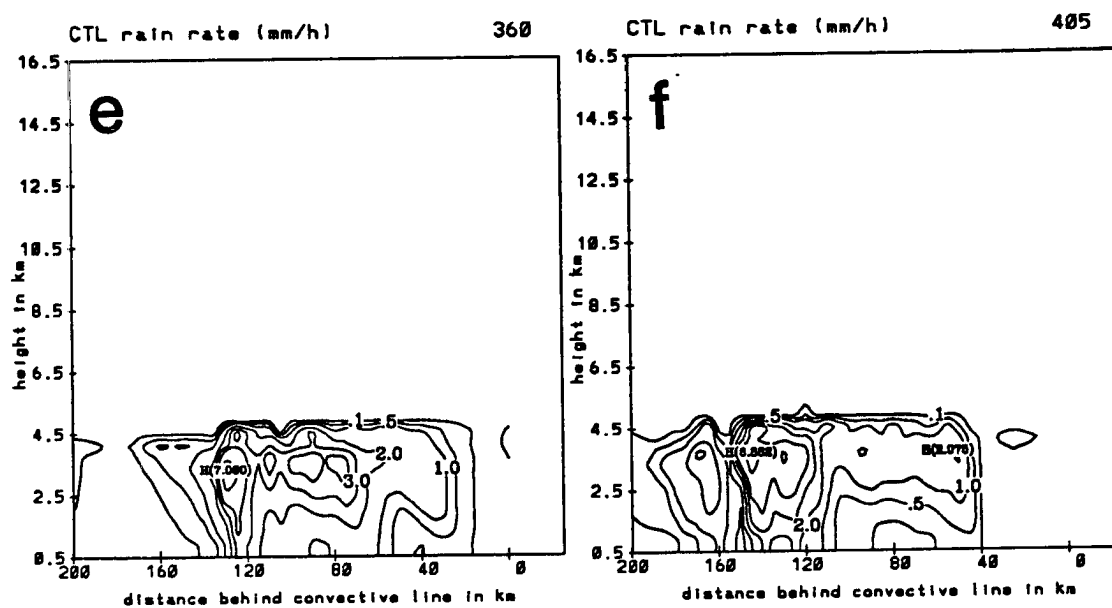
Figure 5.3: continued

observed values were based on the position of the 15 dBZ reflectivity contour, and are rough averages over the 3D system. The area with surface rain increases to include all points within 80 km of the convective line at 180 minutes (Fig. 5.3b), and 105 km at 270 minutes. Starting at 270 minutes, a region with no appreciable rainfall widens just behind the convective line. This is also about the time that echo free (less than 15 dBZ) region grew significantly in the observed system (see Fig. 4.1). This region, the transition zone, is primarily the result of fallspeed sorting in the model. By 315 minutes, rainfall covered the region 25-110 km behind the convective line, 45-145 km behind at 360 minutes, and 90-180 km behind at 405 minutes (some extremely light rainfall occurred at a few grid points closer to the convective line after 360 minutes, but this rain is not significant). Again, at nearly all times, the model surface rainfall region is within 10-20 km of the observed values. The location of peak surface rainfall is also shown in Table 5.1. The values marked observed are the central location of the band of highest reflectivity. The model again reproduces the rearward shift with time of the heaviest surface rainfall. This shift occurs without any prescribed speeding up of the convective line.

Table 5.1: Location of stratiform rain at the surface, and center of region of maximum rainfall, in distance (km) behind the back of the convective line region, from both the model and observations at given times (in minutes).

Time	Model surface rain	Obs. surface rain	Model Peak rain	Obs. Peak rain
90	0-55	0-60		
180	0-80	0-95	35	60
270	10-105	0-130	65	75
315	25-115	30-140	95	105
360	45-145	40-160	125	110
405	90-180	100-200	135	135

The transition zone is simulated well with the model. The 3D simulations of Zhang and Gao (1989) with a relatively coarse 25 km mesh also diagnosed a narrow region of very light rain rates just behind the convective line, although the transition zone was not as pronounced as was observed. Numerical simulations by Yang (1993, personal communication) with a fine 2 km mesh version of the Soong and Ogura (1980) cloud model failed to reproduce the transition zone. That model used horizontally homogeneous initialization based

upon a pre-squall sounding, and did not reproduce the dissipating stage of the system. These results imply the possible importance of several processes in the 11 June case. For instance, the dissipation of the squall line was to a large extent due to its movement into a region less favorable for convection. The modeling study of Zhang and Gao (1989), with initialization based upon several soundings, was able to show this dissipation. The model used in this study allows the convective line to dissipate in agreement with observations, which has a significant impact on the stratiform region. The simulation of Yang which does not have knowledge of the different environment into which the storm is moving fails to show dissipation. In addition, these separate results imply that a significant amount of the broadening of the transition zone and the decreasing intensity of precipitation there may be due to the weakening of the convective line. The transition zone broadened the most in the 11 June system after 0600 UTC. Although fallspeed sorting and enhanced subsidence behind the convective line can result in the formation of a transition zone, the total lack of rain over a broad region which was a characteristic of the 11 June transition zone at later times may require the rapid dissipation of the convective line. In the 11 June system, this rapid dissipation was due to propagation of the system into an unfavorable convective environment (at night).

A similar simulation to CTL without dissipation of the convective line found that rainfall did not decrease substantially over a broad region behind the convective line. Although this area was a region of generally lighter surface rainfall, still meeting the definition of transition zone, rain rates of over 0.5 mm h^{-1} were common within 40 km of the convective line until 405 minutes. The rainfall patterns at late times were relatively unchanged from early times behind the convective line. This again supports the idea that the rapid growth of a transition zone with almost no rainfall late in the lifetime of the 11 June system was primarily due to the rapid dissipation of the convective elements.

The in situ production of condensate becomes increasingly important after 270 minutes in the model simulation. As stated above, the greatest rain quantities occur an hour after the largest hydrometeor advection rates. In fact, peak rain mixing ratios, peak surface rainfall rates, and areal coverage of rain all occur during this hour. By 405 minutes

(Fig. 5.3f), the complete absence of hydrometeor advection from the convective line does result in diminishing rainfall rates, and a smaller area of surface rainfall. In general the model produces the heaviest rain at the surface during the 315-360 minute period, when rates reach 3.4 mm h^{-1}. In a broad sense, the timing of the heaviest rainfall agrees reasonably well with precipitation observations (Rutledge and MacGorman, 1988) and radar reflectivity measurements which indicated the highest reflectivities in the stratiform region occurred between 0430 and 0530 UTC. However, PAM and SAM mesonetwork rain guages showed that peak rain rates in the stratiform region were around 6 mm h^{-1} (Gallus and Johnson, 1991). As will be shown later, the failure of the model to accurately diagnose the intensity of the surface rainfall is at least partially due to the weakness of upward motions simulated at high levels in the anvil cloud. Average rainfall rates at the surface remained rather close to 1 mm h^{-1} throughout the simulation. Gallus and Johnson found average stratiform rain rates to generally lie between 2 and 3.3 mm h^{-1}. Therefore the model values again were roughly one half of the observed. It is also possible that the evaporation scheme used in the microphysical parameterization overestimates evaporation, resulting in less rain reaching the surface than observed. This could occur if the actual raindrop size distribution is significantly different from the assumed Marshall-Palmer distribution.

5.1.2 Microphysical processes

Cooling rates from melting in the simulation lie within the 1 to 6 °C h^{-1} range given by Leary and Houze (1979) for stratiform regions of MCSs (Fig. 5.4a, b). Leary and Houze determined that peak cooling from melting could be comparable to the peak cooling due to the evaporation of falling rain. The melting in the simulation is restricted to a roughly 1 km deep layer near 4 km, with peak melting rates just under 3 °C h^{-1} at 180 minutes (Fig. 5.4a), and approaching 4 °C h^{-1} at the time of heaviest rainfall, 360 minutes (Fig. 5.4b). As stated earlier, the simulated surface rain rates are less than observed, so that more realistic rain rates may be associated with significantly larger cooling rates from melting. The thickness of the melting layer in the simulation is supported by the aircraft observations of Willis and Heymsfield (1989) from this squall line, and the work of Atlas et al. (1969) and Stewart et al. (1984) from other stratiform precipitation regions. Willis
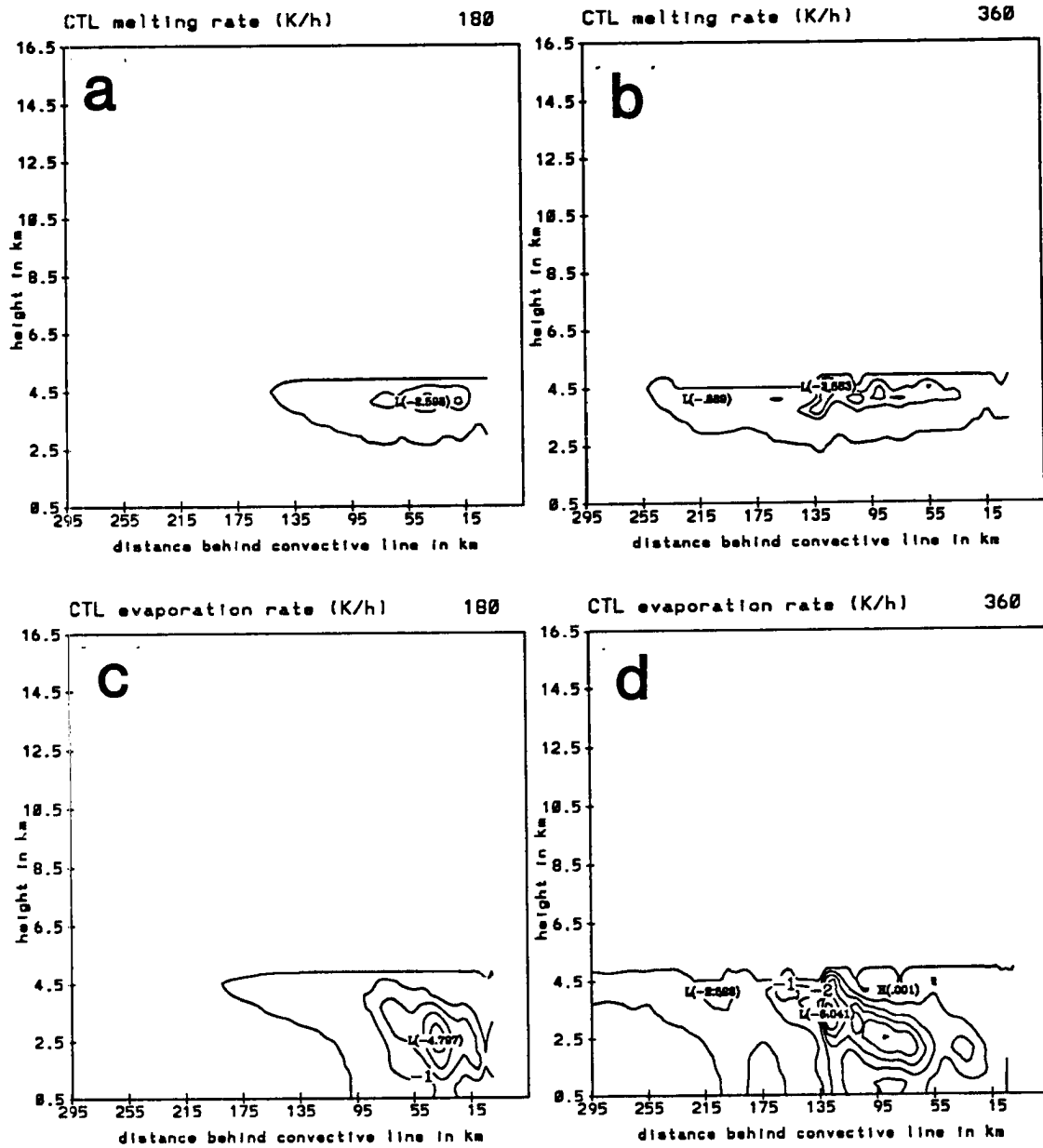
Figure 5.4: Cooling rates from melting at (a) 180 and (b) 360 minutes, and from evaporation of rain at (c) 180 minutes and (d) 360 minutes. Contour interval is 1 °C h^{-1}

and Heymsfield found that a 350 m deep isothermal layer with a temperature just above 0°, 0.5 °C, existed near the melting level in the stratiform region of the 11 June system. Atlas et al. (1969) found that even 1 mm of snow upon melting would make a 350 m deep 0°C layer with a pressure perturbation just over 0.1 mb and 1 m s^{-1} perturbations in the horizontal winds. Willis and Heymsfield (1989) also found a superadiabatic lapse rate confined to a very narrow layer below the melting level. Although the isothermal layer was only 350 m deep, they found some ice far below this layer in air temperatures as warm as 5.5°C. Occasionally large hydrometeors could be found in temperatures as warm as 9 or 10°C. The model results also imply the presence of some snow well below the melting level, with mixing ratios indicative of a few large hydrometeors per cubic meter as low as 1 km below the melting level where the temperature was around 10°C.

The top of the melting layer in the Willis and Heymsfield study was around 4.15 km. They determined a cooling rate of 2.5 - 2.9 °C h^{-1} in the melting layer. A sounding taken at 360 minutes within the main region of surface rainfall in the model is shown in Fig. 5.5a. A nearly isothermal layer with a temperature slightly above 0 °C shows up well around 600 mb. This isothermal layer did not exist until hydrometeors began falling from above. The Wichita 0600 UTC sounding is shown in Fig. 5.5b. At the time of this sounding, Wichita was near the back edge of the stratiform rain region and had experienced several hours of stratiform rain. The melting layer is apparent between 600-620 mb on this sounding, but the isothermal layer appears to be at nearly -1 °C. The differences between the aircraft report, the model result and the rawinsonde data may lie in the different locations of the reports. Wichita was near the back edge of the rainfall, where precipitation intensity was lighter. The model point (Fig. 5.5a) and the aircraft report were both taken near the region of heaviest stratiform rainfall. The heavier rainfall may have led to more pronounced descent and adiabatic warming.

Evaporative cooling occurs over a large area that expands rearward with time (Fig. 5.4c, d). These cooling rates generally exceed those of both melting-induced cooling and sublimative cooling (to be shown later). The peak value is just below 5 °C h^{-1} at 180 minutes (Fig. 5.4c), and around 6 °C h^{-1} at 360 minutes (Fig. 5.4d), although peak
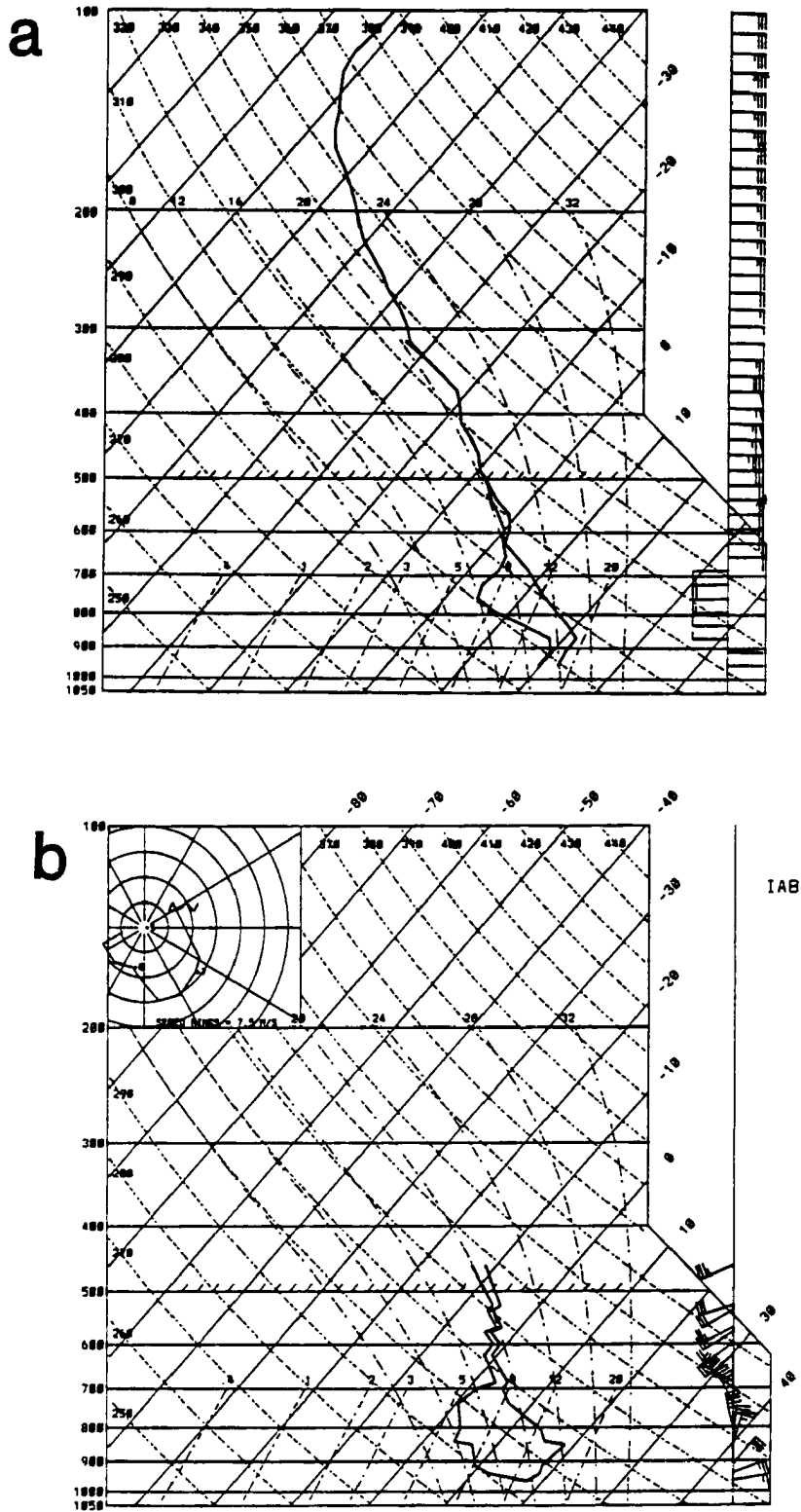
Figure 5.5: Thermodynamic diagrams from (a) the region of heaviest stratiform rain in the model at 360 minutes, and (b) Wichita, KS at 0624 UTC.

cooling reaches 7 °C h^{-1} at 270 minutes (figure not shown). Peak cooling is found in the region of heaviest precipitation. Significant evaporative cooling occurs over a much broader and deeper region than melting. The most intense cooling lies in a band that slopes rearward with height. This band is associated with the dry rear-inflow that develops.

Sublimation results in significant cooling over a larger region than melting, but over less area than evaporation (Fig. 5.6). The greatest cooling occurs just above the melting level where significant amounts of snow and graupel are present in the area where the rear-inflow jet is advecting dry air. Peak cooling rates exceed 3 °C h^{-1} after 270 minutes (Figs. 5.6c, d), and the peak values are comparable to those of melting. The band of sublimative cooling maintains the same rearward slope with height at early times that was present in the evaporative cooling field. At later times, this band becomes more horizontally-oriented, as the rear-inflow current itself descends more gradually. Depositional heating occupies a broad region, but at most grid points, the heating is not intense, generally under 0.5 °C h^{-1}. The most intense depositional heating occurs in regions of strong updraft and water supersaturation that also tend to have substantial condensational heating (Fig. 5.7). Peak depositional heating rates generally do not exceed 2.0 °C h^{-1}. This differs from condensational heating which already has a peak of over 4 °C h^{-1} by 180 minutes (Fig. 5.7b), and nearly 10 °C h^{-1} by 360 minutes (Fig. 5.7d). However, significant condensational heating is restricted to rather small regions within the anvil cloud, especially at early times (e.g. Fig. 5.7a). Because depositional heating of at least a few tenths of a degree per hour occurs over a larger area than condensational heating, it may play a significant role in influencing the circulations that develop in the stratiform region, even though the peak intensity of the heating at any point is never as large as that from condensation.

A water budget of the domain shows that in situ production of condensate through deposition and condensation becomes increasingly important with time (Table 5.2). The water budget terms are averages over 135 minute time periods. During the first third of the model simulation, over 85% of the condensate being made available in the domain is advected there from the convective line. Only 15% of the condensate is produced in situ.
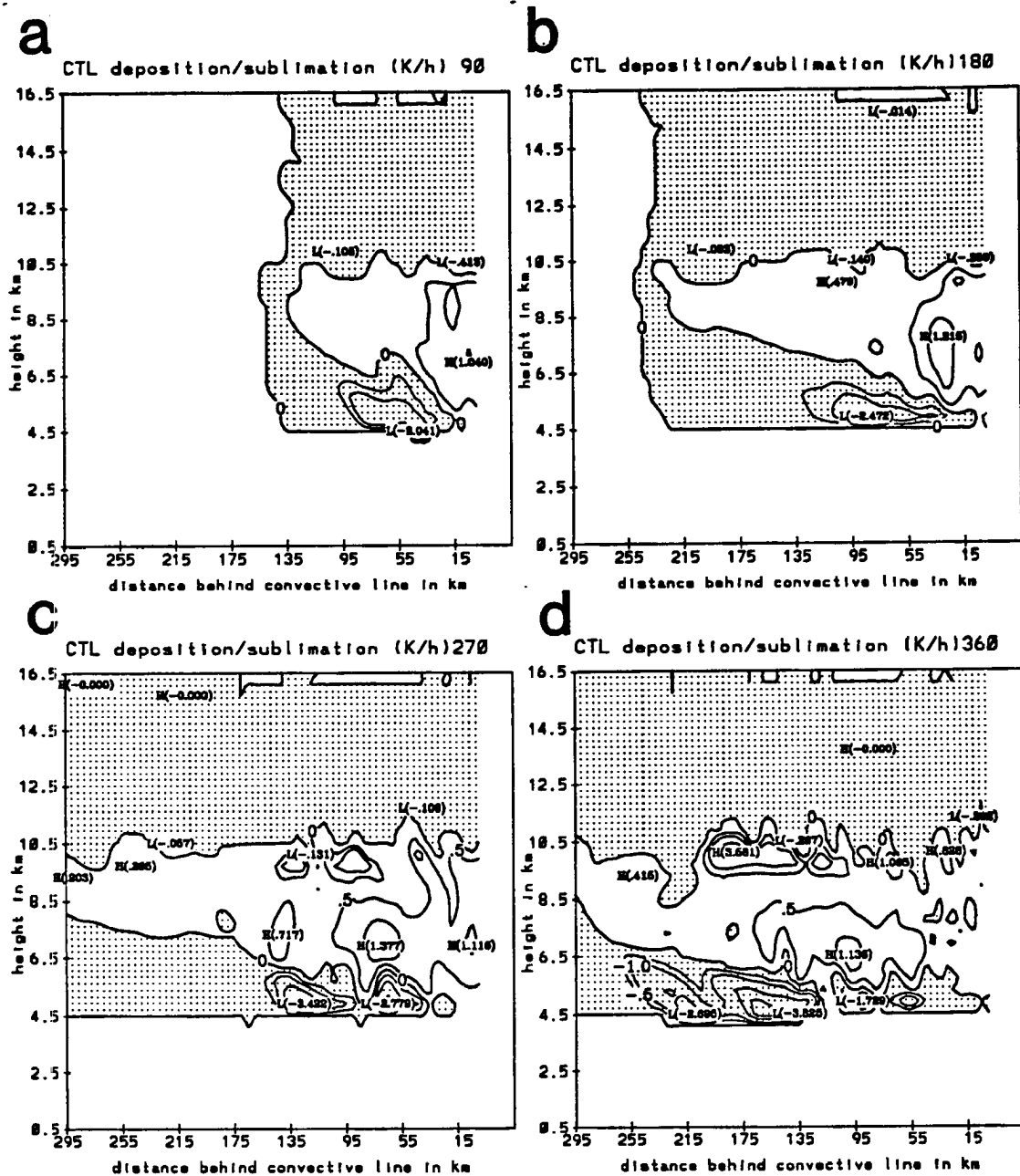
Figure 5.6: Heating and cooling rates from deposition and sublimation at (a) 90 minutes, (b) 180 minutes, (c) 270 minutes, and (d) 360 minutes. Cooling is shaded. Contour interval of .5 °C h^{-1} is used for absolute values less than 1 °C h^{-1}, with an interval of 1 °C h^{-1} for greater rates.
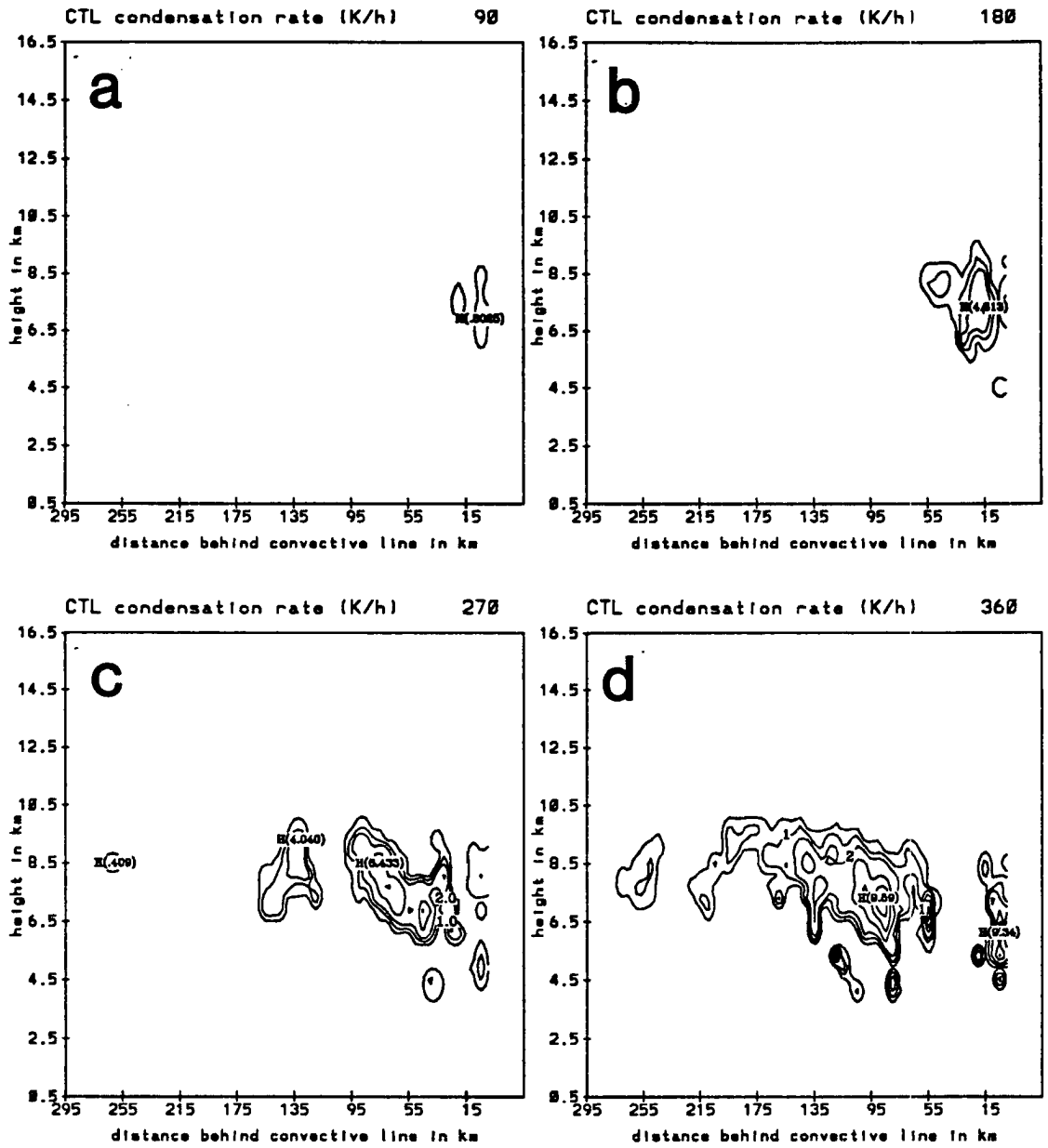
Figure 5.7: Condensational heating rates at (a) 90, (b) 180, (c) 270 and (d) 360 minutes. Smallest contour is for .1 °C h^{-1}, with other contours at 1, 2, 4, 6, 8, and 10 °C h^{-1}.

At this early time, deposition is supplying over twice as much condensate as condensation. During the next third of the simulation, 135-270 minutes, the in situ production of condensate increases to 33%. By the period of heaviest stratiform rainfall, the last third of the simulation, 67% of the condensate made available in the domain is produced in situ, with nearly 75% of that total from condensation. Tao et al. (1993) also found in a numerical simulation of this case that advection of hydrometeors from the convective line supplied nearly all of the condensate in the stratiform region during the initial stage of the system, but less than half during the mature stage. For the entire 405 minutes of simulation, condensate advected from the convective line in this model supplied 55.8% of the total condensate available within the domain. This agrees almost exactly with the 56% figure given in Tao et al. (1993) over the course of their 16 hour simulation.

Table 5.2: Water budget of the control model simulation, expressed in percentage of total condensate mass made available during each time interval. Condensate mass made available during each period is shown in column 2 as the average rate expressed in kg s^{-1}.

Time (min)	Total Mass (kg s^{-1})	ADV	COND	DEP	EVAP	SUBL	RAIN
0-135	67.1	85.8	4.5	9.7	36.8	7.6	13.8
135-270	96.5	66.8	17.8	15.4	75.9	11.7	17.8
270-405	135.2	33.4	49.1	17.5	86.6	15.8	23.5

The in situ condensation production rates after 135 minutes agree fairly well with other water budgets of MCS stratiform regions. Gamache and Houze (1983) found that 25-40% of the surface rainfall in the stratiform region of a tropical squall line was due to in situ production. Gallus and Johnson (1991) estimated roughly equal contributions from advection and in situ production during the later stages of the 11 June squall line. The kinematic model used by Rutledge and Houze (1987) determined that as much as 80% of the stratiform rainfall was due to in situ condensate production. Precipitation efficiencies, expressed as the percent of condensate being made available that falls out as precipitation at the surface at any time, are low throughout the simulation due to the significant amounts of evaporation in the rear-inflow jet. The figure slowly increases from 14% to 24% by the end of the simulation. Evaporation is by far the largest sink term in

the water budget, with 76% of the available condensate lost during the 135-270 minute time period, and 87% lost at the later period. Sublimation removes much less condensate, although, the rates are slightly larger than the creation rates by deposition.

The combined effect from all microphysical processes is an expanding area of heating at nearly all levels above 6.5 km and intense cooling below (Fig. 5.8). The intense convective heating prescribed in the buffer zone is also shown in this figure. Convective heating of 12 °C h^{-1} exists prior to 180 minutes (Fig. 5.8b), with weakening afterwards. Heating within the stratiform region first becomes significant at 180 minutes, and by 270 minutes (Fig. 5.8c), heating of at least a few °C h^{-1} occurs over a 90 km wide layer, with the most intense heating between 7 and 8 km. Peak diabatic heating by 360 minutes (Fig. 5.8d) exceeds 12 °C h^{-1}. Diabatic cooling occurs through a deep layer extending rearward with height. The peak cooling is often near the melting level, and reaches 11 °C h^{-1} at 360 minutes (Fig. 5.8d).

Averaged diabatic heating within the entire stratiform rain region during the 270-360 minute time period agrees reasonably well with the heat budget results of Gallus and Johnson (1991) during the mature and dissipating stages of the system (Fig. 5.9). The Gallus and Johnson curve at 0600 UTC should more reasonably compare with the model average than the 0730 UTC curve, although spatial aliasing of data was a problem in their budget at 0600 UTC. The model appears to simulate the diabatic cooling at low levels realistically, with cooling rates generally slightly larger than observed by the rawinsonde-based budget study. The shape of the curve is very similar to that of the 0730 UTC observation. The rather low crossing from cooling to warming indicated on the 0600 UTC curve is most likely the result of spatial aliasing of rather low convective heating into the stratiform region which probably was experiencing cooling at these low levels, similar to that indicated in the 0730 UTC curve. The crossover from cooling to warming in the model is within 0.5 km of that occurring at 0730 UTC. Because the mesoscale downdraft occurs on roughly the scale of the rainfall region (Biggerstaff and Houze, 1991a), it may have been only partially resolved by the rawinsonde budget, accounting for the slightly larger values of cooling occurring in the model. It is also possible that the microphysical
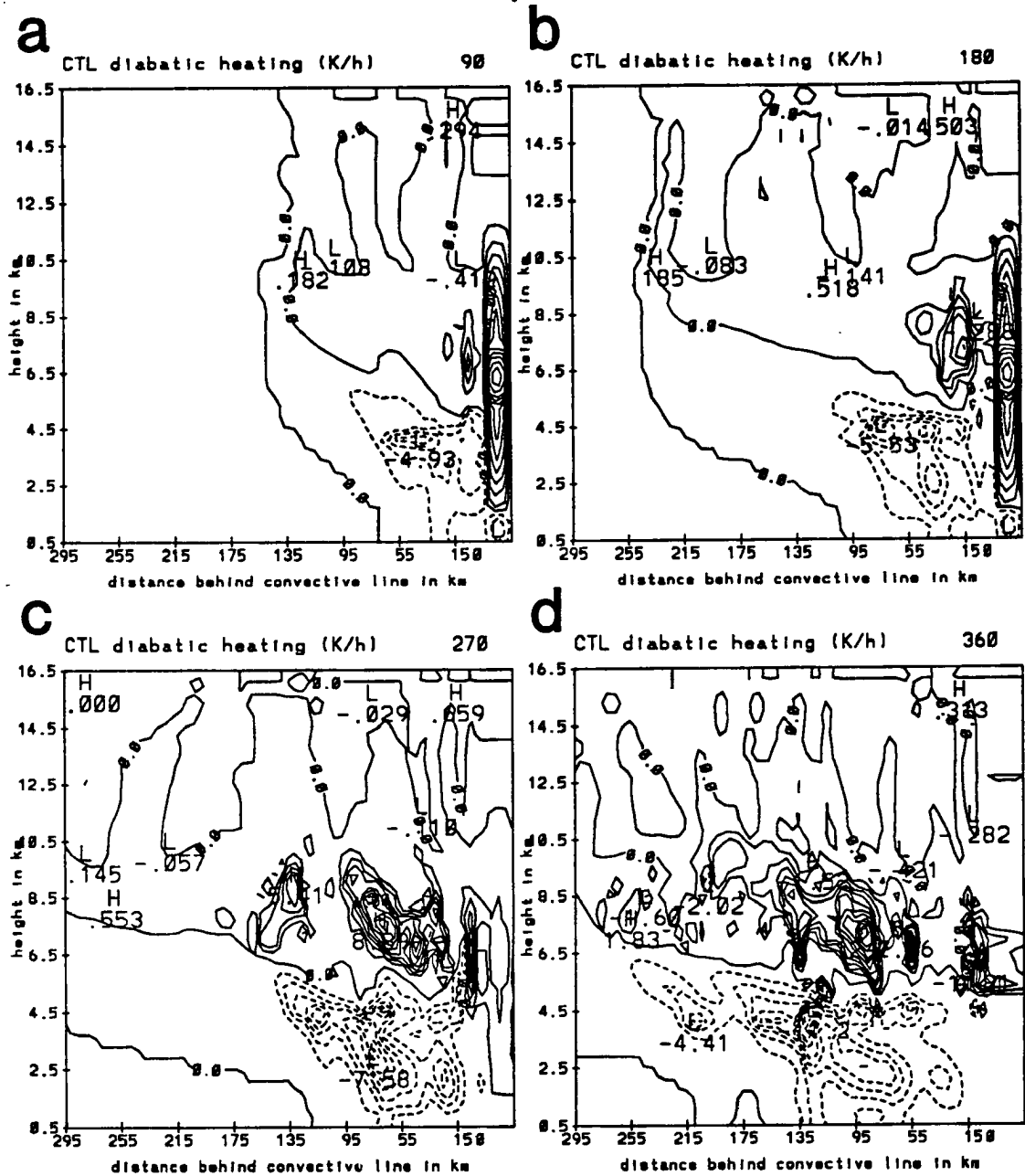
Figure 5.8: Same as Fig. 5.7 except for total diabatic heating from microphysical processes. Cooling rates are shown with dashed contours. Contour interval of 1 °C h^{-1} used on all diagrams. Prescribed convective heating in the buffer zone is shown at all times.
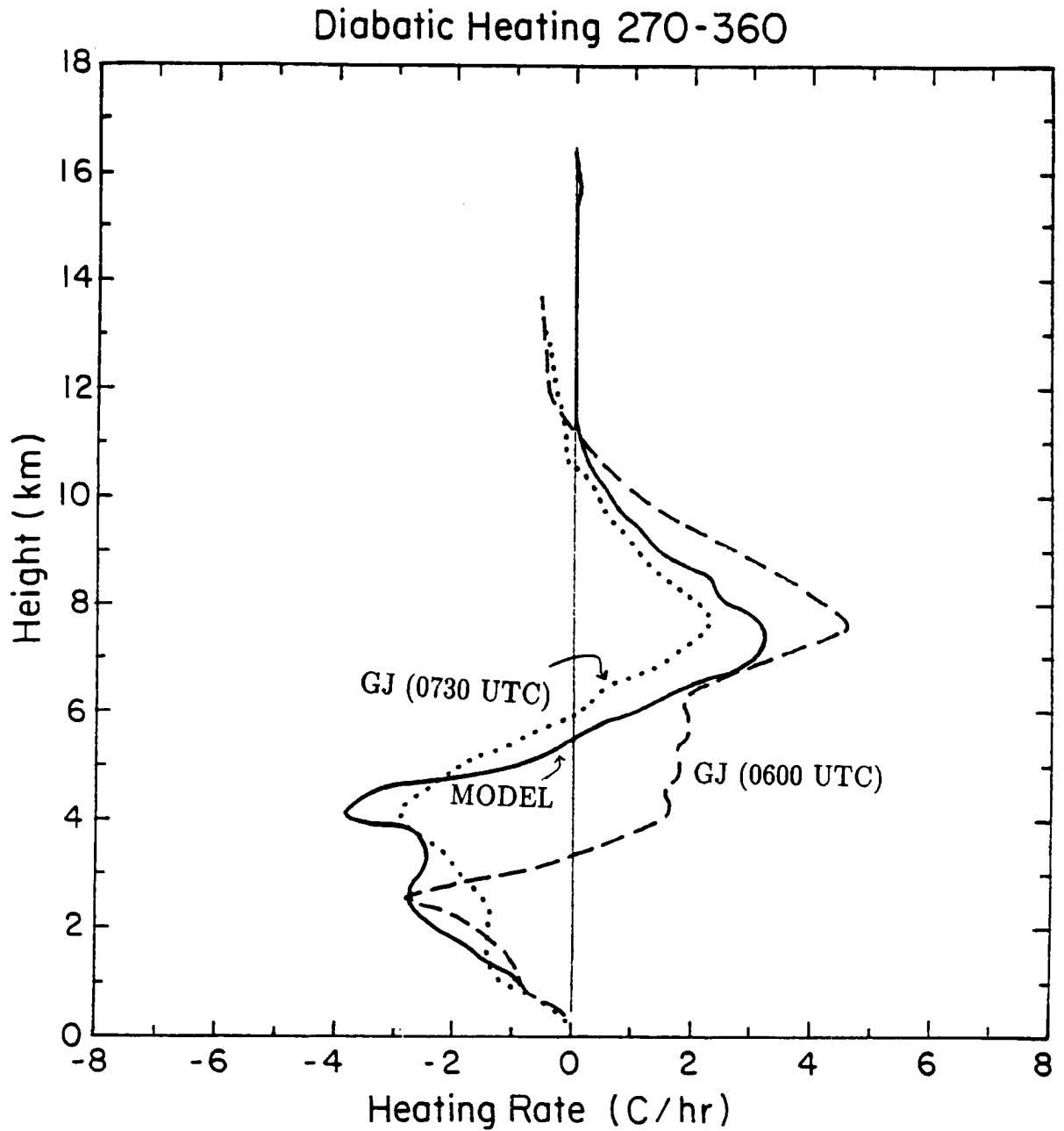
Figure 5.9: Diabatic heating averaged over the region of surface stratiform rainfall during the 270-360 minute time period in the model. Solid curve represents the model heating. Dashed curve is taken from the Q_1 budget of Gallus and Johnson for this case, valid at 0600 UTC, and dotted curve is from the budget at 0730 UTC.

parameterization overestimates evaporation rates slightly, which would help to explain the higher model values of cooling, and additionally, the underestimate of surface rainfall. The model indicates two peaks in the cooling. The lower one is found at around 2.5 km, and the higher one at the melting level. A similar two-peaked structure of the microphysical cooling was found by Chong and Hauser (1990) in the stratiform region of a COPT tropical squall line.

Model estimates of peak heating around 3.5 °C h^{-1} at the 400 mb level agree reasonably well with the rawinsonde-derived curves. The peak heating rate falls between the values at 0600 and 0730 UTC, and the level of peak heating is only 0.5 km lower than that observed. Although some aliasing may have influenced the 0600 UTC heating profile, the profile at 0730 UTC is representative of a dissipating stratiform region, so that the 0600 UTC curve with its higher diabatic heating rates should be a better representation of an active stratiform region, like that occurring in the model. If this is the case, then the model is indeed underestimating diabatic heating by approximately 20%, with the primary underestimation occurring at higher levels in the anvil cloud. This slight underestimate may partially explain the lighter than observed surface rainfall in the model. The diminished diabatic heating may be a natural consequence of the relatively weak ascent at high levels, to be shown later. Possible causes for the light surface rainfall and high-level underestimate in diabatic heating will be discussed later.

The individual contributions to the diabatic heating at 315 minutes averaged over the stratiform region are shown in Fig. 5.10. The lower diabatic cooling peak is due entirely to evaporation of rain, while the peak near the melting level is a function of evaporation, sublimation and melting. The total cooling due to both sublimation and melting are somewhat similar, with each acting in a relatively narrow layer. It can be seen in the figure that diabatic heating in the anvil cloud is due primarily to condensation at this time, although vapor deposition is contributing somewhat uniformly just under 1 °C h^{-1} through the 6-10 km layer. Although condensational heating is more intense, depositional heating is significant and releases heat slightly higher in the anvil cloud than does condensation. As implied in Figs. 5.6 and 5.7, and Table 5.2, at earlier times, condensation played much less of a role.
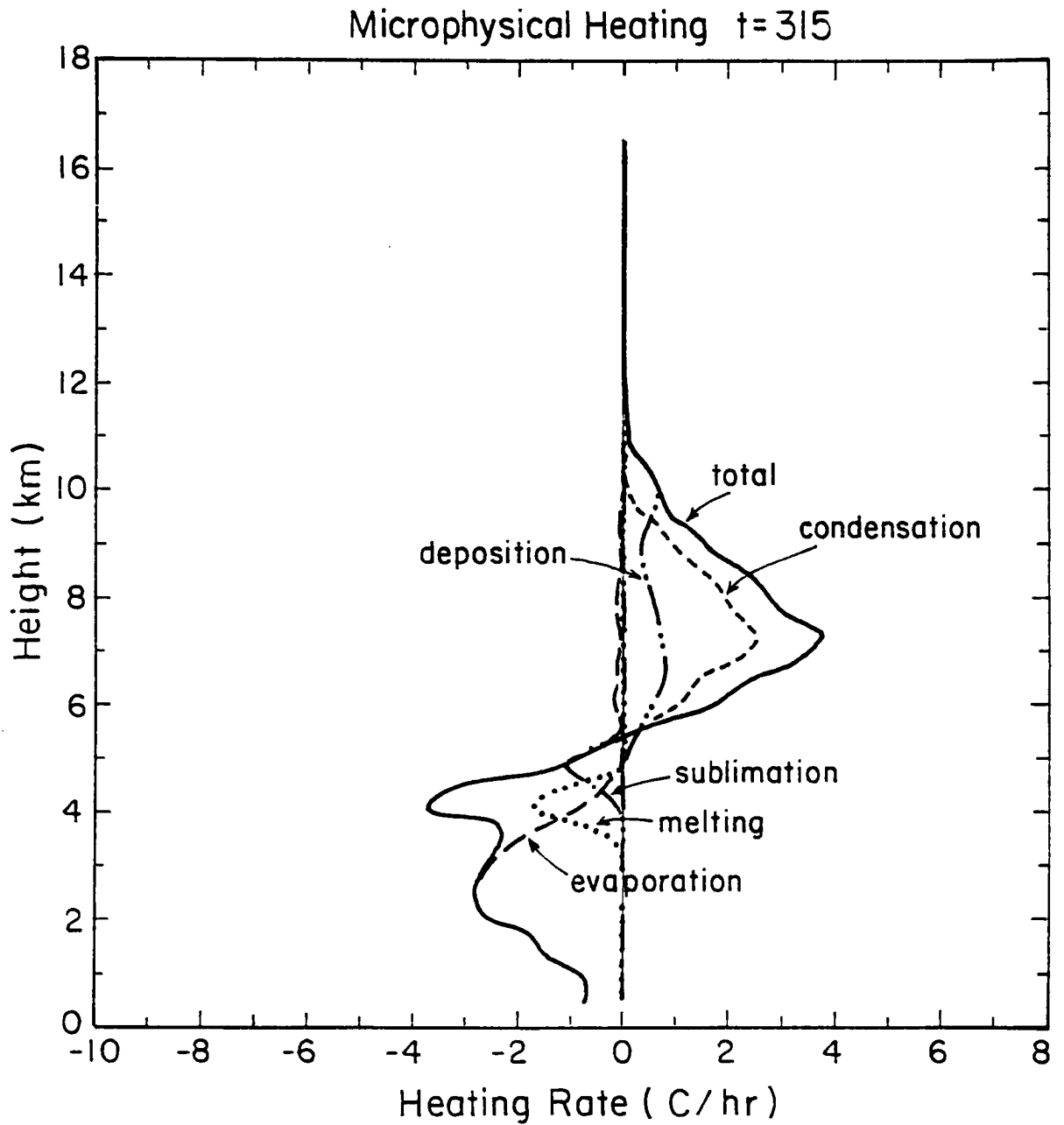
Figure 5.10: Individual microphysical heating and cooling rates at 315 minutes, averaged over the region of surface stratiform rain. Total heating or cooling shown with solid curve, cooling from evaporation large dashes, sublimational cooling dash-dotted, depositional heating dash with double dots, cooling from melting dotted, and condensational heating small dashes.

5.1.3 Vertical motion

Vertical motions develop within the domain that are qualitatively similar to observations (Fig. 5.11). As in the modeling work of Lafore and Moncrieff (1989), large amplitude gravity waves exist in the stratiform region, so to better represent the meaningful circulations, the fields of vertical velocity and horizontal wind were averaged over the twenty minute periods centered at the given times. This time period is far shorter than that used in Lafore and Moncrieff, and no horizontal averaging was performed. This minimal amount of smoothing is generally sufficient to reveal the important circulations. The advection of hydrometeors and resulting melting into rain, and evaporation of the rain rapidly produce a fairly well-developed mesoscale downdraft, which can be clearly seen at 90 minutes (Fig. 5.11a). Peak descent is nearly 30 cm s^{-1} at the 2.9 km level. Significant downward motion occurs over a nearly 50 km wide region, and extends rearward from the region of surface rainfall. A band of subsidence also extends farther rearward near and just above the melting level, reaching up to over 7 km about 90 km rearward from the convective line. This downward motion is the result of sublimational cooling in this region.

The mesoscale downdraft broadens and intensifies through 270 minutes (Figs. 5.11b, c), with peak descent reaching over 50 cm s^{-1}. The most intense downward motion continues to move rearward relative to the convective line. Most of the downward motion is restricted to below the melting level, although there is a tendency for downward motion to exist at higher levels to the rear of the surface rainfall. At 315 and 360 minutes (Figs. 5.11d, e), the strongest descent, over 60 cm s^{-1}, is roughly 100 km rearward from the convective line region. Significant downward motion covers a 110 km wide region. By 405 minutes (Fig. 5.11f), the vertical motion field exhibits more noise, possibly the result of numerical instabilities that slowly build over time. Many cloud model simulations of convection are restricted to time periods under 4 or 5 hours (e.g. Weisman et al., 1988) for similar reasons. In addition, since the Coriolis effect is ignored, results beyond several hours should be interpreted cautiously. At 405 minutes, the general trend of a rearward moving subsidence maximum continues, with the strongest descent 135 km behind the
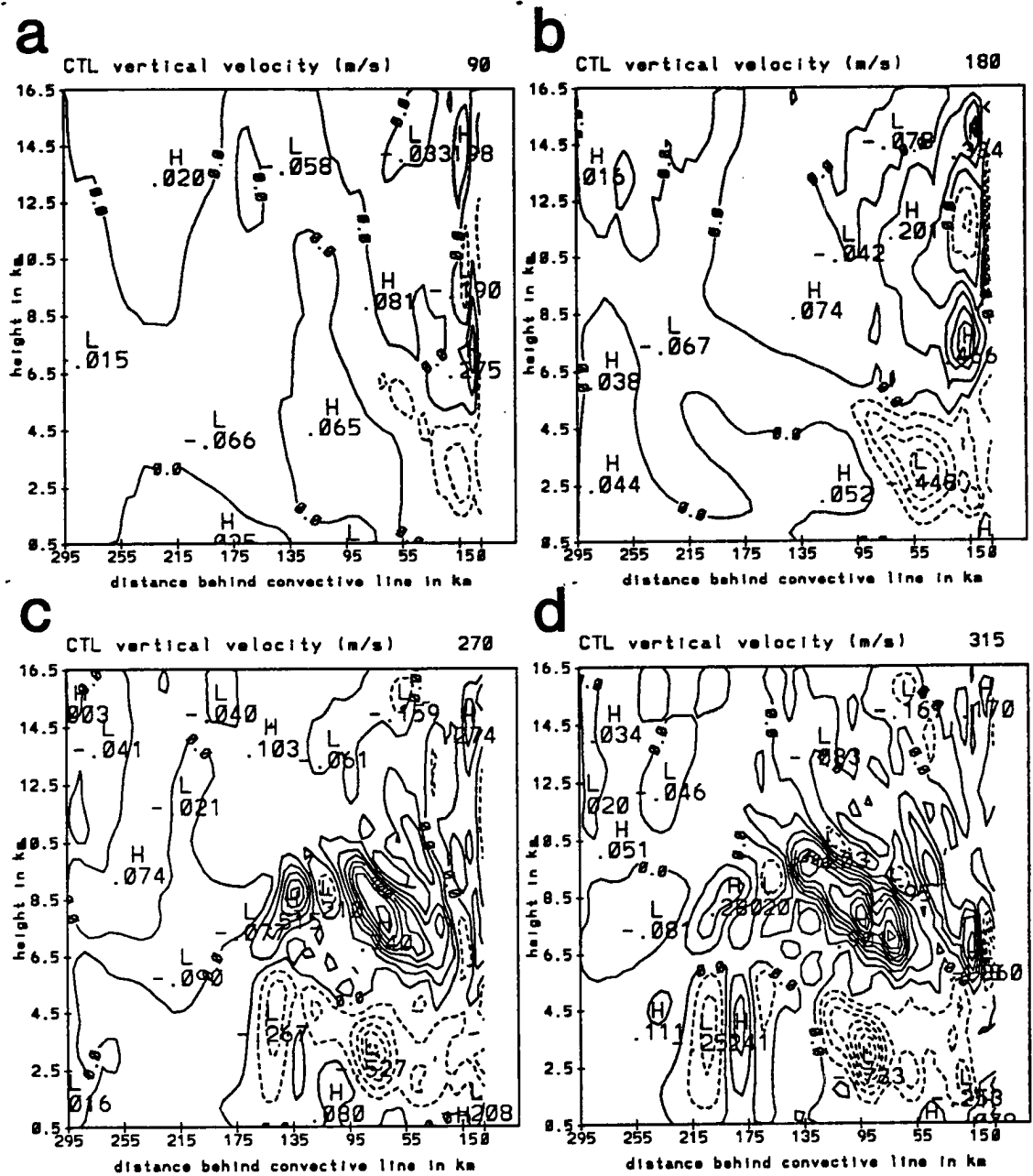
Figure 5.11: Vertical velocities in the model domain at (a) 90, (b) 180, (c) 270, (d) 315, (e) 360 and (f) 405 minutes. Contour interval is .1 m s^{-1} with downward motion dashed.
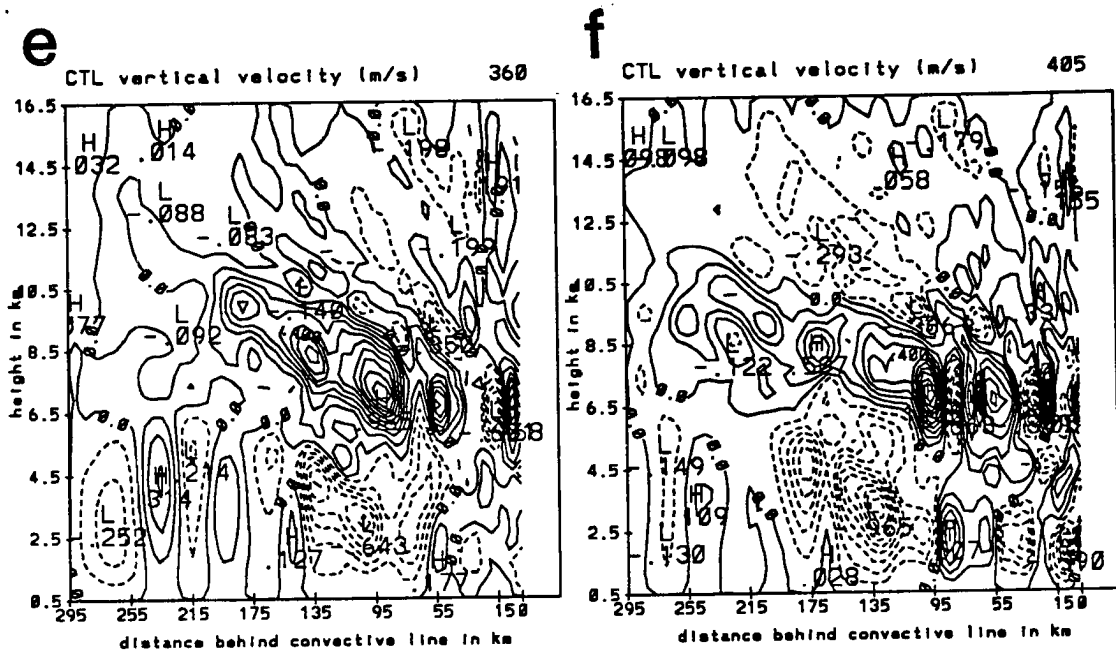
Figure 5.11: continued

back edge of the convective line. At this time the peak downward motion is around 96 cm s^{-1}. Downward motion is rather weak and sporadic at low levels within 90 km of the convective line region.

The mesoscale downdraft appears to be simulated well in this model. Gallus and Johnson (1991) found mesoscale descent over a roughly 150 km region at 0600 and 0730 UTC. These times correspond roughly with the model after 315 minutes. At these times, the model diagnoses 10 cm s^{-1} or greater descent over a 100 km or greater area. The peak descent found in the Gallus and Johnson rawinsonde study was around 40 cm s^{-1}, and the level of peak descent was typically between 3-4 km. Rutledge et al. (1988) found using Doppler data for this case, descent as large as 75 cm s^{-1} and peak descent between the 2.5 and 4.5 km level. The model diagnoses peak descent comparable to the Doppler data, with the strongest downdraft generally between 2.5 and 3.5 km.

The model downdraft magnitude also falls within the range of the mesoscale descent observed in other squall line cases. Smull and Houze (1987a) found using dual-Doppler data average descent of 20 cm s^{-1} in the stratiform region of the 22 May 1976 squall line, with the level of maximum descent between 1.8 and 2.4 km. They did measure stronger descent, up to 45 cm s^{-1} at 2.5 km in the transition zone. Srivastava found descent as large as 25 cm s^{-1} in the 1-5 km layer of an Illinois squall line. In a tropical GATE squall line Houze (1977) found peak mesoscale descent between 2.5 and 2.8 km. Johnson (1982) found the largest descent under WMONEX anvils was at 3.5 km. The mesoscale downdraft produced in this simulation therefore agrees well with the observational evidence.

The model diagnosed vertical motions averaged over the entire stratiform region (defined as in Fig. 5.9) during the 270-360 minute time period compare reasonably well with the rawinsonde diagnosed values averaged at 0600 and 0730 UTC (Gallus and Johnson, 1991) (Fig. 5.12). In addition, the model values averaged over a smaller 40 km region near the heaviest stratiform rainfall also compare well, except for the level of the peak ascent, with an average of the CP3 and CP4 EVAD (Extended Velocity-Azimuth Display) analyses around 0400 UTC (Rutledge et al., 1988) which were also taken over a 40 km wide region. In this figure, comparisons can be made between the large scale vertical velocity
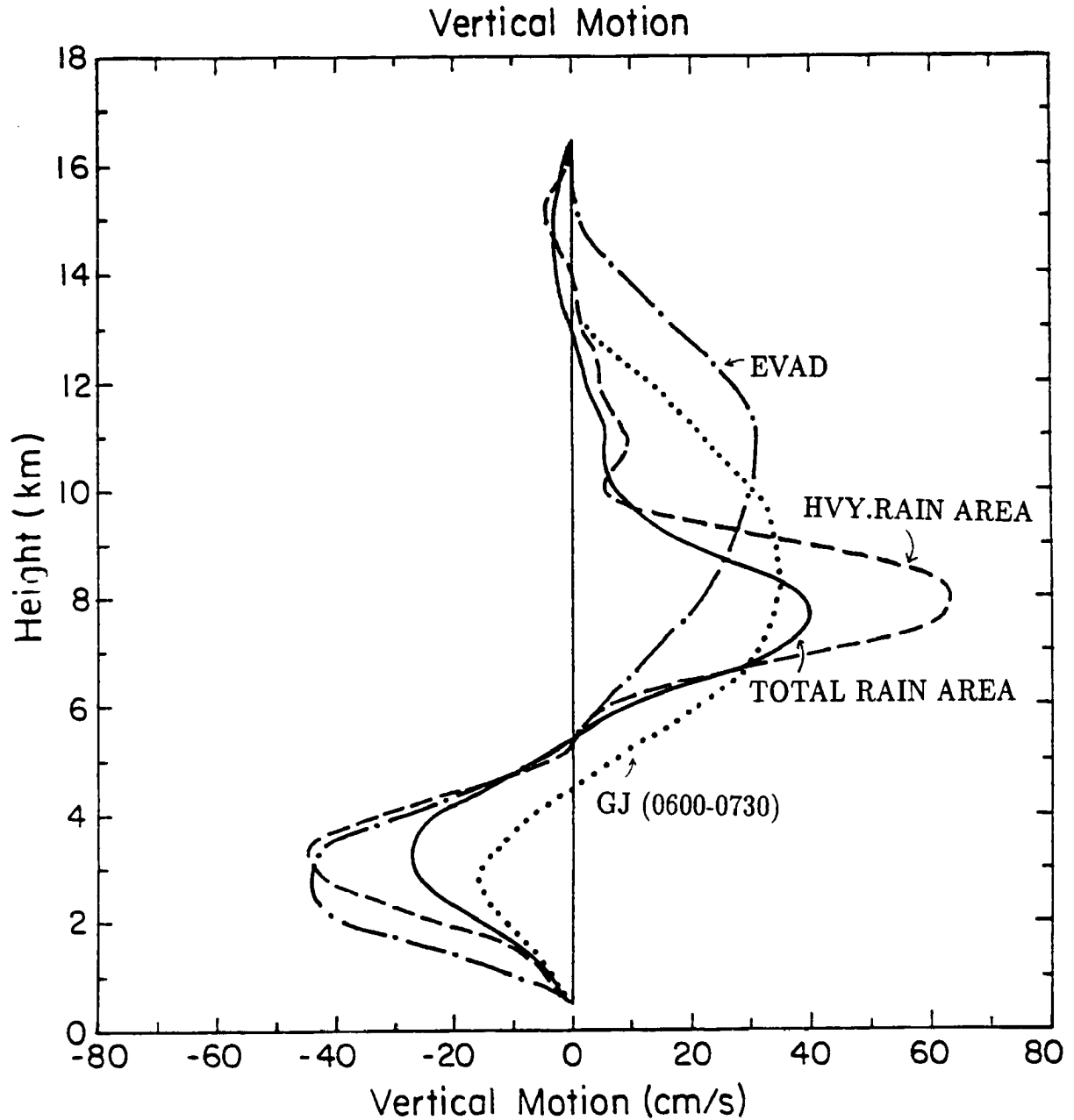
Figure 5.12: Vertical motion averaged over the stratiform rain region in the model during the 270-360 minute time period (solid curve) compared with rawinsonde-derived average over the same region at 0600 and 0730 UTC (dotted curve, from Gallus and Johnson, 1991). Model averaged vertical motion over 40 km region of heaviest stratiform rainfall during the 270-360 minute period (dashed curve) is compared with similar areal average from EVAD analyses of Doppler data (dashed-dotted curve, from Rutledge et al., 1988).

(averaged over the entire stratiform region), and values taken over a smaller-scale region. Over the entire region experiencing stratiform rain, the model indicates only slightly more low-level subsidence than found by rawinsondes, roughly 5-10 cm s^{-1} more. The small difference may be due to the failure of the rawinsonde study to fully resolve the downdraft. Region-wide ascent peaks at nearly 40 cm s^{-1}, in good agreement with the ascent diagnosed from rawinsondes. However, the upward motion in the model is restricted to a narrower depth within the anvil cloud, with the worst agreement occurring above 9 km, where the model significantly underestimates the upward motion. The model peak level of ascent is also about 1 km lower than the rawinsonde-derived value. The omission of radiative effects in the model may account for the underestimate of ascent in the upper portion of the cloud. In addition, momentum transport from the convective line into the stratiform region has been neglected in the model, and it may play a role in generating high-level ascent. However, preliminary modeling work investigating the role of this momentum transport indicates that the transport does not significantly affect the magnitude of ascent above 9 km in the anvil cloud.

On the smaller scale of an EVAD analysis, the mesoscale downdraft is modeled very well. Peak descent exceeding 10 cm s^{-1} agrees exactly with the EVAD average, although the peak may be elevated a few hundred meters from the Doppler average. All four curves show peak descent not far from the 3 km level. The crossover from downward to upward motion in the model occurs near 5 km, in excellent agreement with the EVAD curve. Upward motion in this 40 km region is as large as 65 cm s^{-1} at 8.0 km. This exceeds the peak value of the averaged EVAD curve, but is similar to some measurements made at the CP3 and CP4 radars at specific times. Again, however, the model finds upward motion restricted to a relatively shallow region with upward motions above 9 km underestimated. Some of the difference at high levels may be due to errors in the Doppler results near cloud top. The strong ascent around 12 km diagnosed from the radar is elevated significantly from the levels of peak descent obtained in other squall line studies (e.g. Roux et al., 1988; Ogura and Liou, 1980). Weak subsidence at or above the cloud top in both the EVAD-scale profile and the system-wide average is supported by observations from the stratiform region of this case (Johnson et al., 1990).

The mesoscale updraft within the anvil cloud is known to be important in explaining the surface rainfall rates observed within the stratiform region. In several simulations of squall lines, models have failed to adequately diagnose the true intensity of the updrafts, and in general they underestimate these values (e.g. Dudhia et al., 1987). The same problem occurs to some degree in this simulation. At 90 minutes, there is no broad region of ascent within the domain (Fig. 5.11a). Some weak ascent does exist above the mesoscale downdraft but air motions are generally under 5 cm s^{-1}. One exception is in a narrow band just behind the convective line where saturated conditions allow significant condensation and vapor deposition to take place. Within a 10 km wide band, upward motions reach 27 cm s^{-1}.

By 180 minutes (Fig. 5.11b), a more pronounced mesoscale updraft forms in the domain. Upward motions reach 10 cm s^{-1} within a roughly 75 km wide region. A narrow band of much stronger ascent, nearly 50 cm s^{-1}, can be found within 20 km of the convective line. This location would actually be in the region of the transition zone in the 10-11 June squall line. Doppler radar has shown similar features in two other squall lines. Smull and Houze (1987a) found in the 22 May 1976 squall system that the strongest upward motion occurred above the transition zone, and they diagnosed average ascent of up to 50 cm s^{-1} at 9 km there. The upward motion in the stratiform region in that case peaked around 45 cm s^{-1} at 7.2 km. Peak upward motion was again found in the transition zone in the African squall line studied by Chong et al. (1987), and the peak, 48 cm s^{-1}, was at 8.5 km. In the stratiform region of that case, the maximum upward motion was 35-45 cm s^{-1} at a lower level, 6.5-7 km. Tao and Simpson (1989) found in a GATE case that most of the deposition and condensation was occurring within the front 40-50 km of a stratiform region. This would agree with these results during the first 180 minutes of the simulation, where the strong ascent is restricted to just behind the convective line.

At 270 minutes (Fig. 5.11c), a very broad mesoscale updraft covers much of the model domain, and sizeable regions experience ascent exceeding 20 cm s^{-1}. Peak values exceed 70 cm s^{-1} around the 7.5 km level. The strongest ascent is concentrated in a roughly 4 km deep band between 6.5 and 10.5 km with some hint that updraft maxima sloped rearward

with height. Although the upward motions are significant, they are somewhat less intense over broad regions than those measured by Doppler radar for this case. Rutledge et al. (1988) diagnosed upward motions over broad regions between 30 and 60 cm s^{-1} within the anvil cloud. That same study found that the peak ascent occurred at a rather high level, 11-12 km. This would be several kilometers higher than the peak level diagnosed by the model. However, as stated earlier, the Doppler results may be in error at these elevations near cloud top. The rawinsonde study of Gallus and Johnson (1991) for this case, along with observational studies of other squall lines (e.g. Ogura and Liou, 1980; Chong et al., 1987) and other numerical simulations (Zhang et al., 1989), generally found a somewhat lower level of peak ascent, agreeing more with the results of this simulation. The peak ascent found in this simulation at 270 minutes agrees with the peak value obtained in the 3-D simulation of this case by Zhang et al. (1989). In both cases, however, such intense upward motion was restricted to rather small areas.

At 315 and 360 minutes (Figs. 5.11d, e), significant ascent occurs over a broad region, with peak values of nearly 1 m s^{-1}. At 315 minutes, strong ascent occurs over a 100 km wide region from x=40 to x=140. By 360 minutes, strong ascent occurs over the 170 km wide region between x=40 and x = 210 km. The peak values occur around the 7 km level. Upward motion maxima sloped rearward with height, with the peak ascent occurring above 10 km at the rear of the mesoscale updraft. At this time, both the scale and magnitude of upward vertical motion agree best with observations. By 405 minutes, upward motions, though still strong in places, are generally weakening and the mesoscale updraft is becoming more disorganized.

5.1.4 Temperature and pressure changes

The effect of the diabatic heating, along with adiabatic temperature changes from the vertical motions occurring in the domain, can be seen in the potential temperature field (Fig. 5.13). At 90 minutes (Fig. 5.13a), the melting layer is pronounced with a decrease in θ of nearly 2 K since the start of the simulation. Less intense temperature decreases extend to the surface due to evaporative cooling. Low-level cooling rearward of 95 km is due to the initial cold pool from the convective line itself. Aloft, potential temperatures
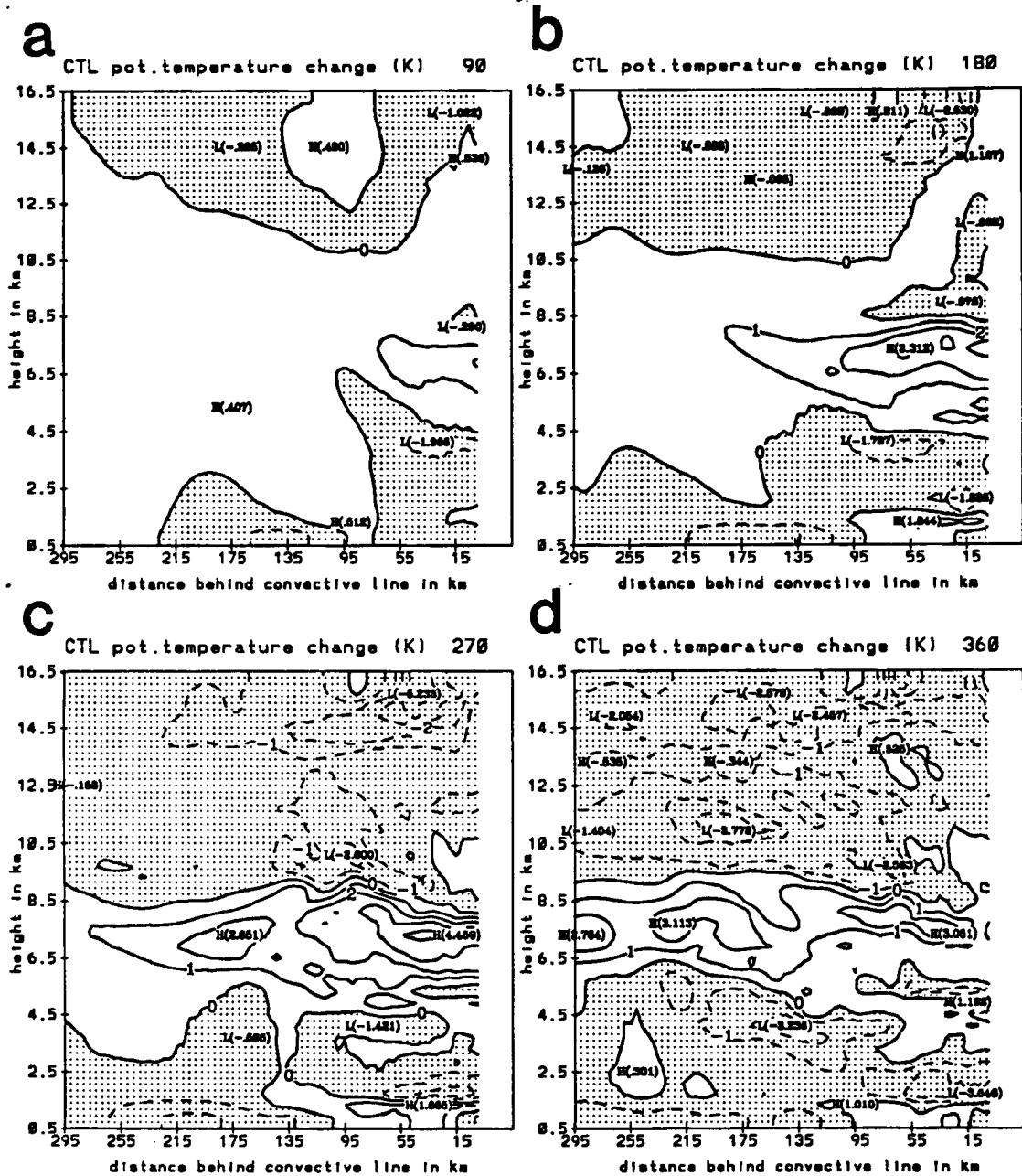
Figure 5.13: Potential temperature change since start of model simulation at (a) 90, (b) 180, (c) 270, and (d) 360 minutes. Contour interval is 1 K. Cooling is shaded.

have warmed nearly 2 K just behind the convective line at 7 km. Similar trends occur at later times, although the mesoscale downdraft and strong adiabatic warming result in θ increases in the lowest 1 km by 180 minutes (Fig. 5.13b). The strongest warming is nearly 2 K just to the rear of the heaviest rainfall. Cooling continues to be pronounced near the melting level, with the greatest cooling moving rearward with time. Cooling from evaporation results in a θ perturbation approaching -3 K at 270 minutes (Fig. 5.13c) and exceeding that at 360 minutes (Fig. 5.13d). Warming aloft spreads rearward, with the greatest potential temperature increases, of over 4 K, occurring at 270 minutes rather close to the convective line. Cooling takes place above 9 km or so after 180 minutes due primarily to adiabatic cooling from the upward motion (Fritsch and Maddox, 1981b), although some weak sublimational cooling also occurs at these high levels.

These temperature perturbations result in hydrostatically-induced mesoscale pressure perturbations (Fig. 5.14). Pressure is not a necessary variable for the integration of the model equations, and is solved for here diagnostically using several simple approximations. The pressure is assumed not to change at the tropopause, 13.3 km, and pressure at each grid point is solved for by integrating a form of the hypsometric equation from this level. The values of pressure shown in the figure are the deviations from the domain-averaged pressure at each level at each time. Because the domain is generally restricted to the stratiform region only, regions of high and low pressure should be considered relative to this area, and not the larger-scale environment. At most times, a relative high in the pressure field occurs near the surface in the area of stratiform rain. At 90 and 180 minutes (Figs. 5.14a, b), the peak perturbation is around + 0.6 mb. At 270 minutes (Fig. 5.14c), the positive perturbation reaches 1 mb. By 360 minutes (Fig. 5.14d), the highest pressures at the surface are slightly rearward of the main rain region, and the maximum perturbation is around 1.5 mb. Regions of relatively low pressure occur at low and mid-levels above the surface, with the strongest "mesolow" at the back of the convective line. The negative perturbation in this area increases from 0.5 mb at 90 minutes (Fig. 5.14a) to around 1.2 mb at 180 and 360 minutes (Figs. 5.14b, d). The influence of this low pressure region expands with time. A weaker region of low pressure can be seen farther
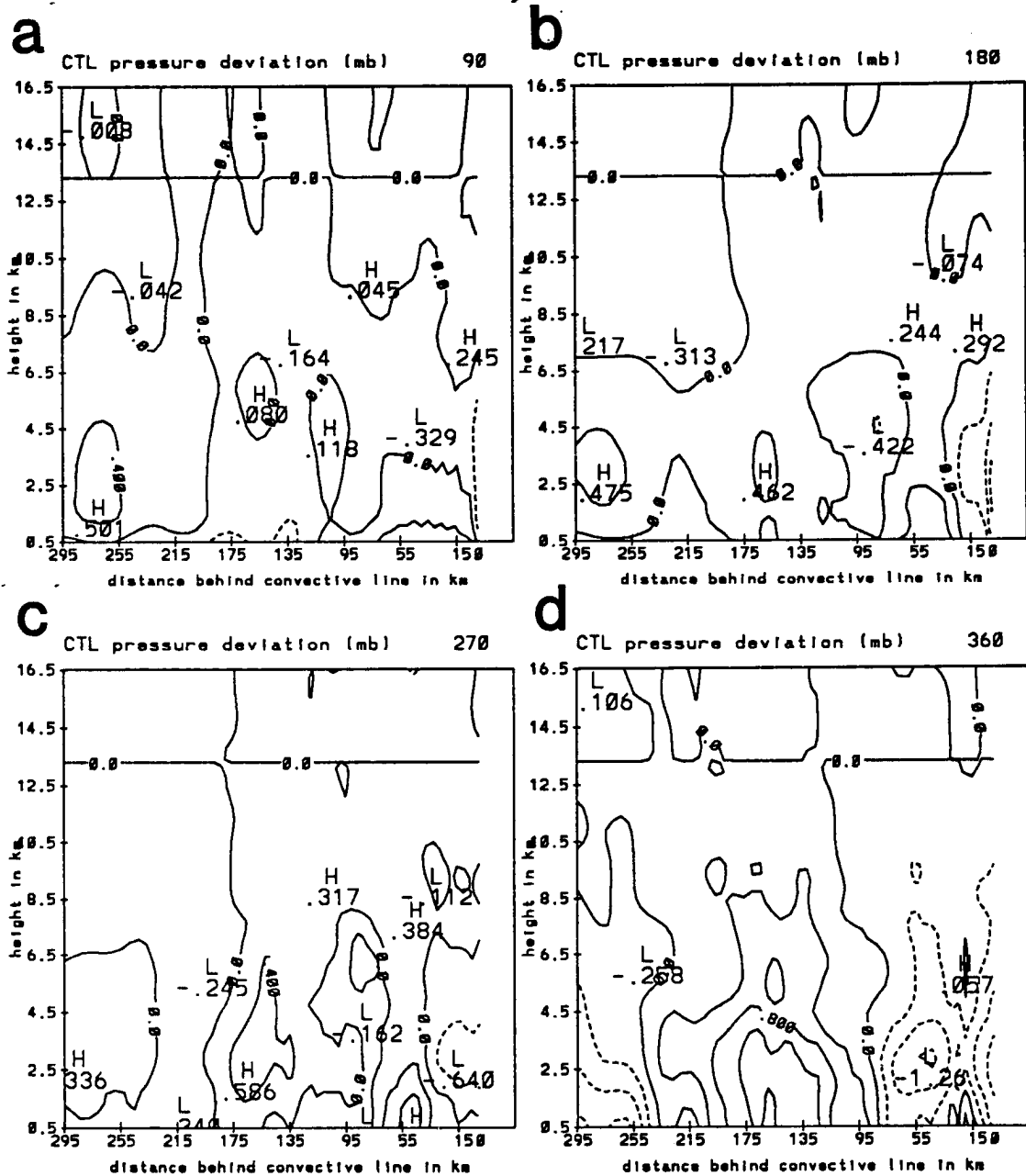
Figure 5.14: Hydrostatically-derived pressure deviation from domain average at (a) 90, (b) 180, (c) 270 and (d) 360 minutes. Contour interval is .4 mb. Negative values are dashed.

rearward near the back of the precipitation region through 270 minutes. The low near the convective line is generally strongest around the 2.5-3 km level. The low farther rearward is most intense near the melting level. A pronounced surface wake low does not occur in this simulation, although there is a hint of slightly lower pressures near the back of the rain region at 180 and 270 minutes (Figs. 5.14c, d). This is the location of the pronounced mesolow observed in this case (Johnson and Hamilton, 1988). The difference in pressure between this negative perturbation and the positive perturbation toward the front of the rain region at these times is around 1 mb, which is less than half of the observed pressure difference on average over the stratiform region of the 11 June system. The failure of the model to reproduce a strong surface mesolow is probably linked to both relatively poor vertical resolution at low-levels, and the weakness of the RTF flow and descent at significant distances away from the convective line. As will be discussed below, the weakness of the flow at distances of 100 km or more from the convective line implies that some outside process like large scale baroclinicity played a significant role in the 11 June system, as discussed by Zhang and Gao (1989).

5.1.5 Horizontal circulations

Almost immediately, the microphysics within the domain induce a positive perturbation horizontal flow (RTF) below 6 km with the strongest RTF perturbation flow just behind the convective line in a steeply sloped zone (Fig. 5.15). At 90 minutes (Fig. 5.15a) this zone is confined to the region within 70 km of the convective line. Peak perturbations are over 3 m s^{-1}. Negative perturbations can mainly be found at this time in a 4 km deep band sloping upwards from the 4-8 km layer near the convective line to the 9-13 km layer at the rear of the domain. The perturbations intensify throughout the simulation with the strongest perturbations occurring after the advection has ceased from the convective line, 360 minutes (Fig. 5.15d). Peak RTF perturbations reach 10 m s^{-1} at the 1.5 km level just behind the convection at 180 minutes (Fig. 5.15b), nearly 14 m s^{-1} at the same location behind the convection at 270 minutes (Fig. 5.15c), and around 17 m s^{-1} rather uniformly in the region within 60 km of the back of the convective line around the 2 km level at 360 minutes. This rear-inflow "jet" becomes increasingly horizontal over time, much the
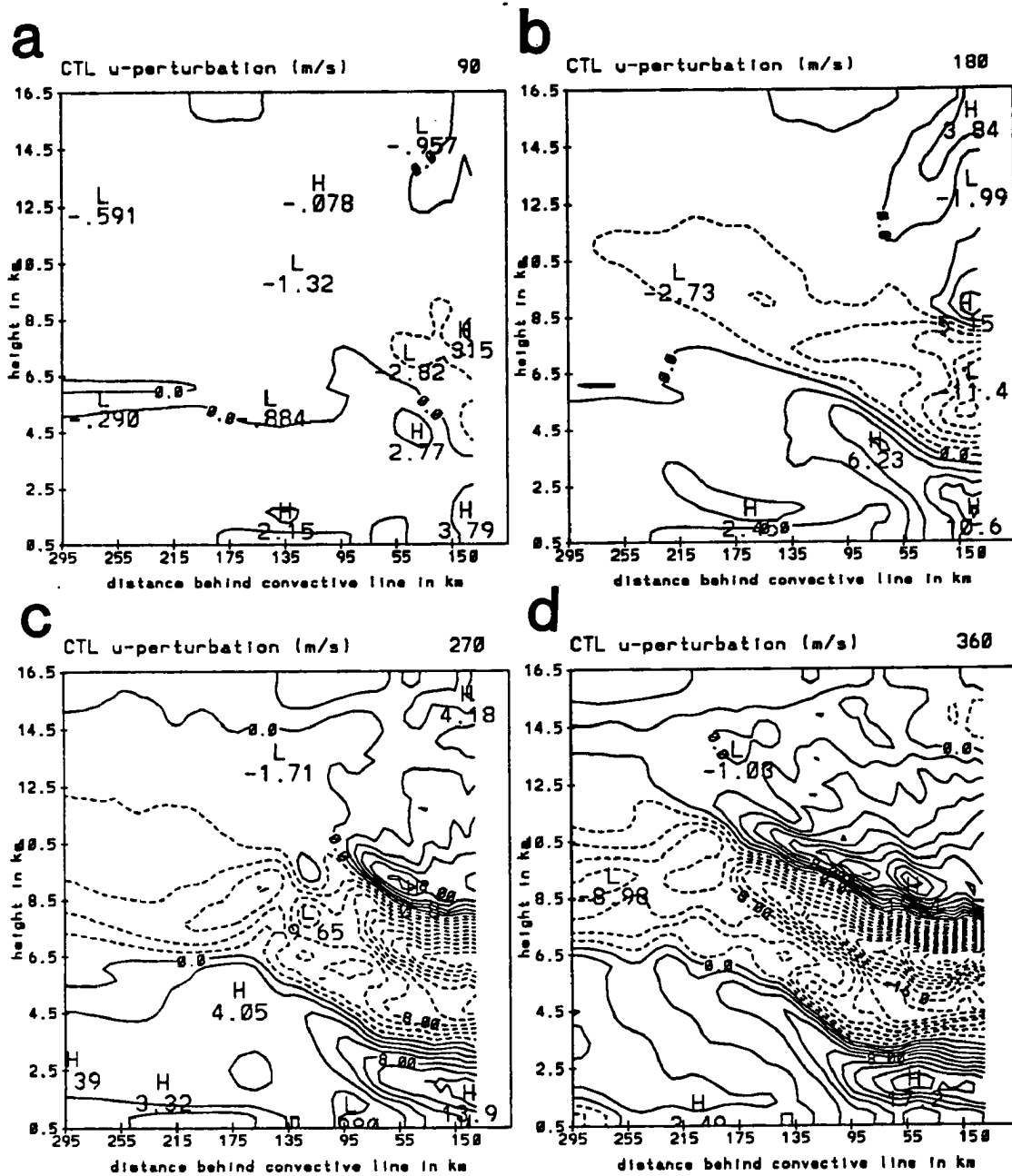
Figure 5.15: Perturbation u-velocities at (a) 90, (b) 180, (c) 270, and (d) 360 minutes. Front-to-rear flow is dashed. Contour interval 2 m s^{-1}.

same as the observed jet for this case (e.g. Gallus and Johnson, 1991). At the earlier times, a weak negative perturbation flow can be seen beneath the rear-inflow jet at the surface as the cold pool from the convection and growing stratiform rain region spreads rearward. The negative perturbation flow aloft also intensifies through 360 minutes and is concentrated in a band that slopes upward toward the rear. The greatest values tend to be nearest the convection at 6.5 km or so, although a fairly uniform maximum exists over a 50 km wide region by 360 minutes. At the later times, generally after 180 minutes, a return branch of positive perturbation velocity exists around the 9 or 10 km level. This location would be just above the most intense mesoscale updraft.

It should be emphasized that these perturbation flows exist within an ambient flow. This ambient flow must be added to give a true picture of the flow in the domain. The total wind (Fig. 5.16) is generally directed from front to rear at 90 minutes (Fig. 5.16a), although some RTF flow has developed in the front portion of the domain. The rear-inflow jet does strengthen, with the peak velocities reaching 14 m s^{-1} by 360 minutes (Fig. 5.16d). The strong current of FTR flow which advects the hydrometeors rearward increases to over 30 m s^{-1} at later times. These diagnosed values of FTR flow, although quite strong, are only slightly larger than the peak values found by the Doppler and rawinsonde observations from this case (Smull and Houze, 1987b, Rutledge et al., 1988, Gallus and Johnson, 1991). The diagnosed rear-inflow jet, however, is slightly weaker than observed. Rutledge et al. (1988) found that RTF flow already exceeded 15 m s^{-1} by 0300 UTC. Peak intensities were generally slightly higher than this value. Rawinsondes also showed isolated values of 15 m s^{-1}, but generally after 0300 UTC. It is believed that the model's underestimate of upward motion in the anvil cloud and subsequent failure to produce enough precipitation also led to underestimates of evaporation and sublimation and this may have prevented the rear-inflow current from strengthening to observed values. The model results also imply, however, that the system itself only generates strong rear-inflow within several hundred kilometers of the system. Even by the end of the simulation, most of the significant rear-inflow was occurring within 150 km of the back of the convective line. The results of Rutledge et al. (1988) and Gallus and Johnson (1991) for this case show strong rear

a
CTL total U-wind (m/s)   90

c
CTL total U-wind (m/s)   270

b
CTL total U-wind (m/s)   180

d
CTL total U-wind (m/s)   360
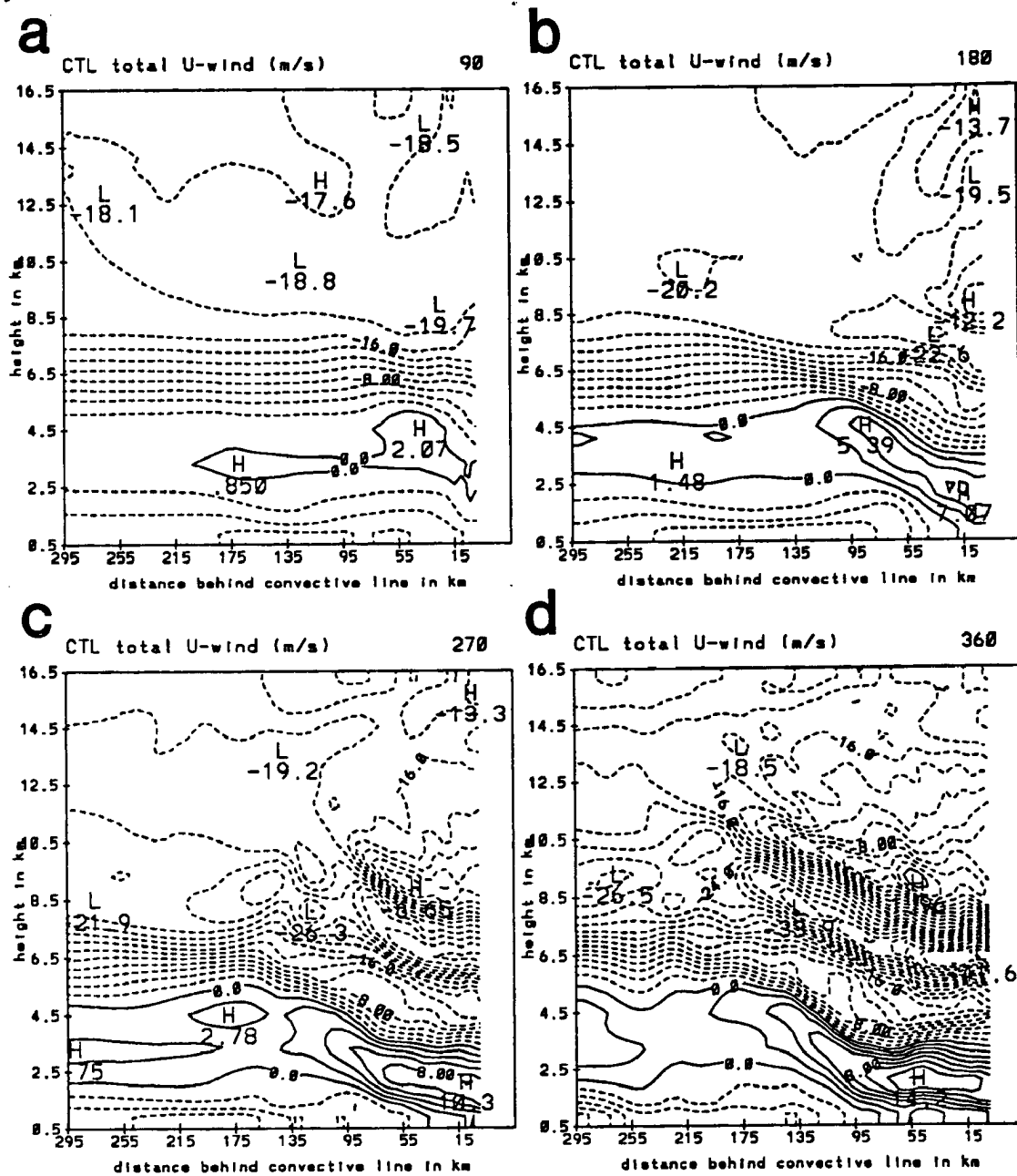
Figure 5.16: Same as Fig. 5.15 except for total u-velocity (includes ambient flow).

inflow well to the rear of this point. The numerical simulations of Zhang et al. (1989) were able to produce significant rear inflow many hundreds of kilometers to the rear of the system, which they attributed to large scale baroclinicity. The failure of this simulation, along with many others using different initial conditions, to produce rear-inflow greater than 10 m s^{-1} well behind the system implies that large scale baroclinicity may indeed be the mechanism responsible for the strong elevated portion of the jet on 11 June, although other factors may also play a role.

5.1.6 Relative humidity

The strong FTR flow at mid and high levels quickly advects vapor across the domain (Fig. 5.17). Humidities with respect to water of over 90% reach the left boundary by 270 minutes (see Fig. 5.17c). Several areas within the anvil cloud are saturated with respect to water. During the first 120 minutes of the simulation, dry air at midlevels retreats, but the strengthening rear-inflow jet begins transporting drier air back into the stratiform rain region at 180 minutes (Fig. 5.17b). Mesoscale descent also leads to drying in this region, so that humidities drop below 55% at 270 minutes near the back of the surface rainfall at an elevation of 3 km. Generally the minimum low-level humidities do not fall below 50% in the main rain region throughout the simulation.

Soundings taken at later times in this relatively dry area (x = 95 km) do show a hint of an "onion" structure (Zipser, 1977), particularly at 405 minutes (Fig. 5.18). The greatest dew point depressions are found around the 800 mb level. This is somewhat higher than typical onion soundings (see Fig. 5.6b), and the elevated dry region is probably due to the relatively coarse resolution of the model at low levels, 400 m. Leary (1980) discusses the ability of one-dimensional models to correctly diagnose onion-like soundings in the unsaturated mesoscale downdraft. The model showed a direct relation between the amount of drying and warming that takes place and the strength of the downdraft. The failure of dry air to extend closer to the surface in the current simulation is associated with the rapid weakening of the downward motion near the surface.

The wind profile at the right side of the skew-T diagram shows that rear-inflow was occurring below 700 mb. Peak values were around 15 m s^{-1} at 800 mb. The strongest
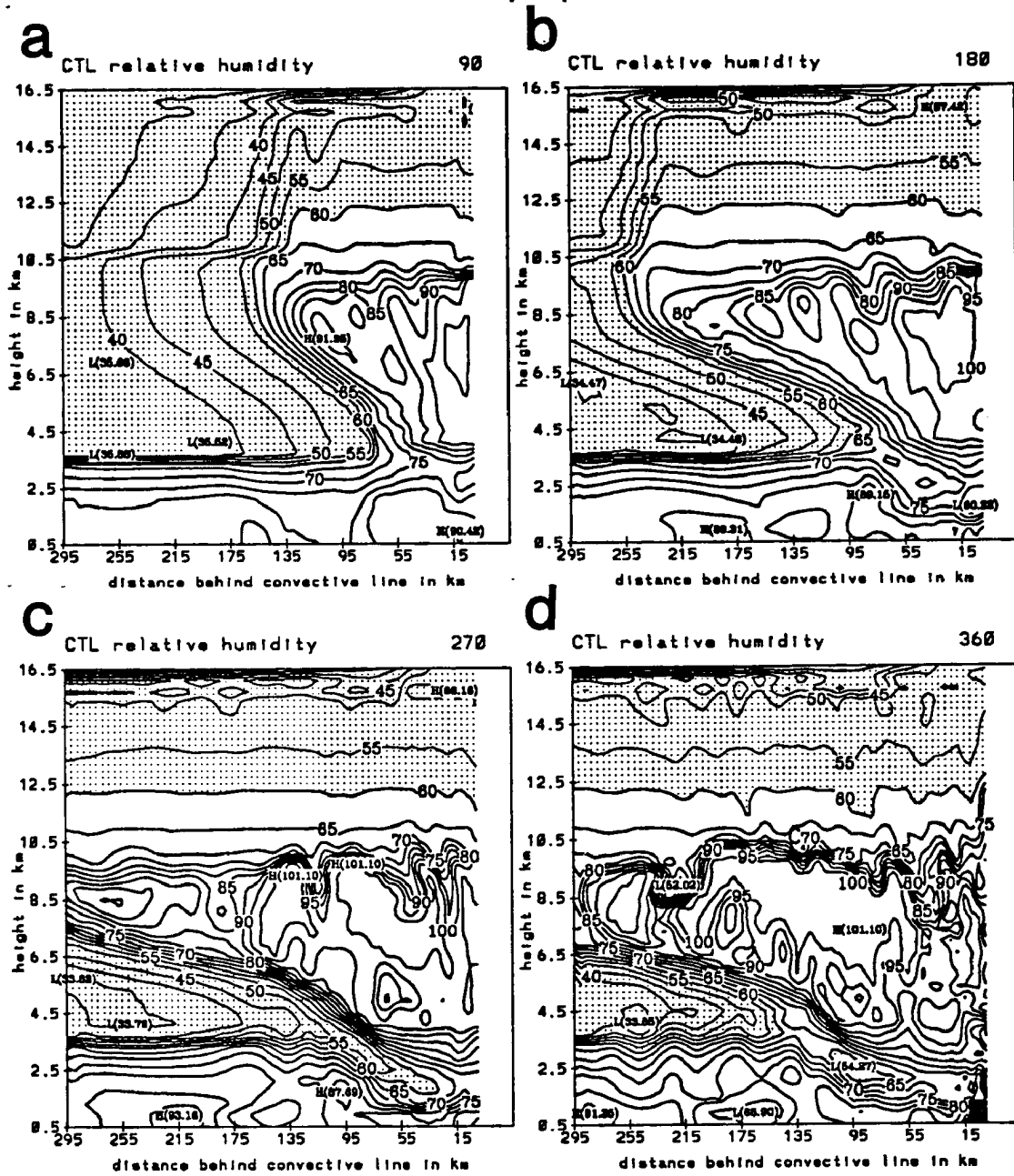
Figure 5.17: Relative humidity with respect to water at (a) 90, (b) 180, (c) 270, and (d) 360 minutes. Contour interval 5 %, with humidities less than 60% shaded.
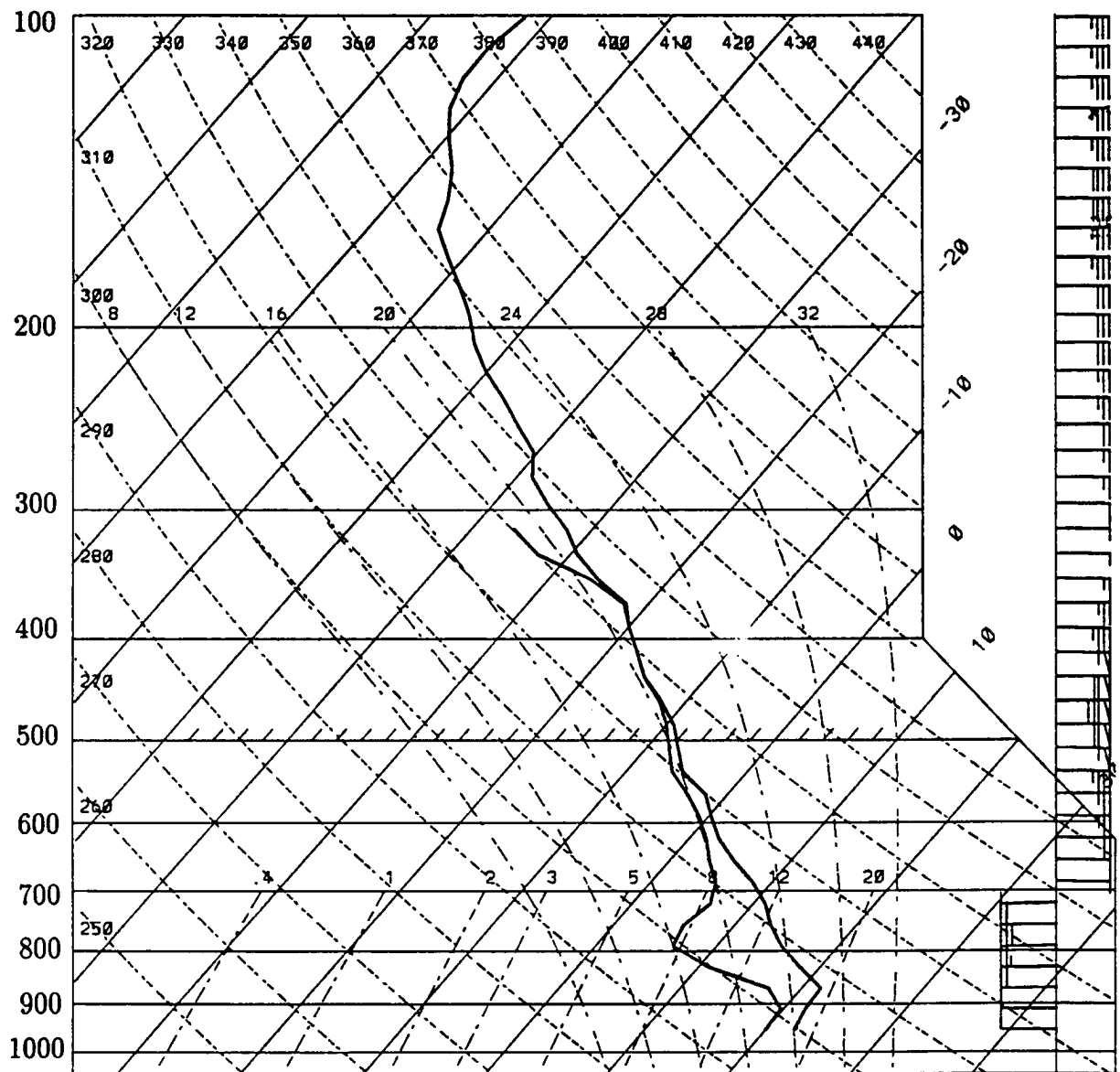
Figure 5.18: Thermodynamic profile taken within region of light stratiform rainfall at 405 minutes. Winds are shown at the right of the diagram.

front-to-rear flow occurred in the saturated region around 450 mb. The roughly 40 m s^{-1} flow at this point exceeds the observed peak values in the stratiform region by 30-40%. This overestimate may be partially due to the two-dimensionality of the model, which has been shown in previous studies to result in strengthened horizontal flow at the expense of vertical motions.

In summary, this particular simulation produces features that reasonably agree with those observed in the 11 June squall line. Initially rain rates and vertical motions are rather weak, but by 315 minutes into the simulation, a time that corresponds roughly with the observed peak intensity of the stratiform region, diagnosed peak ascent in the anvil cloud and descent in the mesoscale downdraft are similar to those values observed by Doppler radar. Averaged vertical motion over the entire stratiform region compares fairly well with rawinsonde-derived values. Peak descent occurs around the 3 km level, and the changeover from descent to ascent is approximately 1 km above the melting level. Strongest ascent on average occurs near 8 km, which is slightly below the level found by rawinsondes for this case, and found in other midlatitude cases.

A water budget of the system shows that the ratio of in situ production of condensate to advected condensate from the convective line increases from less than 20% during the development of the stratiform region, to more than 60% at later times when the mesoscale updraft is well-developed and convective influences are weakening. Hydrometeor advection is therefore most important in producing substantial surface rainfall early in the development of the stratiform region, and in situ production becomes most important later.

Rainfall at the surface is more significantly underestimated in the model, although the diagnosed values of peak surface rate differed by only 30% or so. It is possible that the underestimate of ascent, particularly at levels above 9 km and at early times, results in the reduced values of surface precipitation. In addition, problems with the evaporation term in the microphysical parameterization may result in overestimates of evaporation and hence underestimates of surface rainfall. Other 2D modeling studies have found that vertical velocities are underestimated in the anvil cloud (e.g. Dudhia et al., 1991). One

common characteristic of 2D models is the failure to generate vertical circulations that are as strong as those produced in a 3D model, because of the lack of a third dimension to influence convergence and divergence. The model evolution of the transition zone agrees exceptionally well with observations, and may imply that the rapid dissipation of the convective line causes the rapid broadening observed after 0600 UTC.

The rear-inflow jet in this simulation, although eventually reaching an intensity close to that observed, is generally weaker and confined to a smaller region than observations indicated. It is possible that the differences in the model were due to the restriction of two dimensionality. In addition, radiative effects within and at the top of broad anvil clouds during nighttime hours have been shown to increase circulations within the stratiform region (Tao and Simpson, 1993). Some of the difference between diagnosed and observed circulations and surface rainfall intensity may be due to the lack of a radiation scheme in the model. The jet qualitatively evolves in agreement with observations.

5.2 Hydrometeor advection alone (C2)

Another simulation (C2) was done without convective heating, to test the effect of microphysical processes within the stratiform region acting on hydrometeors alone advected into the domain. In this simulation, it is assumed that the only influence of the convective line after establishing FTR flow into the stratiform region is to supply hydrometeors to that area. As will be shown, many observed features are again simulated with good qualitative agreement to observations, although the magnitudes of the circulations are significantly less than in the simulation which included effects from convective heating.

Snow, ice and graupel mixing ratios are reduced somewhat in C2 due to weaker upward motions and a decrease in vapor deposition and condensation. The decreases are typically around 10-20%. These decreases are reflected in a decrease in surface rainfall (Fig. 5.19) in C2 from that which occurred in CTL. Peak surface rain rates are only around 1.5 mm h^{-1} in this simulation, and occur early, at 90 minutes (Fig. 5.19a). The area of surface rainfall does move rearward during the first 180 minutes (Fig. 5.19b), but rearward progression ceases after this time and measurable rain does not occur rearward
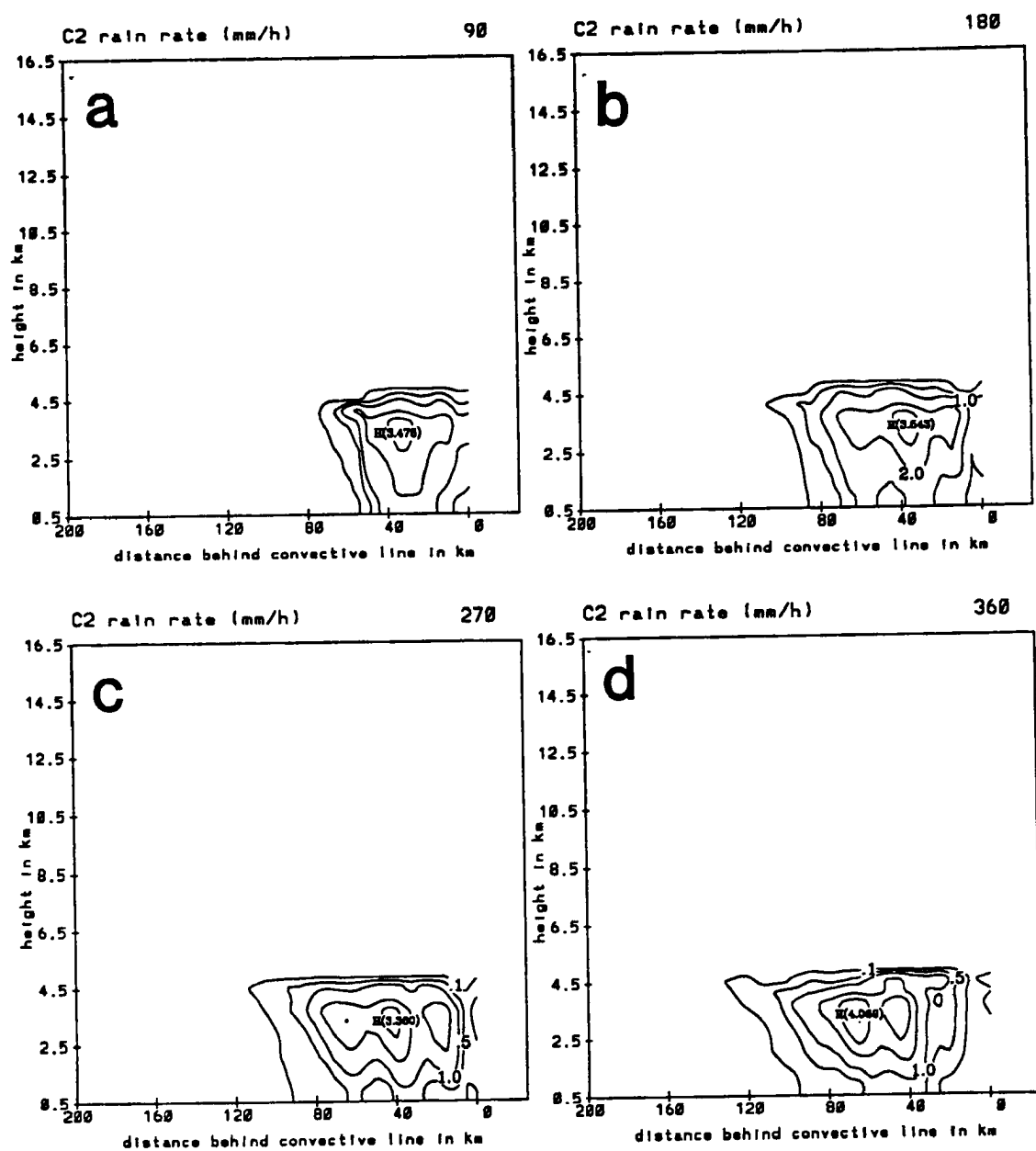
Figure 5.19: As in Fig. 5.3, except for C2, the simulation excluding convective line heating. Rain rates are shown at (a) 90, (b) 180, (c) 270, and (d) 360 minutes.

of 95 km. The diminished circulations in C2 result in the region of light rainfall just behind the convective line not broadening significantly until late in the simulation. This transition region is only around 15 km wide through most of the simulation.

In general, evaporation, melting, sublimation, deposition and condensation rates are all diminished in C2 from their values in CTL, but the changes in the heating and cooling rates are typically under 25%, except for condensation which is reduced much more significantly due to the lack of any strong ascent. The combined effects of all microphysical processes result in a broad region of significant cooling from evaporation, melting, and sublimation that slopes rearward with height (Fig. 5.20). Peak values are roughly 5 C h^{-1}. The cooling spreads slightly farther rearward with time, but not to the extent that it does in CTL. Diabatic heating is much weaker than in CTL. Broad areas of weak heating exist in the 6-10 km layer, but most of the heating is under 1 C h^{-1}. After 270 minutes (Fig. 5.20c), some small regions of enhanced upward motion result in heating greater than 2 C h^{-1}, but overall, diabatic heating is insignificant compared with that in CTL.

The reduction in microphysical processes and surface rainfall from that in CTL can be seen in the integrated water budget (Table 5.3). The total amount of condensate produced in situ in C2 is only around 37% of that in CTL. The weakened circulations also cause a small decrease in the amount of condensate entering the domain from the convective line. A more detailed water budget (not shown) indicates that deposition is an order of magnitude larger than condensation prior to 270 minutes in C2, and still twice as large at later times, due to much diminished ascent in the anvil cloud. The amount of rain reaching the surface in C2 is slightly under 60% of the CTL value. This simulation has similarities to a sensitivity test performed in the kinematic model of Rutledge and Houze (1987) where hydrometeor advection continued, but vertical motion was ignored in the stratiform region. In that simulation, surface rainfall was only 25% that of the CTL run. The Rutledge and Houze result along with the results in C2 imply that although hydrometeor advection from the convective line is significant, much of the stratiform rainfall must be due to in situ condensate production. Precipitation efficiencies in C2 are comparable to those in CTL, since the weaker circulations reduce evaporation and sublimation.

a

C2 diabatic heating (K/h)   90

height in km

distance behind convective line in km

b

C2 diabatic heating (K/h)   180

height in km

distance behind convective line in km

c

C2 diabatic heating (K/h)   270

height in km

distance behind convective line in km

d

C2 diabatic heating (K/h)   360

height in km

distance behind convective line in km
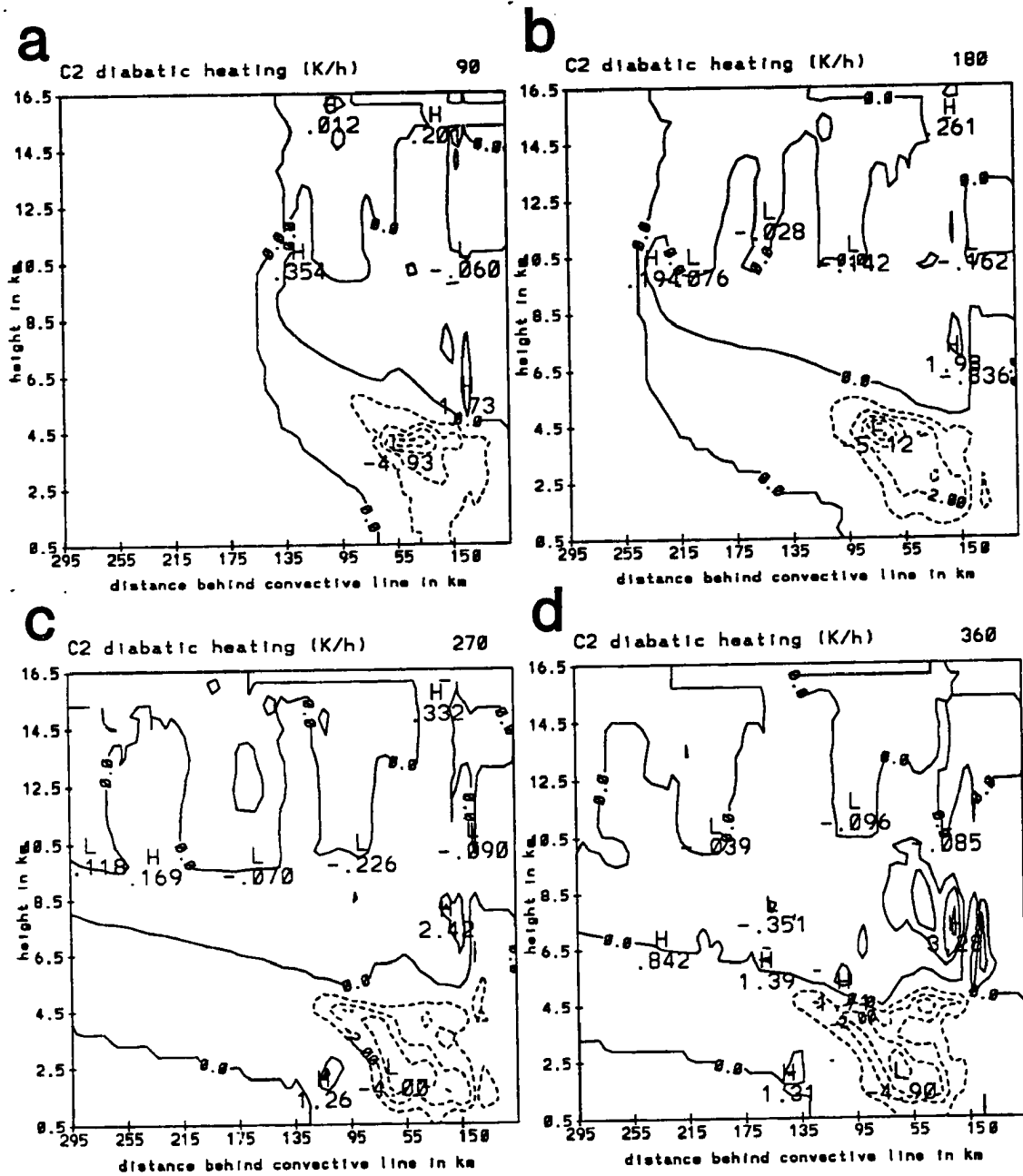
Figure 5.20: As in Fig. 5.8, except for C2, the simulation excluding convective line heating.

Table 5.3: Simplified integrated water budget of the CTL model simulation, the no heat simulation (C2), and the no hydrometeor simulation (C3). Values are in metric tons of water over the entire 405 minute simulation, with percentage change from CTL also shown.

Run	Advected mass	In Situ mass	Mass Sink	Rain sink
CTL	1692.06	1246.98	2285.17	511.98
C2	1475.27 (-13%)	455.19 (-63%)	1458.02 (-36%)	300.42 (-41%)
C3	84.97 (-95%)	573.74 (-54%)	674.01 (-71%)	17.94 (-96%)

Vertical motions throughout the domain are diminished (Fig. 5.21) but the most significant weakening is in the mesoscale updraft. At 90 and 180 minutes (Figs. 5.21a, b) ascent is only on the order of a few cm s^{-1}. Upward motion does not exceed 20 cm s^{-1} until 270 minutes (Fig. 5.21c), and even at that time, most of the ascent is no larger than 10 or 15 cm s^{-1}. By 360 minutes (Fig. 5.21e), some increase in upward motion is observed with peak values exceeding 30 cm s^{-1}.

The mesoscale downdraft, although diminished in strength, is again rather broad and well-organized. Peak values exceed 30 cm s^{-1} by 180 minutes (Fig. 5.21b) and eventually grow to over 50 cm s^{-1} at 405 minutes (Fig. 5.21f). The downdraft expands rearward with time as in CTL, but the more intense subsidence does not extend as far rearward. Heating within the convective line significantly affects the mesoscale ascent in the anvil cloud, but has a less significant, indirect effect on the mesoscale downdraft. The downdraft is more a function of processes within the stratiform precipitation region.

The averaged vertical motions over the stratiform rain region during the 270-360 minute time period (Fig. 5.22) are much weaker than those in CTL. The level of peak ascent is slightly higher, around 9 km, but the magnitude is only around 10 cm s^{-1}. This higher level of peak ascent agrees better with observations, possibly implying that the convective heating profile used in this simulation exerts too much effect on the resulting circulations in the stratiform domain. Strongest descent occurs between 2 and 3 km, with the peak value around 20 cm s^{-1}. The averaged vertical motion profile shows that hydrometeor advection alone induces vertical motions agreeing qualitatively with those observed, but the magnitudes are significantly underestimated. Even the smaller-scale average (curve B) does not have substantially greater vertical velocities.
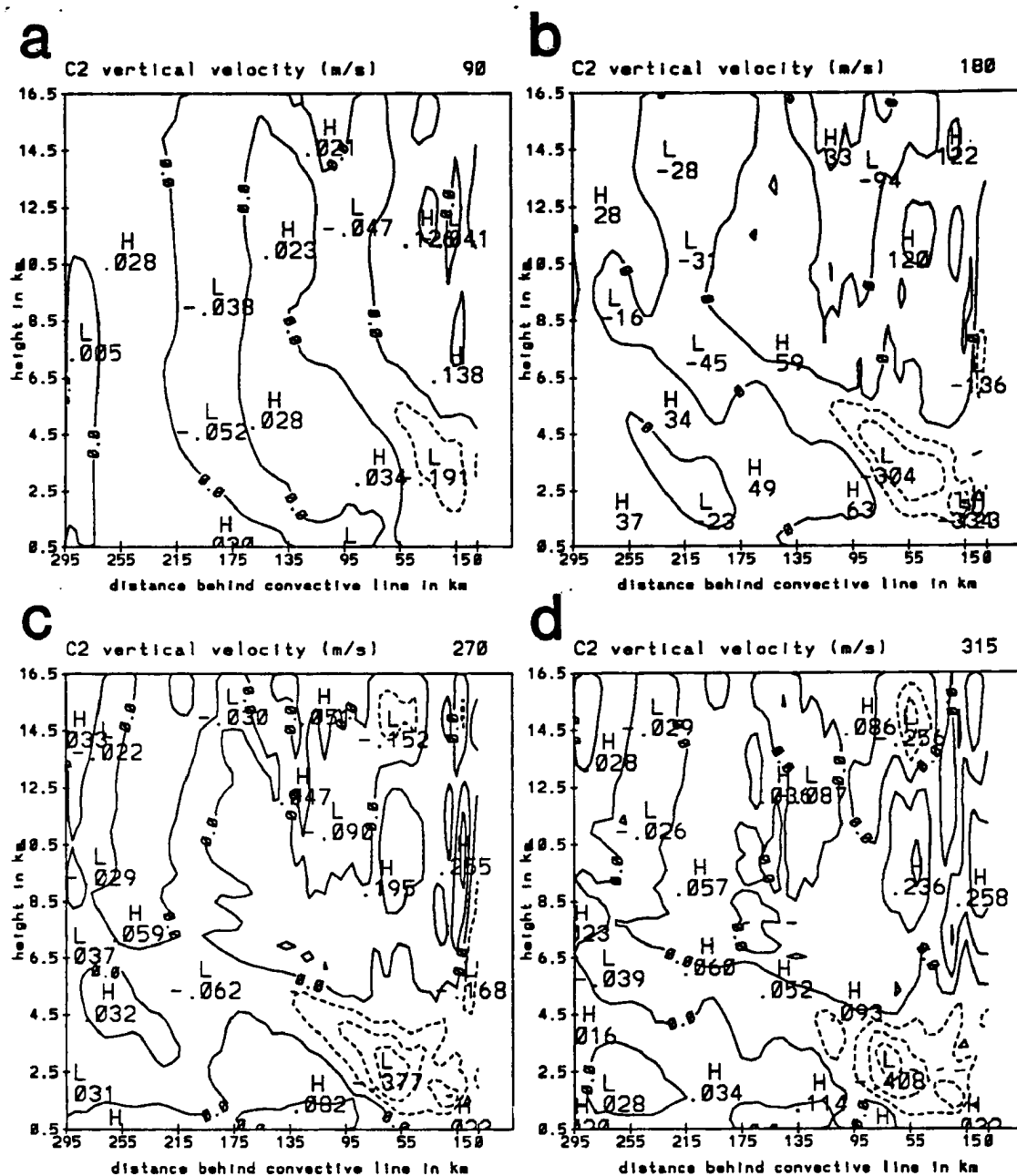
Figure 5.21: As in Fig. 5.11, except for C2, the simulation excluding convective line heating.
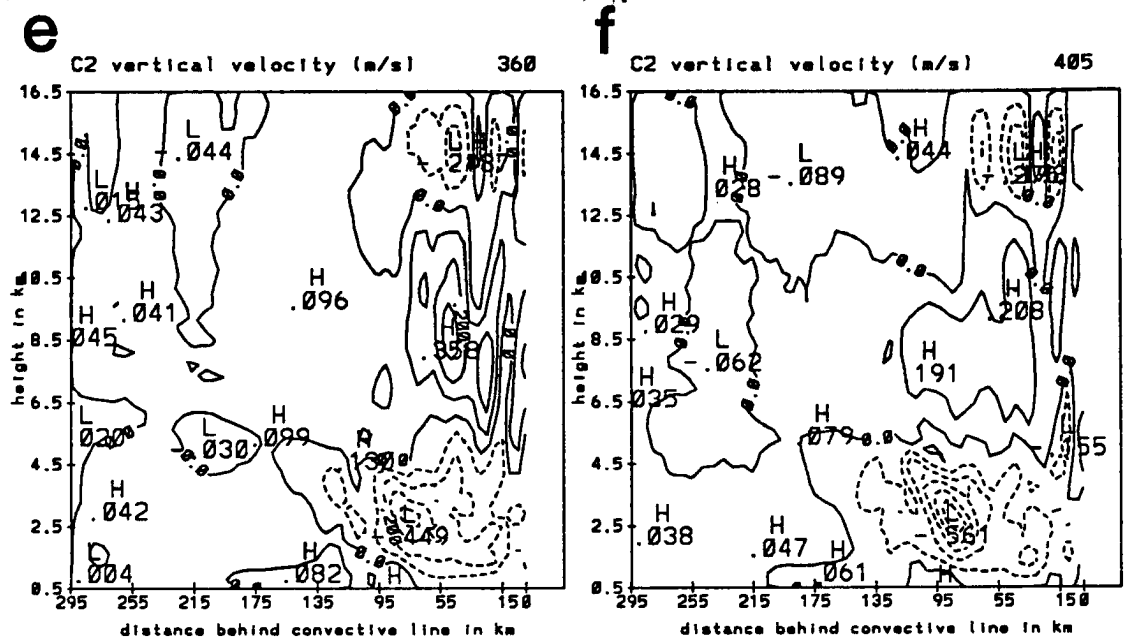
Figure 5.21: continued
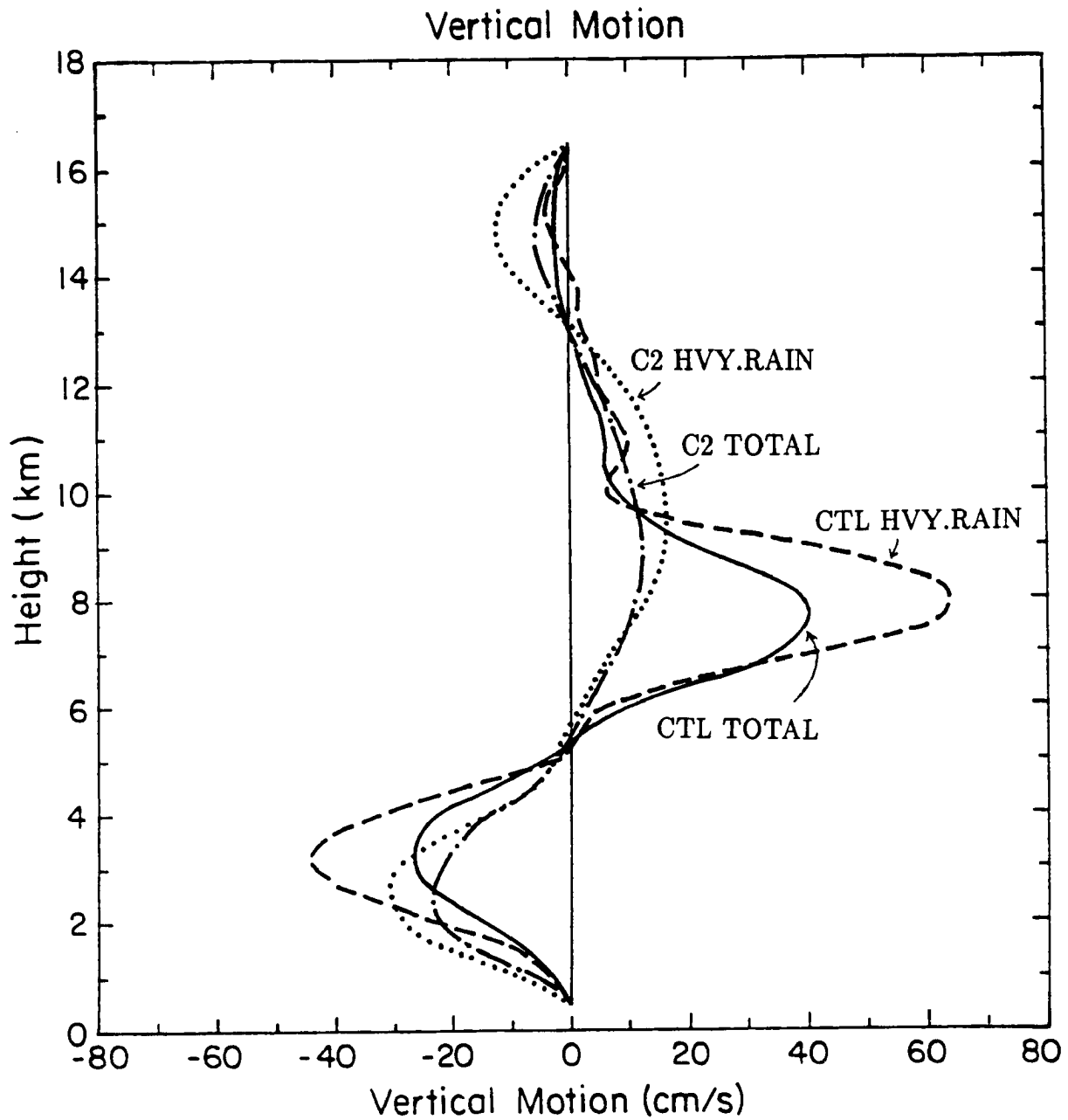
Figure 5.22: Comparison of model vertical motion averaged over the stratiform region of simulations CTL (solid curve) and C2 (dash-dotted curve), and over the 40 km region of heaviest surface rainfall for simulation CTL (dashed curve) and C2 (dotted curve) during the 270-360 minute time period.

Horizontal velocity perturbations are also diminished in C2 (Fig. 5.23). Perhaps the most important difference from CTL is that the rear-inflow near the back edge of the heaviest stratiform precipitation is nearly as strong as that at the front of the stratiform region during the first half of the simulation. By 180 minutes (Fig. 5.23b) rear inflow exceeds 5 m s^{-1} just below the melting level 80 km behind the convective line. This secondary peak in rear-inflow remains relatively constant in magnitude and location throughout much of the remainder of the simulation. Prior to 270 minutes (Fig. 5.23c), the rear inflow in this region is nearly as strong as it was in CTL in the same region. Rear inflow just behind the convective line region is only slightly stronger than at the back of the stratiform rain region. This simulation shows that ice processes can result in a noticeable buoyancy gradient and enhancement in the rear-inflow rather far from the convective line itself. Therefore, Weisman's (1992) conclusions about the rear-inflow jet, based upon simulations neglecting ice, though valid, should be investigated with a model including ice microphysics. In a system where stratiform region rainfall is much more intense, it is conceivable that the maximum buoyancy gradient and rear-inflow could occur near the rear of the stratiform region and not closer to the convective line region. The slope of the rear-inflow jet and its increasingly horizontal axis with time again agree with observations. The peak magnitude is about 65% of what it was in CTL at each time, and is therefore much less than observed values. When added to the ambient flow, only a weak rear-inflow jet exists in this simulation and it is not horizontally extensive. In addition, in C2, the FTR jet at mid and upper levels is enhanced by less than 50% of what it was in CTL. Convective heating therefore must be an important generator of the strong FTR flow found above the rear-inflow jet in the stratiform anvil cloud. It is apparent that microphysical processes within the stratiform region can produce a rear-inflow jet of moderate strength, and these processes may fully explain those squall line cases where rear inflow is relatively moderate, and forms within the stratiform region. Convective heating intensifies the jet as it lowers and approaches the convective line.
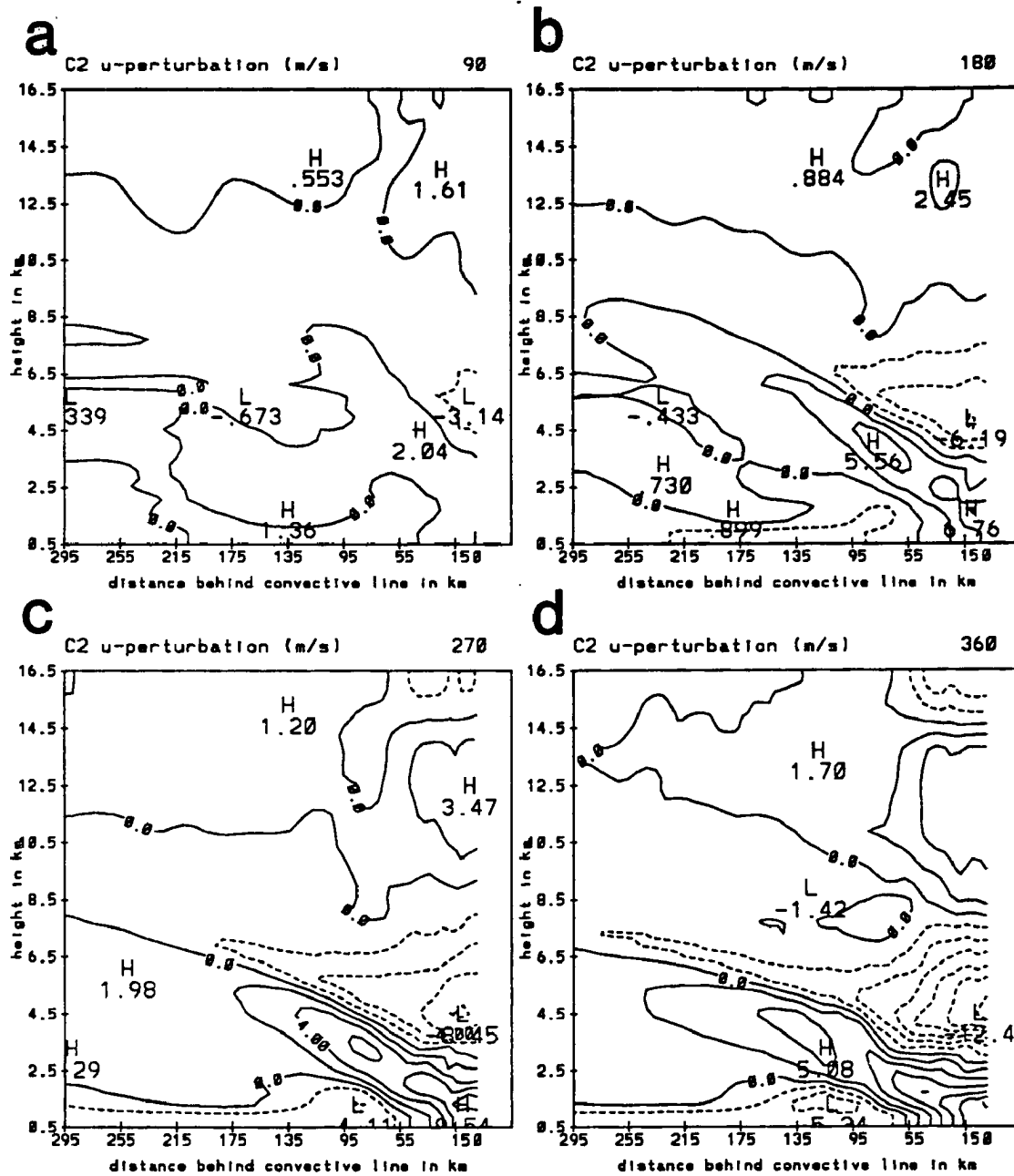
Figure 5.23: As in Fig. 5.15 except for C2, the simulation excluding convective heating.

5.3 Heat advection alone (C3)

Another simulation (C3) was run in which the convective line did not supply hydrometeors to the domain, but did release heat. In addition, the same moist conditions at the right boundary used in CTL are present in C3, so that water vapor also advects across the domain. The strong convective heating induces upward motion in the stratiform domain which produces some condensate. Peak snow mixing ratios, however, remain under 0.7 g kg^{-1}. through 270 minutes, and do not exceed 1 g kg^{-1} until the end of the simulation (figure not shown). These values are generally less than half of the peak values in CTL. Because the in situ production of condensate is rather small, rainfall does not reach the surface until after 315 minutes, and the peak rain rates are less than 1 mm h^{-1} (figure not shown).

Peak upward motion within the domain for C3 is surprisingly strong, and often similar to that in CTL (Fig. 5.24), even though rainfall is negligible at the surface. At 90 and 180 minutes (Figs. 5.24a, b), the peak upward motion is at least as strong as it is in CTL, but the upward motion is confined to an even smaller region just behind the convective line at around the 6.5 km level. By 270 minutes (Fig. 5.24c), upward motion exceeding 10 cm s^{-1} does spread rearward nearly 100 km. Upward motion intensifies at later times, and shows similar patterns to that in CTL. The peak magnitudes, however, remain at 50-90% of those in CTL, and significant upward motion covers smaller regions of the anvil cloud. The fact that surface precipitation is so small in spite of rather significant upward motion implies the importance of hydrometeor advection and the seeder-feeder type processes within the stratiform anvil cloud, as found by Rutledge and Houze (1987). With a kinematic model that study showed in simulations using the same vertical motion field, with one excluding rearward hydrometeor advection, that rainfall at the surface was much lighter without the rearward flux of hydrometeors. This was true even though a majority of the condensate within the anvil cloud could be produced in situ. Hydrometeors from the convective line were necessary to scavenge the condensate produced in the anvil cloud.

Some important water budget terms can be seen in Table 5.3 for this case and compared with CTL. The production of condensate, and therefore also mesoscale ascent, is
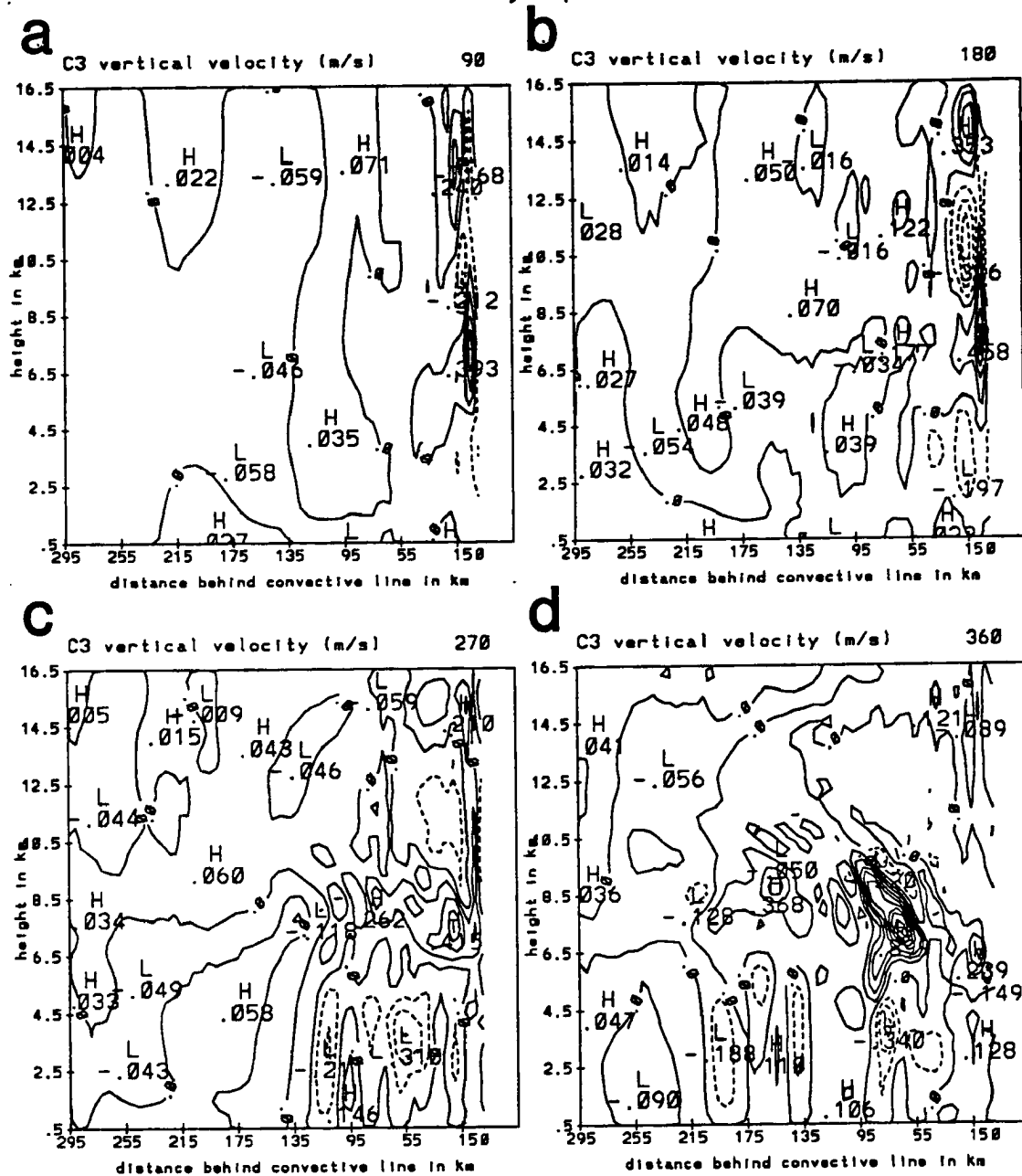
Figure 5.24: Vertical velocities in the model domain at (a) 90, (b) 180, (c) 270, and (d) 360 minutes for C3, the simulation excluding hydrometeor advection from the convective line. Contour interval is .1 m s^{-1} with downward motion dashed.

greater in C3 than in C2, implying the ascent is strongly dependent upon convective heating. However, rainfall at the surface is greater in C2 than in C3, implying the importance of hydrometeor advection in allowing rainfall to reach the surface in the stratiform region. Both in situ production of condensate and surface rainfall are much larger in CTL than in either C2 or C3, showing that both convective heating and hydrometeor advection are necessary to explain significant stratiform precipitation. The processes that add condensate mass to the hydrometeors from the convective line add significantly to the latent heat release and upward motion in the anvil cloud. Other simulations were done in which only high level condensate in the form of ice enters the domain in varying amounts, and these also fell far short in reproducing features as close to those observed as in CTL. Precipitating hydrometeors advected from the convective line are necessary to produce substantial surface rainfall.

Mesoscale descent is significantly less in C3 than in CTL (Fig. 5.24) since the mesoscale downdraft is so strongly dependent upon evaporation, melting, and sublimation of the hydrometeors in the stratiform region. The descent occurs over a much smaller area than in CTL, and the peak values do not exceed 20 cm s^{-1} until around 270 minutes (Fig. 5.24c), and only exceed 30 cm s^{-1} after 360 minutes (Fig. 5.24d).

Without strong diabatic cooling processes in the stratiform region in C3, the perturbation horizontal flows are significantly different than in CTL (Fig. 5.25). Rear inflow does develop at low levels, but the jet does not slope as in CTL. Rear inflow is strongest just behind the convective line, but the peak values here are roughly 40-50% less than in CTL. FTR flow is enhanced in midlevels by the convective heating, but this flow is also reduced by a similar amount from that in CTL. The diminished horizontal perturbations are due in part to the weakened downdraft which induces less midlevel convergence. In addition, a positive feedback may be operating since the reduced midlevel convergence caused by the weakened downdraft probably also results in less forced ascent in the anvil cloud, less in situ production of condensate, and even less forcing of a downdraft.

In summary, simulations CTL, C2 and C3 show the importance of both hydrometeor advection and in situ production of condensate, which is strongly related to the convective
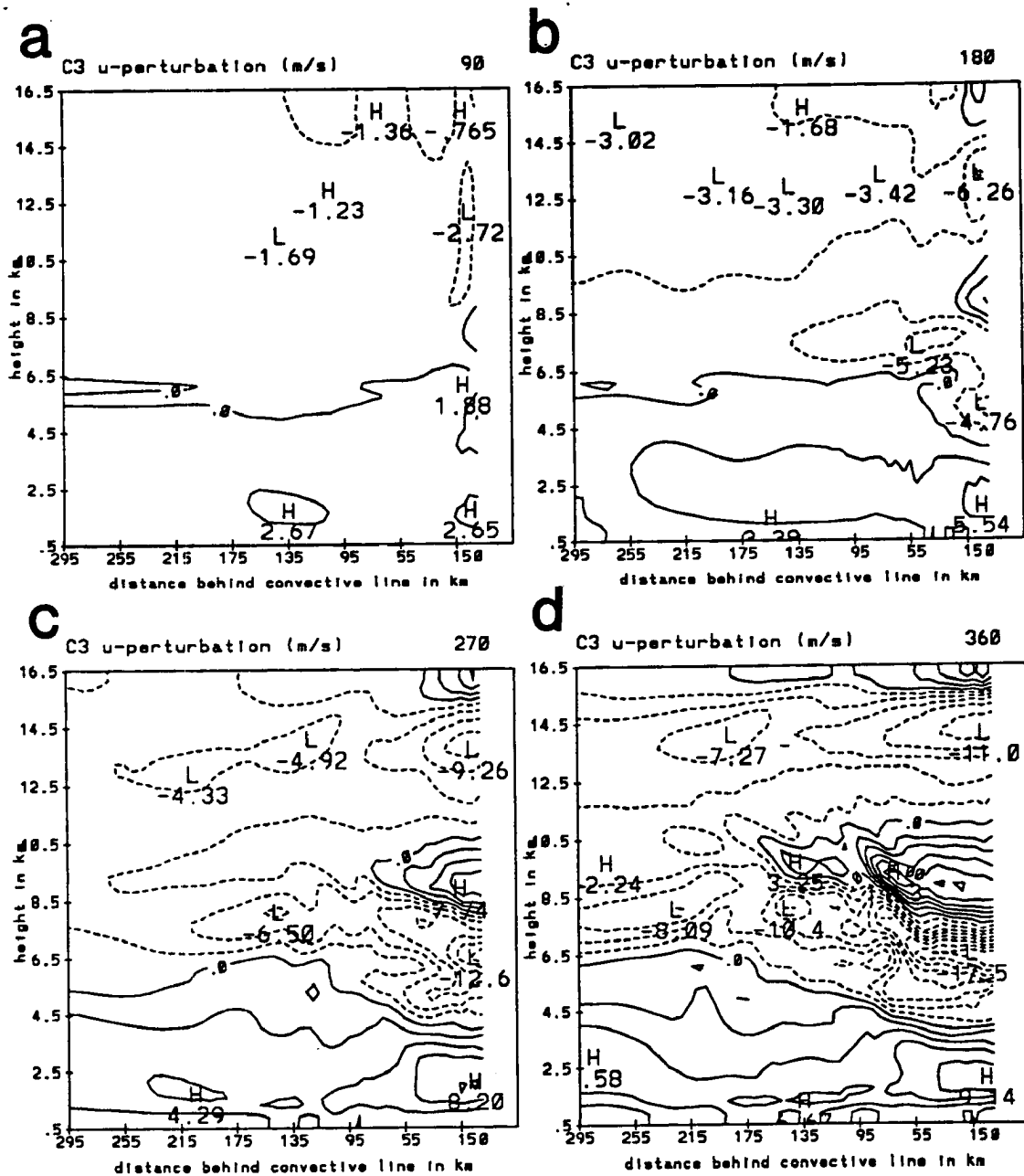
Figure 5.25: As in Fig. 5.15 except for C3, the simulation excluding hydrometeor advection from the convective line.

line heating, in producing broad areas of significant rainfall at the surface, and generating strong horizontal and vertical motions in the stratiform region. Without convective heating, mesoscale ascent is very weak, and although rain does occur over a fairly broad area, the total rainfall is much less than in a simulation where convective heating also plays a role. Convective heating alone, without the advection of hydrometeors, causes almost no surface rainfall, even though in situ generation of condensate is substantial. These results as they relate to surface rainfall support the conclusions of Rutledge and Houze (1987) determined from a kinematic model. The results also elaborate on those earlier findings by showing the importance of hydrometeor advection and convective heating in generating strong circulations.

5.4 Individual processes

A series of simulations were performed in which one or a series of processes were neglected as sources or sinks of diabatic heating. In these simulations, all processes take place and influence the mixing ratios of hydrometeors and vapor present, but only certain ones provide diabatic heating or cooling. This set of simulations is designed to test the roles of individual processes in developing the circulations that occur in the stratiform region. In C4-C8, convective heating is neglected so that only specific microphysical processes within the stratiform region influence circulations. In C6',C7' and C9', convective heating is prescribed to add additional insight into the roles of certain processes under the most realistic physical conditions.

Simulation C4 investigates the role of melting-induced cooling within the stratiform region in the absence of convective line heating. All other diabatic heating terms are turned off. Because melting is restricted to such a small layer, it has far less impact on the circulations that develop than other microphysical processes. A strong downdraft does not form in this simulation (Fig. 5.26); therefore, rain evaporation is minimized. Weak descent occurs near the melting level but it only extends down to 3 km, and the peak values only intensify to 10-15 cm s^{-1} at 270 and 360 minutes (Figs. 5.26c, d). No organized ascent develops, although melting alone does induce a few cm s^{-1} of upward motion in the domain above the melting level.

134

Figure 5.26: As in Fig. 5.24 except for C4, the simulation with melting only influencing the circulations, and no convective heating.

With the lack of strong ascent in the anvil cloud, peak rain rates near the melting level are relatively light, around 3.5 mm h^{-1}. A sizeable area experiences surface rain, but the peak values are only around 1.5 mm h^{-1}. The total mass of rain reaching the surface in this simulation greatly exceeds that of the corresponding control, C2, and also exceeds that of the control run including heating, CTL (Table 5.4). The increased surface rainfall is due to the almost total lack of strong drying within a mesoscale downdraft. Melting causes a temperature drop of nearly 3 K at the melting level in the region of stratiform rain (figure not shown).

Table 5.4: Simplified integrated water budget of the CTL model simulation, and simulations investigating individual microphysical processes. Values are the same as in Table 5.3, with percentage change from appropriate control run, CTL for primed runs, C2 for others. The following runs do not allow convective heating: C4 = melting only, C5 = melting and evaporation, C6 = all but deposition and sublimation, C7 = all but condensation and cloud water evaporation, C8= sublimational cooling only. Convective heating included in C6′ which allows all processes except deposition, C7′ which allows all processes except condensation, and C9′ which allows all processes except evaporation.

Run	Advected mass	In Situ mass	Mass Sink	Rain sink
CTL	1692.06	1246.98	2285.17	511.98
C2	1475.27	455.19	1458.02	300.42
C4	1453.40 (-1%)	307.74 (-32%)	968.84 (-35%)	605.83 (+102%)
C5	1484.49 (+1%)	338.46 (-26%)	1401.81 (-4%)	290.32 (-3%)
C6	1518.57 (+3%)	390.72 (-14%)	1482.82 (+2%)	314.46 (+5%)
C7	1420.60 (-4%)	487.14 (+7%)	1499.08 (+3%)	302.80 (+1%)
C8	1462.94 (-1%)	291.62 (-36%)	900.90 (-36%)	559.23 (+86%)
C6′	1757.85 (+4%)	986.50 (-21%)	2155.13 (-6%)	400.06 (-22%)
C7′	1790.66 (+6%)	1038.19 (-17%)	2200.32 (-4%)	391.88 (-23%)
C9′	1637.30 (-3%)	1248.89 (+0%)	1908.71 (-17%)	738.91 (+44%)

Horizontal perturbation flows are very weak (Fig. 5.27). The initial cold pool at the lower right of the domain produces the most noticeable perturbations through 180 minutes (Figs. 5.27a, b), and even these are under 2.5 m s^{-1}. A weak circulation can be seen near the melting level at later times (Figs. 5.27c, d), but the magnitudes from the melting remain under 4 m s^{-1}, except for a small region just behind the convective line. This simulation indicates that although melting produces a rather sharp cool layer, the small depth of the cooling prevents it from inducing significant circulations over the stratiform

Figure 5.27: As in Fig. 5.15 except for C4, the simulation with melting only influencing the circulations and no convective heating.

region. Melting may be able to weakly enhance rear-inflow in regions where precipitation is heavy, but it is unlikely to cause a significant rear-inflow jet if evaporation is minimal.

Simulation C5 adds evaporative cooling to melting-induced cooling in the domain. Again no convective heating occurs in this simulation. The addition of evaporation greatly increases the strength and size of a mesoscale downdraft, reducing surface rainfall totals (Table 5.4). Rainfall quantities near the melting level in C5 are reasonably close to those in C4 (Fig. 5.28), but the amount that reaches the surface is decreased by 10% at 90 minutes (Fig. 5.28a) to around 50% at 180 and 270 minutes (Figs. 5.28b, c), and eventually by 75% (Fig. 5.28d). The total amount of rain reaching the surface over the simulation is less than half that of C4 (Table 5.4). Surface rainfall does not differ significantly from C2, which implies that the additional condensate added in the anvil cloud by condensation and deposition is countered by enhanced losses in simulations that include those processes.

The addition of evaporation increases the depth of the cooled layer during the simulation, but the stronger downdraft and adiabatic warming result in less of a peak temperature drop (figure not shown). The greatest temperature decreases occur near the melting level, but now they are only around 2 C. Warming of up to 2 C occurs in the lowest 1 km of the simulation due to the rather strong downward motion.

The moisture sink from evaporation and melting in C5 is comparable to that of C2 with all microphysical processes (Table 5.4). The downdraft in C5 is nearly the same size and magnitude (Fig. 5.29) as that in C2 (Fig. 5.21). Peak descent is generally within 10% of the control values. Somewhat more upward motion takes place in the anvil cloud than in C4. Even though no latent heat is released, evaporation encourages a circulation above the rain region where ascent reaches 12-14 cm s^{-1} after 180 minutes (Figs. 5.29b, c, d). In C2, with latent heating, the ascent was rarely much above 20 cm s^{-1} until after 270 minutes (Fig. 5.29c). In situ production of condensate is therefore only 26% less in C5 than in C2 (Table 5.4).

The horizontal perturbations that develop (Fig. 5.30) are also very similar to those of C2, the full microphysical run (Fig. 5.23). Evaporation is obviously the main process contributing to the development and maintenance of the rear-inflow jet in the simulations
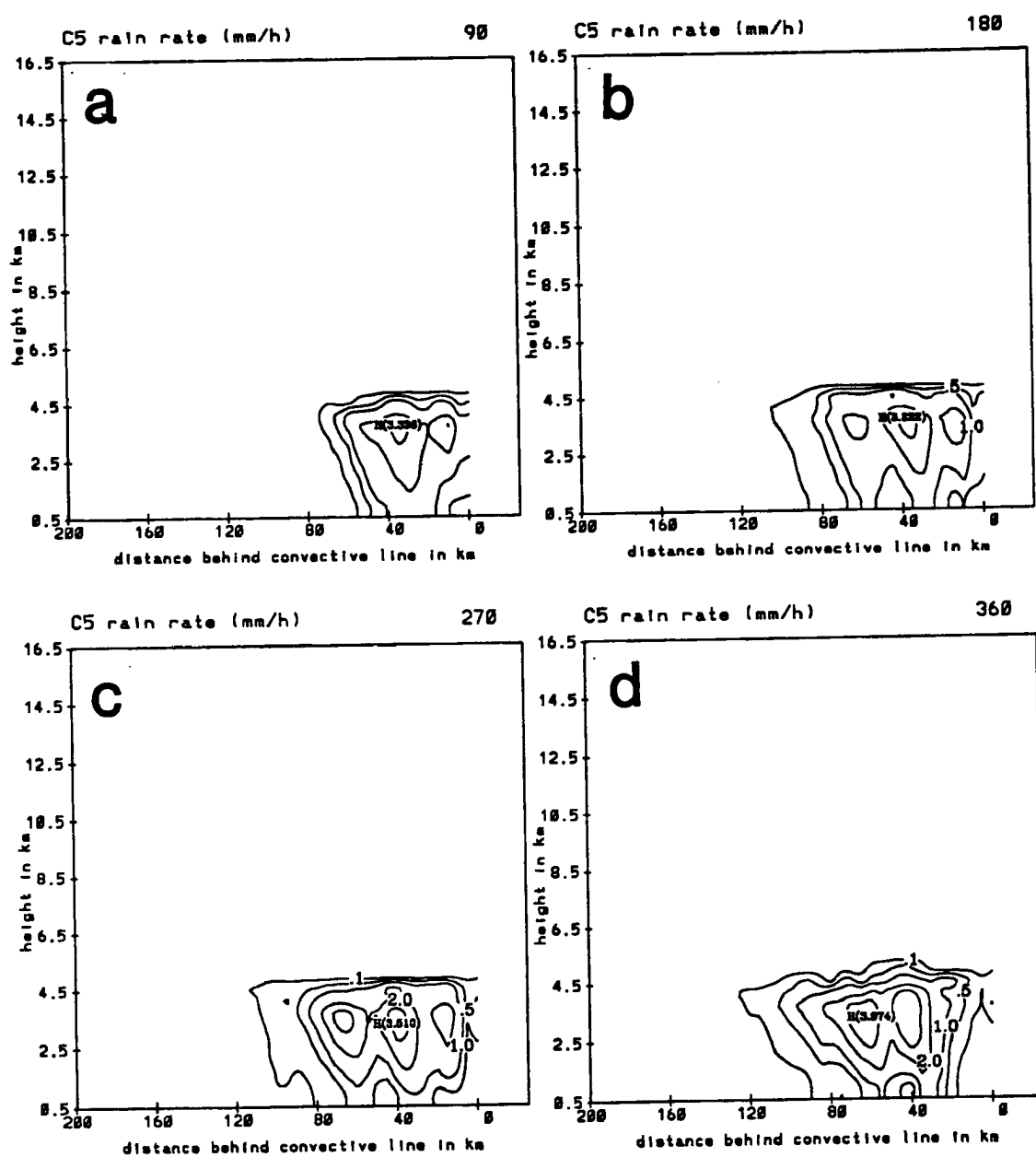
Figure 5.28: As in Fig. 5.19 except for C5, the simulation with melting and evaporation only influencing the circulations and no convective heating.
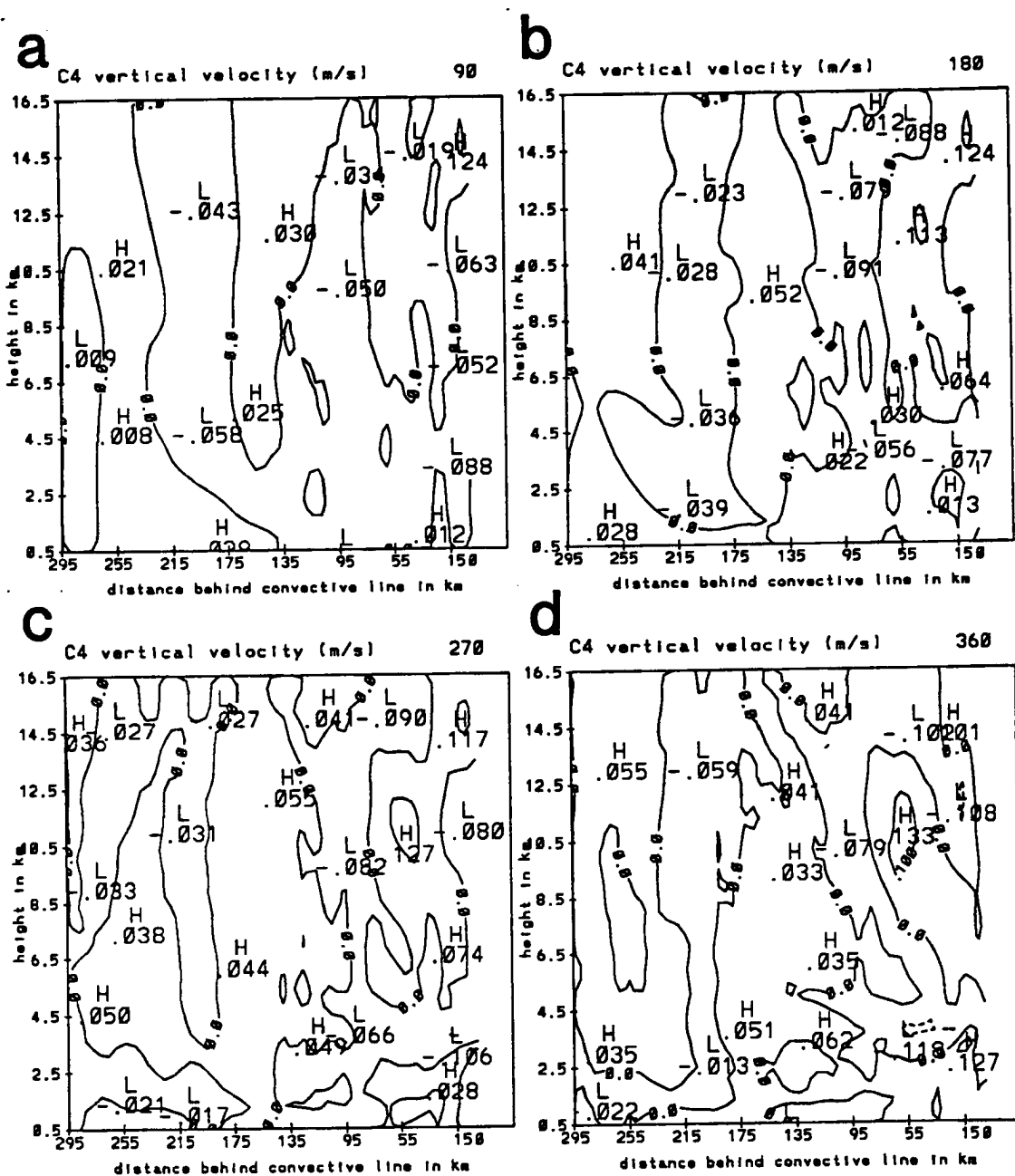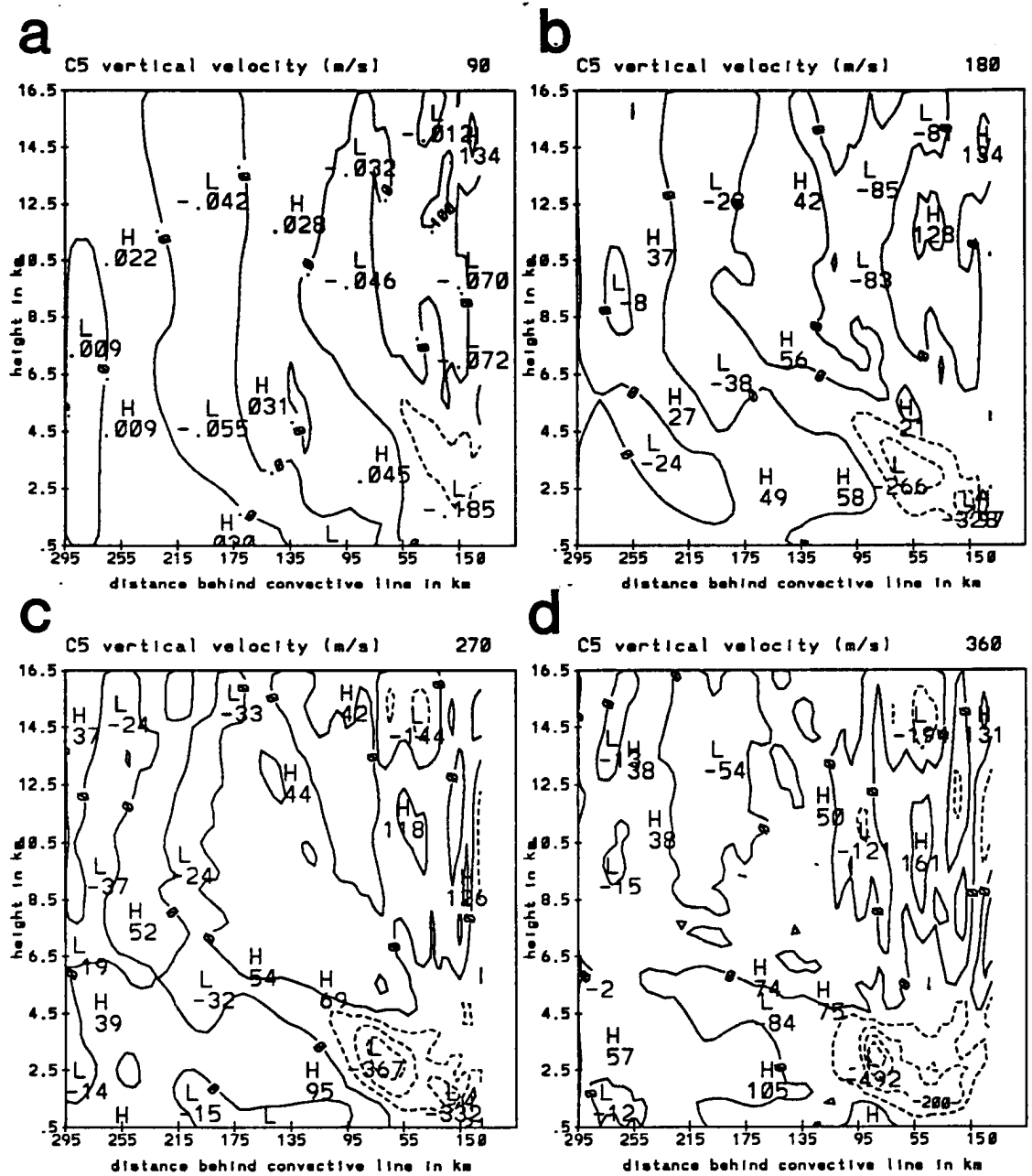
Figure 5.29: As in Fig. 5.24 except for C5, the simulation with melting and evaporation only influencing the circulations and no convective heating.
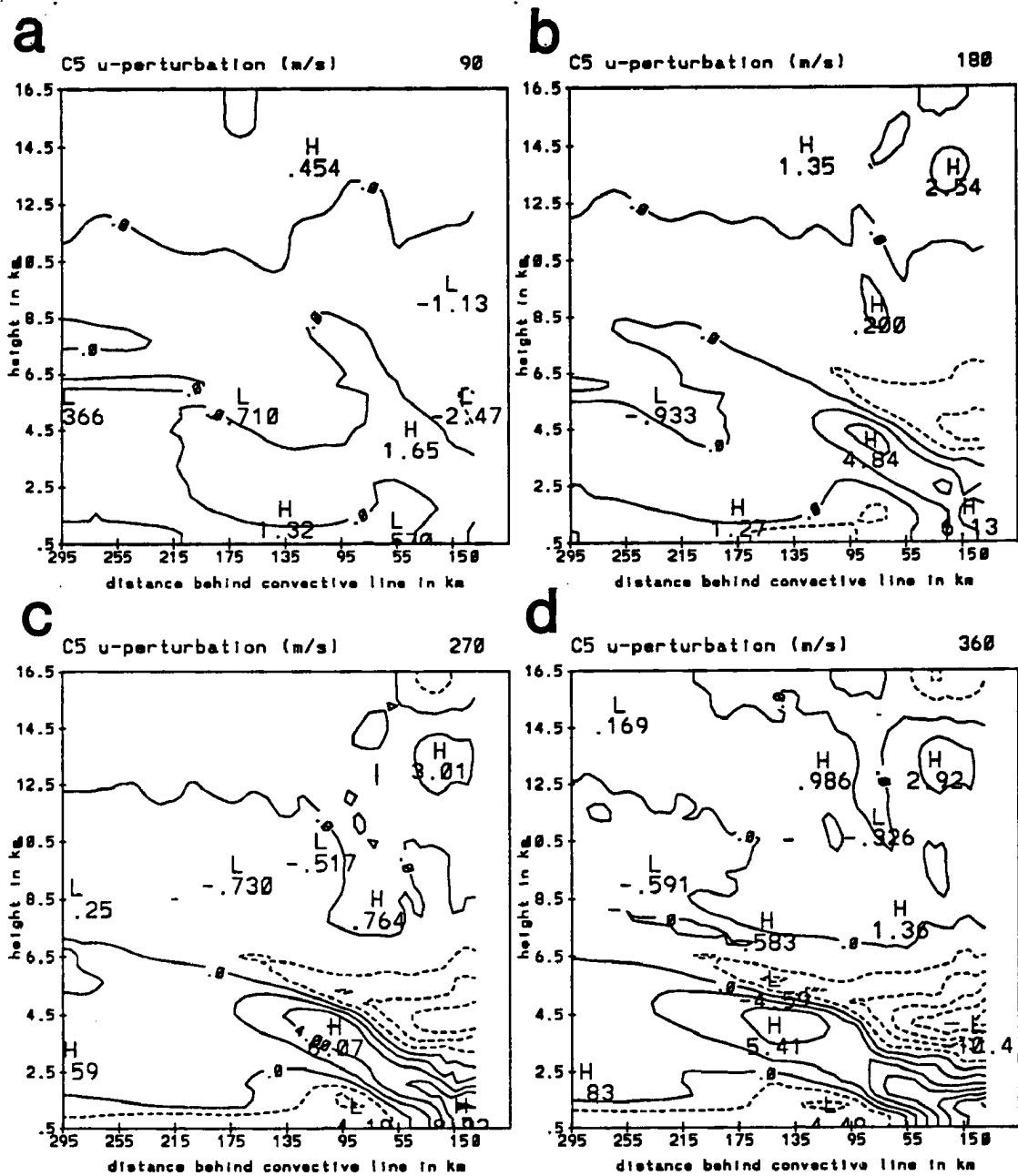
Figure 5.30: As in Fig. 5.15 except for C5, the simulation with melting and evaporation only influencing the circulations and no convective heating.

of the 11 June system. Peak RTF flow is generally only 15% less than in C2. Evaporation and the downdraft it drives also contribute to the enhancement of FTR flow at midlevels. This enhancement again is not significantly less than that in the run in which latent heat was occurring. Differences in the strength of FTR flow are within 30%.

This simulation shows that the primary contributor to the rear-inflow jet in the stratiform region is evaporative cooling. The midlevel mesolow that forms in C5 due to the low-level evaporative cooling is nearly as strong as the low that forms in the case with full microphysics (C2). In fact, evaporative cooling at low levels and the convergence that results in midlevels may also be a prominent process enhancing FTR acceleration at midlevels in the stratiform cloud.

In simulation C6, all processes contribute to the diabatic heating term except for deposition and sublimation. A comparison with C2 should single out the effects of these two processes within the stratiform region on the circulations. The effects of these two processes are relatively minor compared with those of evaporation in C5 (Table 5.4). The amount of condensate produced in situ does decrease by 14% with the exclusion of vapor deposition. However, surface rain rates increase slightly since the mesoscale downdraft is weakened by 5-10% and evaporation is not as strong. Only minor changes occur in the horizontal velocity perturbation field, with fluctuations in the peak magnitudes of the FTR and RTF flow generally under 20%. The exclusion of deposition and sublimation allows negative velocity perturbations to extend 1-2 km higher at upper levels in the stratiform domain (figure not shown).

All processes except condensation and its inverse, the evaporation of cloud water, contribute to diabatic heating in simulation C7. Interestingly, without condensation, the in situ production of condensate increases slightly over C2 (Table 5.4). This is probably because the evaporation of cloud water is also neglected in C7, and this evaporation normally decreases buoyancy in the cloud and weakens upward motion. In general, at most times C7 changes little from C2 since condensation plays a small role in the simulation that neglects convective heating. The only noticeable change in vertical motion occurs within the mesoscale downdraft where peak descent increases approximately 10% because of the

increased amount of hydrometeors present due to the increased in situ production term. FTR flow is increased by nearly 30% at midlevels just behind the convective line in C7. Elsewhere in the domain changes are small. FTR perturbations are confined primarily below 8 km in C7. The results in C6 and C7 seem to imply that condensation is the process that results in FTR flow, however weak, at very high levels in the anvil cloud, whereas deposition and sublimation induce RTF flow at these high levels.

In simulation C8, only sublimational cooling influences the circulations, and changes from C2 are insignificant. Air descends in only a 1-2 km deep layer roughly 100 km rearward of the convective line at less than 10 cm s^{-1} (figure not shown). Other motions induced by the cooling are weak and restricted to small areas. Some weak ascent occurs at high levels over the region of surface rainfall, which is increased over C2 because of the lack of a strong mesoscale downdraft. Surface rainfall increases by over 80%, as a result of a substantial decrease in the amount of water lost to evaporation and sublimation (Table 5.4). In situ production of condensate is much weaker in this run. The sublimational cooling has almost no effect on the horizontal winds, producing less than a 1 m s^{-1} RTF perturbation at midlevels rearward of the maximum downward motion. This result differs somewhat from that of Stensrud et al. (1991) who found that sublimation could produce rather strong circulations. In that 1-D model study, however, sublimation initiated a strong downdraft (as large as 4 m s^{-1}) and horizontal circulations that were also enhanced by the effects of melting and evaporation. In addition, the model was initialized with much drier conditions in the presence of snow in the anvil cloud. In all of the 11 June simulations in this study, strong FTR flow advects vapor sufficiently far rearward so that sublimation rates are rather small. This sensitivity test, C8, also restricts diabatic heating to sublimation only, and therefore differs from the procedure of Stensrud et al. (1991). In the specialized simulations to be discussed in Chapter 8, it will be shown that sublimation can play a much more important role in cases where water vapor is "blocked" from advecting rearward and hydrometeors are able to pass through regions of relative humidity less than 30 or 40%.

Simulations C6 and C7 were both re-run allowing convective heating to take place in the buffer as in CTL. In C6', changes were made so that only vapor deposition was

excluded. Total in situ production of condensate decreases by 21% as less heating aloft reduces the strength of the mesoscale updraft (Table 5.4). Surface rainfall decreases by 22%. In C7', only condensational heating was excluded, and similar reductions occur in the in situ production and surface rainfall. As in C6 and C7, the changes in circulations produced by the exclusion of these processes were relatively small compared to those that occurred in C5, implying that evaporation plays a larger role in driving the jets and vertical motion than any other microphysical process in the stratiform region. (A different simulation in which condensational and depositional heating combined were the only processes influencing circulations supported this result. Even with both processes contributing to heating, horizontal perturbations were typically less than half of those in C5, the simulation with evaporative and melting-induced cooling only. Ascent was just slightly increased from C5 aloft, and no descent occurred at all beneath the anvil cloud.) Simulations C6' and C7' also imply that both condensation and deposition contribute fairly equally to the amount of latent heating, upward motion, and in situ condensate production in the anvil cloud.

Simulation C9' was run to test the effect of evaporation when convective heating occurs. In this simulation, the reverse was done from C5, so that all processes contributed to diabatic heating except for evaporation. The in situ production term changes little (Table 5.4), indicating that evaporation has only a minor impact on the amount of upward motion occurring at middle and high levels. Surface rainfall increases greatly because of the lack of low-level cooling and the failure of strong descent to develop (Fig. 5.31). Mesoscale ascent is comparable to that in CTL, although it does not affect as large an area at later times. Melting and sublimation induce some downward motion, but it is restricted to near the melting level through much of the simulation. Peak descent only reaches 30 cm s^{-1} or so.

Without evaporative cooling, the perturbation horizontal flow looks similar to that in C3, the simulation with heating only and no hydrometeor input (figure not shown). RTF flow develops at low levels, but it is reduced by nearly half in magnitude, and does not occur within a sloping band as in CTL, but instead is strongest in a relatively horizontal
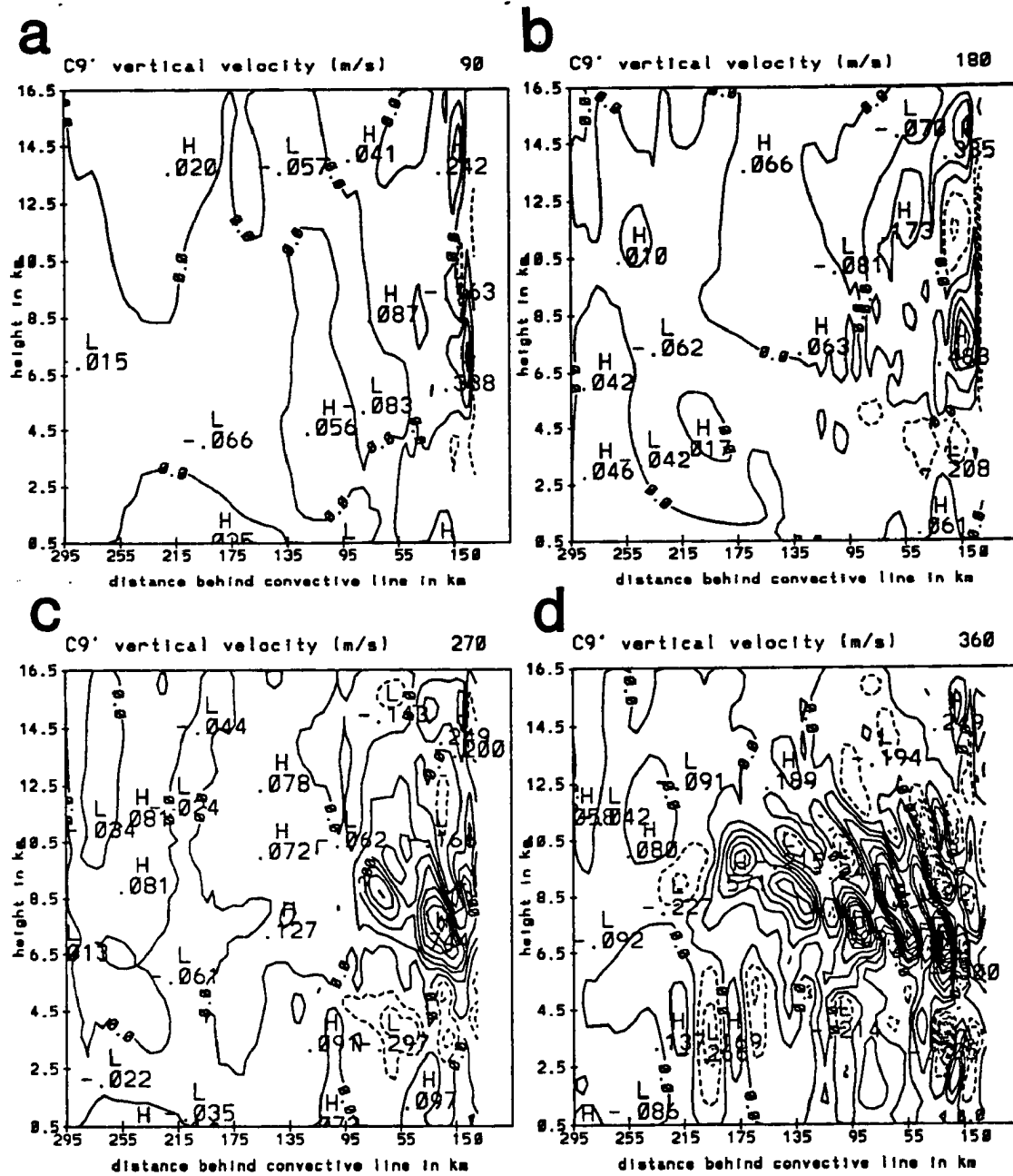
Figure 5.31: As in Fig. 5.24 except for C9', the simulation with all processes except evaporation influencing the circulations.

layer below 3 km. FTR flow is enhanced in midlevels by the convective heating and latent heating in the anvil cloud, but the flow is generally 20-40% weaker than in CTL, showing the importance of evaporative cooling in driving all circulations, not only the rear-inflow jet.

In summary, this series of simulations found that evaporation of falling rain has the largest effect of any specific microphysical process on the development of circulations in the stratiform region. Its effects even exceed those of deposition and condensation combined. Evaporative cooling of at least 1 °C h^{-1} occurs over an area that can exceed 100 km, and over a depth of 4 km. No other process heats or cools the atmosphere in the stratiform region over such a broad area through a substantial time interval. The effects of evaporation extend beyond the obvious driving of a descending rear-inflow jet. Convergence is induced at the top of the mesoscale downdraft, and this contributes strongly to an increase in front-to-rear flow at midlevels. The convergence also contributes to some upward motion, induced entirely by evaporative cooling, but the ascent in the anvil cloud is more strongly tied to the processes of vapor deposition and condensation. These heating processes increase ascent in the anvil cloud, and increase the intensity of the front-to-rear perturbation flow over that induced by evaporation alone. Deposition and condensation indirectly intensify the mesoscale downdraft and rear-inflow jet by increasing the amount of hydrometeors present in the cloud, which later results in an increased amount of evaporative cooling.

The simulations described above also show that heating in the convective line plays the most significant role in creating mesoscale ascent in the trailing anvil. Convective heating also plays a significant direct role in producing strong rear-inflow at the front of the stratiform region. The convective heating plays a less prominent indirect role in the evolution of the rear-inflow jet farther to the rear in the stratiform region by increasing upward motion and in situ condensate production in the anvil cloud. These in turn increase the amount of microphysical cooling and extend the area influenced by the cooling so that the rear-inflow jet is strengthened farther rearward from the convective line. Even though the convective heating alone is sufficient to generate significant mesoscale ascent in the

stratiform region, rearward advection of hydrometeors is necessary to generate significant rainfall over large regions.

Chapter 6

SENSITIVITY TO INITIAL ENVIRONMENTAL CONDITIONS

Although a significant amount of data is available for the 11 June case, initialization of this model required information from a rather small region at a particular time. Approximations and some interpolation were necessary to derive reasonable conditions for an area that experiences the initial growth of the stratiform anvil cloud. Because some subjectivity enters the determination of initial conditions, it is important to test the sensitivity of the model to these conditions. These simulations can also help explain reasons for differing behaviors of stratiform regions under different environmental conditions. Variables that may be particularly important include humidity, stability, ambient winds, hydrometeor content of the convective cells, and the amount and vertical distribution of convective heating. The pulsing of heating and hydrometeor advection could also be important. Simulations were performed with adjustments made to all of the above parameters. Important integrated water budget terms for each of the eleven simulations discussed below are shown in Table 6.1.

6.1 Humidity

The first of the sensitivity tests to be discussed investigates the changes that occur when a dry, horizontally homogeneous domain is used for initialization of the model, instead of a domain where a vapor gradient exists. In this simulation (S1), the initial humidity at all points except the right boundary is the same as the rather dry conditions present at the left of the CTL domain. As might be expected in this case with hydrometeors immediately advecting into a dry environment, sublimational cooling and descent are enhanced initially. Because of the enhanced sublimation, rain rates at 90 minutes are less than those in CTL (Fig. 6.1a). Through the first two thirds of the simulation
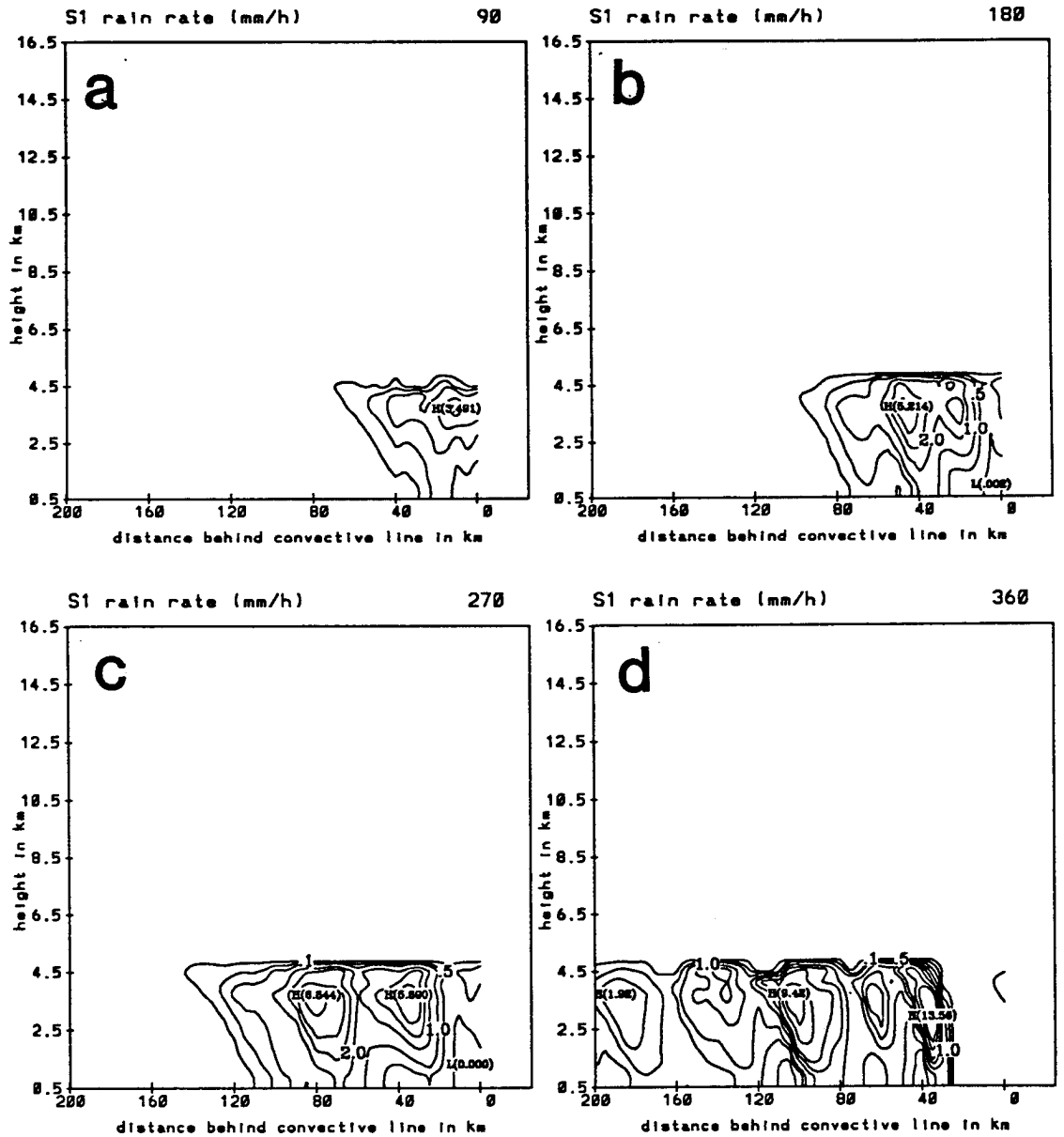
Figure 6.1: As in Fig. 5.19 except for S1, the simulation with initially dry horizontally homogeneous domain.

Table 6.1: Simplified integrated water budget of the CTL model simulation, and sensitivity tests. Values are in tons of water over 405 minute period with percentage change from control also shown. Humidity is varied in S1 (horizontally homogeneous dry domain) and S2 (more moist). Stability varies in S3 (more unstable) and S4 (more stable). Winds vary in S5 (weaker winds) and S6 (wind profile changed). Hydrometeor contents vary in S7 (50% less) and S8 (50% more). Convective heating is changed in S9 (more heating) and S10 (profile changes shape). Pulsing is neglected in S11.

Run	Advected mass	In Situ mass	Mass Sink	Rain sink
CTL	1692.06	1246.98	2285.17	511.98
S1	1816.64 (+7%)	2365.50 (+90%)	3166.19 (+39%)	495.45 (-3%)
S2	1632.16 (-4%)	1060.51 (-15%)	1978.17 (-13%)	593.77 (+16%)
S3	1750.45 (+3%)	2256.36 (+81%)	3039.52 (+33%)	815.69 (+59%)
S4	1686.28 (-0%)	936.30 (-33%)	1839.25 (-19%)	595.18 (+16%)
S5	1225.24 (-28%)	1200.94 (-4%)	1724.64 (-24%)	452.44 (-12%)
S6	1514.70 (-10%)	1114.94 (-11%)	1904.68 (-17%)	493.47 (-4%)
S7	982.30 (-42%)	1027.11 (-18%)	1729.68 (-24%)	258.03 (-50%)
S8	2468.77 (+46%)	1491.48 (+20%)	2798.00 (+22%)	865.37 (+69%)
S9	1756.75 (+4%)	1503.87 (+21%)	2570.05 (+12%)	525.70 (+3%)
S10	1652.09 (-2%)	647.01 (-48%)	1707.03 (-25%)	360.31 (-30%)
S11	1365.99 (-19%)	848.42 (-32%)	1995.12 (-13%)	277.17 (-46%)

(Figs. 6.1a, b, c), rainfall continues to be less than that in CTL. However, the presence of so much dry air near the convective line and the enhanced sublimation and evaporation eventually leads to stronger circulations than were present in CTL, so that rainfall rates become comparable to CTL at the surface by 270 minutes (Fig. 6.1c). At later times (Fig. 6.1d), convective-like elements within the anvil cloud are more vigorous, so that peak rain contents aloft are greater than those in CTL.

Vertical motions in S1 are enhanced, and this is particularly evident at 90 minutes (Fig. 6.2a). Instead of a 27 cm s^{-1} downdraft at this time (Fig. 5.11a), a 70 cm s^{-1} downdraft occurs. Upward motion is weaker due to the initially drier conditions and less heating from vapor deposition and condensation. By 180 minutes (Fig. 6.2b), and through the rest of the simulation (Figs. 6.2c,d), the mesoscale descent is approximately 25% larger than in CTL, with some enhancement to the ascent in the anvil cloud. Most of the features agree qualitatively with CTL with the peak motions in roughly the same locations. The vertical motion averaged over the stratiform region and an EVAD-scale region during the 270-360 minute time period in S1 are similar to CTL (Fig. 6.3). The
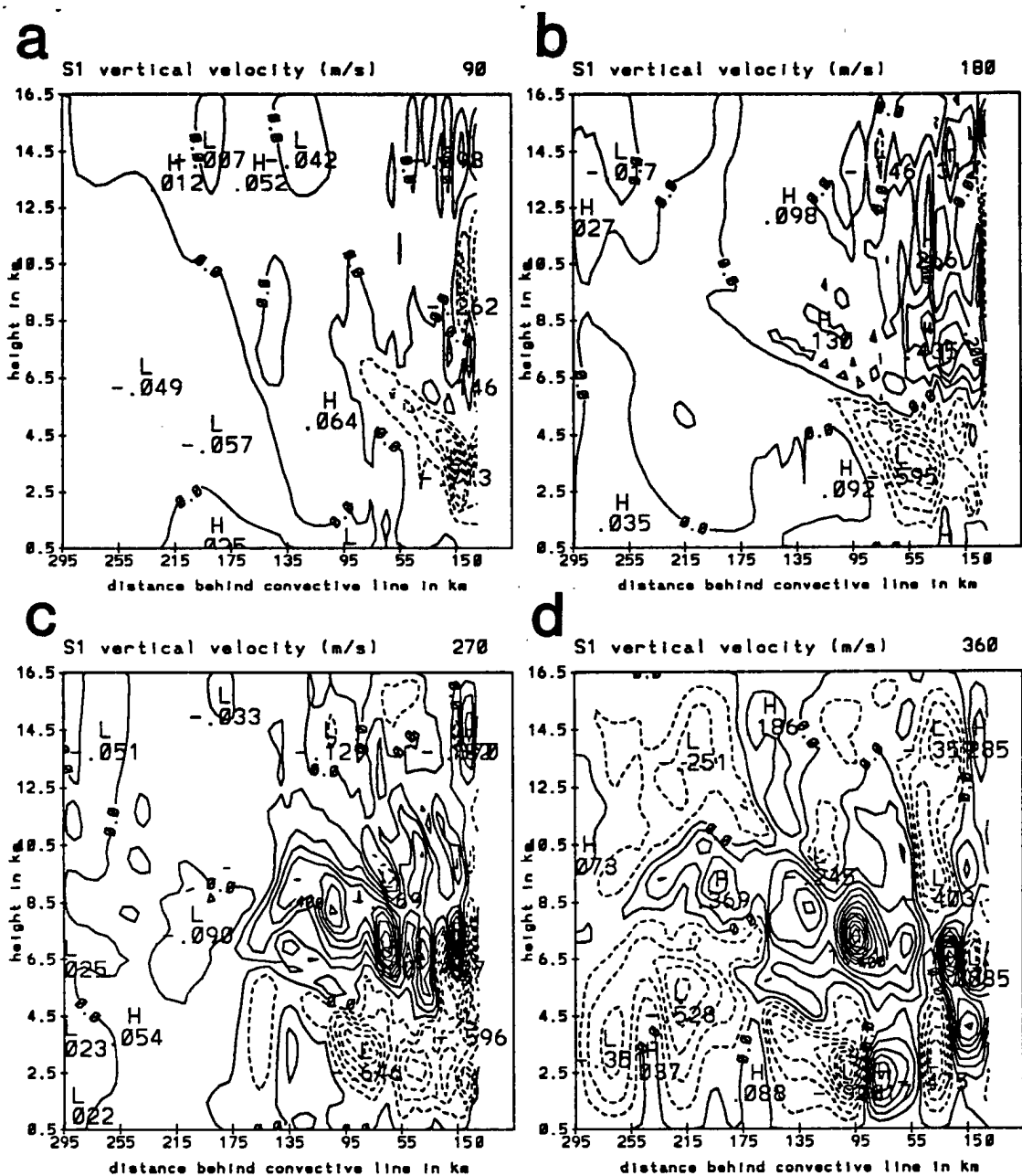
Figure 6.2: As in Fig. 5.24 except for S1, the simulation with initially dry horizontally homogeneous domain.

Vertical Motion
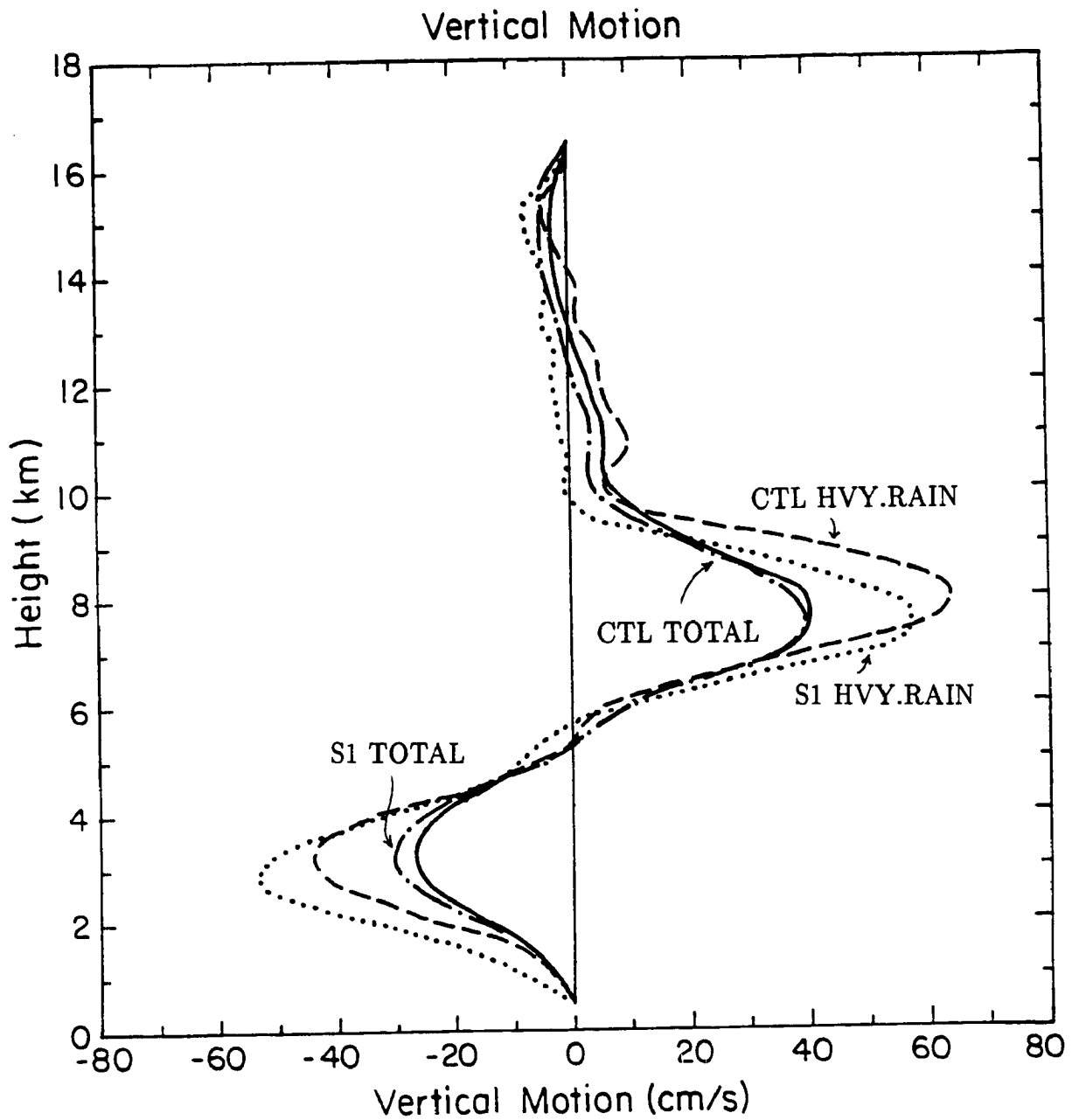
Figure 6.3: As in Fig. 5.22 except for comparison between S1, the simulation with initially dry horizontally homogeneous domain, and CTL.

total stratiform rain region curves are almost exactly the same, but the peak intensities of the downdraft and updraft are slightly more intense on the EVAD-scale in S1.

Perturbation u-velocities are also increased in S1 an average of 10-20% (Fig. 6.4), but the locations of the features agree well with those in CTL. The increased strength of horizontal circulations accounts for the slight increase in hydrometeors advected into the domain in S1 (Table 6.1). In general, for much of the simulation, differences from CTL are not especially significant, with the horizontally homogeneous dry domain simply resulting in the more rapid formation of strong descent, and a delay in the formation of mesoscale ascent in the anvil cloud. The presence of dry air does enhance some of the circulations, but does not result in better agreement with observations in the two areas of biggest discrepancy in the control case, upward motion at high levels, and surface rainfall rates. Table 6.1 details the total water mass advected into the domain, created within the domain, lost within the domain, and reaching the surface as rain during the full 405 minutes of simulation for the CTL case and eleven sensitivity runs. The model is somewhat sensitive to the rather significant change in initial humidity between CTL and S1. In situ production of condensate increases more than in any other sensitivity test (Table 6.1). Likewise, the amount of water mass lost to evaporation and sublimation is greater than in any other run. The increases in these terms cancel out, resulting in a slight drop in total surface precipitation. Realistically, in the 11 June system, some vapor would advect to the rear of the convective line prior to the advection of hydrometeors, since vapor would move rearward faster than hydrometeors. The initial vapor field in CTL would therefore better represent the squall line environment than the field in S1. This simulation may imply, however, that in other situations where drier conditions may exist in close proximity to a developing squall line, stronger circulations will develop, at least initially, than in the 11 June case. A possible example of this is the 23-24 June PRE-STORM case (Johnson and Bartels, 1992).

Another simulation was done to test model sensitivity to humidity (S2) by using initial humidities roughly 5% higher than those in CTL below the melting level and up to 10% higher at the rear of the domain. The increased humidity reduces the evaporative cooling
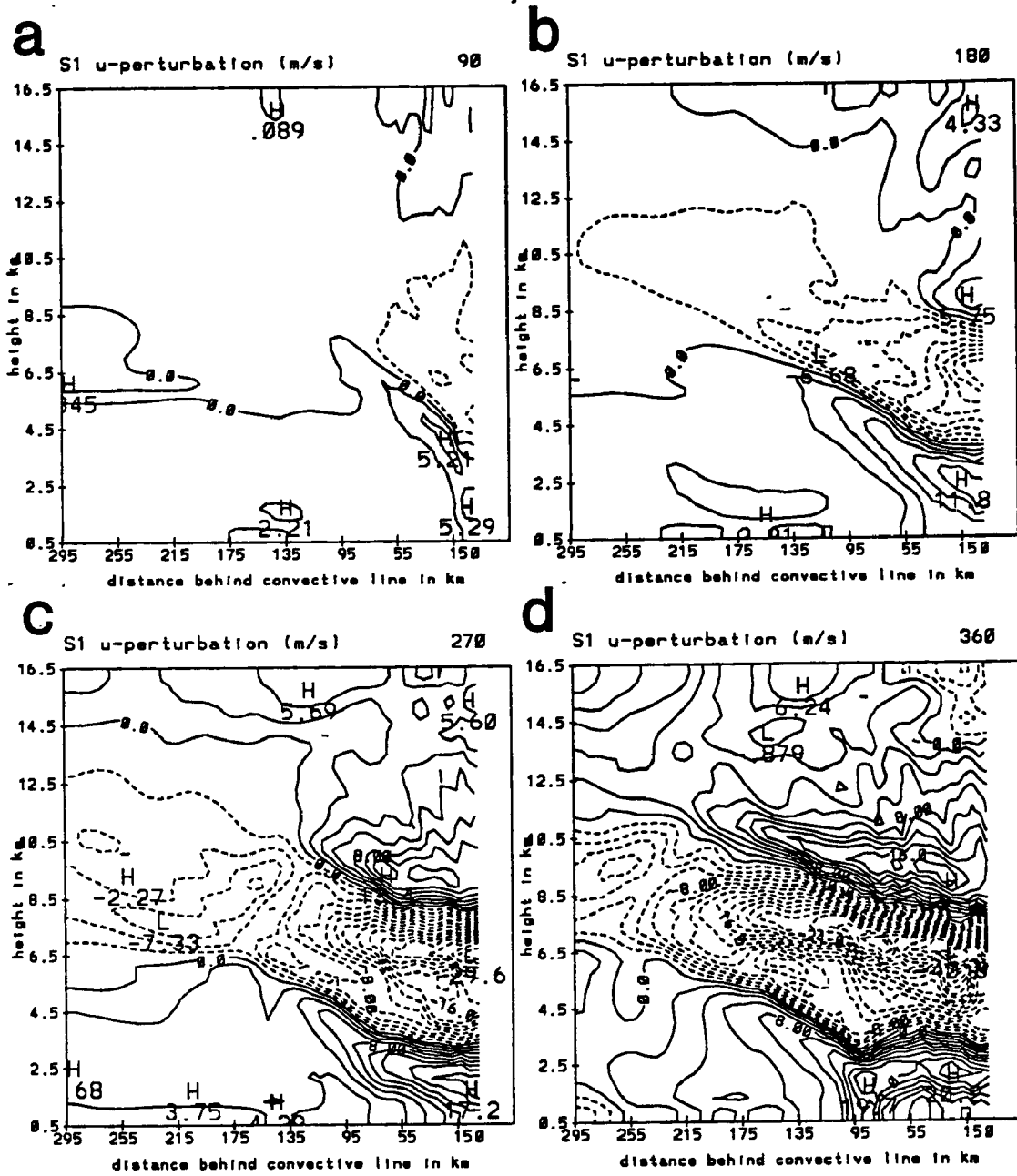
Figure 6.4: As in Fig. 5.15 except for S1, the simulation with initially dry horizontally homogeneous domain.

at most grid points by 20-30%, reducing the loss in rain content between the melting level and the surface. This can be seen in the water sink term for S2 (Table 6.1). Prior to 225 minutes, the reduced evaporation results in an increase in surface rainfall rates of up to 0.5 mm h^{-1} (figure not shown). Sublimative cooling is also reduced to a lesser degree. The reduced diabatic cooling decreases the strength of the mesoscale downdraft, as much as 25% at certain times, which in turn decreases the amount of midlevel convergence and weakens the horizontal velocity perturbations. RTF flow decreases by 10-20% in the simulation, and a similar reduction occurs in the FTR flow. The diminished circulations reduce the ascent in the anvil cloud, decreasing the in situ production of condensate so that rain rates at the surface after 225 minutes are not larger than in CTL, and in some cases are in fact diminished. The cumulative effect is a reduction in the in situ production of condensate and the water sink by similar percentages (Table 6.1).

Although initial relative humidities are increased, a descending dry current with humidities occasionally below 60% forms at later times in the simulation, much as it does in CTL (figure not shown). This particular sensitivity test shows that an increase in low-level moisture does not necessarily increase surface precipitation significantly. A negative feedback of sorts leads to surface rain rates not dramatically different from CTL. Although some changes in updraft and downdraft strength and circulation intensity do occur at certain points with this variation in initial humidity, the model does not appear to be overly sensitive to reasonable uncertainties in the initial vapor field. Averaged values of quantities undergo only minor changes, and qualitatively features within the domain are unchanged.

6.2 Stability

The model was run using many different vertical profiles of temperature that were supported by soundings taken in the 11 June system at different times. Of all the initial conditions, stability variations resulted in the greatest sensitivity in the model. Variations in stability in these sensitivity tests were restricted to a narrow range at middle and high levels since temperature profiles applicable to the stratiform region were in rather

close agreement at these levels. Low level stability varied more in the soundings used for initialization. Two simulations were run to test model response to lapse rates. In the first, S3, the entire troposphere is assumed to be more unstable, and the lapse rate is increased by 0.6 K km^{-1} at all levels. In the second, S4, the troposphere is made more stable by decreasing the lapse rate by 0.5 K km^{-1}. Both the temperature profile in S3 and in S4 are in less agreement overall with observations than that used in CTL; however, soundings could be found at certain times within or near the 11 June system that had lapse rates over deep layers more similar to those of S3 and S4 than CTL. In S3 and S4, the temperature at 500 mb is held at its CTL value.

The more unstable environment in S3 produces markedly stronger vertical motions in the domain. Increased upward motion in the anvil cloud increases snow contents 20-40%. Rain contents increase similarly below the melting level, although a stronger mesoscale downdraft lessens the increase in surface rain rates somewhat (Fig. 6.5). Peak rain rates at the surface are about 1 mm h^{-1} greater than those of CTL at early times, reaching 3.2 mm h^{-1} by 180 minutes (Fig. 6.5b). By 270 minutes (Fig. 6.5c) rather intense convective cells form in the anvil cloud, greatly enhancing the surface rainfall in small regions. Peak surface values are 6.5 mm h^{-1} at 315 minutes (Fig. 6.5d), over 10 mm h^{-1} at 360 minutes (Fig. 6.5e), and still around 5 mm h^{-1} at 405 minutes (Fig. 6.5f). These peak values are often more than double those of CTL, not only reaching those observed, but actually exceeding them at 315 minutes. The average surface rain rates in the stratiform region in S3 are generally between 1.5 and 2.0 mm h^{-1}. This is an increase of just under 1 mm h^{-1} from the rates in CTL, and the total rainfall at the surface over the simulation is nearly 60% greater than in CTL (Table 6.1). These rates, however, are still about 1 mm h^{-1} below those observed. Even though isolated areas receive heavier rain, rain is still underestimated over much of the stratiform region.

Vertical motions in the domain are stronger throughout the simulation (Fig. 6.6). Through 180 minutes (Figs. 6.6a, b), the peak ascent is nearly doubled in magnitude from CTL. Updrafts exceeding 1 m s^{-1} develop shortly after 180 minutes. The area of strongest ascent continually moves rearward and is generally toward the back of the surface
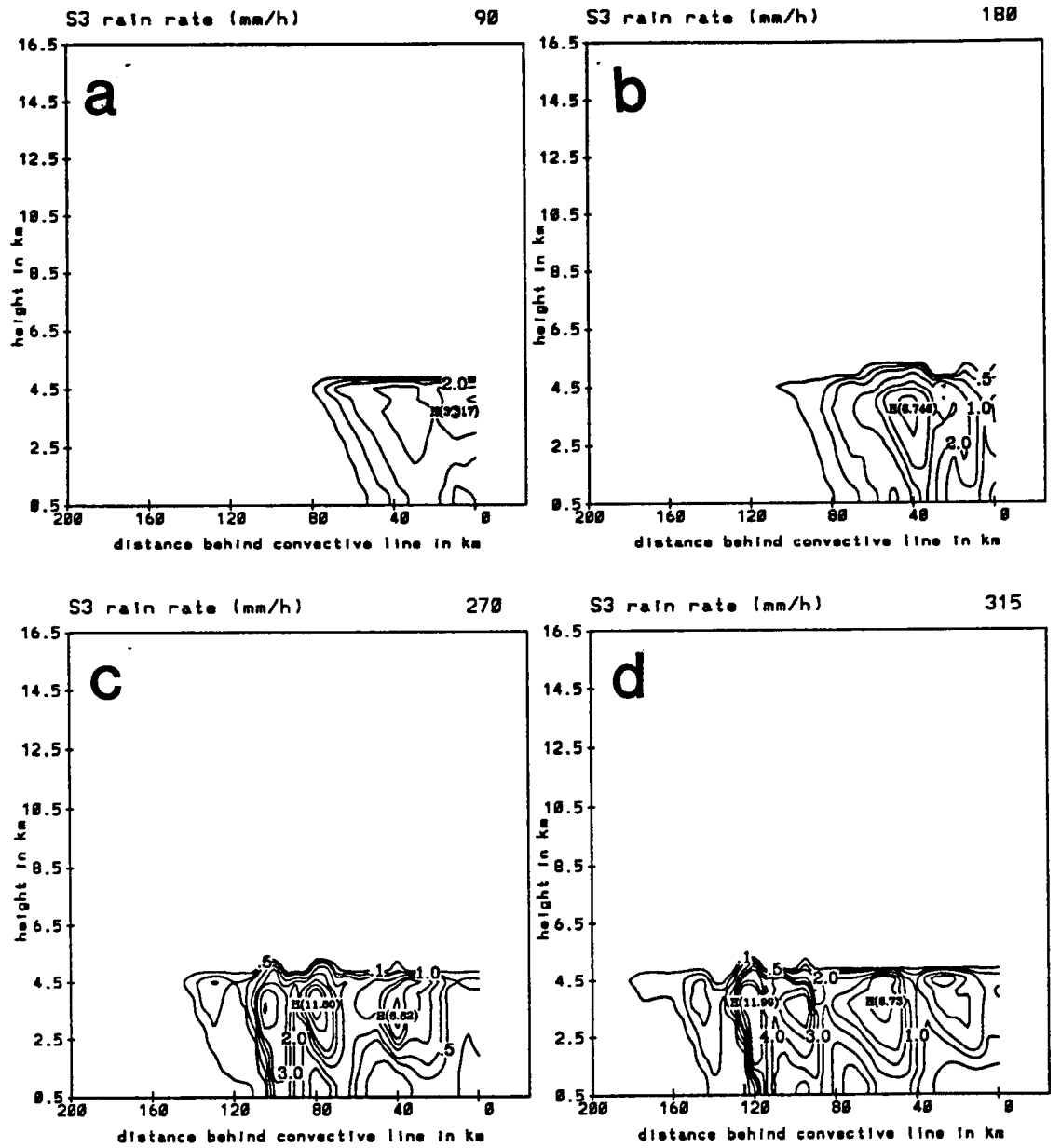
Figure 6.5: As in Fig. 5.3 except for S3, the simulation with increased instability.
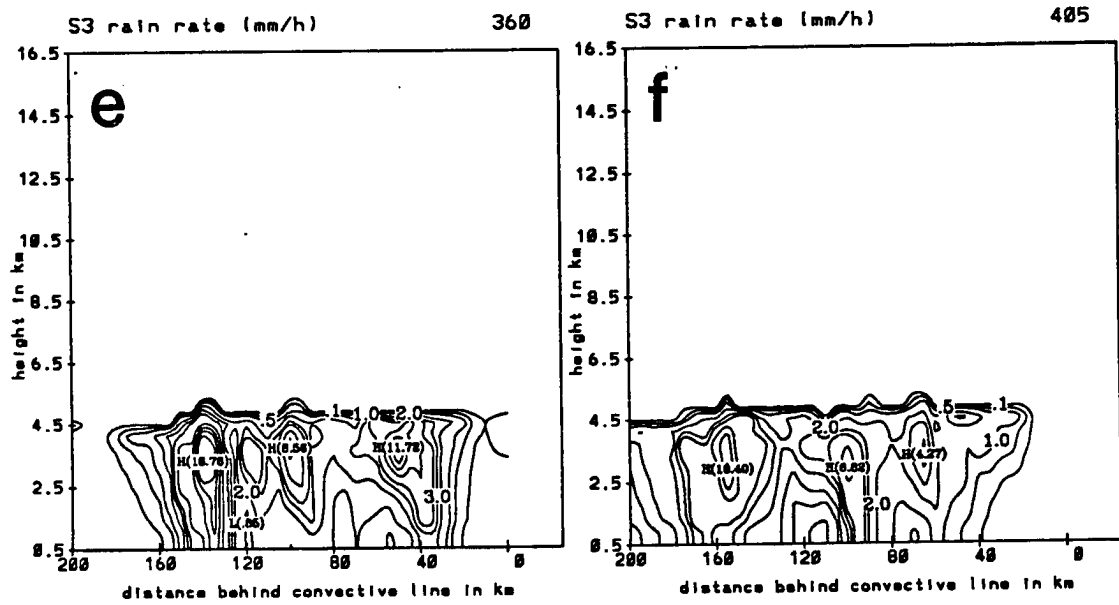
Figure 6.5: continued
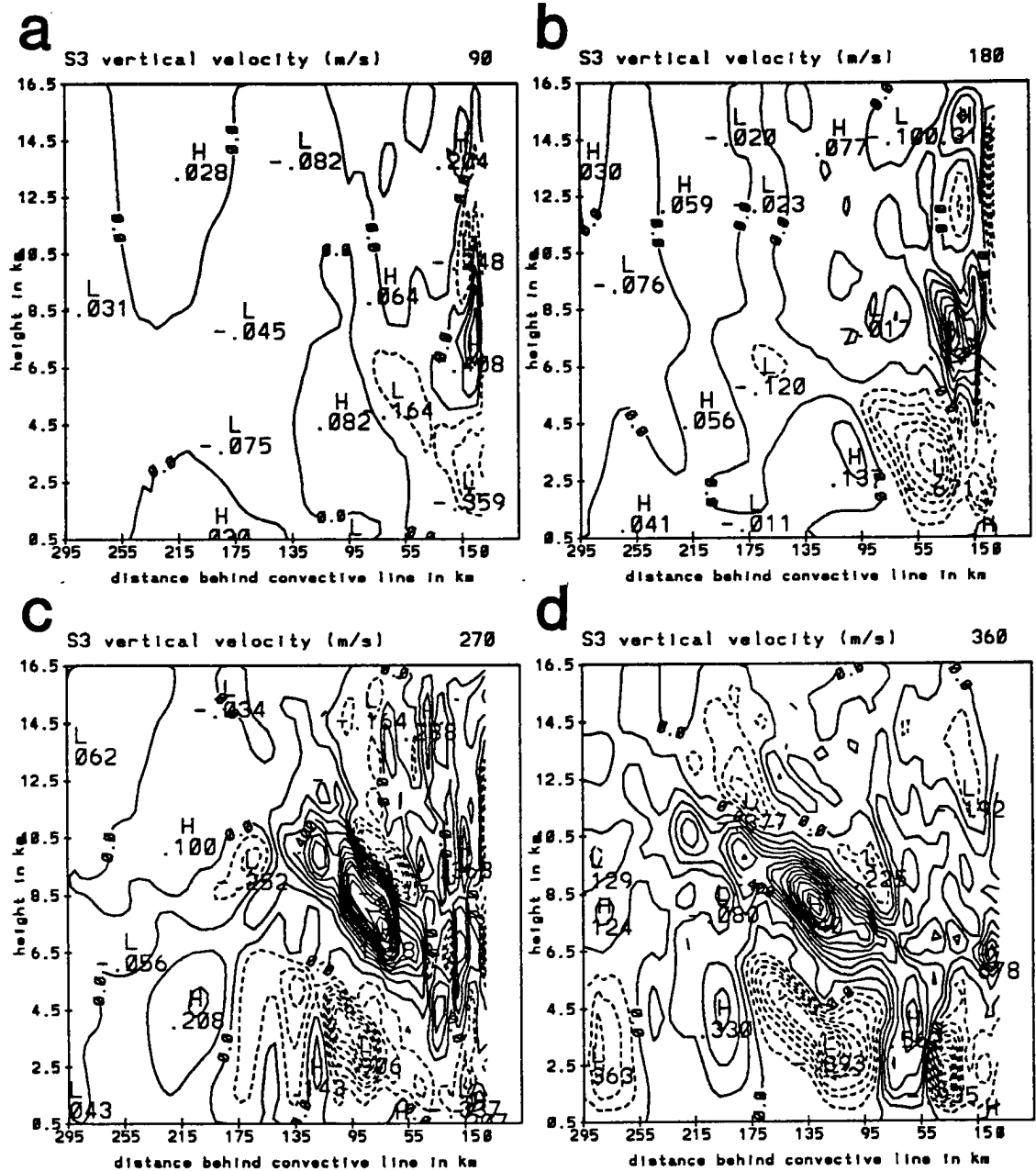
Figure 6.6: As in Fig. 5.24 except for S3, the simulation with increased instability.

rainfall region. Peak ascent approaches 2 m s^{-1} at 315 minutes (not shown). Mesoscale descent is also stronger than in CTL, varying from only slightly larger at some times to over 50% larger at others. The in situ production of condensate increases by over 80%, while the water sink increases 33% (Table 6.1).

Averaged vertical motion over the stratiform rain region and the smaller EVAD-scale region during the 270-360 minute time period is stronger in S3 than CTL, especially over the 40 km EVAD-scale region (Fig. 6.7). Ascent is particularly enhanced around the 8 km level where the peak value on the EVAD curve is over 1 m s^{-1}. The upward motion, however, is still restricted to a relatively small layer. Downward motion increases much less. The averaged values for the entire rain region are only slightly larger than CTL, and the locations of peak ascent and descent are similar. The peak values from the smaller scale area in S3 are somewhat larger than those implied by the rawinsonde study of Gallus and Johnson (1991) and the Doppler study of Rutledge et al. (1988). It therefore appears that although the increased surface rain rates are in better agreement with observations, the cause of the increased rainfall, significantly stronger upward motion in the 7-9 km layer, may not be reasonable.

Horizontal velocity perturbations increase in S3 by 20-30% (Fig. 6.8). Peak RTF exceeds 13 m s^{-1} at 180 minutes (Fig. 6.8b), instead of 10 m s^{-1} (Fig. 5.15b). FTR flow now reaches its peak intensity at 360 minutes, and not at 405 minutes. The most significant difference between S3 and CTL is in the behavior of these jets. The RTF jet is much more strongly sloped, with the axis of the jet at 270 minutes (Fig. 6.8c) descending 2.5 km over 45 km at the back of the stratiform rain region, as opposed to the more gradual 2.0 km descent over 60 km in CTL. A rather sudden and strong descent of the rear-inflow jet continues at 360 minutes (Fig. 6.8d) at the back of the rain region. RTF flow approaching 10 m s^{-1} can be found 250 km behind the convective line by the end of the simulation, at an elevation of 6.5 km (figure not shown). This is over 100 km rearward of where the same intensities could be found in CTL, and much higher in elevation. Strong FTR flow exists at this location around the 10.5 km level. This again is much further rearward and elevated from positions in CTL. Some of the features depicted in S3 resemble those in MCS cases
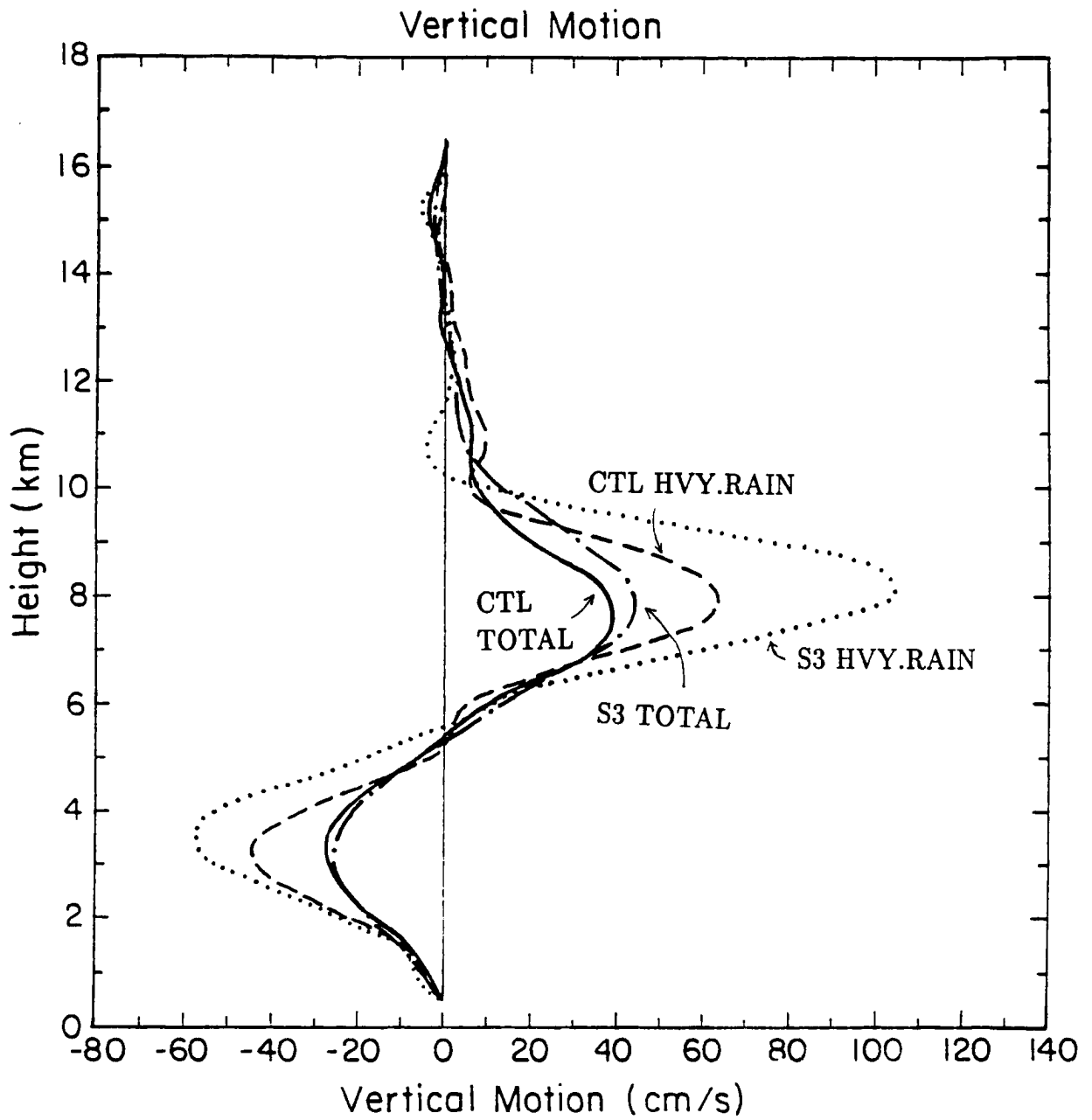
Figure 6.7: As in Fig. 5.22 except for comparison between S3, the simulation with increased instability, and CTL.
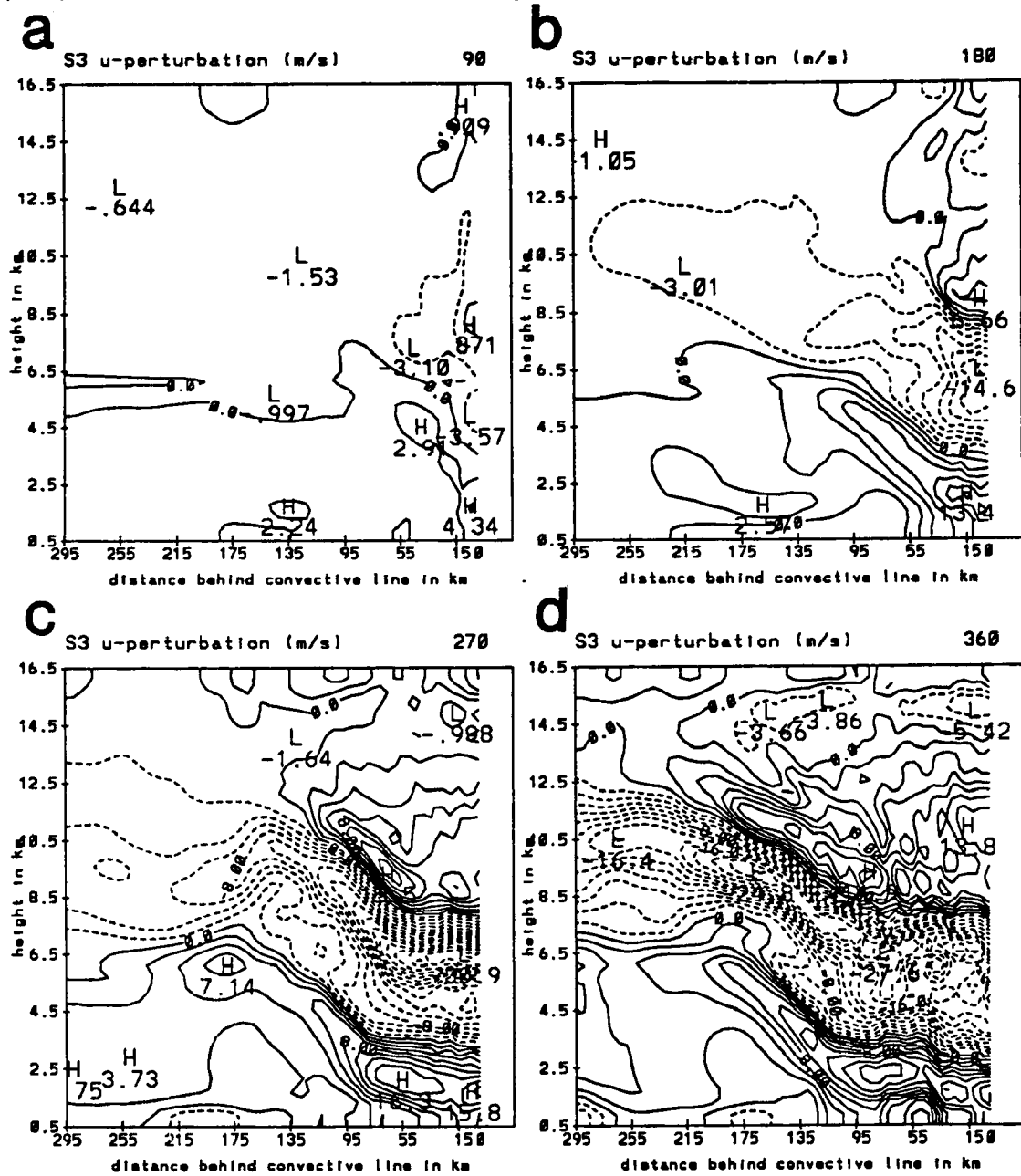
Figure 6.8: As in Fig. 5.15 except for S3, the simulation with increased instability.

where the rear-inflow appears to be blocked and descends abruptly to the surface well behind the convective line (Stumpf et al., 1991). In the 3-4 June case discussed by Stumpf and others, the sudden descent of the jet occurred near a region of enhanced reflectivity toward the rear of the stratiform area. In this simulation, the strong ascent, over 1.5 m s^{-1} and intense rainfall occur near the back edge of the rain region. The downdraft here is as large as 1 m s^{-1}. As will be shown in a specialized simulation in Chapter 8, the presence of an isolated convective-like cell near the back of the stratiform region may account for the intense downward motion and descent of the rear-inflow jet observed in cases like the 3-4 June PRE-STORM MCS.

The stronger descent in S3 from that in CTL results in more drying at low levels within the stratiform rain region. From 270 minutes through the end of the simulation, humidities drop below 50% at isolated locations below the 2.5 km level (figure not shown). Soundings taken in these areas better resemble an onion sounding than any generated in CTL (e.g. Fig. 6.9). This particular sounding represents one point in the main rain region at 270 minutes. The better simulation of an onion sounding may indicate that within the 11 June system, certain areas were more unstable than the region average assumed for CTL. The model results indicate a strong sensitivity to stability. Knupp and Cotton (1987) also found that vertical motions within the stratiform region are rather dependent upon the stability.

Another simulation, S4, was done with a more stable troposphere. As might be expected from the S3 results, vertical motions in this stable simulation are weaker than in CTL. This is evidenced by reduced in situ production of condensate (Table 6.1). Although in situ production decreases by over 30%, the weaker downdraft and diminished evaporation compensate for the reduction in hydrometeors aloft, so that surface rainfall actually increases a small amount.

Vertical motions in this more stable simulation are weaker than in CTL (Fig. 6.10). Downward motion reaches 36 cm s^{-1} at 180 minutes (Fig. 6.10b) and remains around this value through 360 minutes (Fig. 6.10c, d). Even at the end of the simulation peak descent is only 60 cm s^{-1}. These values are generally 20-30% lower than those in CTL.

Figure 6.9: Thermodynamic diagram from within the stratiform rain region at 270 minutes, with storm-relative winds shown at the right.
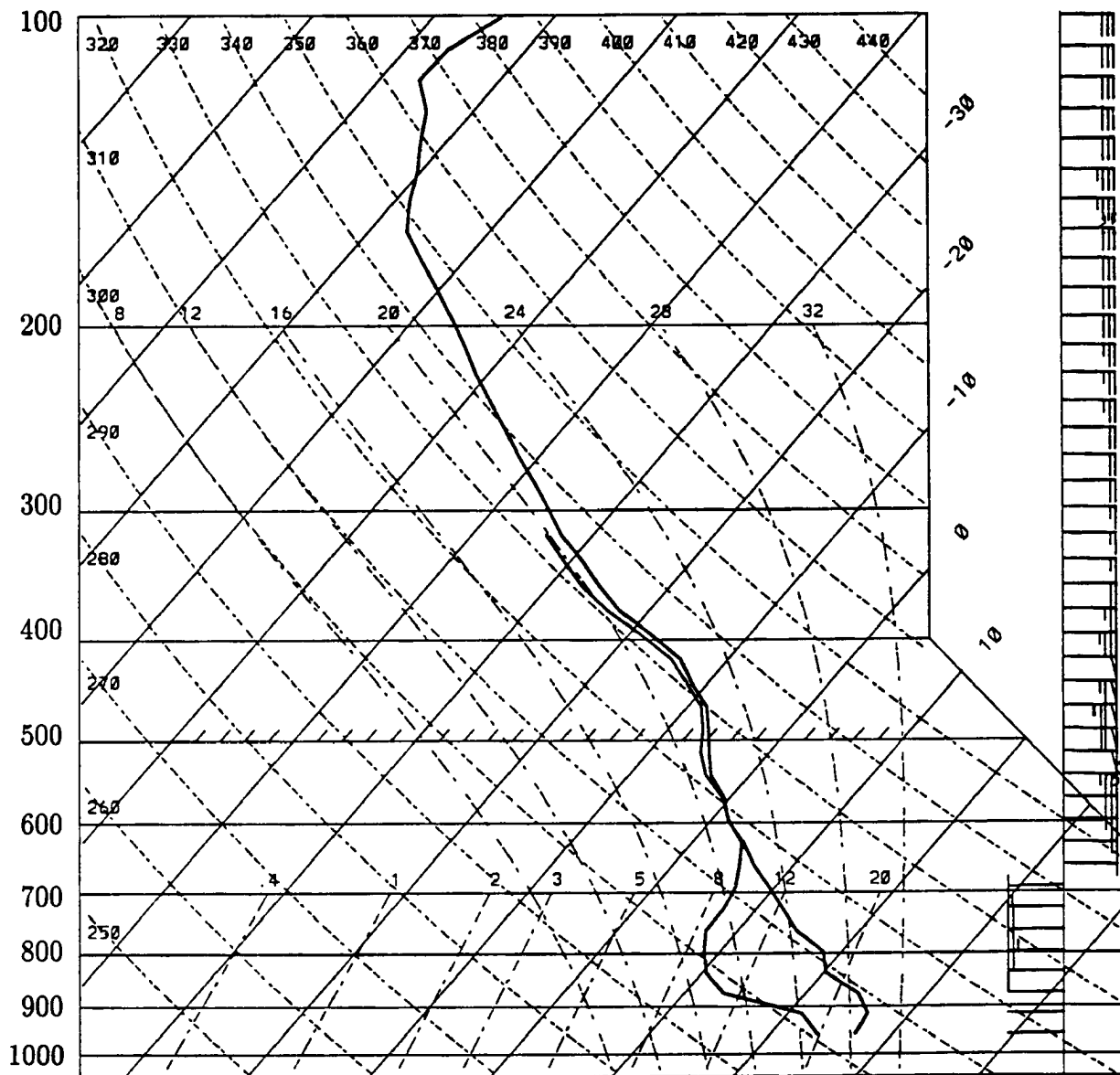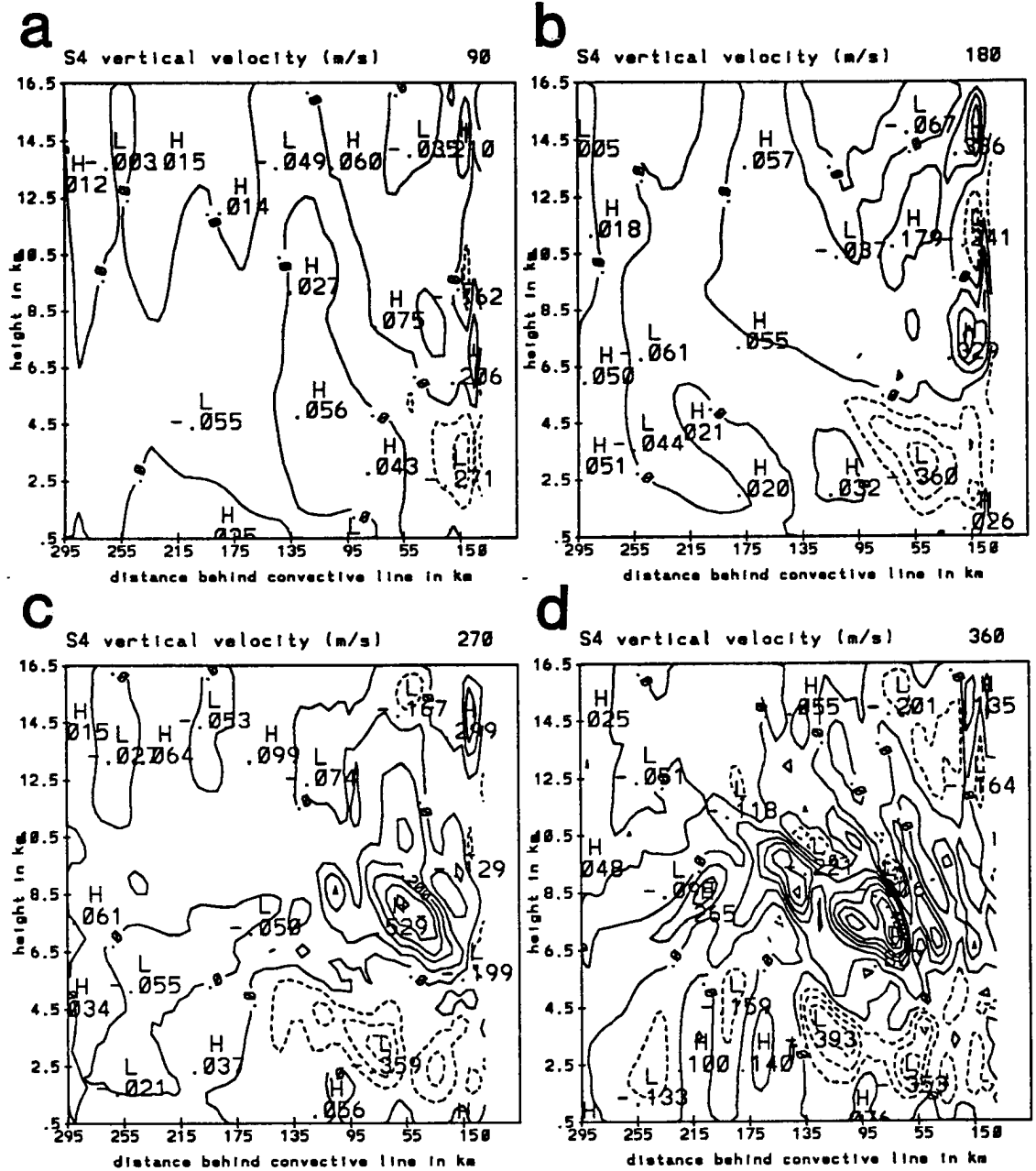
Figure 6.10: As in Fig. 5.24 except for S4, the simulation with decreased instability.

Peak upward motion also decreases at least 20-30% at most times. Horizontal velocities similarly decrease in the stable environment, but changes in the peak values are only around 10-15% (figure not shown). Again, the model displays significant sensitivity to a change in lapse rates, but variations are not as extreme as they are in the more unstable case.

6.3 Ambient wind

As discussed in Chapter 3, an idealized wind profile is used in most of the model simulations. Winds are initialized from front to rear at all levels with a distinct minimum around the melting level. The initial wind field ideally should be one that has been influenced by the developing convective line prior to formation of a stratiform region. Wind information from Gallus and Johnson (1991) and the model results of Zhang and Gao (1989), along with other soundings from the 10-11 June event implied that the developing convective line produced a wind field similar to that used in the initialization of this model. The primary uncertainties in the field include the speed of the wind within the midlevel minimum, the strength of the FTR flow aloft exiting the convective line, and the depth of the layer through which the FTR jet occurs. At later times on 11 June, when the stratiform region was well-established, the data clearly show the horizontal winds present. During the initiation of the stratiform region the data are far more unclear.

Two simulations were done to test the response of the model to variations in the initial wind field. The variations are shown in Fig. 6.11. The first of these simulations (S5) decreases the strength of the FTR flow aloft from a peak magnitude of 17.5 m s^{-1} to 10 m s^{-1}. The levels of peak FTR flow and minimum FTR flow remain unchanged. In the second simulation (S6), stronger FTR flow occurs within the midlevel wind minimum, and the stronger FTR flow aloft is unchanged in magnitude but restricted to a more shallow, elevated layer.

Weaker FTR flow aloft significantly slows the rearward expansion of the stratiform rain region (figure not shown). By 315 minutes, the rear edge of surface rainfall is 40 km closer to the convective line in S5 than in CTL. The 7 m s^{-1} reduction in peak FTR
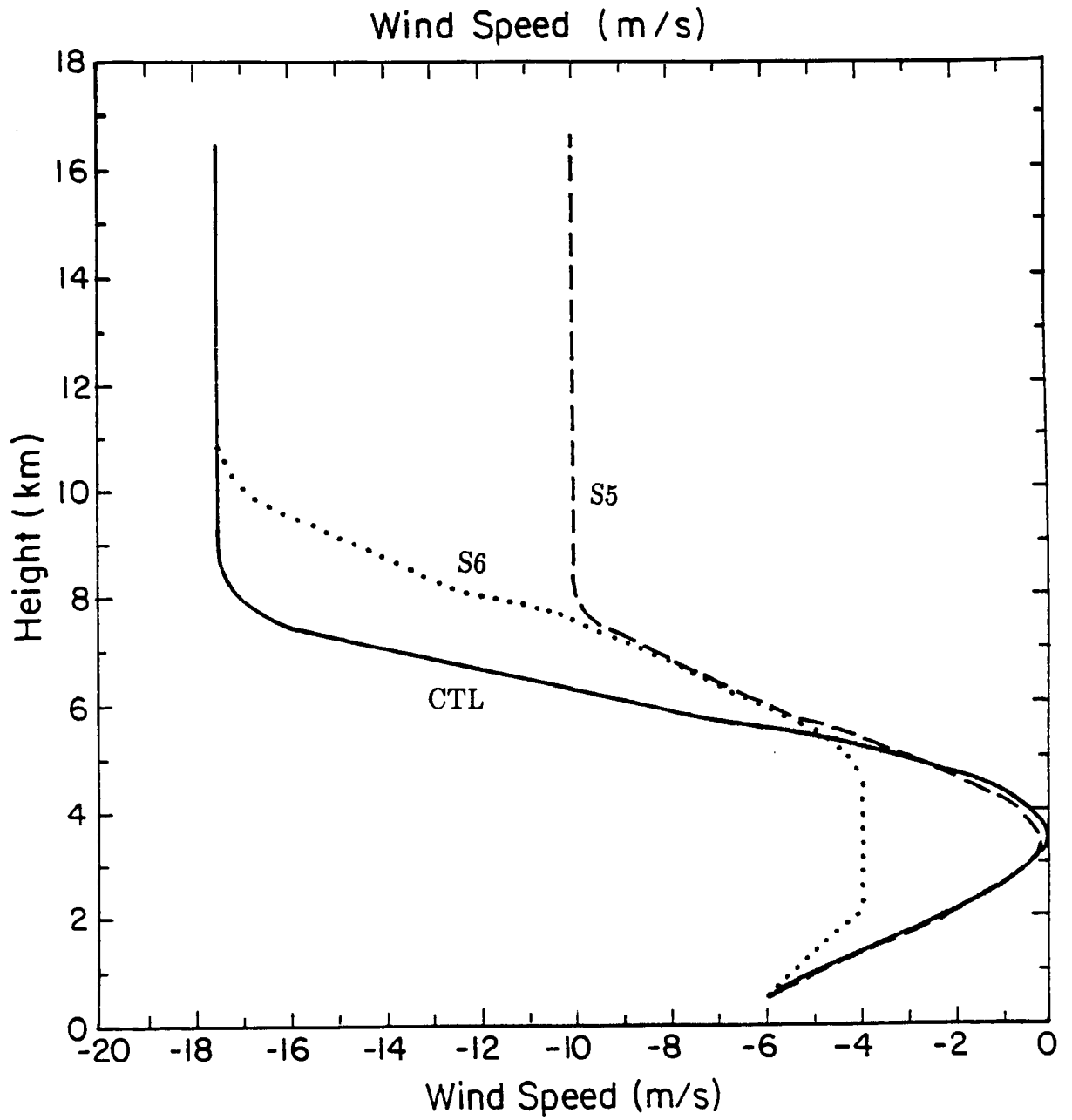
Figure 6.11: Vertical profiles of ambient wind for simulation S5 (dashed curve) and S6 (dotted curve), compared with CTL (solid curve). Values are in m s^{-1}.

flow aloft, however, should correspond to a distance of over 125 km at this time, if simple advective arguments are considered. Because the rear edge of the rain area is only 40 km closer to the convective line and not 125 km closer, in situ production of condensate must play an important role in the stratiform anvil cloud. Rain rates at the surface are slightly decreased through 315 minutes, but convective elements develop in the anvil cloud by 360 minutes, so that peak surface values exceed those of CTL. The total rain reaching the surface is 12% lower in S5 than in CTL (Table 6.1).

Upward motions are weaker in S5 than in CTL until 270 minutes, at which time somewhat stronger ascent forms in the front part of the stratiform region. Peak ascent remains within 50 km of the convective line through the rest of the simulation, unlike CTL where the peak values progress rearward. Within this 50 km region, ascent is strong, with peak values comparable to those of CTL. However, since the ascent is confined to a smaller region, total in situ production of condensate is diminished by 4% (Table 6.1). The mesoscale downdraft is also confined to a narrower region closer to the convective line, with peak values somewhat less than those of CTL. This results in a 24% decrease in mass lost to evaporation and sublimation (Table 6.1).

Horizontal perturbations change only slightly in S5, with a roughly 10% decrease in RTF flow, and a small increase in the FTR flow at mid and upper levels (figure not shown). This increase becomes more significant at later times, and results in narrowing the gap between the total flow in this simulation and that in CTL. Because the ambient wind in CTL is FTR over a larger layer aloft, the total wind in S5 is still significantly less than in CTL at high levels. This is evidenced by the significant reduction in hydrometeor advection into the domain (Table 6.1).

A second simulation (S6) was done with an altered wind profile which included stronger FTR flow in the midlevel wind minimum, and raised the region of strongest FTR flow aloft. Peak FTR flow was still -17.5 m s^{-1} but it occurred in a narrower layer. The amount of condensate advecting into the domain is again reduced from that in CTL (Table 6.1), but not by as much as in S5.

The small variations in the wind profile of S6 do not significantly change results, although the amount of condensate advecting into the domain is reduced by 10% (Table

6.1). Rain rates at the surface decrease some from those in CTL, but the total mass reaching the surface only decreases by 4%. Peak rain rates at most times are comparable to those in CTL. The upward motion in the anvil cloud does not change significantly from CTL, with peak values 20-30% larger during the first 180 minutes, and roughly 10% smaller at later times. The total in situ condensate production falls by 11%. The mesoscale downdraft is generally a little weaker in this simulation, probably because the stronger mid-level FTR flow maintains moister conditions in the region that experiences significant evaporation. This also is evident in the horizontal perturbation velocity field (figure not shown), where rear-inflow is significantly weaker in the upper part of the jet (the region 50 km or more rearward from the convective line in the 3-6 km layer). Peak RTF flow is within 10% of that of CTL, but the peak occurs at low levels near the convective line in a region not affected by the midlevel ambient wind variation. Most changes in the FTR flow are small, although FTR perturbations are smaller in S6 in the rear of the domain through much of the simulation. Simulation S6 indicates that rather small variations from the wind profile used in CTL do not significantly affect results.

6.4 Convective cell hydrometeor content

The hydrometeor contents used in most of the simulations were taken from Rickenbach's (1990) values calculated from the Ferrier and Houze (1989) model. As stated in Chapter 3, these values with pulsing are supported by the water budget of Gallus and Johnson (1991), and may therefore allow less room for error than the other initial variables. Two sensitivity tests investigating the model response to hydrometeor content are discussed below. The first test (S7) reduces the solid hydrometeor content of the convective cells by 50%. The second test (S8) increases the contents by 50%. Changes in the cumulative water mass of certain terms in the water budget in S7 and S8 from those in CTL can again be seen in Table 6.1.

As might be expected with a 50% reduction in snow, ice and graupel entering the domain, rain rates are diminished in S7 (Fig. 6.12). Peak rates aloft are about 40% less than CTL at most times, and the greatest surface rates remain below 1.2 mm h^{-1} at
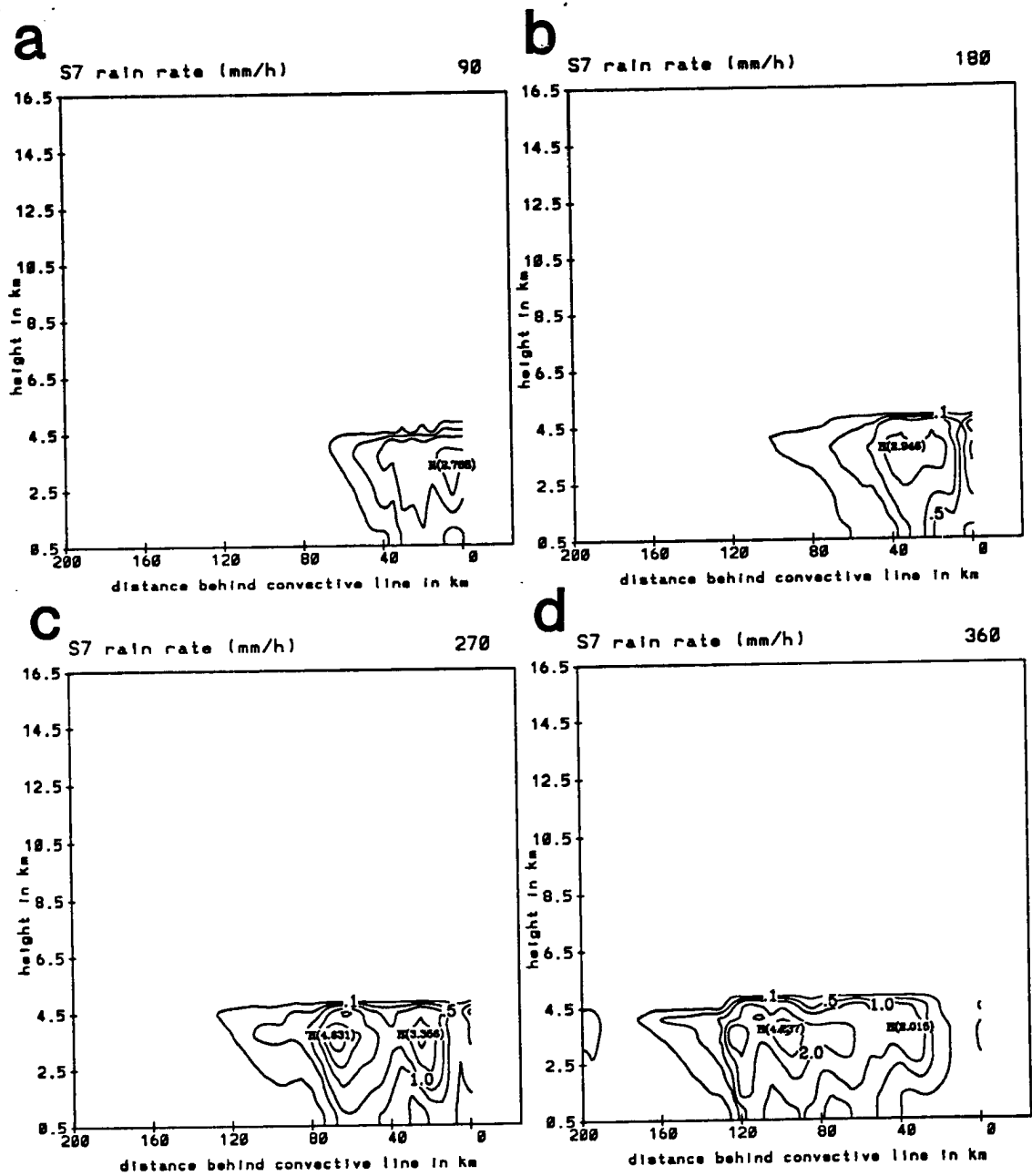
Figure 6.12: As in Fig. 5.19 except for S7, the simulation with reduced hydrometeor advection into the domain.

all times. The relative reduction in total mass of rain reaching the surface during the simulation is rather close to the relative reduction in the mass advecting into the domain (Table 6.1).

Mesoscale ascent is slightly reduced in S7, with the exception being at 90 minutes when the reduced water loading allows an increase of 30% in the peak ascent (figure not shown). In general it appears the decrease in depositional and condensation heating due to the reduced amount of hydrometeor mass is nearly compensated by the reduced water loading so that upward motion is only slightly diminished. The small decrease in upward motion can be seen in the profile of average vertical motion within the stratiform rain region during the 270-360 minute period (Fig. 6.13). Mesoscale descent is also diminished, with peak downward motion decreased by roughly 20% at most times. The diminished descent also reduces the amount of evaporation and sublimation occurring, so that rain rates at the surface are not as low as might be expected from the decrease in both in situ production and advection (Table 6.1). The decrease in evaporational and sublimational cooling weakens horizontal perturbation flows.

When hydrometeor advection from the convective line is increased (S8), surface rainfall rates also increase, by an even larger percentage than the increased hydrometeor input (Table 6.1). Increased hydrometeor advection generates stronger circulations in the stratiform region so that more condensate is produced in situ. The positive feedback of increased hydrometeor advection increasing the in situ production of condensate significantly increases surface rainfall in the domain (Fig. 6.14), especially at early times. The peak surface rain rates are over 3.0 mm h^{-1} already at 90 and 180 minutes (Figs. 6.14a, b). After this time, increased evaporation causes the peak rain rates to be only slightly larger than those in CTL. Rainfall occurs over a slightly larger area than in CTL, with the transition zone not as wide at later times. Of all the sensitivity tests discussed in this chapter, the increase of hydrometeors from the convective line causes the greatest increase in total rain mass reaching the surface (Table 6.1). Peak rainfall generally occurs in the same locations as in CTL, but secondary peaks are more prominent in S8.

In situ production of condensate increases by nearly 20% in S8 (Table 6.1). During the first 180 minutes of the simulation, peak upward motion is less than in CTL, probably
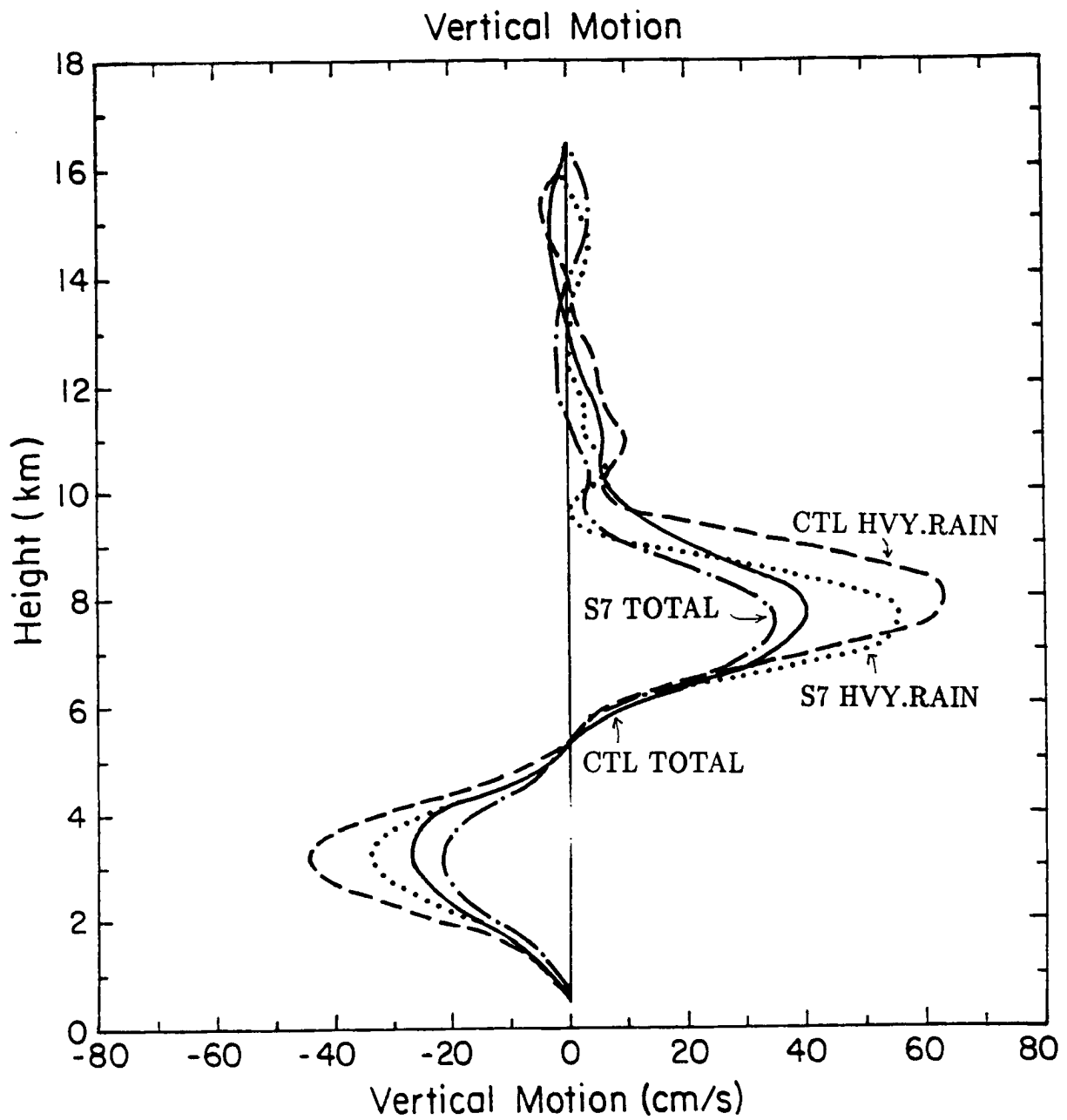
Figure 6.13: As in Fig. 5.22 except for comparison between S7, the simulation with reduced hydrometeor advection, and CTL.

172
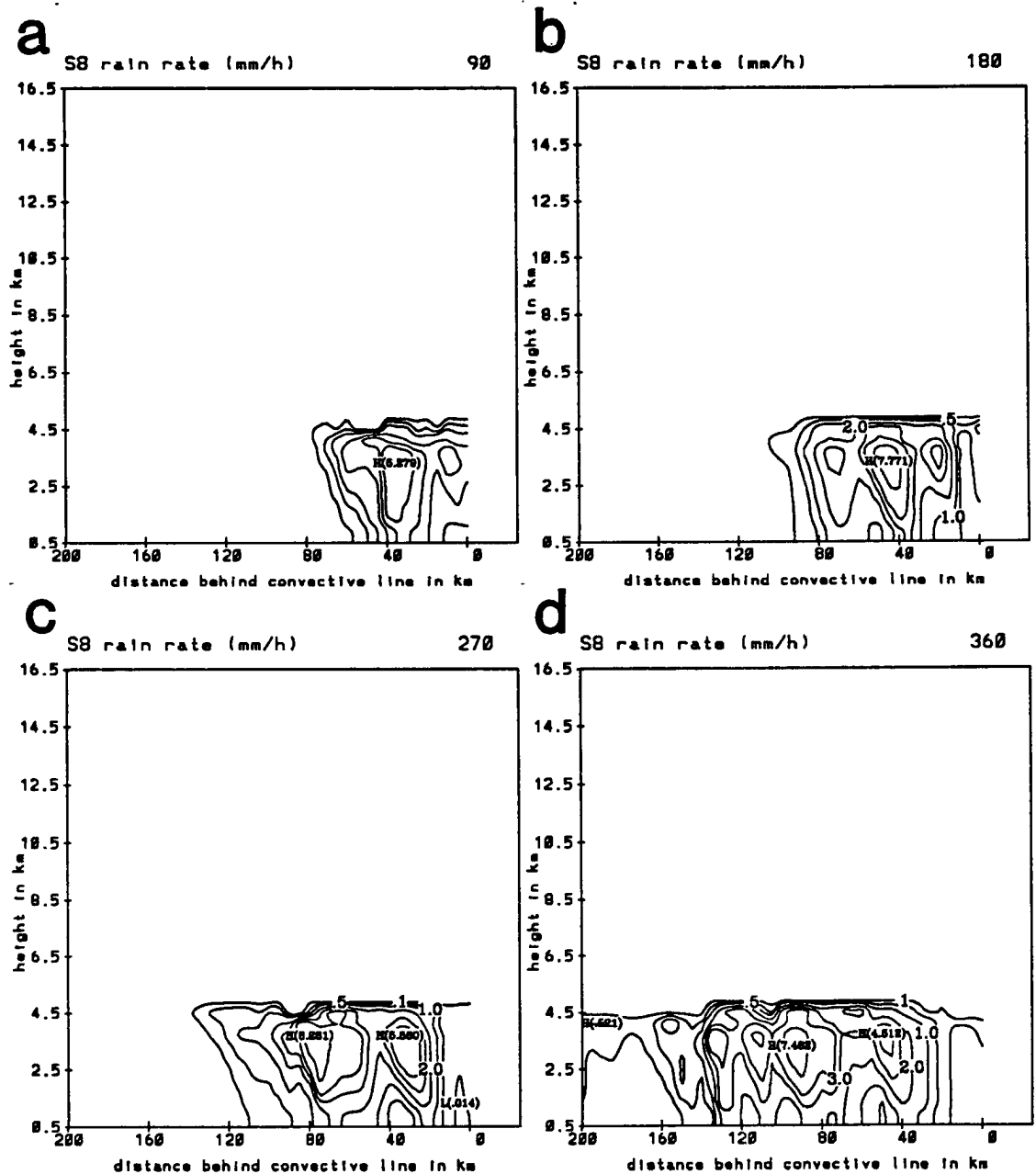
Figure 6.14: As in Fig. 5.19 except for S8, the simulation with increased hydrometeor advection into the domain.

due to the effects of increased water loading (figure not shown). Peak ascent exceeds that of CTL during the 270-360 minute time period. The increased rain leads to stronger evaporation and a stronger mesoscale downdraft. Peak values are generally 10-30% higher at most times, but the locations of vertical motion extrema are the same as in CTL. The increased evaporation leads to a 15% increase in the strength of the RTF velocity perturbation. FTR flow does not change as significantly. The jet axes are comparable in both simulations.

Both simulations S7 and S8 show that the amount of rain reaching the surface in the stratiform region depends highly on the amount of hydrometeor mass advecting rearward from the convective line. A positive feedback operates so that any increase/decrease in the amount of hydrometeors advecting into the region increases/decreases the amount of condensate produced within the anvil cloud. In fact, the changes in surface precipitation shown in Table 6.1 are greater for variations in hydrometeor content than for any other sensitivity test run in this chapter. This result has significant implications. For instance, it shows that accurate measurements or estimates of hydrometeor content within convective cells is extremely important for any modeling of stratiform regions. This is supported by Ferrier and Houze (1989). In addition, the intensity of the stratiform region, both from a rainfall and circulation perspective, may depend heavily on the amount of hydrometeors that are advected away from the convective line. This may be a function of the intensity of the convection itself, or the environmental flow in the vicinity of the convective line.

6.5 Convective cell heating

The heating rates prescribed within a 15 km region in the buffer zone to represent convective line heating were chosen from the heat budget of Gallus and Johnson (1991) for this case. The vertical profile of heating is patterned after the 0300 UTC budget results, which are the closest of the three budgets in that study to the time of the initial growth of the stratiform region. Although the rawinsonde-based study probably underestimates the true magnitude of heating within small convective cores, the magnitude of the heating used in most of the simulations is fairly close to that found at 0300 UTC in the Gallus

and Johnson study. The magnitude of the heating was chosen with the belief that heating prior to 0300 UTC, which was close to the time of maximum intensity of the convective line, was probably less intense. The following simulations were done to determine what errors might enter the CTL results if the convective heating profile is not entirely accurate. In S9, the magnitude of the peak heating was increased by 5 C h^{-1}, so that heating at most levels was increased by 45-70%. In S10, the peak heating was the same as in CTL, but the main region of heating was elevated by 2 km, and the total amount of heating in the depth of the troposphere was the same as in S9.

The increased convective heating in S9 increases the amount of condensate produced in situ in the anvil (Table 6.1) so that peak snow, graupel and ice quantities are larger than in CTL. The melting of these hydrometeors produces rainfall that also exceeds that of CTL (Fig. 6.15). At most times the peak rain rates above the surface are greater than those in CTL, but this is not always true at the surface. Peak surface rates are generally greater than those in CTL through 270 minutes (Figs. 6.15a, b, c), when they are around 2 mm h^{-1}. After this time, stronger downdrafts lead to increased evaporation so that rainfall at the surface is actually lower than in CTL. Over the course of the simulation, total rain mass reaching the surface is not significantly changed by a 45-70% increase in convective heating (Table 6.1).

Vertical velocities within the stratiform region are significantly increased in S9 (Fig. 6.16). Peak ascent is almost 50 cm s^{-1} by 90 minutes (Fig. 6.16a), nearly double the ascent in CTL at that time. Ascent slowly intensifies through 360 minutes (Fig. 6.16d), with values near or exceeding 1 m s^{-1} at both 315 and 360 minutes. The increased ascent over CTL is not as pronounced at later times in the simulation. Averaged vertical motion over the stratiform rain region and the smaller EVAD-scale region does not change significantly from CTL (Fig. 6.17). Downward motion increases by only a few percent over that in CTL. The level of peak ascent is raised by 0.5 km or so, but the peak ascent is not significantly different from CTL. In general, the shape of the curves is the same. Most of the increase in the in situ production shown in Table 6.1 is due to stronger ascent before 270 minutes. The increased water sink term is also related most strongly to the increase in descent prior to 270 minutes in the simulation.
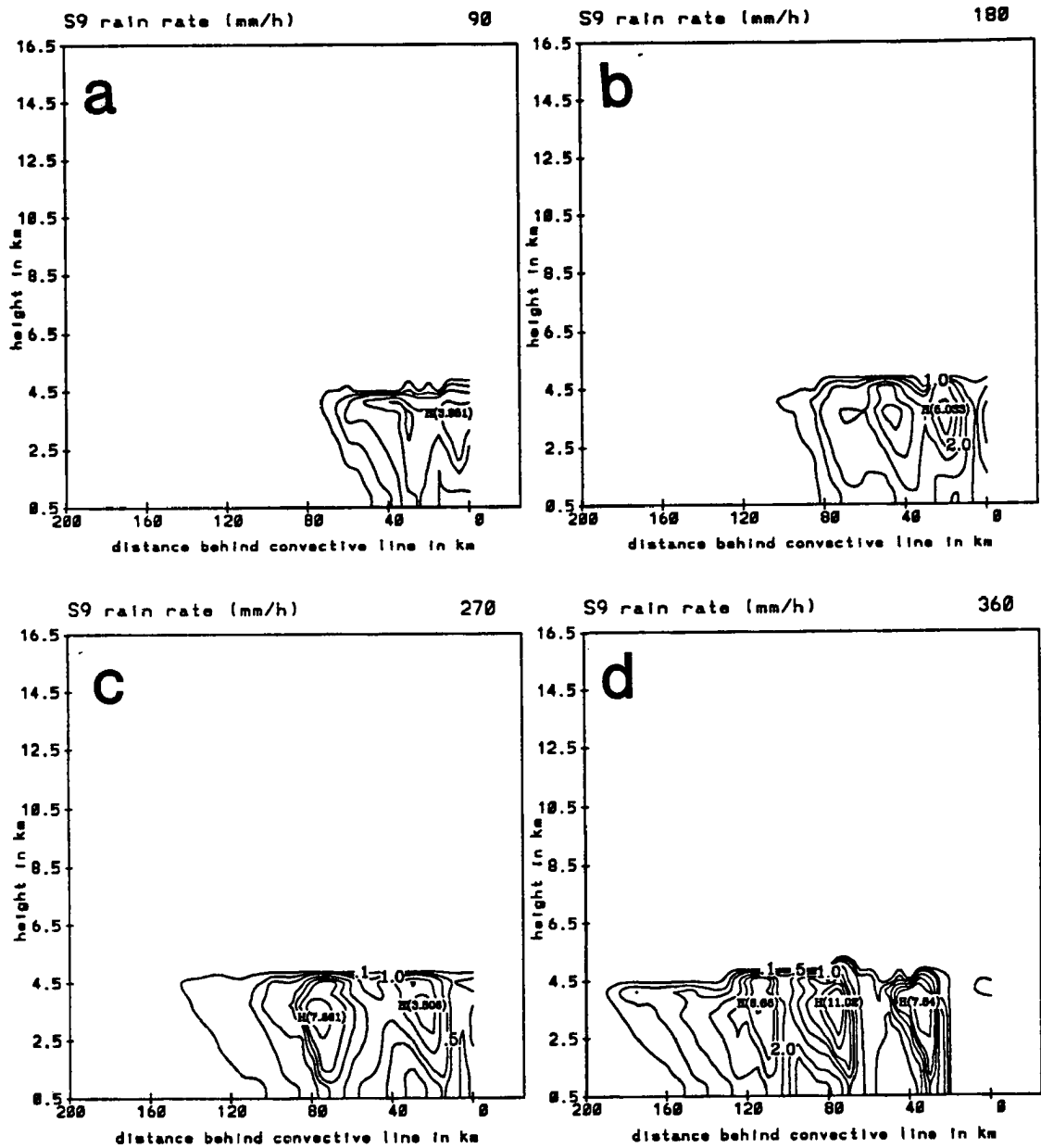
Figure 6.15: As in Fig. 5.19 except for S9, the simulation with increased convective line heating.

a

S9 vertical velocity (m/s)   90

b

S9 vertical velocity (m/s)   180

c

S9 vertical velocity (m/s)   270

d

S9 vertical velocity (m/s)   360
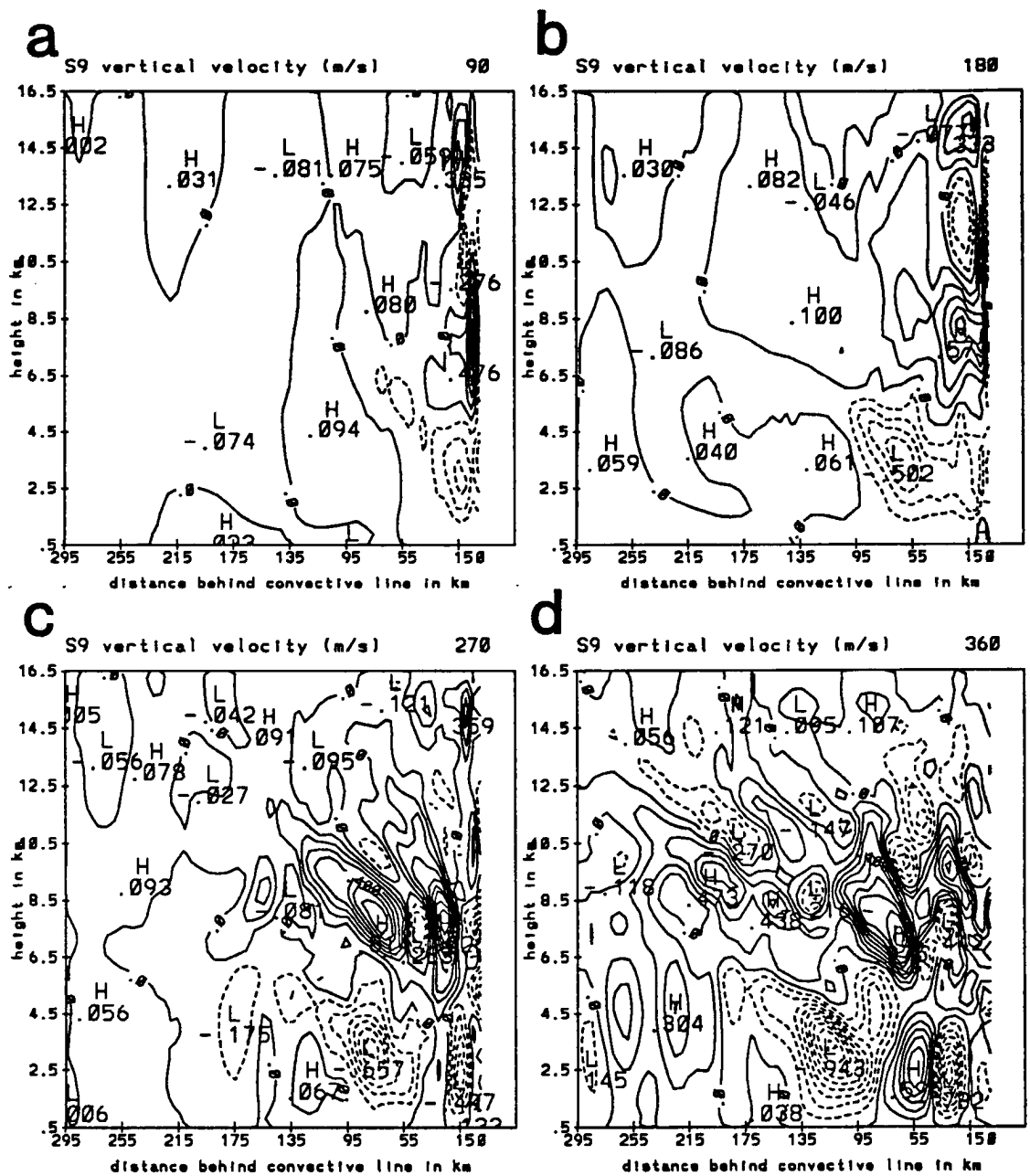
Figure 6.16: As in Fig. 5.24 except for S9, the simulation with increased convective line heating.

Vertical Motion
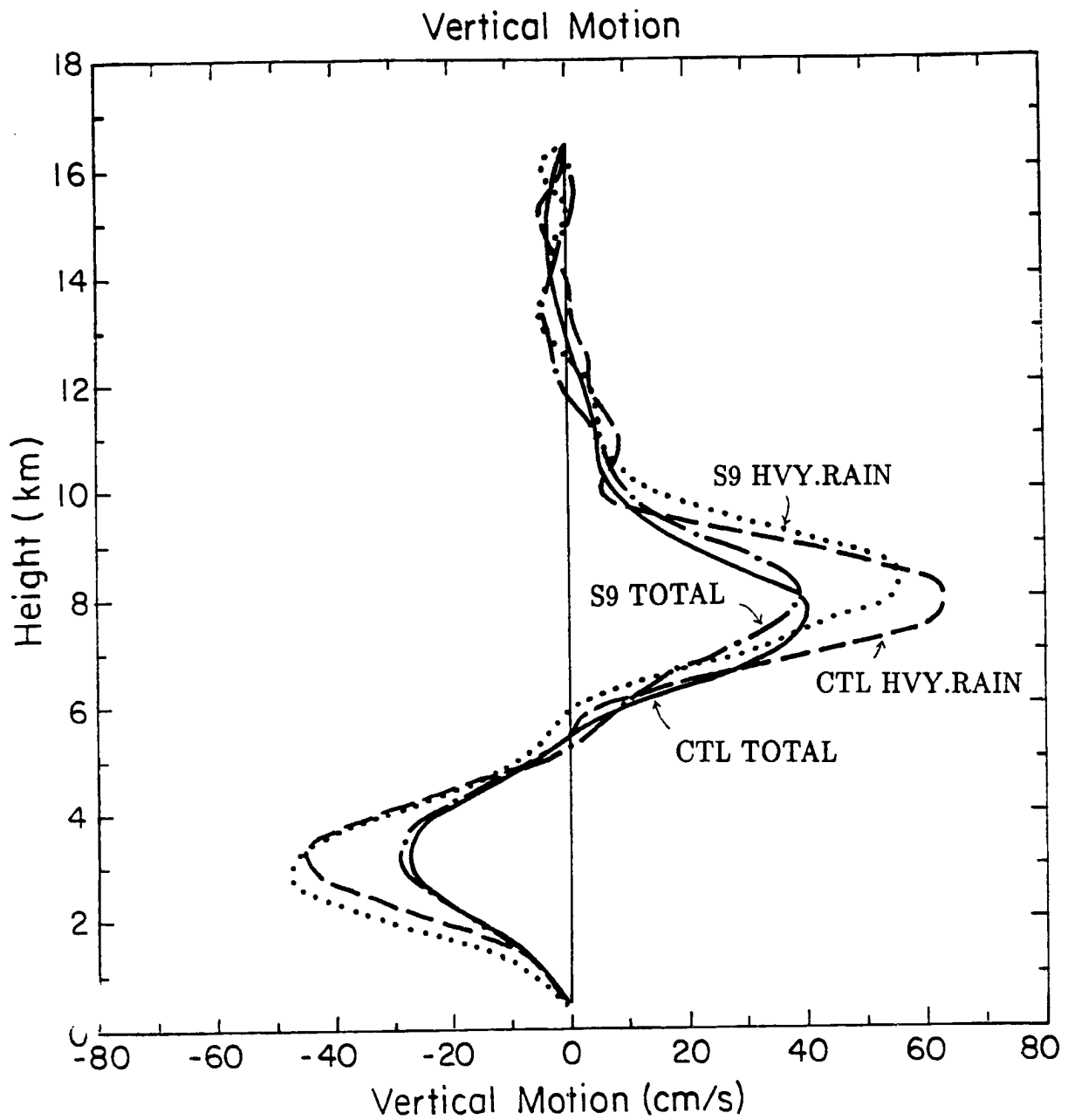
Figure 6.17: As in Fig. 5.22 except for comparison between S9, the simulation with incre ased convective line heating, and CTL.

Horizontal velocities increase in S9 (figure not shown) but are generally within 15% of the values in CTL, and the location of the perturbation jets is unchanged. The model therefore appears to be only slightly sensitive to small changes in the magnitude of convective heating in the buffer. Upward motion increases, but the increased in situ production of condensate is nearly balanced by increased evaporative losses within a stronger downdraft so that surface rainfall is similar.

Simulation (S10) was done to see if the shape of the vertical heating profile in the convective line had a strong influence on circulations in the stratiform region. The peak heating in S10 is equivalent to that in CTL, 12 C h^{-1}, but occurs 2 km higher, around the 8 km level. The shape of the heating profile is changed so that the total heating through the depth of the troposphere is greater than in CTL, and matches that of S9. By neglecting the secondary sinusoidal enhancement used in CTL, heating varies more smoothly with height in S10.

The variation of the shape of the convective heating curve causes significant model differences from CTL. Rainfall rates in general are significantly reduced from those of CTL (Fig. 6.18). Peak rain rates aloft and at the surface at 90 minutes (Fig. 6.18a) agree with CTL, but the peak rates aloft later remain relatively constant throughout the simulation, and do not increase as in CTL. Surface rainfall rates generally decrease throughout the simulation as evaporation increases. The total rain mass reaching the surface (Table 6.1) is 30% less than that in CTL. The rainfall patterns in S10 resemble those of C2, the simulation that excluded convective heating.

Both mesoscale ascent and descent decrease in S10 (Fig. 6.19). Peak ascent is only 10 cm s^{-1} at 90 minutes (Fig. 6.19a), 20 cm s^{-1} at 180 minutes (Fig. 6.19b), and never exceeds 30 cm s^{-1}. The ascent occurs rather uniformly through the anvil cloud in a broad region, with far less variation than in CTL. Because the ascent is much weaker than in CTL, the in situ production of condensate is reduced by roughly one half (Table 6.1). Mesoscale descent is also diminished, with peak values 10-40% less than those in CTL. The water sink through evaporation and sublimation is 24% less than in CTL.

Rear inflow is similar in the region just behind the convective line where the peak velocities are found (Fig. 6.20). However, RTF flow is more substantially reduced at later
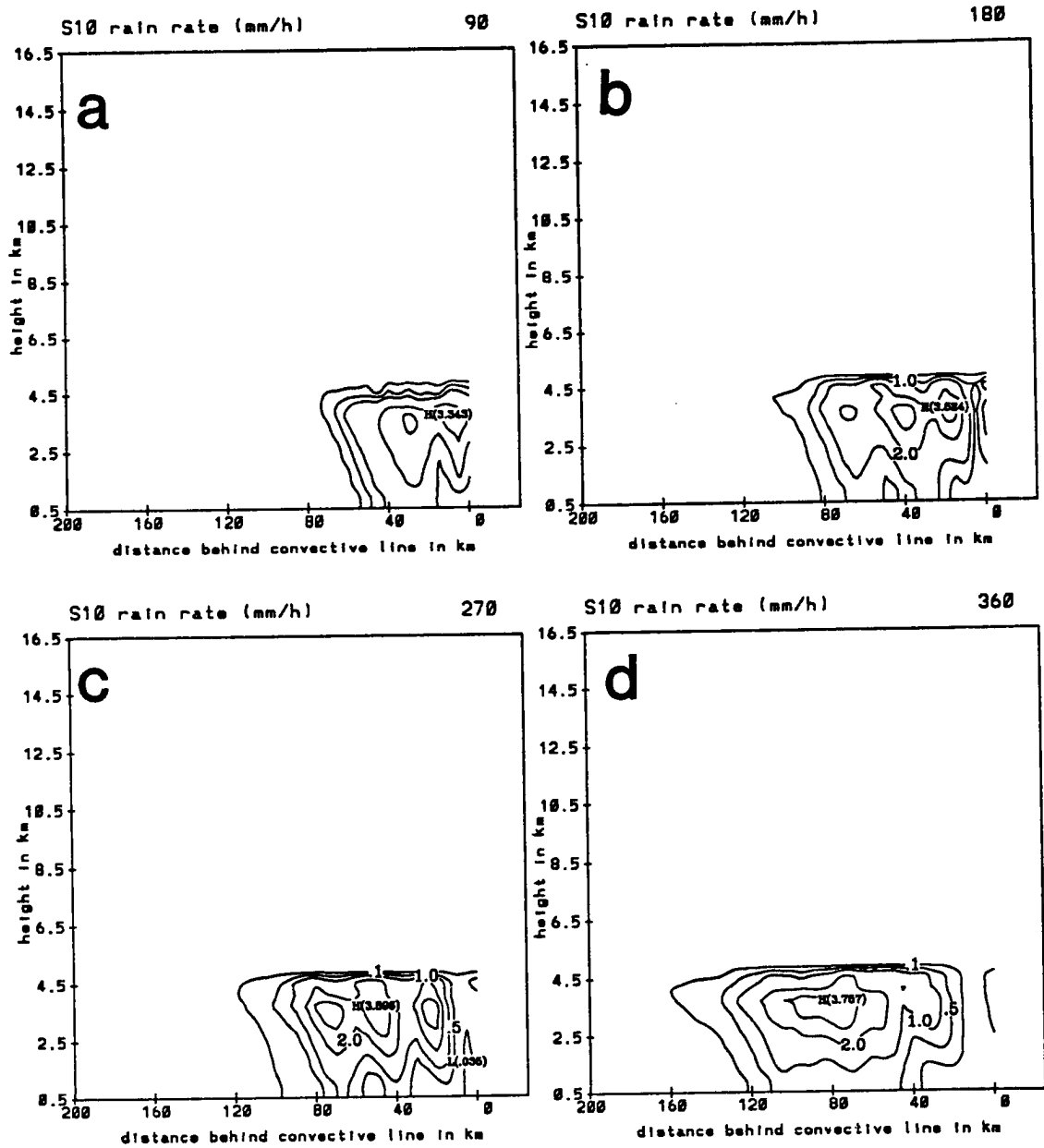
Figure 6.18: As in Fig. 5.19 except for S10, the simulation with different convective heating profile.
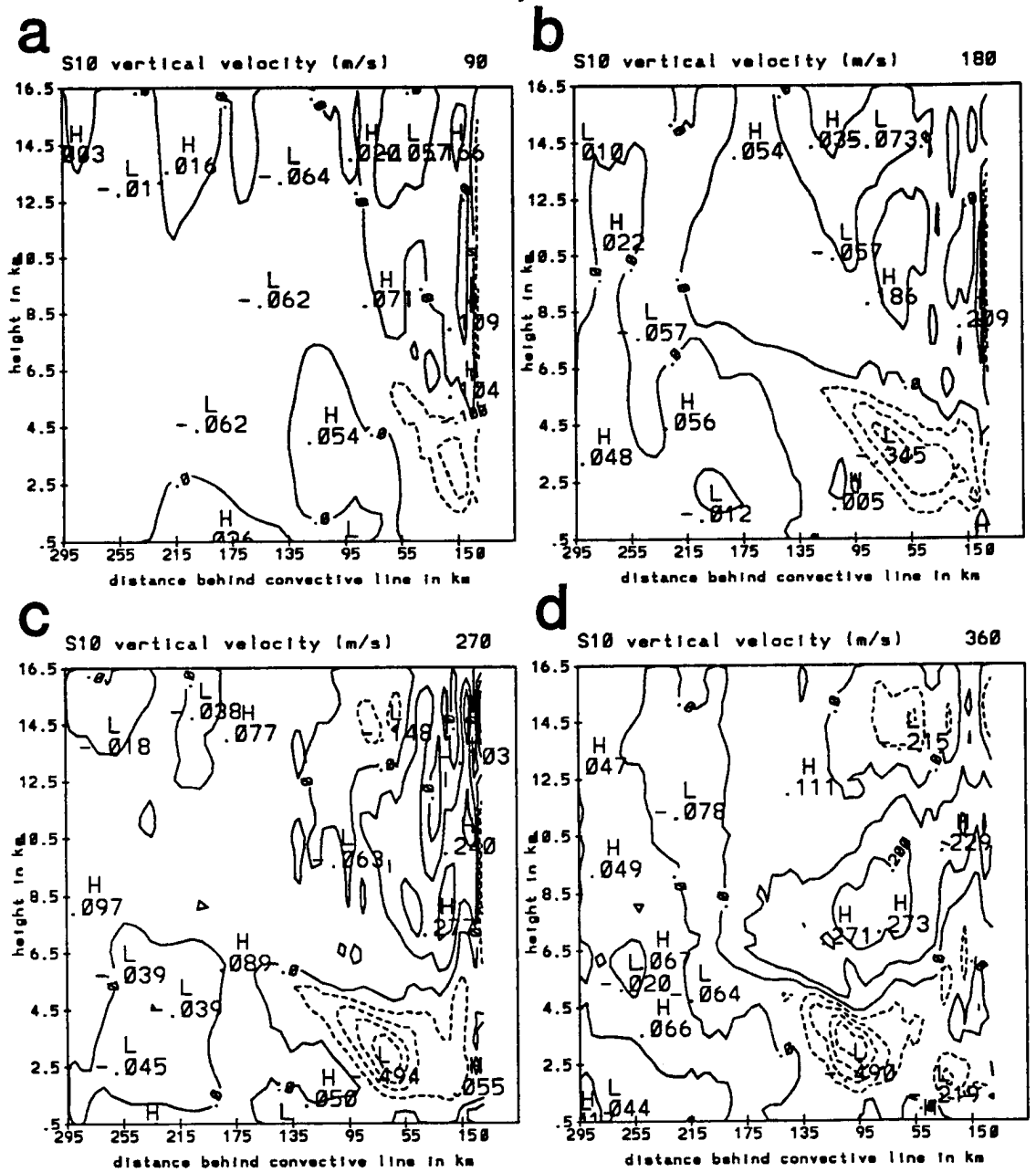
Figure 6.19: As in Fig. 5.24 except for S10, the simulation with different convective heating profile.
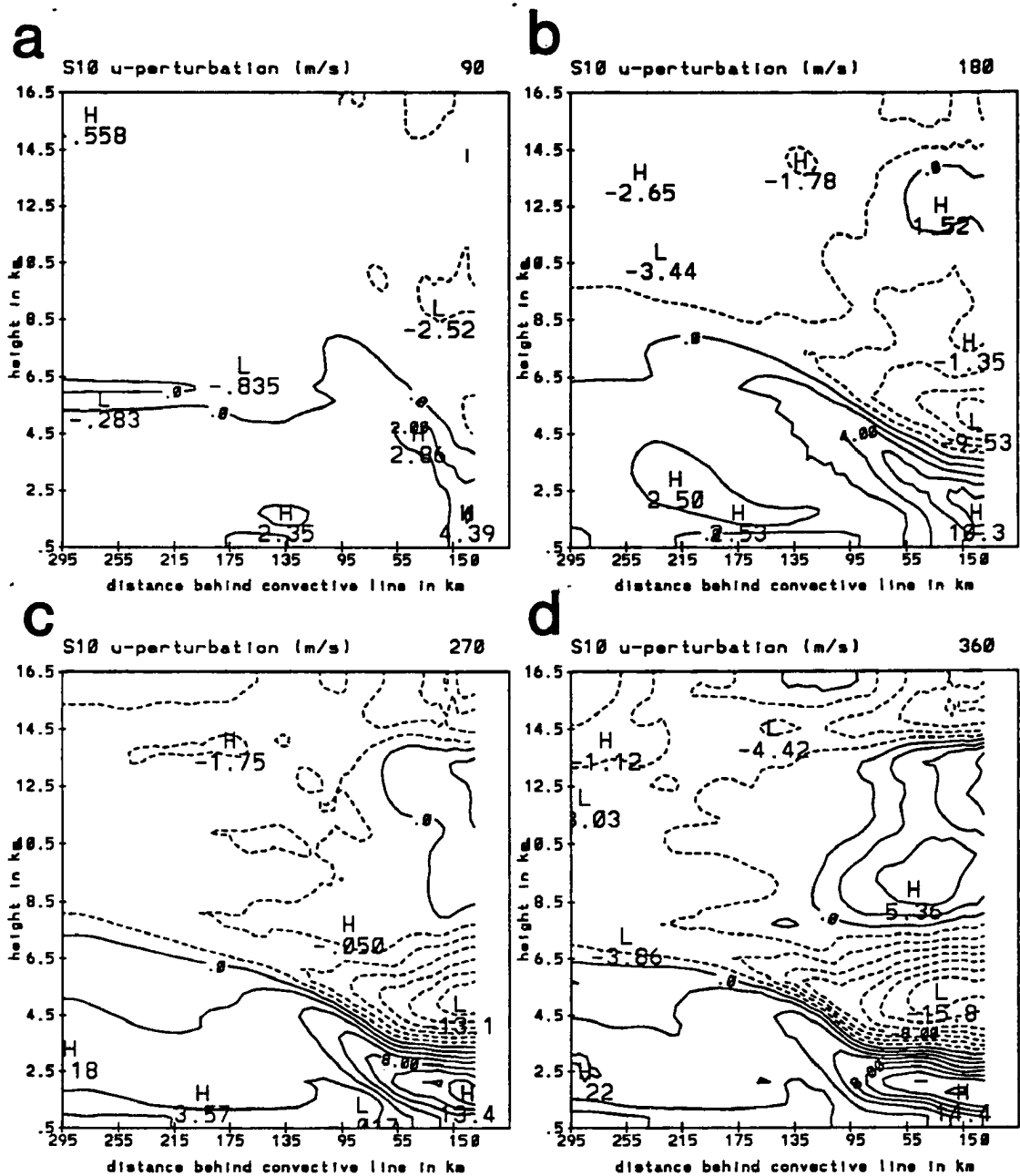
Figure 6.20: As in Fig. 5.15 except for S10, the simulation with different convective he ating profile.

times within the region of stratiform rainfall. The different shape of the convective heating curve greatly decreases the RTF flow that develops at high levels near the top of the anvil cloud. The peak FTR enhancement in mid-levels now occurs at a somewhat lower level, and the magnitudes are reduced. The reduction grows with time, reaching 40% at 270 minutes (Fig. 6.20c), and over 50% by the end of the simulation. This result is significant since the changes in the shape of the heating profile are not unusually large. This result also has ramifications for other modeling studies in which a heating profile is prescribed to represent the convective line of a squall line system. The effects of convective heating may be underestimated if the heating is prescribed with too smooth a vertical variation. Fortunately, the profile used in the CTL case is supported by the 03 UTC heat budget of Gallus and Johnson (1991) which showed rather strong vertical gradients of convective heating. The rain rates and vertical motions that occur in CTL are also in closer agreement with those observed on 11 June.

6.6   Pulsing

Finally, the importance of pulsing of both the heat and hydrometeors advecting from the convective cells was investigated. In S11, constant values of hydrometeor content and heating are assumed in the convective cores, and the peak values are reduced so that the same amount of water mass and heat enter the domain over the duration of the simulation.

Although the same amount of water mass is permitted to enter the domain in the simulation without pulsing (S11) as in CTL, rain rates and vertical motions are significantly weaker during the last half of the simulation. At 90 and 180 minutes (Figs. 6.21a, b), the rain field is comparable to that of CTL. However, at 270 and 360 minutes (Figs. 6.21c, d), rain is greatly diminished, both aloft and at the surface. Peak surface rain rates generally decrease in this simulation after 90 minutes. The total amount of rain reaching the surface is among the lowest of the eleven simulations discussed in this chapter, and is lower than in the simulation that completely neglected convective heating (C2, see Table 5.3). The surface rain area undergoes a similar evolution to that in CTL and the areas are surprisingly similar at all times. A transition zone does broaden after 270 minutes as in CTL.
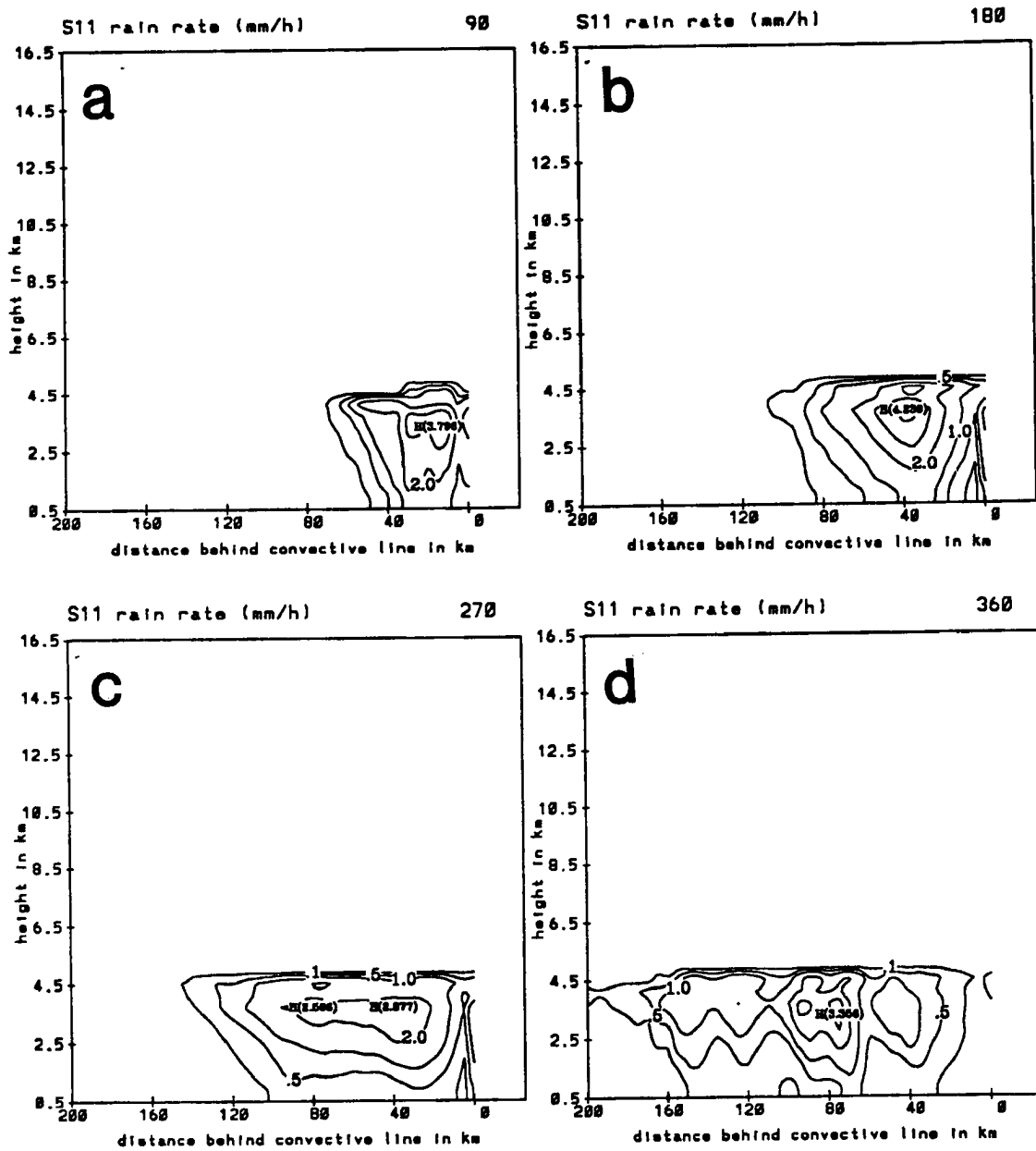
Figure 6.21: As in Fig. 5.19 except for S11, the simulation without pulsing.

Similar trends occur in the vertical velocity field (Fig. 6.22). Through 180 minutes (Figs. 6.22a, b) the vertical motions are as strong as in CTL, with no significant changes. At 270 and 360 minutes (Figs. 6.22c, d) both mesoscale ascent and descent are typically 40% less than in CTL. Somewhat surprisingly the vertical motion field contains many of the same smaller-scale features in the same locations as in CTL, in spite of the removal of pulsing. Enhanced upward motion occurs in small-scale regions scattered within the anvil cloud, in generally the 6-9 km layer. This implies that the peaks in CTL are not dependent upon the location of heat pulses. Peak ascent in S11 is on the order of 40 cm s^{-1} at 180 and 270 minutes (Figs. 6.22b, c), and reaches 60 cm s^{-1} at 360 minutes (Fig. 6.22d). These values, though substantial, are significantly less than those observed. In situ condensate over the duration of the simulation is reduced by 32% (Table 6.1).

Horizontal velocity perturbations are not significantly different in S11 compared with CTL. Peak RTF and FTR flow perturbations are within 10% of those in CTL. Rear inflow does not extend as quickly rearward in S11 as in CTL, probably because the diminished vertical velocities do not allow as much hydrometeor mass to travel rearward, extending microphysical influences further from the convective line.

An additional simulation was done increasing the pulsing frequency by a factor of two. Pulses occurred 15 minutes apart instead of 30. Although some finer scale variations were introduced within the vertical motion field, in general, changes from CTL were not significant. Surface rainfall, in situ condensate production and the amount of water lost through evaporation and sublimation changed by less than 10%.

In summary, these simulations find that the general circulation pattern produced in the CTL run does not change for reasonable variations in the initial conditions. Variability does occur in the strength of mesoscale ascent and descent, but the locations of the peak vertical motions and the time evolution are comparable in most of the sensitivity tests. The same variations that increase upward motion generally increase downward motion as sublimation and evaporation rates are increased by the presence of more condensate created in the anvil cloud. Stronger mesoscale descent helps to reduce rain rates by the time the rain reaches the surface so that these surface values are surprisingly insensitive to
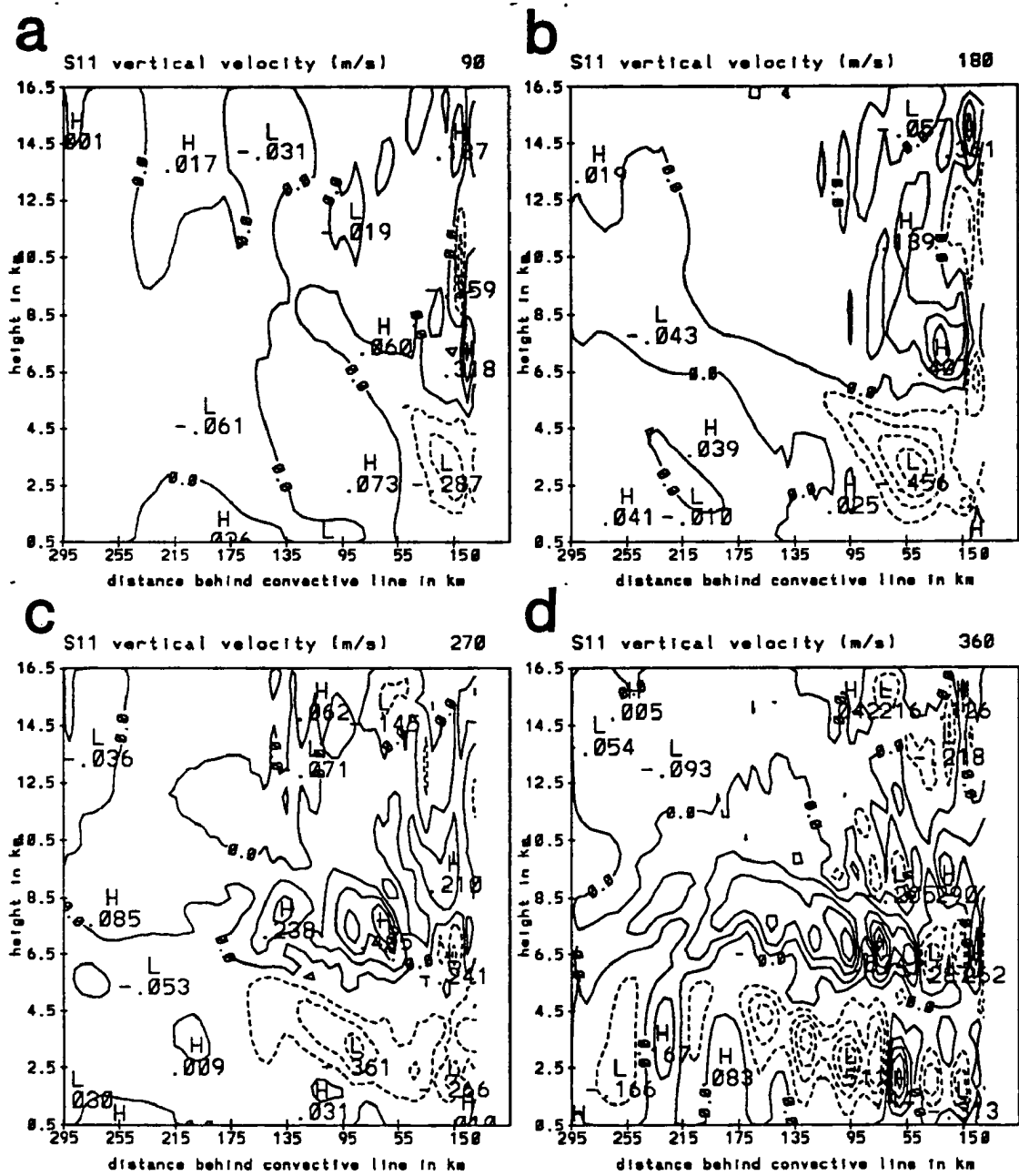
Figure 6.22: As in Fig. 5.24 except for S11, the simulation without pulsing.

the variations in initial conditions tested in this study. The most sensitive parameters in the model appear to be the initial stability, and the shape of the convective heating profile. Significant differences can occur in some results if an initially dry horizontally homogeneous domain is used. Although the homogeneous simulation did not produce results that would discount significant findings from this work, it did result in more powerful circulations. As discussed in the humidity section above, it seems a more reasonable initialization approach is the one used in the control run of this study. Finally, the pulsing of convective heating and hydrometeors into the domain significantly changes the intensity of features within the stratiform region from that of a simulation where heat and hydrometeors enter the domain at a constant rate. Circulations are much weaker when constant values are used, but qualitatively most features are similar. Pulsing is supported by observations and other larger-scale modeling work.

From these sensitivity tests it can also be concluded that the environmental stability plays a strong role on the behavior of the flows within stratiform regions of squall line systems. Mesoscale ascent and descent are significantly stronger in regions of steeper lapse rates. The behavior of a squall line system may therefore be dependent on larger scale weather systems that influence the temperatures in middle and upper levels of the atmosphere. Three-dimensional variations in rainfall and the behavior of circulations may also be linked to variations in stability. Rainfall in the stratiform region is significantly dependent upon hydrometeor advection from the convective line. It was shown in Chapter 5 that this advection was necessary to explain the broad region of substantial rainfall in the stratiform region. Sensitivity tests in this chapter show that surface rainfall increases or decreases strongly if hydrometeor advection likewise varies. A positive feedback increases the sensitivity.

Chapter 7

MODEL SENSITIVITY TO INTERNAL PARAMETERS

The previous chapters showed that the two-dimensional numerical model, initialized with appropriate conditions, was able to reasonably simulate many aspects of the stratiform region of the 11 June squall line. Varying the initial stability, moisture and winds led to some changes in the fields, but the stratiform region circulation remained qualitatively unchanged. The purpose of this chapter is to investigate the sensitivity of the model to certain internal parameters that are rather hard-wired and independent of environmental conditions associated with the 11 June case. In particular, model sensitivity will be discussed with respect to domain size, assumptions on ice crystal activation scheme, raindrop size distribution, snowflake slope intercept values, diffusion parameters, time step and mesh size.

7.1 Domain size

Because the model uses open radiative boundary conditions, problems due to a small domain are diminished, and simulations with both reduced and expanded domains change rather little from CTL. In simulation I1, the domain is reduced to 200 km. (Several of the sensitivity tests to be discussed later in this chapter are run with a smaller domain version of the model to reduce computation costs and will be compared with I1.) Changes in the reduced domain simulation are insignificant until late in the simulation. Rain rates in I1 (Fig. 7.1) look generally similar to those in CTL (Fig. 5.3). Through 270 minutes (Figs. 7.1a, b, c), changes in the rain rates from CTL are less than 5%. At 360 minutes (Fig. 7.1d), however, more substantial changes occur, especially near the rear boundary. Peak rain rates decrease by nearly 20% in this region. The total rainfall reaching the
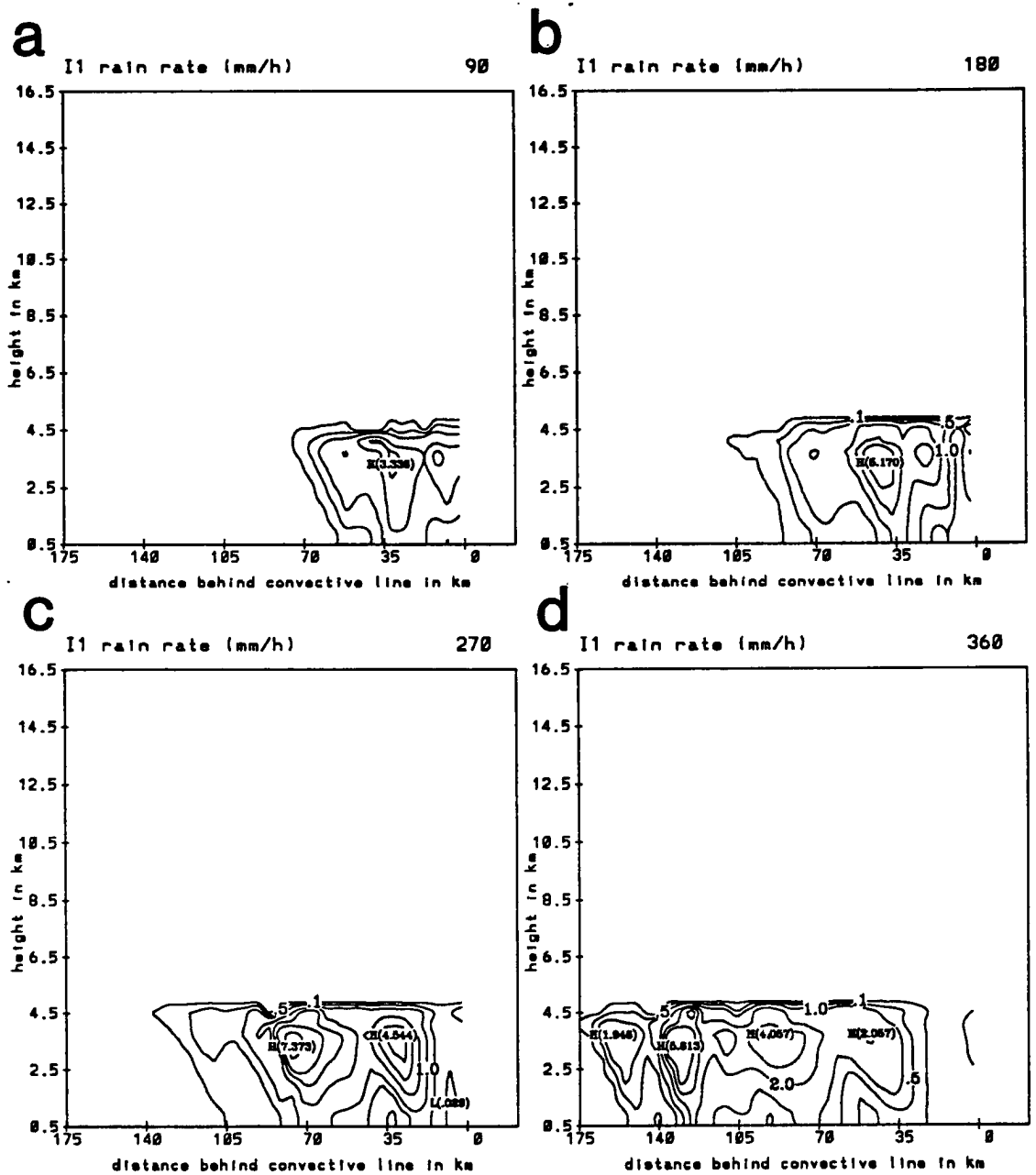
Figure 7.1: As in Fig. 5.19 except for I1, the simulation with reduced horizontal domain.

surface over the entire simulation also decreases by 12% from the similar portion of the CTL domain, with most of the change occurring after 270 minutes (Table 7.1).

Table 7.1: Simplified integrated water budget of the CTL model simulation compared with simulations changing internal model parameters. I1 is a smaller, 200 km domain version of the model. The appropriate 200 km portion of CTL has also been shown for comparison purposes (CTL′). I2 is an expanded 400 km domain version of the model. I3 investigates sensitivity to the ice activation scheme, I4 the raindrop size distribution, I5 the snowflake slope intercept value, and I6 a reduced 3km horizontal mesh. Values are as in Table 5.3. Percentage changes are taken from appropriate control runs. For I1, the appropriate control is CTL′. For runs I3 and I4, the control is I1. For I2 and I5 it is CTL. For I6, it is C2′.

Run	Advected mass	In Situ mass	Mass Sink	Rain sink
CTL	1692.06	1246.98	2285.17	511.98
CTL′	1692.06	1143.19	2092.52	510.37
C2′	1475.27	427.03	1420.15	300.42
I1	1703.44 (+1%)	1069.52 (-6%)	2088.79 (-0%)	448.79 (-12%)
I2	1687.45 (-0%)	1225.43 (-2%)	2218.21 (-3%)	537.26 (+5%)
I3	1676.64 (-7%)	962.90 (-10%)	1984.90 (-5%)	441.20 (-2%)
I4	1727.39 (+1%)	1118.45 (+5%)	2452.32 (+17%)	468.14 (+4%)
I5	1687.21 (-0%)	1164.79 (-7%)	2211.33 (-3%)	504.89 (-1%)
I6	1479.39 (+0%)	477.43 (+12%)	1512.09 (+6%)	256.27 (-15%)

Vertical motions are enhanced slightly in the smaller domain, but peak values generally change by less than 5% (Fig. 7.2). Even though peak ascent is increased slightly in I1, the total in situ production of condensate decreases in the domain (Table 7.1), as the updrafts occupy slightly smaller areas, with somewhat stronger subsidence between the regions of ascent at later times than was present in CTL. The water sink term in the integrated water budget is basically unchanged. Overall, the reduction of domain size by 33% has only minor effects, and does not appear to adversely affect results, especially during the first 4-5 hours of the 7 hour simulation.

The model domain was expanded to 400 km in simulation I2. Again, changes from CTL are relatively small (see Table 7.1). At early times the boundaries have little impact on features within the domain. After 270 minutes, peak vertical motions change slightly, generally under 10%. Only at the end of the simulation near the rear boundary of the domain do vertical motions differ in I2 from CTL by more than 10%. At late times in
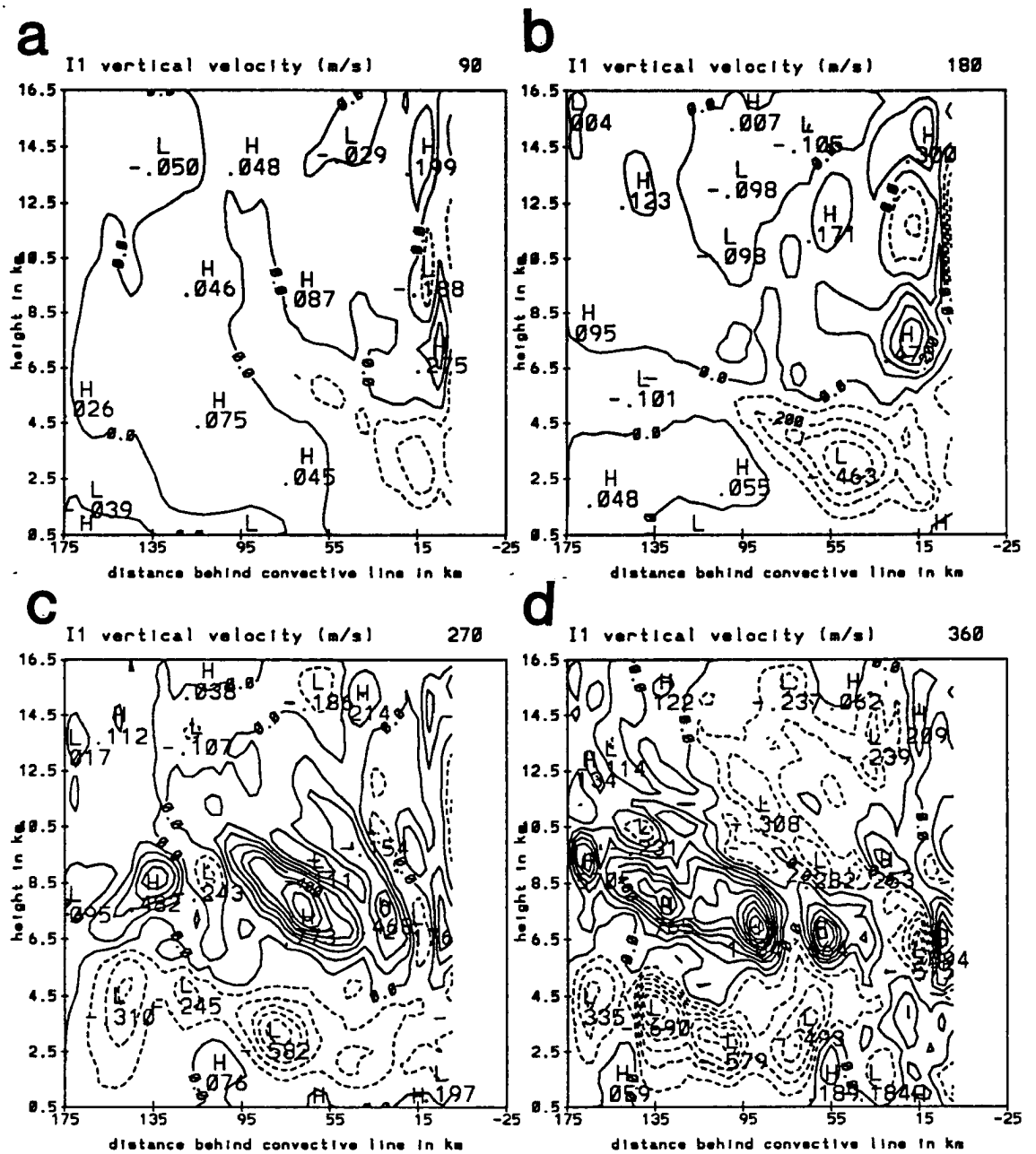
Figure 7.2: As in Fig. 5.24 except for I1, the simulation with reduced horizontal domain.

the simulation, the larger domain does not experience as strong vertical motion near the rear boundary as the smaller domains do. It appears that vertical motions in the smaller domain simulations may be artificially enhanced after many hours by the effects of the rear boundary. Because the changes are only significant in a small region at this late time, model results presented with the 300 km domain can be assumed to not have been adversely affected by the size of the domain.

7.2 Ice activation

As in the earlier kinematic model of Rutledge and Hobbs (1983; 1984), ice activation and indirectly, deposition, is assumed to follow the Fletcher (1962) formulation which implies that the number of ice nuclei activated in regions of ice supersaturation is dependent only upon the temperature of the air. As in these works, and the work of Rutledge (1986) and Rutledge and Houze (1987), an upper bound is prescribed on the number of ice nuclei that can be activated in a given volume. This is necessary since abnormally high numbers are predicted in the very cold upper parts of the anvil cloud. The Fletcher scheme has often been questioned for its lack of dependence on moisture content. Some studies have determined that the Fletcher scheme underestimates the number of ice nuclei activated at relatively warm temperatures ($\geq$ -25 C) in regions of high ice supersaturation (Myers et al., 1992). Myers et al. (1992) propose a new ice nucleation scheme where the number of ice crystals activated is simply a function of humidity. That study found that in simulations of intense convection, the new scheme improved results. One simulation was done with the 2D model in this study to investigate the effect of changes in the ice nucleation scheme. Because the Myers et al. scheme is designed primarily for relatively warm conditions, in this sensitivity test (I3), it was only applied in regions of the anvil warmer than -25 C. This particular sensitivity test was done with a 200 km domain version of the model.

With the relatively weak dynamics present in the stratiform region, the simulation using the Myers et al. formulation at warm temperatures is almost exactly the same as the smaller domain version of the control run (I1). It can be seen in the integrated water

budget (Table 7.1) that the values from I3 are within 10 % of those from I1, which is the appropriate control run for this simulation. The amount of rain reaching the surface is reduced by only 2%. This indicates that for these simulations of the stratiform region only, any problems with the Fletcher formulation might be insignificant. Large amounts of ice are present in the domain at temperatures colder than -25 C, having advected from the upper regions of the convective line. At these cold temperatures there is little evidence of a more realistic scheme than that of Fletcher. Problems at warm temperatures do not appear to play a role in the stratiform region.

7.3 Raindrop size distribution

A simulation (I4) was done in which the gamma distribution for raindrop size is substituted for the Marshall-Palmer distribution. Willis (1984) showed that the gamma distribution may reduce errors in estimating the evaporation of rain at low surface rainfall rates, typical of those experienced in the stratiform region. The equations describing this distribution are found in Appendix A. In this particular simulation, N_{0R} is not a constant as in CTL, but instead must be calculated at every point as a function of α and q_R. Values of N_{0R} and λ_R are often significantly different from those in the Marshall-Palmer distribution.

Peak rain rates with the gamma distribution are increased significantly just below the melting level (Fig. 7.3), with peak values generally 10-50% greater than in I1 at all times. Rain rates drop off somewhat more sharply toward the surface due to increased evaporation, but the integrated rainfall total at the surface ends up being slightly larger, 4%, than in I1. The location of surface rain does not differ significantly from the control runs, and the heaviest surface precipitation also generally falls in the same areas as in CTL and I1. Rickenbach (1990) also found using a kinematic model that the choice of either a gamma raindrop distribution or a Marshall-Palmer distribution had only minor impact on the surface rainfall, and no effect on the location of rainfall features. He also found that the gamma distribution resulted in a slight increase in surface rainfall.

The gamma size distribution increases evaporation significantly, especially during the first 180 minutes when evaporative cooling rates are as much as 50% greater than in I1 in
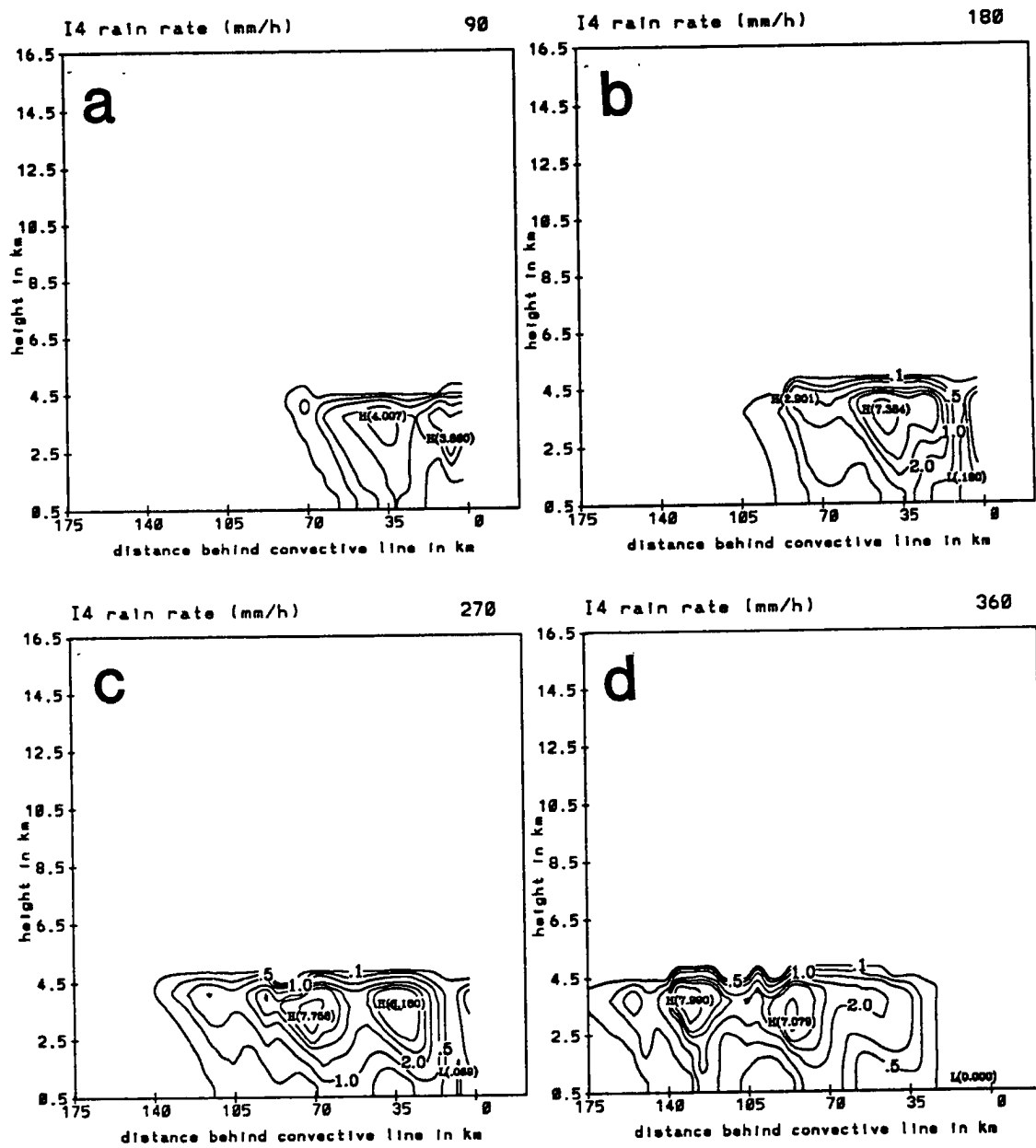
Figure 7.3: As in Fig. 5.19 except for I4, the simulation with gamma raindrop size distribution.

the region of heaviest rain. This enhanced cooling results in a much stronger downdraft at early times, with peak values nearly 10 cm s^{-1} larger than in CTL through 180 minutes (Fig. 7.4a, b). After this time, both the evaporative cooling and downdraft strength are in closer agreement, although the gamma distribution is still associated with about 10% more evaporation and descent in general. The stronger downdraft results in enhanced midlevel convergence, strengthening both the mesoscale ascent and horizontal circulations slightly. The peak ascent at 180 minutes (Fig. 7.4b) in I4 is roughly 10% greater than that in I1, but ascent after this time is similar to that of I1. The total in situ production of condensate over the full 405 minutes of simulation only increases by 5% (Table 7.1). The amount of water lost through evaporation and sublimation increases by 17%. The gamma distribution generally does not result in a change in the location or orientation of vertical motion features, but simply affects the magnitudes of the features.

Horizontal circulations also increase by roughly 5-10%, but the perturbation jets remain in the same locations with the same slopes. Qualitatively the use of a different raindrop size distribution does not change the model results. Increases in the strength of the updraft and downdraft are noticeable but not significant. As in many of the sensitivity tests, the increased ascent and production of condensate is opposed by the increased descent and evaporation so that rainfall at the surface is relatively unchanged. This result implies that a gamma distribution may not be a better representation of the raindrop sizes in the stratiform region than the Marshall-Palmer distribution. The increased strength of the downdraft, in fact, results in less agreement with observations, so that the Marshall-Palmer distribution may be the better size distribution of the two. The most important result of this sensitivity test is that the only changes in the circulations are in magnitude. The location and orientation of the fields of hydrometeors, microphysical processes and circulations are unaffected by a change in size distribution.

7.4 Snowflake slope intercept

To test the sensitivity of the model to certain hard-wired parameters relating to the size distributions of hydrometeors, a simulation was run (I5) in which the size of the
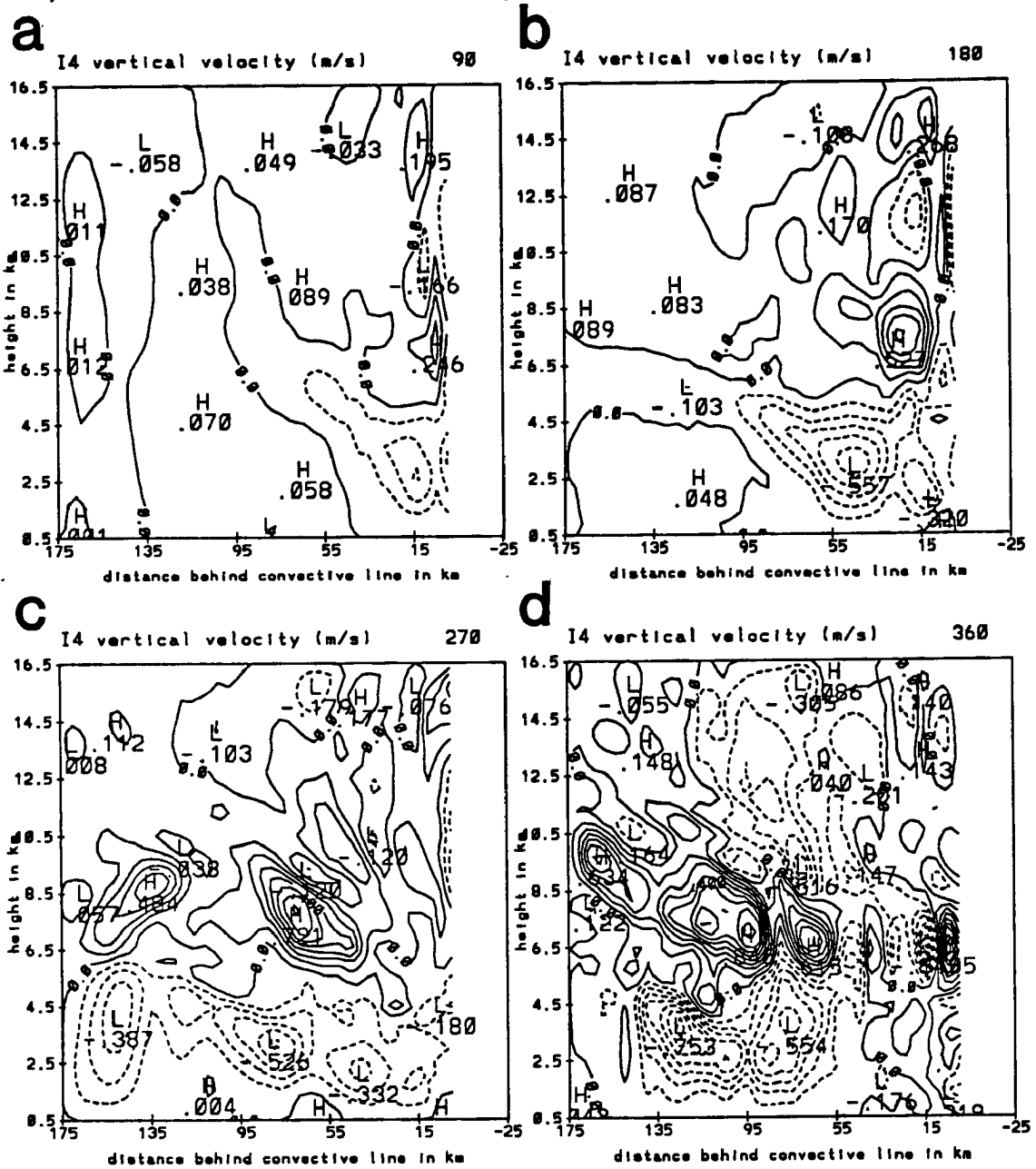
Figure 7.4: As in Fig. 5.24 except for I4, the simulation with gamma raindrop size distribution.

snowflakes was changed by assuming a different value for the slope intercept. Snow is the dominant ice species in the model simulations, and it is believed that changes due to variations in the snow parameter are an upper bound on the model sensitivity to size distribution parameters. In Rutledge and Hobbs (1983), simulations were done using two values for N_{0S}, with one being twice the value in this study, and the other three times the value. In this sensitivity test, N_{0S} is doubled, representing smaller snowflakes that might be present in an environment of minimal lifting.

The snow mixing ratio field changes very little in this simulation, with peak values reduced by only a few percent. Similarly rain rates are nearly unchanged. Circulations in I5 are also not significantly changed, with the biggest differences occurring in the vertical motion field where peak magnitudes are reduced by 5-10% at later times. This can be seen in the slight decrease in integrated in situ condensate production (Table 7.1). The horizontal perturbations are basically unaffected by the different snowflake slope intercept value. Table 7.1 shows that the in situ production of condensate, water sink, and surface rainfall are within a few percent of CTL. The model is rather insensitive to changes in the snow slope intercept parameter.

7.5 Diffusion parameters

Several simulations were run in which constants in the turbulence parameterization were changed. The background values of eddy vertical diffusivity and viscosity were varied four times from half of the 0.6 control value to ten times that value. This covered the range of values used in other studies with the same turbulence parameterization, from the small mesh model of Szeto et al. (1988a) to the larger mesh model used by Orlanski and Ross (1977).

The simulations show the model to be insensitive to the 50% reduction in the value of K_{z0}, and even with the highest value of K_{z0}, the fields are not appreciably changed, although as would be expected, extrema in the circulations are reduced. The constant, c, which determines the magnitude of the diffusivity and viscosity in absolutely unstable regions was varied from 80% smaller than the CTL value of 0.5 to ten times larger.

Because absolutely unstable conditions are isolated within the domain, and only occur at certain times in the vicinity of the most intense heating or vertical motions, variations in the parameter have almost no effect on the model results. Finally, the parameter, D, which relates the horizontal turbulence terms to the vertical values was reduced by 60%. Again, changes in the simulations are minor. Changes in the turbulence parameterization constants produced more significant changes in several test simulations (not shown) that were done with a much smaller mesh size to study the initiation of convective elements. In the test simulations, the largest values of diffusivity and viscosity produced the most realistic features. In the stratiform region, the turbulent terms are small enough that sensitivity to the parameterization is not significant.

7.6 Time step and mesh size

The time step in one simulation was reduced to 10 seconds from the standard 15. No changes resulted. This indicates that 15 seconds is a sufficiently small time interval to accurately integrate the model.

More significant changes can be expected by varying the mesh size of a model. As stated earlier, the horizontal grid spacing in this model falls within a gap of sorts between the mesh sizes commonly used in modeling work. Mesoscale models that are used to study large MCSs and their impact on the immediate environment generally use a mesh of at least 10 km, if not 25 km. Cloud scale models generally restrict the mesh to 1 or 2 km at most. Resolution of convective elements may be difficult with the 5 km resolution in this model, although the results of Hemler et al. (1993) implied that 5 km is adequate to reproduce the convective portion of an MCS.

Many early simulations performed with this model used a 7 km resolution. In general, the changes between the 7 and 5 km mesh size were small. Qualitative agreement between the fields was excellent. More recently, a simulation was done (I6) using a 3 km mesh size without convective heating. Convective heating was ignored to simplify comparisons, since the prescribed heating profile would have had to be adjusted for the smaller mesh, and questions would arise as to whether the heating should simply occur at the same

number of grid points as in CTL, or over the same area as in CTL. An improvement in resolution of 40% between I6 and CTL produces small changes in the simulation. Because no convective heating was prescribed in I6 and the total domain size was around 200 km, the results must be compared with simulation C2' in Table 7.1. Circulations are increased slightly in I6 from C2'. In general, vertical motions (Fig. 7.5) are roughly 10% greater with the 3km horizontal resolution than with the 5 km resolution (Fig. 5.21). The total in situ production of condensate in the domain increases 12% (Table 7.1). The stronger downward motion increases the water mass lost by 6%. At the surface, rainfall rates are decreased by 15%. Although these changes with a smaller resolution are noticeable, they are still not overly significant, and all diagnosed features within the stratiform region remain qualitatively unchanged.

The results in this chapter imply that internal model parameters do not overly influence the simulations of the 11 June system. Although choice of raindrop size distribution and mesh size exert noticeable influences on some diagnosed fields, the general conclusions of the simulations remain unchanged. The model is insensitive to domain size, time step, ice activation scheme and the snowflake slope intercept value.
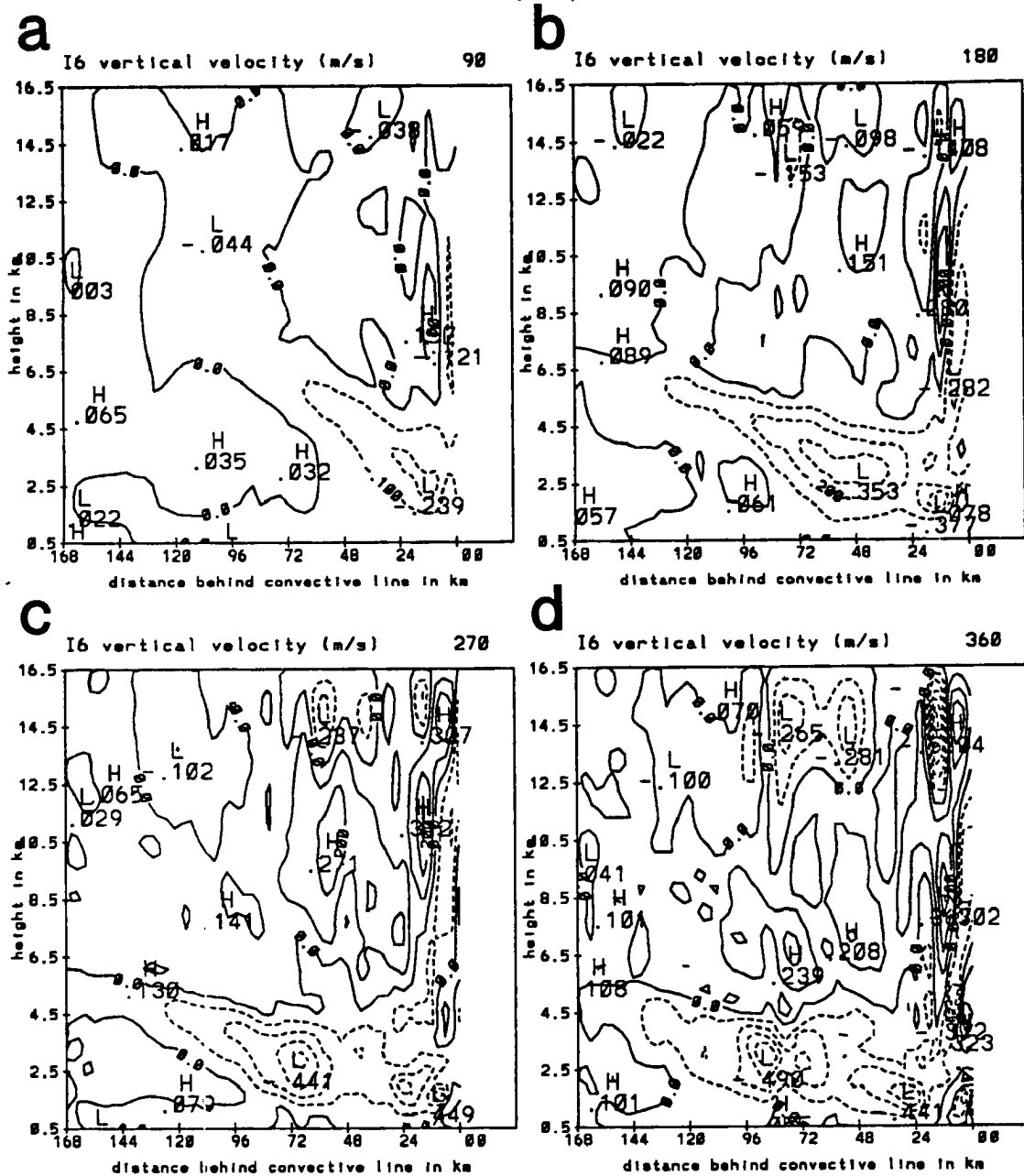
Figure 7.5: As in Fig. 5.24 except for I6, the simulation with increased horizontal resolution (3 km mesh).

Chapter 8

WAKE LOW SIMULATIONS

The previous chapters have investigated the role of microphysical processes and environmental cond tions in the development of circulations in the stratiform region of the 11 June squall lin e. One question, however, that is not adequately answered with the structure of the m odel used in those simulations is whether microphysical processes alone can force a downc raft as strong as several meters per second and induce an intense surface wake low like tha t observed in both the 3-4 June and 23-24 June PRE-STORM MCSs (e.g. Stumpf et al., 1991; Johnson and Bartels, 1992). It is unclear whether microphysical cooling can induce sufficient descent so that adiabatic warming exceeds the cooling and results in signific nt pressure falls at the surface.

The simulations of the 11 June system shown earlier failed to produce an intense surface wake low although a rather strong wake low did occur during this case. In other MCS cases like the 3-4 June system (Stumpf et al., 1991), much stronger wake lows with pressures several millibars lower than nearby regions (within 50 km) have been found where intense su bsidence as large as 6 m s^{-1} occurs near the back of the stratiform rain area. In this region, the rear-inflow jet descends suddenly toward the surface. In these cases in particul r, the question arises whether microphysical processes in the stratiform region can fully explain the intensity or behavior of these observed features.

In this chap er, simulations designed to answer the above question are discussed. The resolution of the model is increased, and the domain is shifted to look at only a portion of the stratiforn region where existing rear-to-front flow comes in contact with falling hydrometeors. The finer resolution should reduce underestimates in dynamics that are due to coarse resolution. These simulations may show whether microphysical processes

can produce enough downward motion and adiabatic warming to counter the microphysical cooling driving the downward motion. The initialization of the domain with an existing rear-inflow jet will answer some questions about possible inadequacies in the 11 June runs discussed in previous chapters, where ambient FTR flow exists at all levels, and is strong above 7-8 km.

8.1 Simulations with steady precipitation rates

Several simulations were done using a domain centered on the back edge of the snow field in the stratiform region. This section will discuss simulations in which snow mixing ratios in the anvil cloud were held constant over the length of the simulations. These simulations used a 2 km horizontal mesh and a 300 m vertical mesh, and were restricted to an 80 km wide region. The top of the model domain was 12.5 km, or just below the tropopause. The time step was decreased to 10 seconds in these simulations, and the model was integrated for 80 minutes. Only one of the simulations will be discussed in detail.

Initialization of these simulations is based on the Russell soundings shown in Stumpf et al. (1991) for the 4 June MCS at 00 and 0130 UTC. Some modifications are made based upon other soundings that occurred near the back of the stratiform rain regions of both the 11 June and 4 June system. The ambient wind is simplified by assuming no horizontal velocity except in the 2-7 km layer where RTF flow existed. This rear-inflow jet is assigned a peak magnitude of around 15 m s^{-1} at the melting level, around 4 km. This wind profile in effect assumes that the domain is moving with the same speed as the FTR flow at middle and high levels in the anvil cloud. As was shown earlier in Fig. 4.3, RTF flow did occur over a substantial depth near the rear of the stratiform region in the 11 June system. Similar deep RTF flow existed at the back of the 4 June system. The initial temperature and moisture profile of the domain is shown in Fig. 8.1. These fields are assumed to be horizontally homogeneous. The layer of RTF flow can be seen in the winds plotted at the right of the diagram. A low-level temperature inversion exists in the lowest 1 km. Relative humidities with respect to water fall from around 80% at the surface to
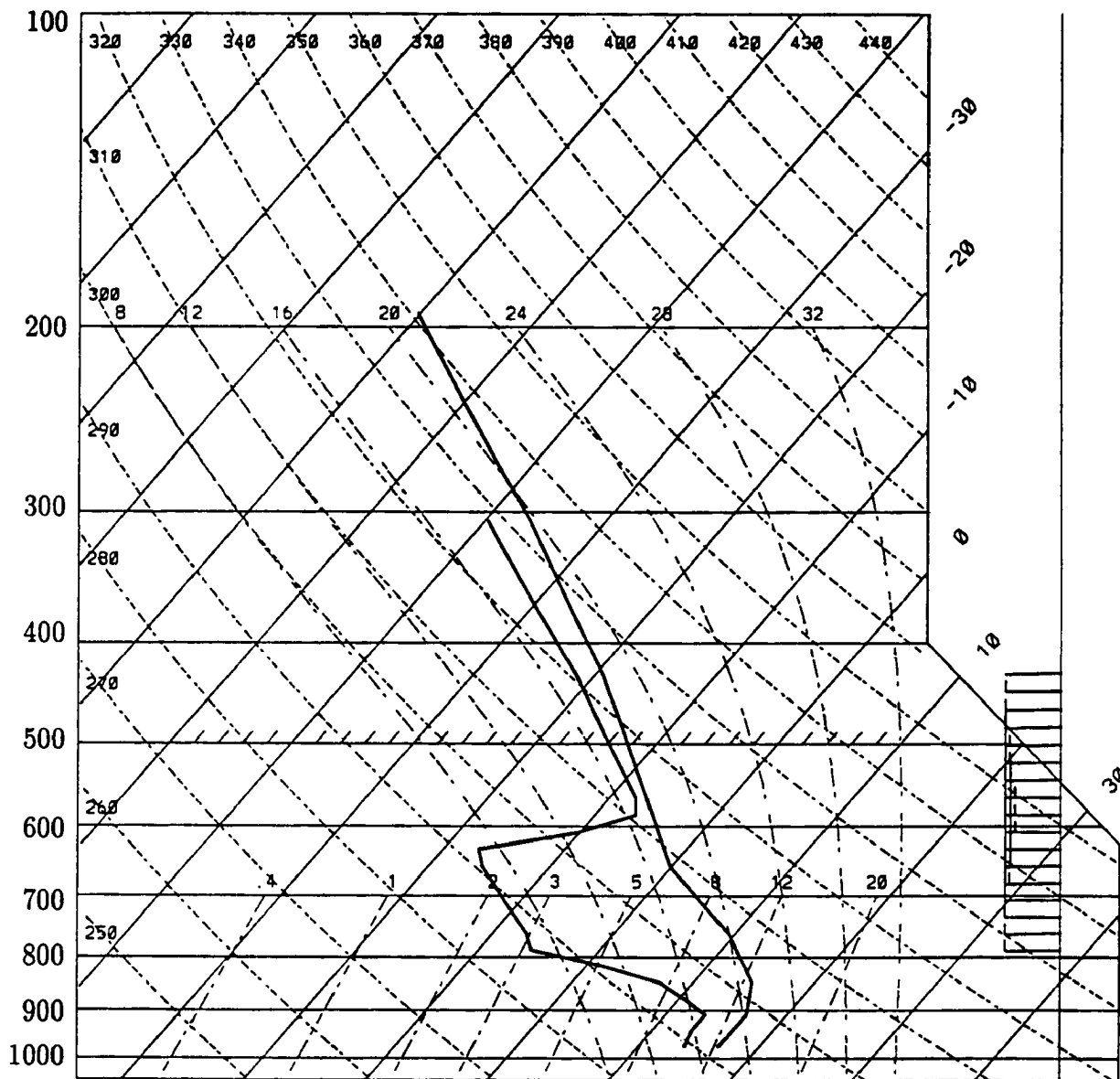
Figure 8.1: Initial thermodynamic diagram for SP, the specialized stratiform domain simulation. Relative winds are shown at the right.

30% in a dry layer that coincides with the lowest one half of the rear-inflow zone. Nearly water saturated conditions occur above 4 km. The lapse rates are nearly moist adiabatic from the melting level upwards, and rather unstable in the 2 km below the melting level.

Snow is the only ice hydrometeor assumed to be present at the time of initialization, and it occurs in the rightmost 70 km of the domain. The snow field is constant and prescribed at all times above about 6 km. The snow field at 60 minutes (Fig. 8.2) shows that peak mixing ratios were around 3.3 g kg^{-1} with a decrease to around 2.2 g kg^{-1} to the right of the maximum. The enhancement of the snow toward the rear of the stratiform region is to represent a case like the 3-4 June PRE-STORM MCS where reflectivities were enhanced at the back edge of the surface precipitation. In that case (Stumpf et al., 1991) the strongest surface wake low and mesoscale downdraft occurred over about a 10 km wide region around 01 UTC June 4.

The rain rates produced by the melting of this snow at 60 and 75 minutes are shown in Figure 8.3. The enhanced snowfall corresponds to a rain rate near the melting level that increases to 13 mm h^{-1} at 60 minutes (Fig. 8.3c) and over 30 mm h^{-1} at 75 minutes (Fig. 8.3d). Peak low-level reflectivities ($\approx$ 2 km) here are just over 40 dBZ, which is only slightly greater than observed values in portions of the 4 June system between 01 and 02 UTC (Stumpf et al., 1991). Rainfall reaches the surface after 30 minutes (Fig. 8.3a), but substantial rain does not occur until 60 minutes (Fig. 8.3c) when peak rates reach 8 mm h^{-1}. By 75 minutes, surface rainfall reaches 16 mm h^{-1} (Fig. 8.3d). Elsewhere in the area beneath the snow field, rainfall is much lighter. The heaviest surface rainfall occurs in the region from x=32-35 km.

The sublimation that occurs when the snow falls into the strongly subsaturated air, along with melting and the evaporation of rain produce a strong downdraft, which is most pronounced near the region of heaviest rainfall. Sublimational cooling rates (not shown) are as large as 7-8 °C h^{-1}, with peak evaporative cooling rates generally reaching 15-19 °C h^{-1}. Melting-induced cooling in the region of heaviest precipitation is as large as 5-6 °C h^{-1}, which is at the upper end of the values given in Leary and Houze (1979) for stratiform regions.
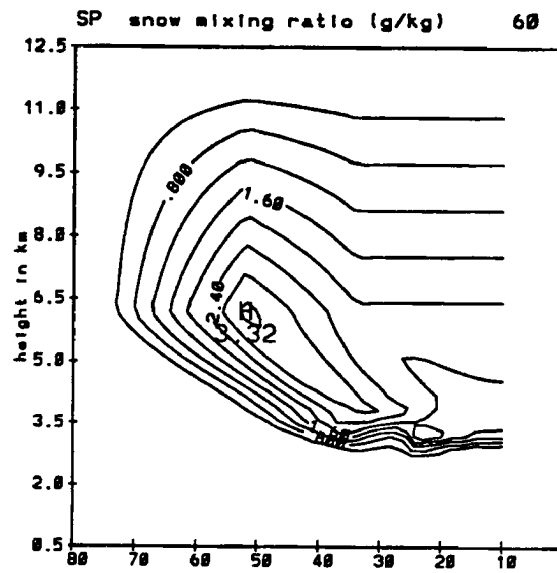
Figure 8.2: Snow mixing ratios in SP at 60 minutes. Contour interval is 0.4 g kg^{-1}.
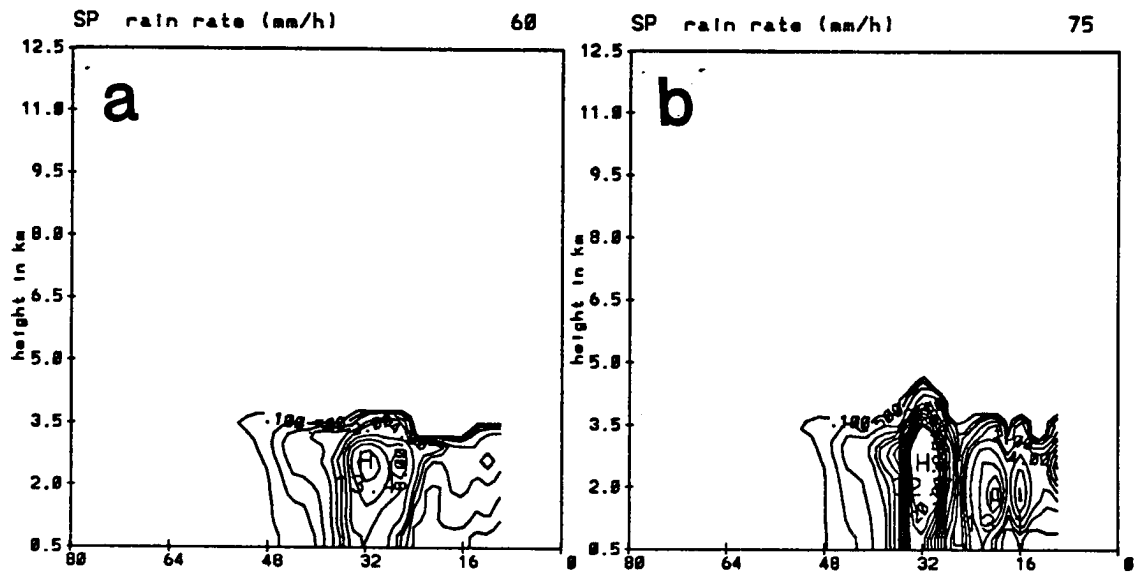
Figure 8.3: Rain rates (in mm h^{-1}) for SP at (a) 60 minutes and (b) 75 minutes. Contour intervals are as in Fig. 6.3, with contouring every 2 mm h^{-1} from 6 mm h^{-1} through 20 mm h^{-1}.

Downward motion intensifies rapidly and occurs in a well-defined band at 60 and 75 minutes (Fig. 8.4a, b). The maximum downdraft velocity is around 2 m s^{-1} at 60 minutes, and around 3.4 m s^{-1} at 75 minutes. The most intense descent occurs around the 2.5 or 3.0 km level very near the location of heaviest surface rainfall. Enhanced descent extends rearward from this region along an axis extending as high as 8 km. The level of peak descent agrees rather well with that found by Doppler radar in this case (Stumpf et al., 1991). The peak descent is not as strong as was observed, which could be due to insufficient microphysical cooling or inadequacies of a 2D model simulating 3D convergence. The latter seems more likely since the reflectivities and humidities in the domain are reasonably close to those observed. At 75 minutes, when the descent is strongest, 1 m s^{-1} subsidence extends to nearly the surface.

The strong downward motion and adiabatic warming partially oppose the intense cooling from sublimation, melting and evaporation. Potential temperature increases above the melting level in the region of subsidence where microphysical cooling is not pronounced (Fig. 8.5). Significant cooling generally occurs below this level, with some warming very near the surface in the region of strongest descent and heaviest rainfall. By 60 minutes (Fig. 8.5a) θ has fallen by over 6 K around the 2.7 km level in the region of heaviest rainfall. Warming of up to 1.2 K has occurred around the 1 km level below this strong cooling. Warming aloft is as large as 2.4 K in the same general region. At 75 minutes, the cool anomaly in the heaviest rainfall has remained around 6 K, while up to 7.5 K cooling has taken place downwind of this region. The level of peak cooling at around x=30 km has fallen, and this trend was persistent throughout the 80 minute simulation. Warming at the surface at this time increases to over 3 K in the area where subsidence was very strong close to the surface. Warming aloft at the top of the main downdraft reaches over 5 K at this time.

A sounding taken in this region of strong low-level warming at 75 minutes shows the changes that have taken place in 75 minutes (Fig. 8.6). Significant cooling has occurred in the 700-900 mb layer, so that the lapse rate has become nearly dry adiabatic there. Substantial warming occurs below 900 mb, with the other region of warming showing up
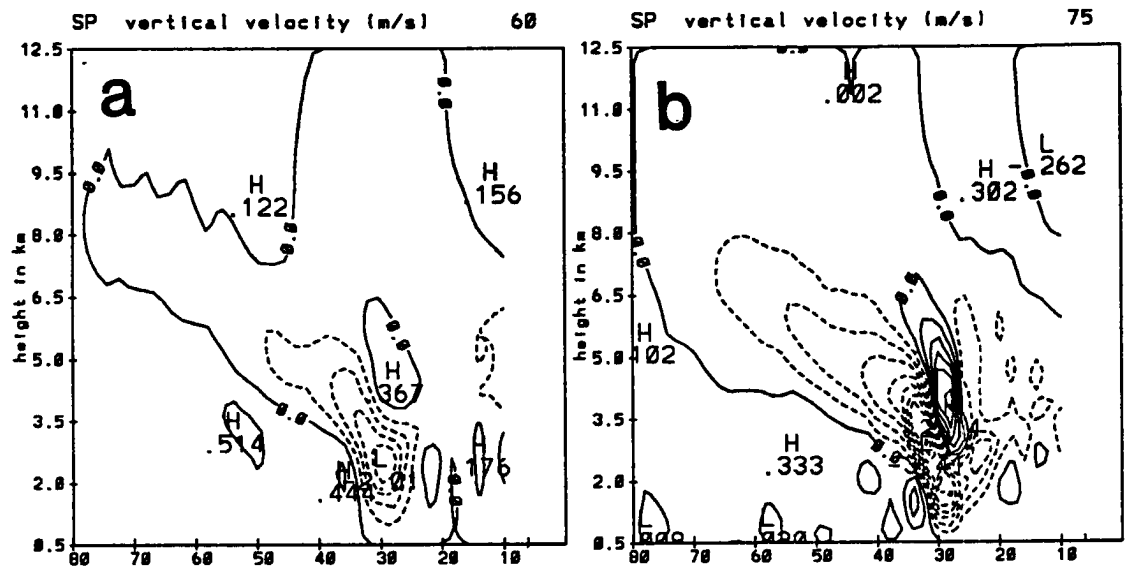
Figure 8.4: As in Fig. 8.3 except for vertical velocities, with contour interval of .5 ms^{-1}.
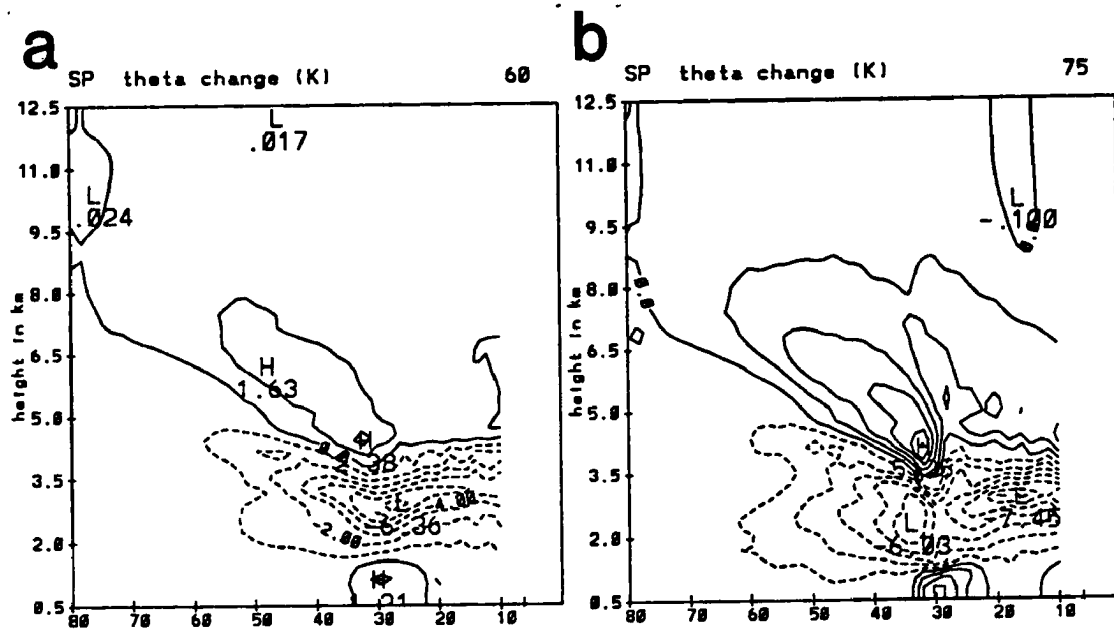
Figure 8.5: As in Fig. 8.3 except for potential temperature change in K, with contour interval of 1 K.
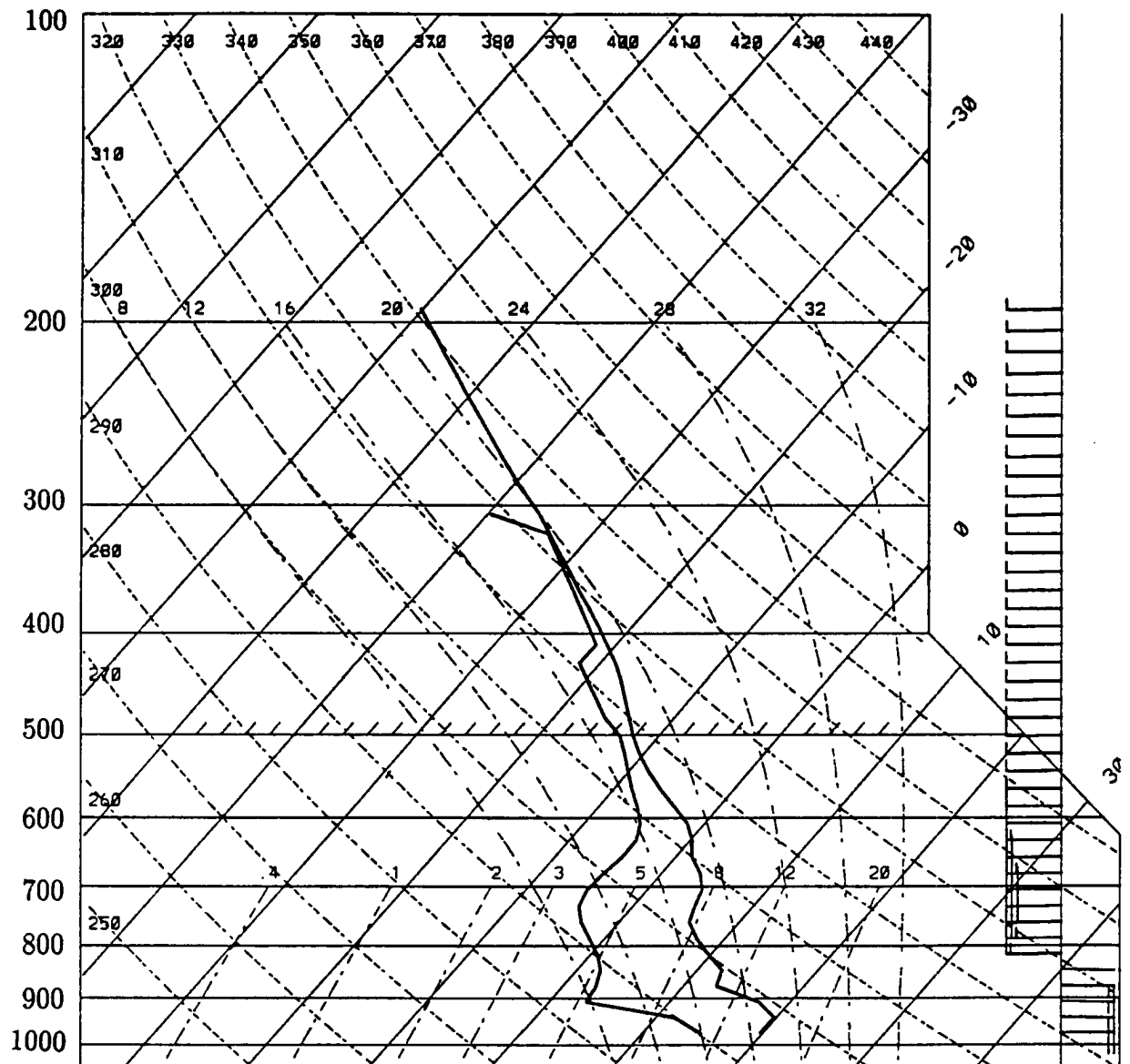
Figure 8.6: Thermodynamic diagram taken from region with strong low-level warming (x = 30 km) at 75 minutes in simulation SP.

around 600 mb. Drying has also taken place in the lowest 1-2 km, with moistening above this level.

The temperature changes that occur in this simulation are significant and induce substantial pressure variations in the domain (Fig. 8.7). The hydrostatic pressure deviation from the domain average at 60 minutes (Fig. 8.7a) shows a relatively weak low pressure area at midlevels in the region of heavy precipitation. At the surface, a weak pressure gradient exists with lower pressure behind the system. Highest pressures are just downwind of the heaviest surface rainfall. An extremely weak wake low is beginning to form at the surface around x=38, where pressures are lower than any other value within a 15 km wide region to either side. At 75 minutes (Fig. 8.7b), perturbation pressure features strengthen significantly. The midlevel mesolow has lowered to around 3 km with pressures nearly 2.5 mb lower than those 30 km away in both directions. At the surface relatively lower pressure continues to be found to the rear of the precipitation region with higher pressures in the rain region. A small-scale pronounced lowering in the pressures occurs around x=32, or very near the area experiencing heaviest rainfall, strongest descent and greatest warming. The perturbation from the domain average is nearly 1 mb at this point, and the pressures are lower than any other surface value except at the leftmost boundary of the domain. This wake low has pressures a little more than 1 mb lower than those to its rear, and nearly 2 mb lower than pressures in front of it. An intense pressure gradient exists ahead of the low with a change of nearly 1.5 mb over a distance of 5 km. The wake low and the pressure gradient are much more intense than those found in the earlier simulations of the 11 June system. However, they are not as strong or as widespread as observed on 4 June. Stumpf et al. (1991) found a pressure gradient as large as 2 mb over a 5 km distance around 01 UTC 4 June, with a 1 mb $(10 \text{ km})^{-1}$ gradient occurring over a rather wide area (50-70 km). Stumpf et al. determined that 90% of the pressure changes were hydrostatically-induced. The lowest pressure in the wake low occurred just inside the tight reflectivity gradient, which is a little in front of that observed. Stumpf et al. (1991) found that the lowest pressure occurred just behind the tight reflectivity gradient, with the tightest gradients of reflectivity and pressure coinciding.
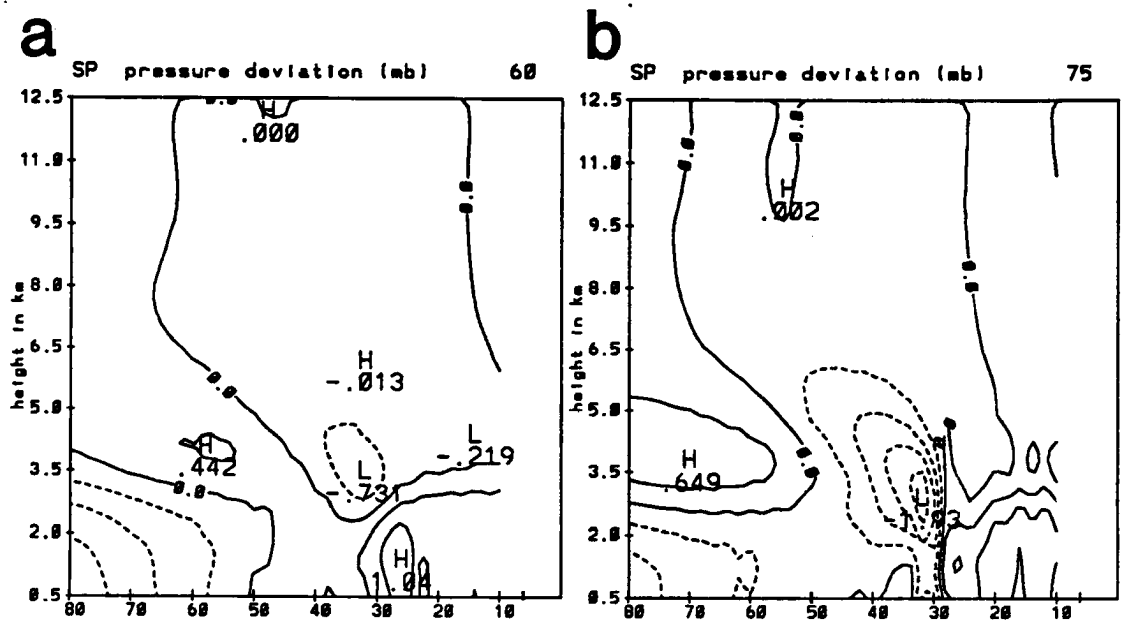
Figure 8.7: Hydrostatically calculated pressure deviation (in mb) from domain average in SP at (a) 60 and (b) 75 minutes, with contour interval of .4 mb.

The wake low in this simulation does produce 75% of the intense gradient observed, with the maximum intensity not far from the back edge of the surface rainfall. In these respects, the low appears to be simulated rather well. However, the large gradient over a substantial distance found by Stumpf et al. (1991) is not simulated, and the pressures behind the wake low are not much higher than in the wake low. Some of these differences may be due to restraints imposed by the small domain and the initially homogeneous wind field. Many simulations like this one were run initialized with different soundings, and using different amounts of snow aloft. These simulations were unable to produce a wake low of stronger intensity or broader scale. In general, stronger descent, as large as 5 m s^{-1} in some simulations, required heavier snowfall aloft and drier conditions near the melting level, which resulted in increased microphysical cooling that easily opposed adiabatic warming so that pressure falls at the surface were not increased. To reduce microphysical cooling required less snow, or moister conditions that weakened the downdraft and the adiabatic warming. A fragile balance existed between the cooling necessary to drive strong subsidence and the adiabatic warming produced by the descent. The failure to simulate the broad pressure gradient over a 50 km distance observed in the 4 June case may be due to the limited domain initialized homogeneously. The simulation is designed primarily to study the "blocking" effect that sometimes occurs near an enhanced precipitation region at the rear of the stratiform region. Details about differences in the environmental conditions behind the system or ahead of the enhanced band are neglected and these may extend the influence of the mesolow over a larger distance. A deeper cold pool closer to the convective line, along with different lapse rates aloft may lead to pressure increases ahead of the wake low that approach the 5-6 mb observed over a 50-70 km region.

Strong perturbation horizontal flows develop in the simulation (Fig. 8.8a). The existing RTF flow is intensified in a band that extends from high levels at the rear of the domain to around 3 km in the region of heaviest precipitation. Perturbations reach nearly 8 m s^{-1} at 60 minutes (Fig. 8.8b) and 18 m s^{-1} at 75 minutes (Fig. 8.8b). The intense microphysical cooling that occurs when rear-inflow of dry air meets significant amounts of snow in the stratiform anvil cloud appears able to force RTF flow to develop at higher
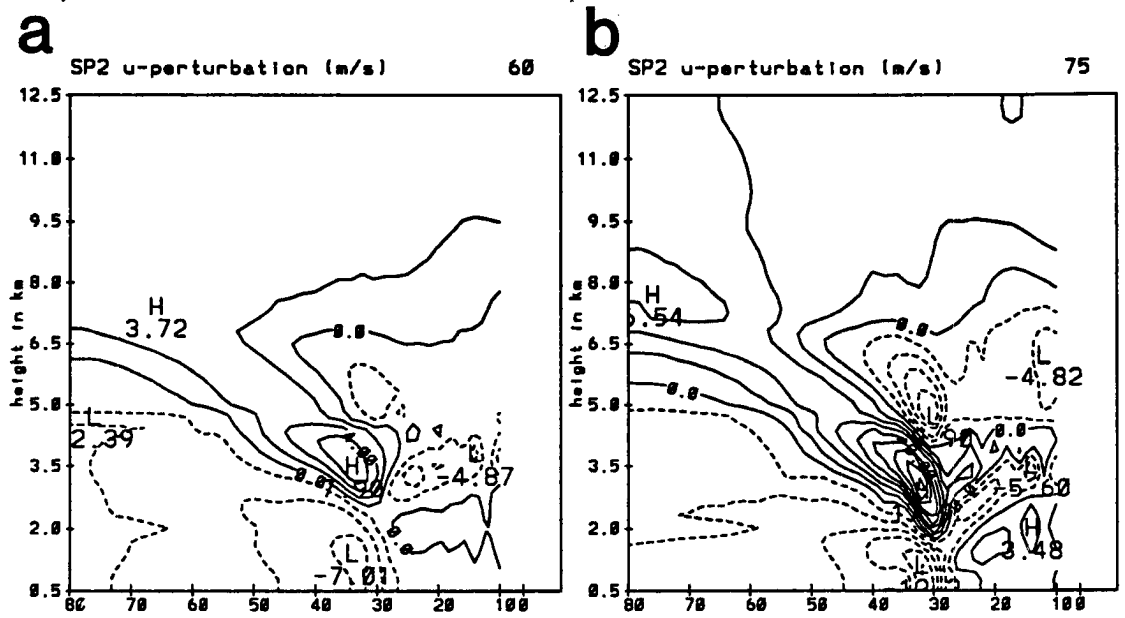
Figure 8.8: As in Fig. 8.3 except for u-perturbation velocities (in m s^{-1}) for SP with contour interval of 2 m s^{-1}.

levels than existed initially. Strong convergence is induced just above the melting layer as air rushes into the region of heavy precipitation to compensate for the strong subsidence. Near the surface, FTR flow strengthens to 10 m s^{-1} behind the rain region, helping to spread cool air rearward from the system. The rapid intensification of the jet at 75 minutes and the sudden change from RTF to FTR flow create a wind field similar to the "blocked" rear-inflow jet that occurred on the 4 June case. This can better be seen in the total wind field (Fig. 8.9). Since the domain was initialized relative to the general motion in the anvil cloud, some of the positive perturbation could be subtracted out in this figure to represent storm-relative winds. If this were done, at 75 minutes (Fig. 8.9b), the rear-inflow jet would indeed stop at the region of heaviest rainfall.

Although this simulation produced a much stronger wake low at the surface than in the 11 June simulations shown earlier by allowing hydrometeors to advect into drier air in an environment whose stability was already altered by the stratiform region, the wake low still was not as intense, and was far more limited in its extent than observed on 4 June. Other simulations performed using different lapse rates, humidity profiles and hydrometeor contents did not produce a more intense wake low. Descent in the simulations was as large as 4-5 m s^{-1}, which is close to the observed values of 5-6 m s^{-1} in the 4 June case. Evaporative cooling was strong enough to almost completely oppose adiabatic warming in the downdraft. When hydrometeor contents were reduced, which lowered the amount of evaporative cooling, the downdraft and adiabatic warming weakened accordingly. The model was unable to produce strong descent and warming from the effects of light precipitation. A three-dimensional model would better simulate the full convergence and probably increase the intensity of the downdraft which might increase the intensity of the wake low toward observed values. As will be shown below, however, the underestimate of wake low intensity may be the result of the prescribed constant precipitation intensity and not the result of a model deficiency.

8.2 Simulations with a collapsing precipitation core

Simulations were also done with the 2km horizontal mesh version of the model allowing precipitation rates to decreases significantly over time. These simulations can be
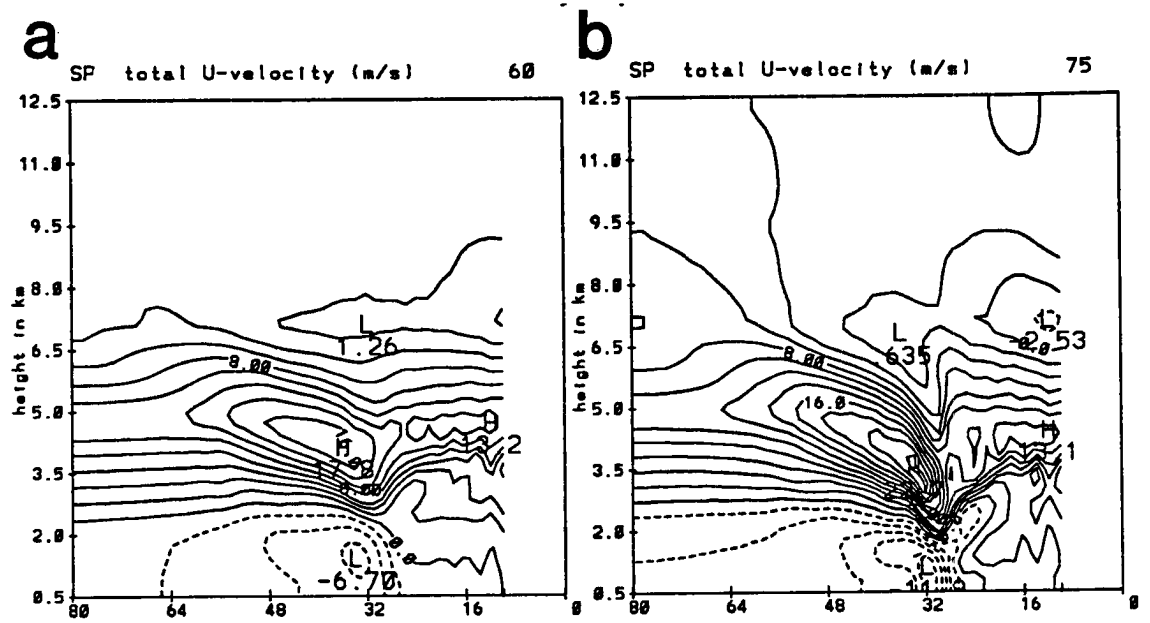
Figure 8.9: As in Fig. 8.3 except for total u component of the wind (in m s^{-1}) for SP with contour interval of 2 m s^{-1}.

thought of as representing systems where collapsing precipitation cores exist within the stratiform region. The domain has been expanded to 128 km in these simulations, and the model is integrated for 95 minutes. These simulations generally produced similar features to SP, but with more intense warming, and a more pronounced wake low that better agreed with observations. One simulation, SP1, will be discussed in detail below.

The initial conditions for SP1 are similar to those in SP, with only a few minor changes. The low-level inversion is slightly deeper, and the lapse rate is assumed to be more unstable directly above the inversion (Fig. 8.10). The dry layer is also roughly 1 km deeper, with dry conditions extending upward to above 550 mb. The wind field is similar to that in SP, but with the RTF jet shifted approximately 500 m lower.

Snow again is the only hydrometeor present initially in the simulation, and the mixing ratios at 15 minutes are shown in Fig. 8.11. Snow contents are largest again near the rear of the cloud, with peak mixing ratios exceeding 4 g kg^{-1}. These values produce reflectivity fields and rainfall fields at early times that are in good agreement with observations. Snow contents are prescribed to decrease starting at 20 minutes to only 20% of their initial magnitude by 40 minutes. The snow mixing ratios are then maintained at this smaller level throughout the rest of the simulation.

The evolution of the snow field causes the heaviest rainfall to occur at around 45 minutes near x = 82 km (Fig. 8.12a). Peak surface rain rates are around 7 mm h^{-1}, or rather similar to those at 60 minutes in SP, and generally typical of heavier observed stratiform region rainfall. By 60 minutes (Fig. 8.12b) rain rates decrease significantly with peak values below 3 mm h^{-1}. Rainfall continues to decrease through 75 minutes when all values are less than 1 mm h^{-1} (Fig. 8.12c).

The initially heavy precipitation induces a strong downdraft that is most intense around 60 minutes (Fig. 8.13a). Peak descent occurs just in front of the heaviest rainfall and is around 2 m s^{-1}, or 40% less than the peak descent in SP which occurred at 75 minutes. The downdraft weakens slightly in SP1 at 75 minutes (Fig. 8.13b) with peak descent of 1.6 m s^{-1} at that time.

The strong downward motion and adiabatic warming are again opposed significantly by evaporative cooling, but low-level warming is increased in SP1 from that in SP (Fig.

Figure 8.10: As in Fig. 8.1, except for SP1, the simulation in which precipitation rates decrease with time.

Figure 8.11: As in Fig. 8.2, except at 15 minutes for SP1, the simulation in which precipitation rates decrease with time.

Figure 8.12: As in Fig. 8.3, except at (a) 45 minutes, (b) 60 minutes and (c) 75 minutes for SP1, the simulation in which precipitation rates decrease with time.
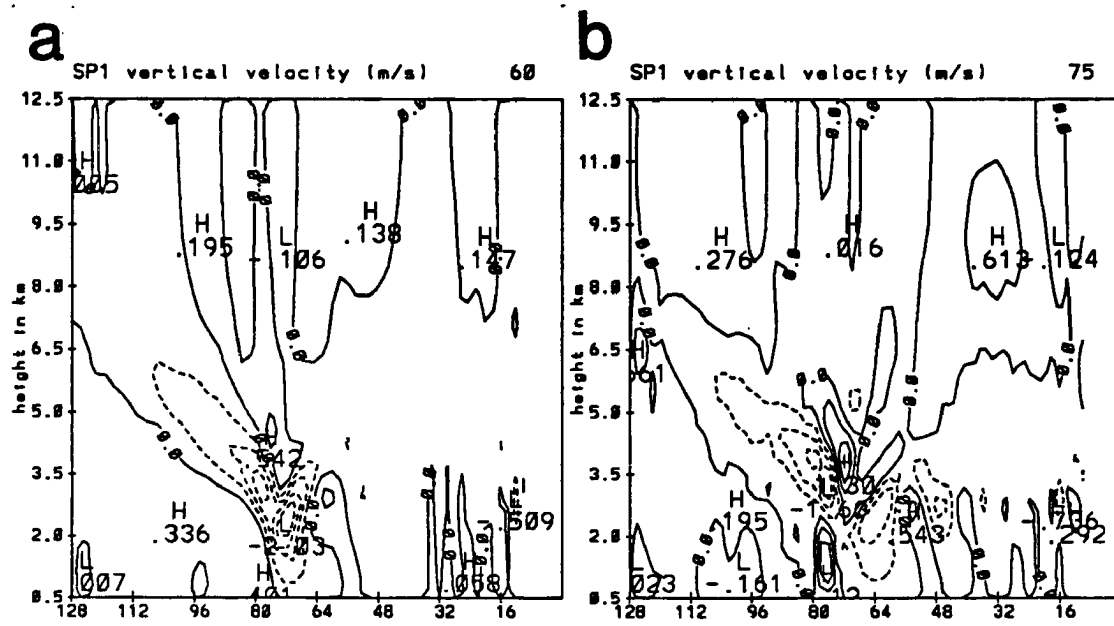
Figure 8.13: As in Fig. 8.4, except for SP1, the simulation in which precipitation rates decrease with time.

8.14). Peak cooling near the melting level is similar to that in SP1, even though rainfall rates are less, because of the changes in the initial temperature and humidity profiles. Warming above the melting level is not as strong in SP1 as in SP for similar reasons. Low-level warming in SP1 is approximately 3 K greater at 60 minutes (Fig. 8.14a) than in SP, and 2 K greater at 75 minutes (Fig. 8.14b).

The warming that occurs results in a hydrostatically-induced wake low that is significantly deeper relative to nearby regions than in SP (Fig. 8.15). At 60 minutes (Fig. 8.15a) the relative pressure minimum first develops at $x = 78$ km with a perturbation of 1.0 mb. A pressure gradient of roughly 1.3 mb over a 5 km distance exists immediately ahead of the low. By 75 minutes, the wake low has rapidly intensified with pressures having fallen 1.5 mb in 15 minutes. (The perturbations shown in the figure are deviations from the domain-averaged pressure at each level at the given time. The averaged domain surface pressure dropped .3 mb between 60 and 75 minutes, and this additional drop must be added to those shown in Fig. 8.15b to determine the true pressure decrease between 60 and 75 minutes within the wake low.) Unlike in SP, pressures in the wake low are over 1 mb lower than anywhere else within the domain. A significant pressure gradient occurs over a much larger region in SP1 than in SP, with pressures changing by 3 mb over a 30 km region. This agrees better with the observed 5 mb gradient over 50 km. The lowest pressure occurs in an area that is basically just behind the main region of light surface rainfall (Fig. 8.12c). This agrees better with observations from Stumpf et al. (1991). The wake low weakens slightly at 90 minutes (figure not shown) but is still rather pronounced. The large pressure falls at 75 minutes are occurring with descent that is only half as strong as in SP. With greatly reduced evaporative cooling, the adiabatic warming is able to induce a stronger wake low.

The horizontal velocity perturbations produced in SP1 are similar to those in SP, but the apparent blocking of the RTF jet is possibly even more pronounced (Fig. 8.16). At 60 minutes (Fig. 8.16a), a RTF perturbation of nearly 10 m s^{-1} develops at 3.2 km, with a FTR perturbation of nearly 8 m s^{-1} only 15 km ahead of it. The RTF perturbation increases slightly through 75 minutes (Fig. 8.16b). The perturbation velocities added to

Figure 8.14: As in Fig. 8.5, except for SP1, the simulation in which precipitation rates decrease with time. Contour interval of .4 m s^{-1}.
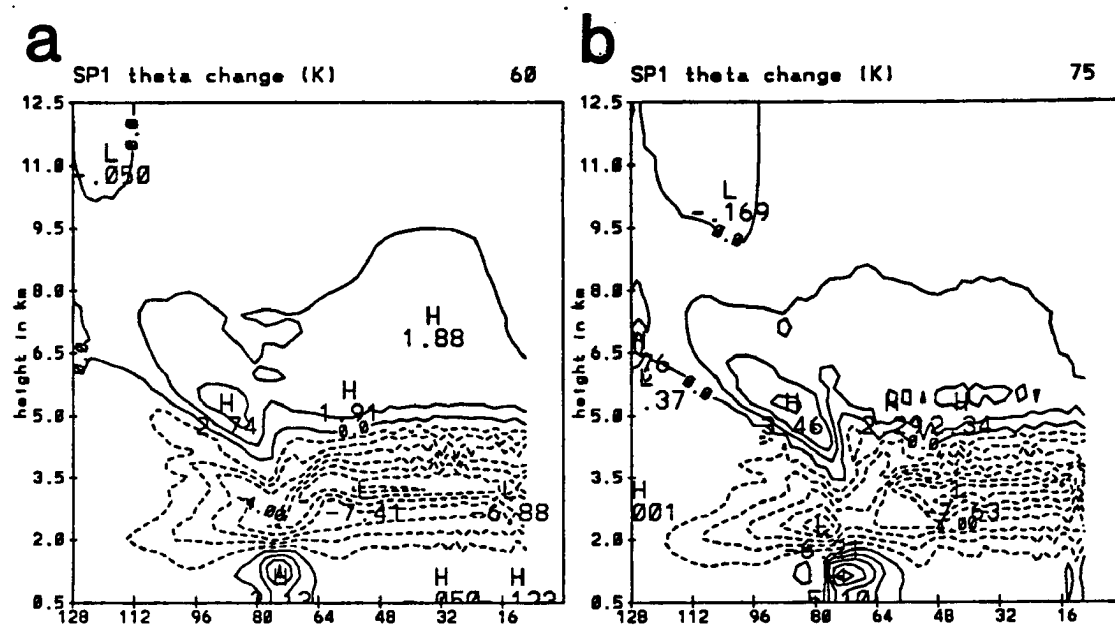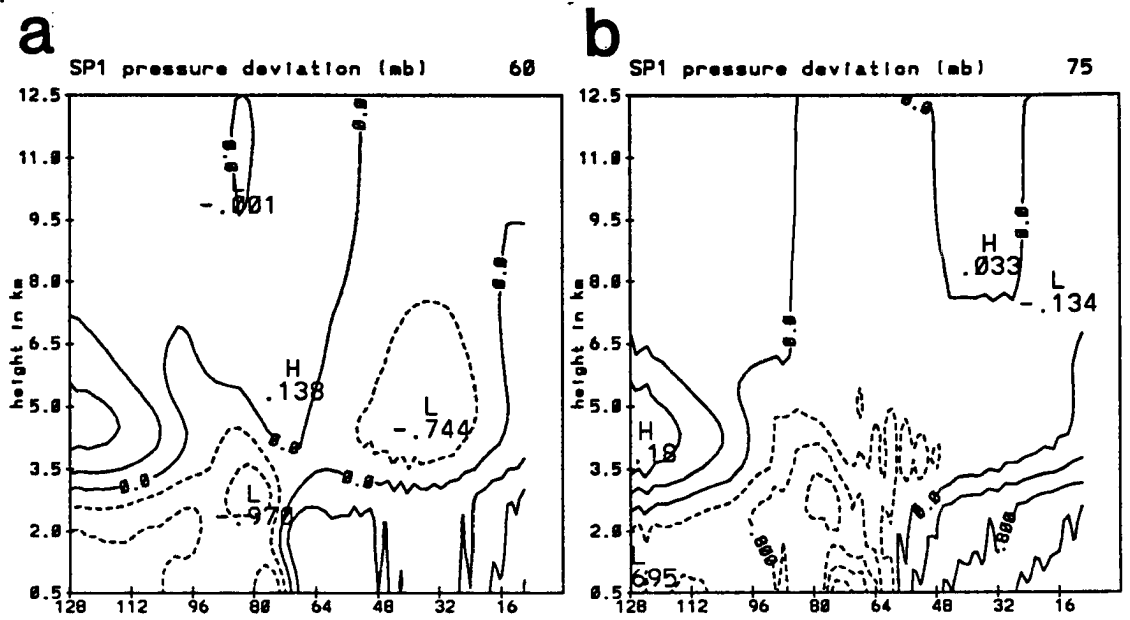
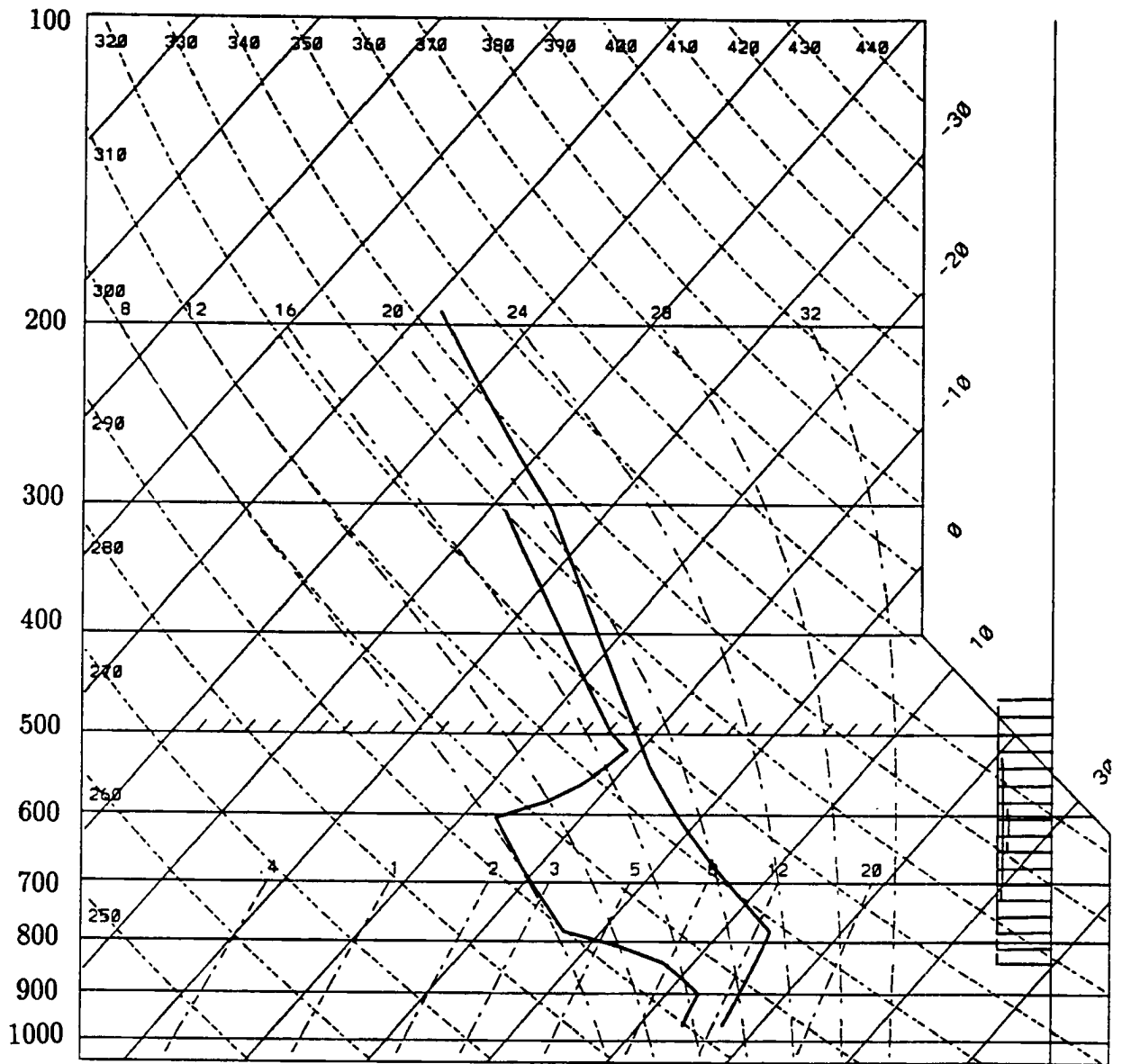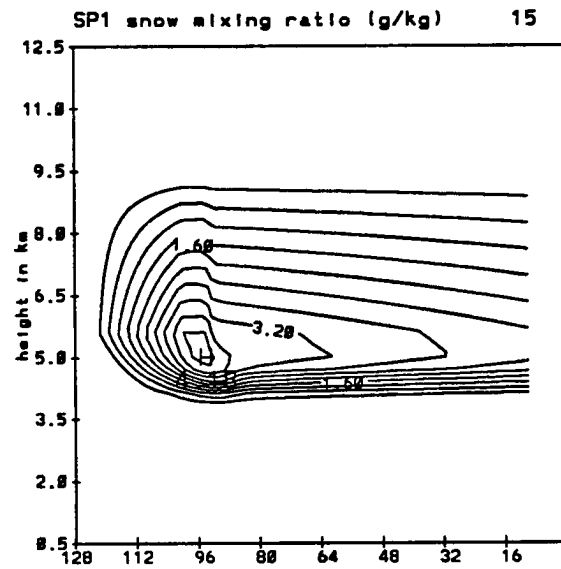Figure 8.15: As in Fig. 8.7, except for SP1, the simulation in which precipitation rates decrease with time.

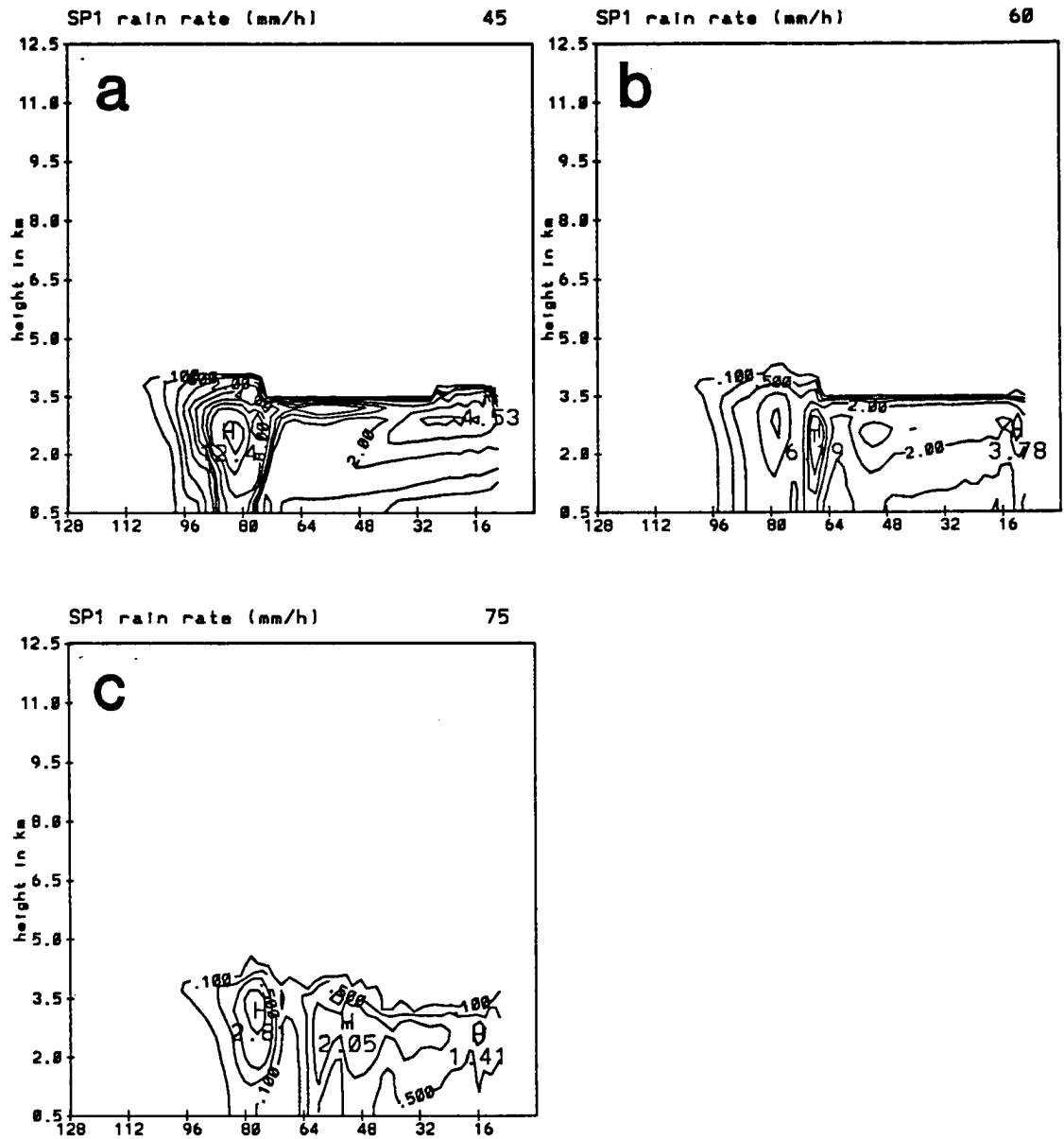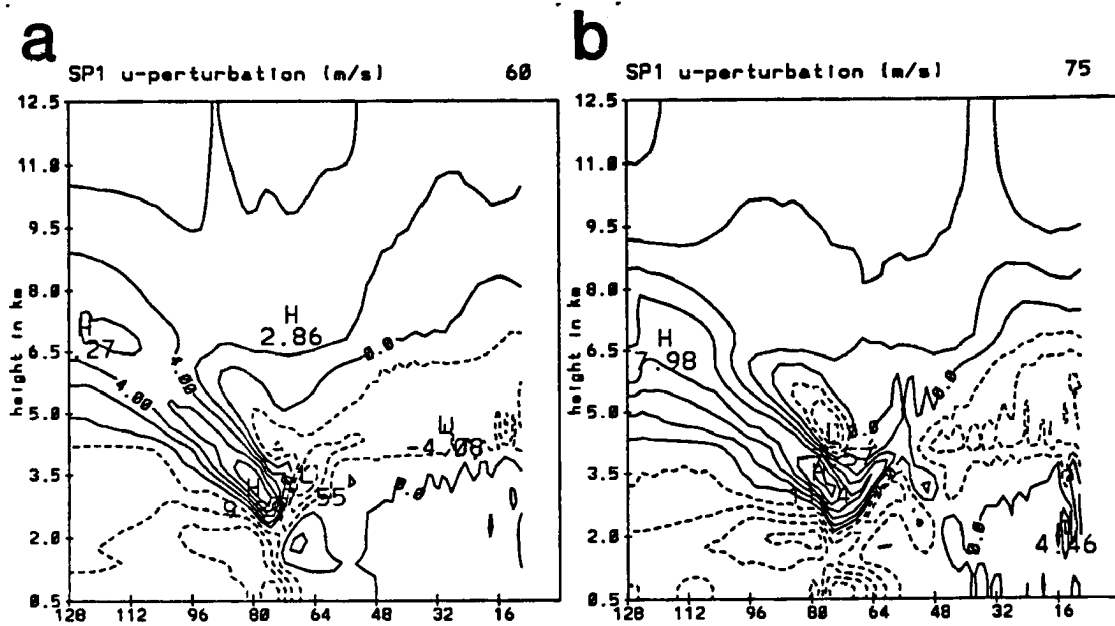Figure 8.16: As in Fig. 8.8, except for SP1, the simulation in which precipitation rates decrease with time.

the ambient wind are similar to those shown for SP in Fig. 8.9, except that the convergence in the region of heaviest rainfall is slightly greater (figure not shown).

Simulation SP1 implies that temporal or spatial variations in the precipitation intensity may be crucial in the development of an intense wake low. Although descent was stronger in SP than in SP1, the heavy rainfall occurring over a long time period did not permit adiabatic warming to oppose the microphysical cooling sufficiently to reduce pressures markedly from those in other portions of the domain. Collapsing precipitation cores, as idealized in simulation SP1, appear to induce fairly strong descent that continues even after the precipitation rates have become very light. Because descent of 1-2 m s^{-1} continues in the presence of rain rates less than 1-2 mm h^{-1}, adiabatic warming is not as strongly opposed by microphysical cooling, and pressures can drop much more in a small region than in nearby areas. This result agrees well with observations. Several simulations were also done similar to SP1 with variations in the precipitation evolution and initial conditions, and these generally produced similar features to SP1.

The results from SP and SP1 imply that microphysical processes alone can explain much, if not all, of the observed intense subsidence and pressure perturbations near the rear of some stratiform regions. Intense descent in SP agreed better with observed values than in SP1, but the wake low and warming in SP1 agreed better with observations than those in SP. This implies that the actual situation on 4 June was probably somewhere between the scenarios presented in these simulations. Heavy precipitation rates are necessary to produce downward motion greater than a few m s^{-1}, but the precipitation must decrease in intensity fairly quickly so that the subsidence can produce sufficient warming to induce a strong wake low. These simulations do not exclude the possibility that some other dynamic effect plays a role in cases of strong subsidence and intense surface pressure falls. This model uses a horizontally homogeneous initial wind field, and it is possible that interactions between existing jets and possible blocking mechanisms could enhance the subsidence and adiabatic warming. These factors would not be simulated fully with this model. However, the fact that such strong subsidence and such an intense wake low were simulated even with the limitations of a 2D model implies that microphysical cooling may indeed be the only mechanism necessary to produce these features.

Chapter 9

SIMULATIONS OF A GATE CASE

In this chapter, the model is applied to a GATE squall line case, to investigate whether microphysics similar to those occurring in midlatitude cases can explain the behavior of tropical squall lines in moist oceanic regions. Two simulations are discussed using data from the 12 September 1974 case which has been studied extensively from both observational (e.g. Houze, 1977; Gamache and Houze, 1982; 1983; 1985) and modeling (e.g. Nicholls, 1987; Nicholls et al., 1988) perspectives. These simulations explore the ability of the model to reproduce observed stratiform region features in an environment with moister low-levels and different hydrometeor advection from convective cells. The ambient wind for that case was substantially different from the 11 June case, and the hydrometeor contents within the convective cells, taken from the kinematic modeling study of Rutledge (1986), were dramatically different. One simulation (GATE) is run with convective line heating, and the other (GATE1) without the heating.

Initial thermodynamic diagrams from both lateral boundaries for the tropical oceanic case are shown in Fig. 9.1. Data were taken from the ship, Quadra, and from previous studies of this case (e.g. Nicholls, 1987). As in the PRE-STORM case, there is a moisture gradient with saturated conditions present at the immediate back edge of the convective line. Both soundings are somewhat more stable than in the 11 June case. The dry air at midlevels toward the rear of the domain is not as pronounced as in the PRE-STORM case. Wind profiles are shown at the right side of each sounding. There are similarities with the 11 June case, including the presence of a midlevel minimum in FTR flow. In this case, the data indicated that the convective line in its early stages already had resulted in some weak RTF flow at midlevels, so the domain is initialized with up to 2 m s^{-1} RTF
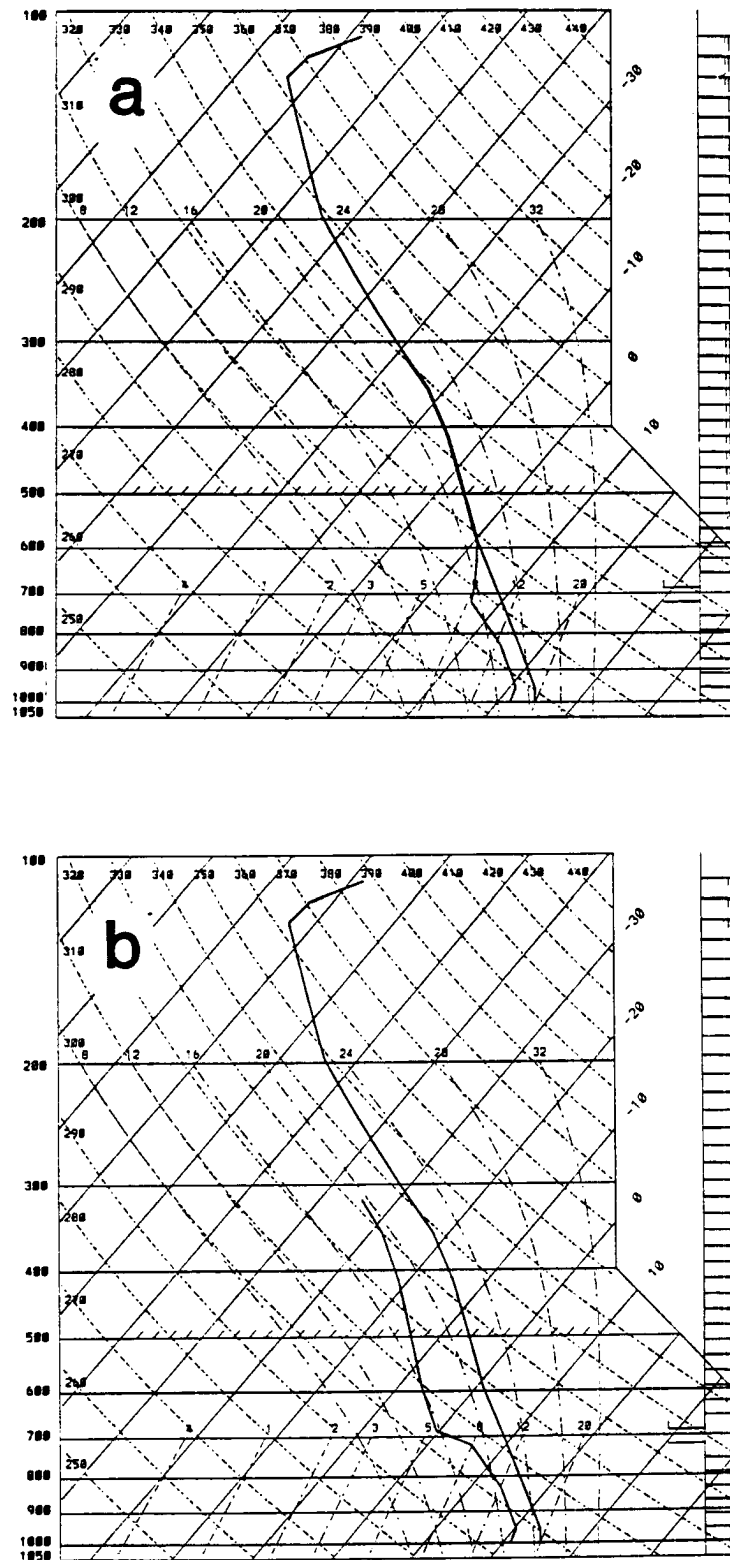
Figure 9.1: Initial thermodynamic diagrams at the (a) right and (b) left boundaries of the domain used for the GATE simulations. Winds relative to the system are shown at the right side of the diagrams.

flow around the 3 km level. FTR flow increases toward the surface, and toward an upper level peak of 14 m s^{-1} in the 6-9 km layer. A relative minimum in this flow occurs around 12 km.

Initial relative humidities with respect to water were highest below 2 km and within 50 km of the convective line (Fig. 9.2). Low-level humidities are roughly 5% greater than in the midlatitude case. In addition, although dry air exists at midlevels over much of the domain, the minimum humidities are substantially greater than in the midlatitude case.

For the hydrometeor contents of the convective cells, the three dimensional kinematic cloud model results for this case by Rutledge (1986) are used, with averaging done over his three dimensional domain for input in this 2D model (Fig. 9.3). Graupel is the primary hydrometeor present, with peak mixing ratios exceeding 3.5 g kg^{-1}. The peak graupel content occurs at a higher level than in the PRE-STORM case, 7.5 km compared with 6.5 km. Snow occurs in much smaller quantities with a constant amount in the 5-11.5 km layer. Slightly more cloud water is present than in the PRE-STORM case, with the peak occurring about 0.5 km higher than in the 11 June case. Ice quantities are about 40% less than in the midlatitude case, with the ice not extending as high in the troposphere.

9.1 GATE control run

Because of the large amount of graupel advecting rearward from the convective line hydrometeor advection into the domain is much greater than in the PRE-STORM case, with 76% more mass advecting into the domain (Table 9.1). The increased amount of advection from the convective line results in more rainfall at the surface in the stratiform region (Fig. 9.4). Peak rainfall rates near the melting level are generally between 10 and 13 mm h^{-1} through 270 minutes (Figs. 9.4a-c), and almost 8 mm h^{-1} at 360 minutes (Fig. 9.4d). Evaporation is not as strong in the GATE case because of increased low-level humidity so that surface rainfall rates are much greater than in the PRE-STORM case. Peak surface rates are around 5 mm h^{-1} at 90 minutes (Fig. 9.4a), 7 mm h^{-1} at 180 minutes (Fig. 9.4b), 6 mm h^{-1} at 270 minutes (Fig. 9.4c) and 3 mm h^{-1} at 360 minutes (Fig. 9.4d). The surface rainfall area expands with time, and this region is generally larger
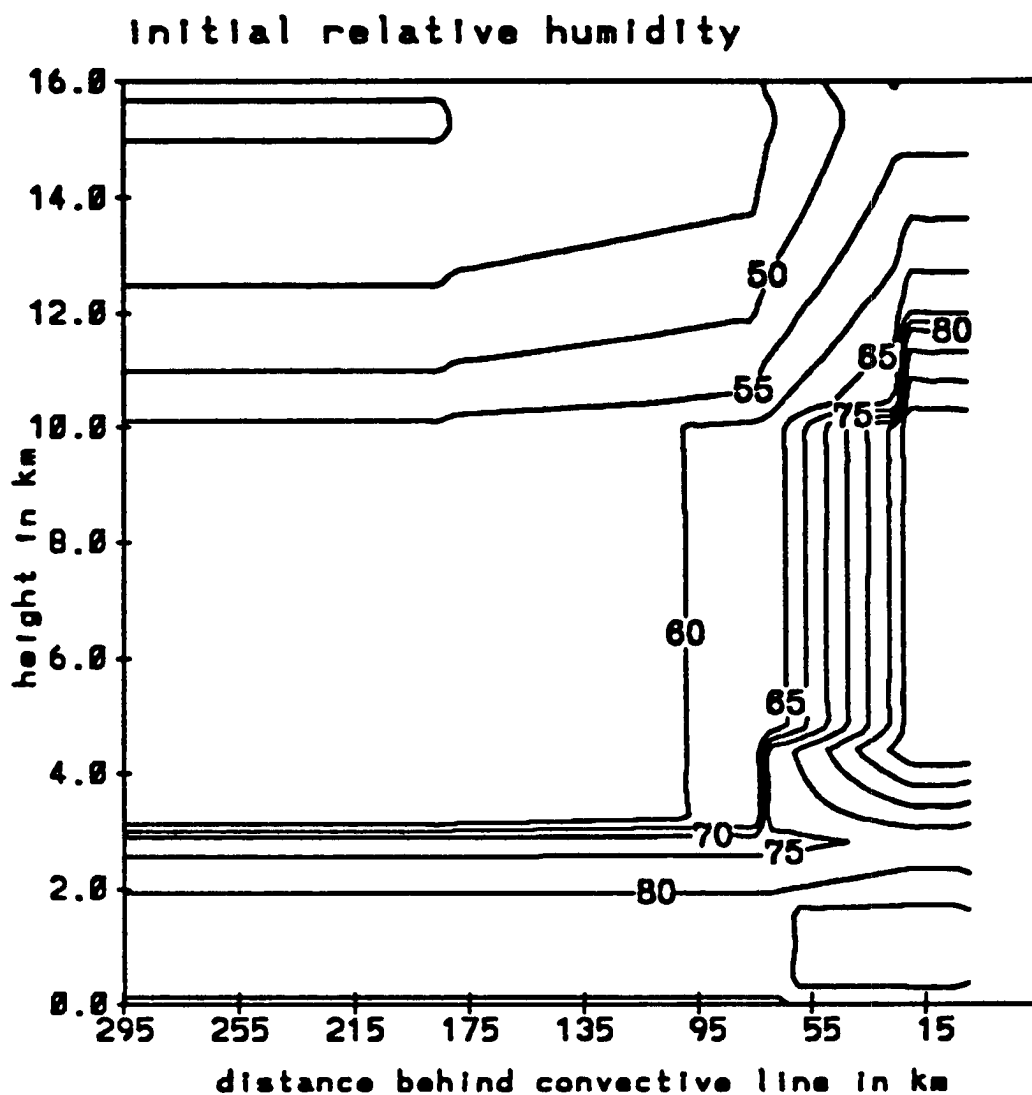
Figure 9.2: Initial relative humidity with respect to water for the GATE simulations. Contour interval is 5%.

Hydrometeor Content
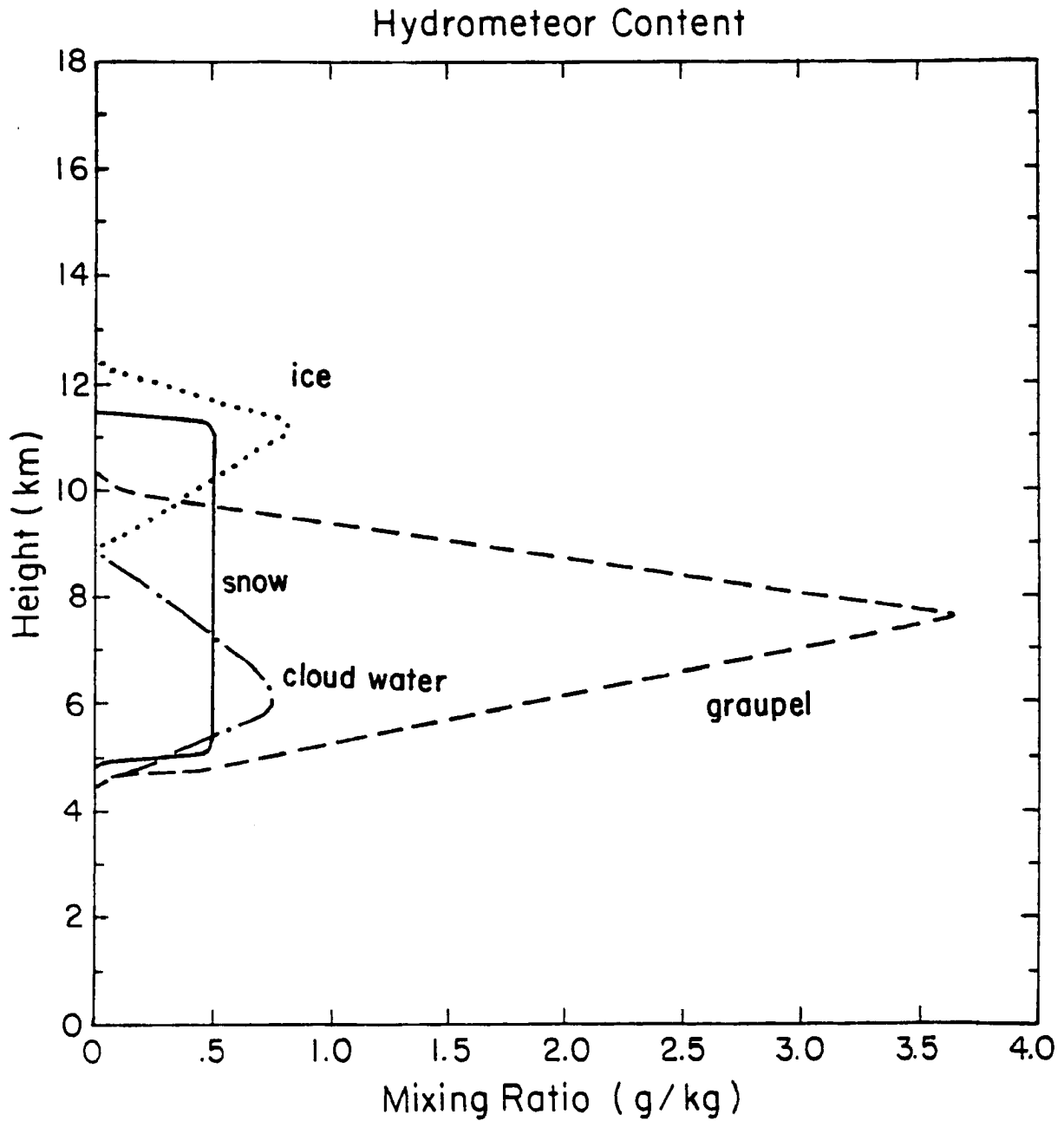
Figure 9.3: Initial hydrometeor contents (g kg^{-1}) of the convective cells for the GATE simulations, taken from Rutledge (1986). Snow is shown with a solid curve, graupel dashed, ice dotted and cloud water dash-dotted.
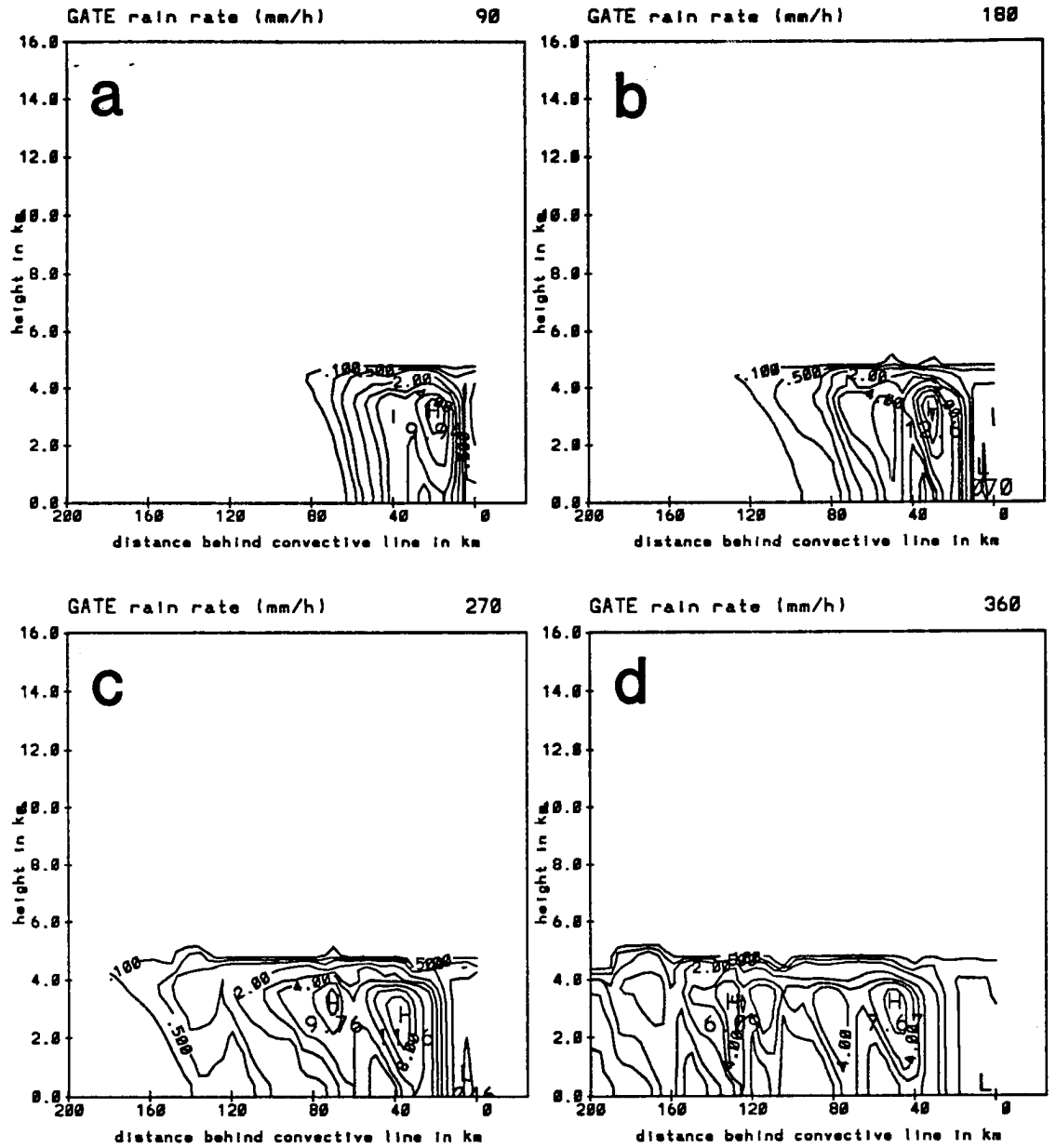
Figure 9.4: As in Fig. 5.19 except for the GATE simulation with convective heating.

than in CTL, with surface rainfall up to 190 km rearward from the convective line at 360 minutes. The region of heaviest rainfall also moves rearward with time, but is generally closer to the convective line than in the PRE-STORM case. A transition zone exists at all times near the convective line, but it does not expand rearward as rapidly as in CTL. In addition, rainfall in the transition zone is not as light as in CTL, with at least some rain reaching the surface. The total amount of rain reaching the surface over the entire simulation is over 200% greater than in the PRE-STORM case (Table 9.1).

Table 9.1: Simplified integrated water budget for the GATE case with convective heating (GATE) and without convective heating (GATE 1). Values are in metric tons of water over the entire 405 minute simulation, with percentage change from CTL shown for GATE, and percentage change from GATE shown for GATE 1.

Run	Advected mass	In Situ mass	Mass Sink	Rain sink
GATE	2984.09 (+ 76%)	1794.86 (+44%)	2580.92 (+13%)	1559.75 (+205%)
GATE 1	2532.28 (- 15%)	1097.12 (-39%)	1623.79 (-37%)	1353.77 (-13%)

Composited rainfall rate data for this case were estimated by Gamache and Houze (1983). Because the composite was for a large portion of the lifetime of the system, the modeled evolution of the rainfall pattern cannot be compared directly with observations. The composite study indicated that rain rates were as large as 7 mm h^{-1} locally in one area within the stratiform region. Most of the rainfall rates in the stratiform region were between 2 and 5 mm h^{-1}, with heavier rates near the convective line. That study also showed little evidence of a transition zone. Because most of the rainfall rates in the simulation are under 5 mm h^{-1}, it appears likely that the 2D model again underestimates the actual surface rainfall, although probably to a lesser extent than in the PRE-STORM simulation. Roughly 63% of the total condensate mass made available in the domain enters through advection from the convective line (Table 9.1). This figure agrees well with the water budget of Gamache and Houze (1983) which estimated that 60-75% of the surface rainfall was attributable to advection of condensate from the convective line.

Much of the increased surface rainfall is due to the greatly increased advection of condensate into the stratiform region from the convective line. However, in situ production

also increases over CTL by nearly 45%. Vertical motion is comparable in magnitude and scale to that in CTL (Fig. 9.5). Significant ascent in the anvil cloud develops quickly, and at 90 minutes (Fig. 9.5a), it exceeds 10 cm s^{-1} over a 30 km wide region with peak ascent of 35 cm s^{-1}. The upward motion at this time is much more developed than in CTL. The area of ascent grows with time in a similar fashion to the PRE-STORM case. Peak ascent reaches 62 cm s^{-1} by 180 minutes (Fig. 9.5b) and exceeds 90 cm s^{-1} at both 270 and 360 minutes (Figs. 9.5c, d). The peak ascent generally occurs at a higher level than in the PRE-STORM case, with peak ascent around 8 km through 180 minutes. After that time, ascent is strong in a deep layer with the greatest upward motion between 9 and 10 km.

The mesoscale downdraft is developed by 90 minutes (Fig. 9.5a), with a peak magnitude of 28 cm s^{-1}, roughly the same as in CTL. Peak descent occurs near the melting level. The downdraft increases in intensity through 180 minutes (Fig. 9.5b) when it reaches 38 cm s^{-1}. At later times the maximum downward motion varies between 28 and 37 cm s^{-1}. The descent is greatly reduced in magnitude from the midlatitude case, due to the moister conditions at low levels and the significantly larger amounts of hydrometeors present which help to moisten the lower troposphere. The weaker descent does occur over a broad region, however, and by 360 minutes, the downdraft is broader than in CTL. The amount of water lost to evaporation and sublimation over the 405 minute simulation increases 13% from that in CTL (Table 9.1). This is far less of a relative change than in the other water budget terms and reflects the importance of the moister conditions along with the large amounts of hydrometeors. One substantial difference between the GATE run and the CTL run is the presence of strong subsidence at midlevels just behind the convective line. This subsidence can be seen at all times, and is most pronounced at 270 minutes (Fig. 9.5c) when descent as large as 48 cm s^{-1} occurs around the 5.5 km level. The significantly larger amounts of hydrometeors leaving the convective line may contribute to this downward motion through precipitation drag. As discussed earlier, enhanced subsidence is often found just behind the convective line in the transition zone. The area of subsidence in the transition zone broadens through 270 and 360 minutes.

Observational data depicting the evolution of the vertical motion field with time are not available for this case, although some comparisons can be made with a composite study

234
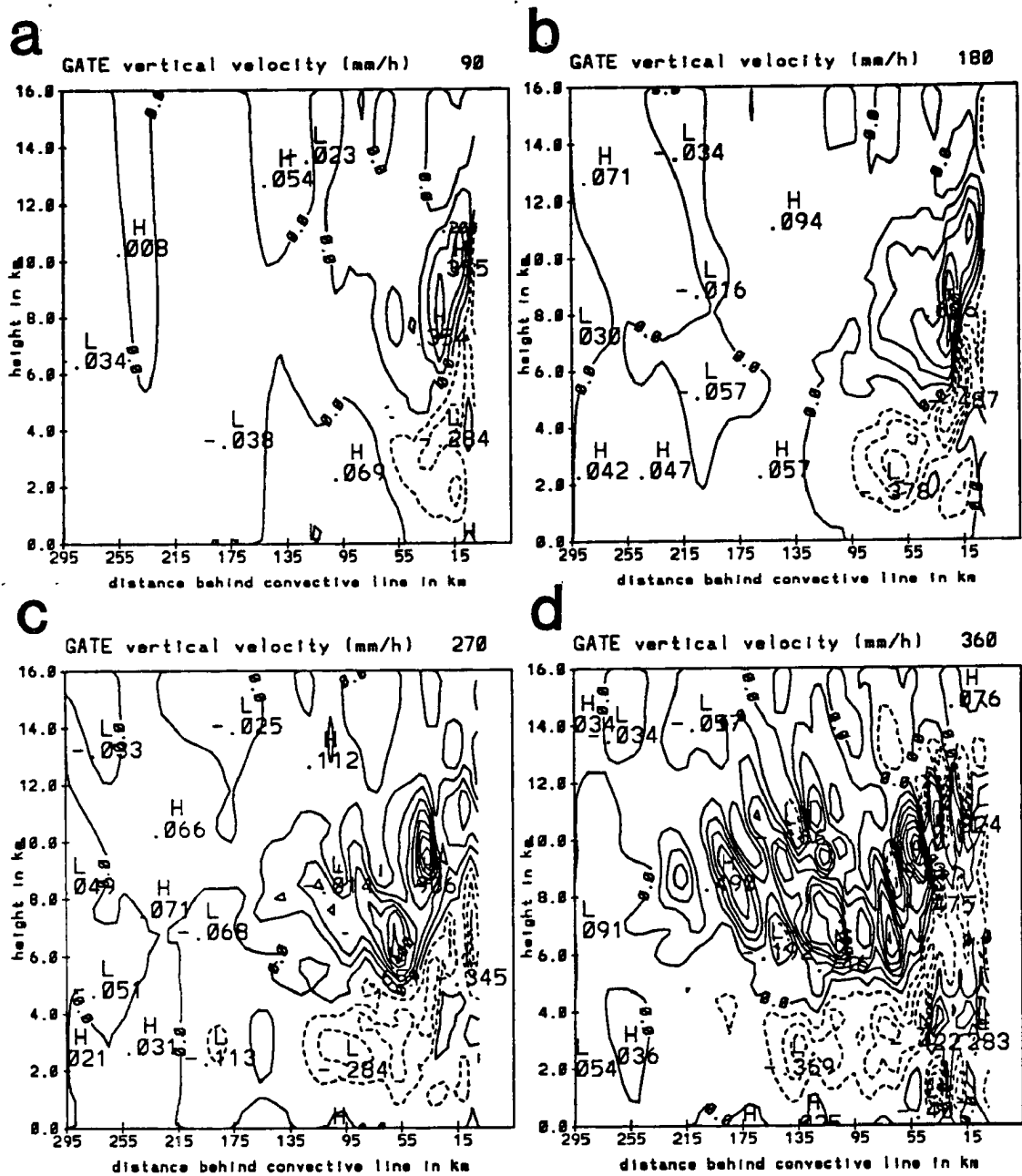
Figure 9.5: As in Fig. 5.24 except for the GATE simulation with convective heating.

of this case by Gamache and Houze (1982). From rawinsonde data, that study found peak downward motion in the 1.5-3 km layer depending upon the position within the anvil cloud. The squall line was not as strictly two-dimensional as the 11 June case. The peak downward motion was generally around 35 cm s^{-1}. The model mesoscale downdraft is therefore reasonably close to these observations. The crossover from descent to ascent in the Gamache and Houze study was typically around the melting level, but varied from around 3 km in the front portion of the anvil to 5 km toward the rear. Because rawinsonde data with a rather coarse horizontal resolution were used to compute the vertical motions, some aliasing of data between the convective line region and the stratiform region was probably occurring, as argued by Rutledge (1986).

Gamache and Houze (1982) found ascent aloft to be greatest between 7 and 9 km level in the anvil cloud with a tendency for the upward motion to occur at higher levels farther rearward from the convective line. Peak ascent was around 35 cm s^{-1}, similar in magnitude to the mesoscale downdraft. Larger values of ascent were found closer to the convective line, but these may be influenced by aliasing. Significant upward motion extended at least 100 km rearward of the convective line. The model results therefore are in fair agreement with these observations, particularly at 270 and 360 minutes.

The vertical motion averaged over the stratiform rain region during the 270-360 minute period (Fig. 9.6) agrees reasonably well below 8 km with that diagnosed from rawinsondes by Gamache and Houze (1982). The greatest descent on the Gamache and Houze curve is around 20 cm s^{-1} in good agreement with the model results. The peak descent from the rawinsonde study is about 1 km lower than what the model indicates. The simulated descent is stronger toward the melting level than in the Gamache and Houze study. The observed crossover point is around 4 km, a little lower than the model results. The peak upward motion found by Gamache and Houze was 55-60 cm s^{-1} in a broad region from 10-12 km. This implies that the model is underestimating the mesoscale ascent, particularly toward cloud top. Some of the discrepancy may be due to aliasing of the rawinsonde data and timing differences, although the model's lack of radiative effects may also account for the differences.

Figure 9.6: Vertical profiles of vertical motion averaged over the entire stratiform rain region (solid curve) and over an EVAD-scale region of heaviest stratiform rainfall (dashed curve) during the 270-360 minute time period for the GATE case with convective heating. Observed curve for the anvil region of the composite Gamache and Houze (1982) study is dotted.

The mesoscale downdraft in the GATE simulation is case averaged over the rain region is slightly weaker than in the PRE-STORM case (Fig. 5.12). The peak descent occurs slightly lower than in CTL with the crossover from subsidence to ascent also a few hundred meters lower than in CTL, but still near the 5 km level. This is within 1 km of the melting level. The ascent aloft occurs through a much deeper layer than in CTL, and both the stratiform average (A) and the EVAD-scale average (B) curves are noticeably different from those in the CTL run. The higher tropopause in the tropics can allow the ascent to extend to higher levels (see Figs. 3.2 and 9.1). Peak ascent over the stratiform region is almost 35 cm s^{-1}, which is only around 5 cm s^{-1} less than in CTL. The level of peak ascent on both curves is around 7 km, or slightly lower than in CTL. However, a secondary peak occurs in the EVAD-scale curve around 10.5 km, and there is evidence of this secondary peak in the stratiform region average. Significant ascent can be seen as high as 12 km.

The horizontal perturbation velocities that are produced in this case are slightly different from those in CTL (Fig. 9.7). Strong rear-inflow is generally restricted to the lowest 3km, although some weak RTF flow does develop at later times in the 3-6 km layer well to the rear of the rain region. Peak RTF flow reaches 8 m s^{-1} at 180 minutes (Fig. 9.7b), 12 m s^{-1} at 270 minutes (Fig. 9.7c) and 16 m s^{-1} at 360 minutes (Fig. 9.7d). These values are within 10% or so of those in CTL. FTR flow is enhanced at midlevels by around 10 m s^{-1} at 180 minutes, 20 m s^{-1} at 270 minutes, and 30 m s^{-1} at 360 minutes. The axis of the FTR perturbation maximum slopes rearward with height.

In the total horizontal velocity field (Fig. 9.8), the rear-inflow jet can be seen to intensify and descend toward the surface, primarily after 180 minutes (Fig. 9.8b). The strongest RTF flow occurs about 35-55 km behind the convective region at all times. RTF flow at the rear of the domain is stronger than in CTL. Data showing the evolution of horizontal velocities over the lifetime of this system are also not available for this case as it is for the 11 June squall line. Gamache and Houze (1982) do show detailed circulation data for this case but the data are composited over a rather long time interval and only shown at a few specific levels. From that data, rear-inflow appeared to be restricted to
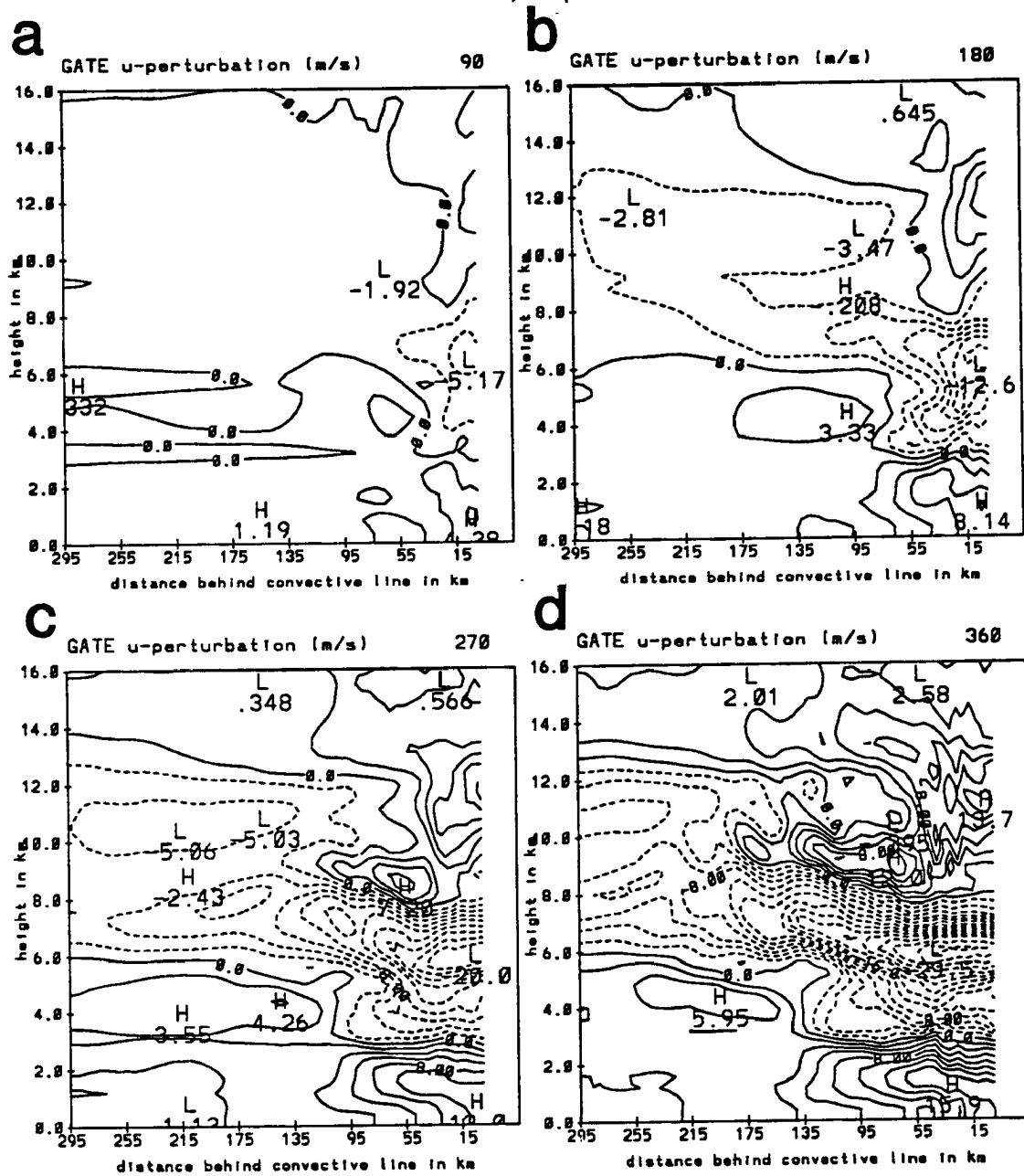
Figure 9.7: As in Fig. 5.15 except for the GATE simulation with convective heating.

239
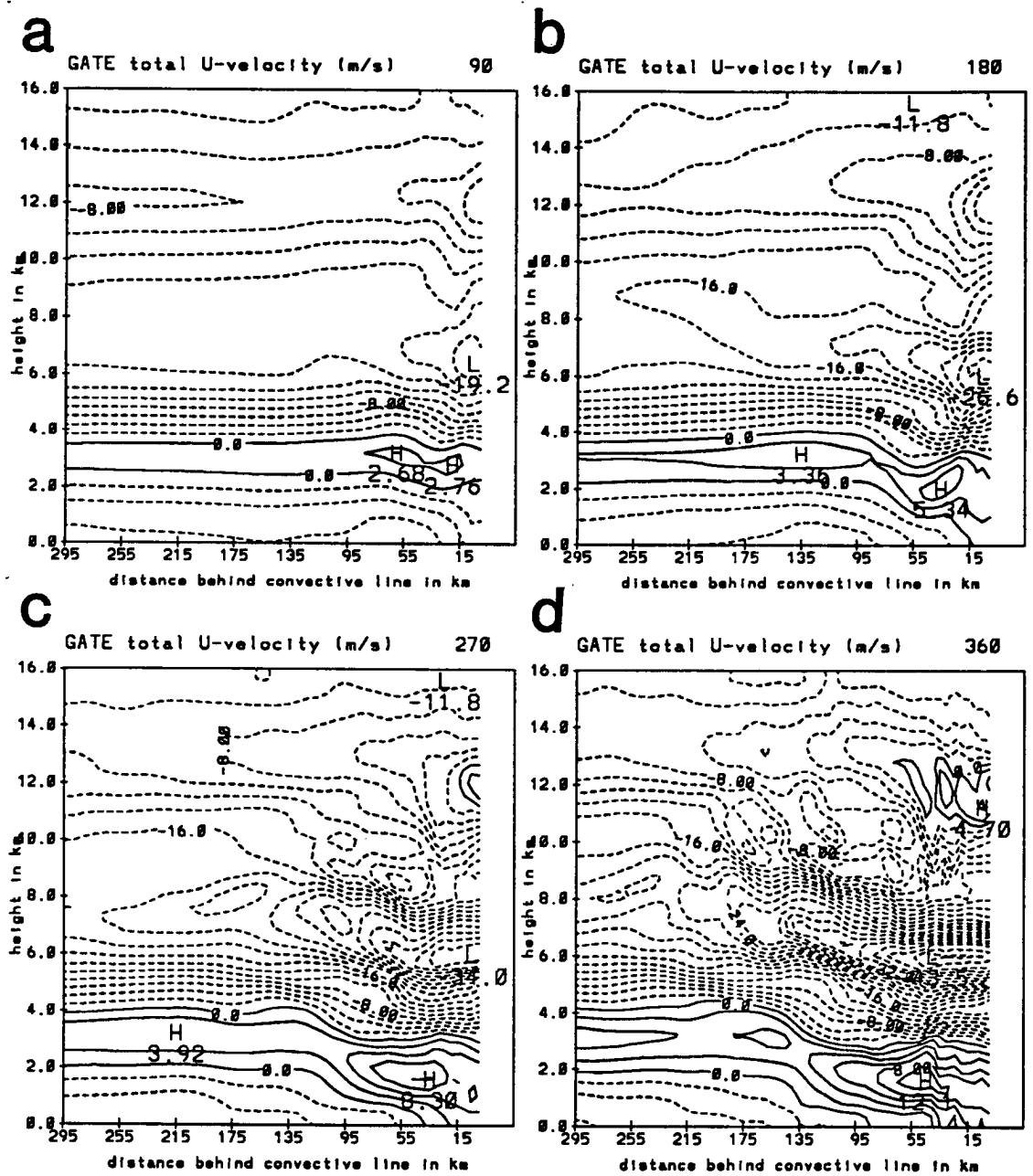
Figure 9.8: As in Fig. 5.16 except for the GATE simulation with convective heating.

levels below 4.5 km in this case, so the model results are in good agreement with this observation. Peak RTF flow around 850 mb was shown to approach 10 m s^{-1}. An average over the stratiform region of that case would indicate peak RTF flow much weaker, with no rear-inflow occurring in some portions of the stratiform region. The strongest RTF flow occurred around 100 km rearward from the convective line region. The model maximum RTF flow is therefore closer to the convective line region, but within about 50 km of the observed peak region. The strongest FTR flow aloft occurred around the 6-6.5 km level with relative wind speeds exceeding 20 m s^{-1} in much of the stratiform region. The levels of peak FTR and RTF flow are therefore diagnosed well by the model, although the speeds, especially in the FTR jet are overestimated.

9.2   GATE simulation neglecting convective heating

Another simulation was run in which convective heating was ignored. This was partially motivated by the fact that the prescribed heating used in the PRE-STORM case may not be applicable to the tropical east Atlantic. Accurate data are not readily available for this GATE case, so this simulation is thought to put an extreme bound on the influence of convective heating. Because the heating used in the PRE-STORM cases was somewhat smoothed, it is possible that that heating profile accurately represents what occurred in this GATE case. The simulation without convective heating will also allow some comparisons to be made which may better explain the role of different processes in squall line systems.

In this simulation (GATE 1), peak rain rates at the surface are comparable to those in the control GATE run. However, the total amount of rain reaching the surface decreases by 13% without convective heating (Table 9.1). This is far less of a reduction than occurred in the midlatitude case with simulations investigating the role of convective heating (CTL and C2). Peak surface rainfall is generally greater than 5 mm h^{-1} at all times, with peak values of around 7.5 mm h^{-1} at 180 and 270 minutes (Figs. 9.9b, c). The heaviest surface rainfall at all times tends to be relatively close to the convective line. Only at 360 minutes does the maximum surface precipitation advance more than 50 km rearward from the back

241
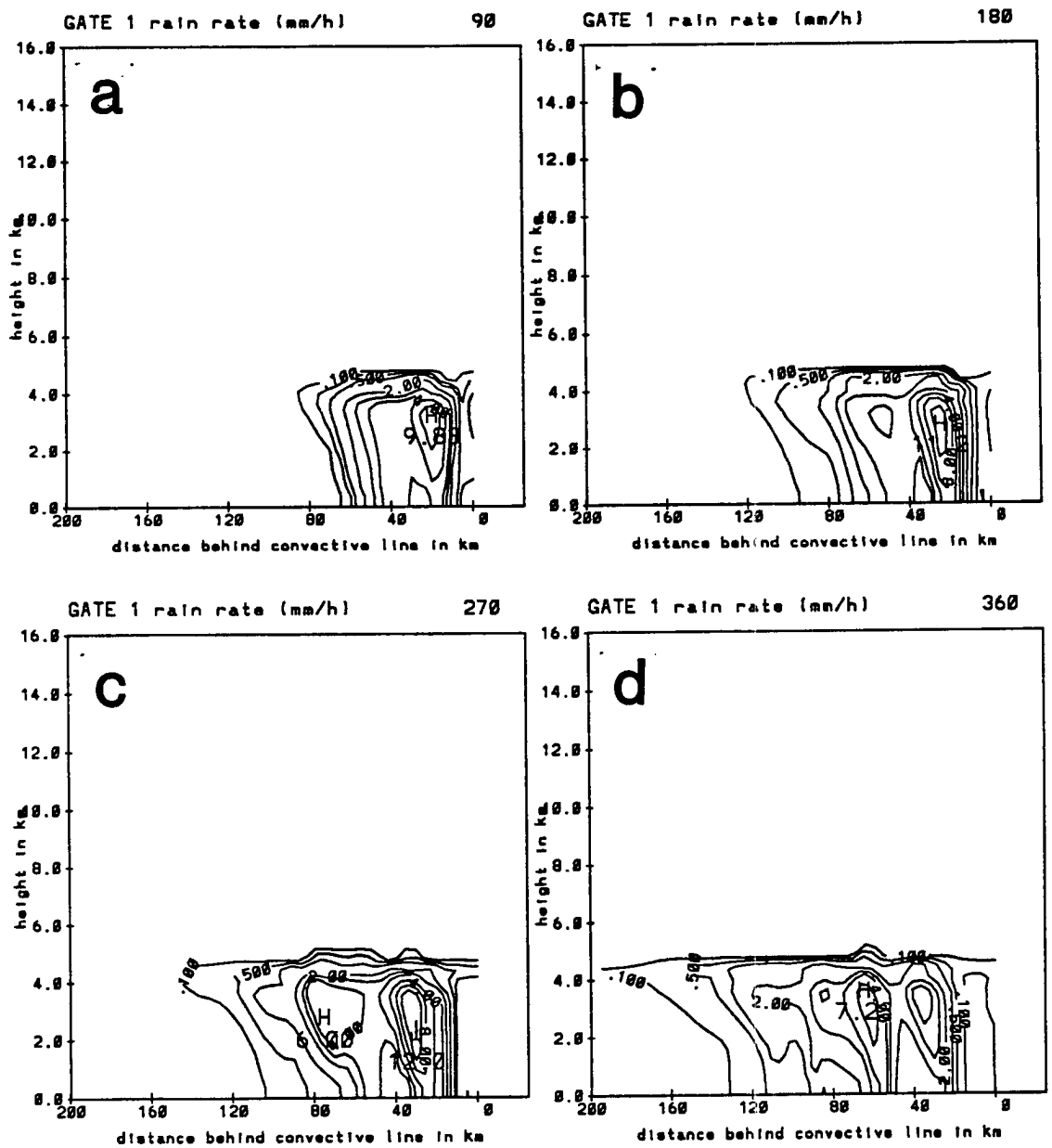
Figure 9.9: As in Fig. 5.19 except for the GATE simulation without convective heating.

of the convective line. The convective heating appears to play a major role in where the heaviest precipitation occurs. As will be shown later, circulations are significantly weaker in GATE 1 than in GATE, so that hydrometeors are not carried rearward as rapidly. The area of rainfall at the surface is similar to GATE through 180 minutes, but smaller at later times. By 360 minutes (Fig. 9.9d) the back edge of surface rainfall is 60 km closer to the convective line than in the simulation with convective heating.

Vertical velocities within the stratiform region are diminished, especially at later times (Fig. 9.10 . Through 180 minutes (Figs. 9.10a, b), the ascent is similar in scale and magnitude to GATE. At later times, however, upward motion is restricted to a much smaller portion of the domain, and the peak values are as much as 40% less than in GATE at 270 minutes (Fig. 9.10c). Downward motion below the melting level is also weaker in this simulation, with peak values at most times not much more than 20 cm s^{-1}. The in situ production of condensate decreases by nearly 40% from the convective heating run, and the water sink term decreases by almost the same percentage (Table 9.1). The decrease in the water sink term is similar to that which occurred between CTL and C2 for the midlatitude case. The reduction in the production of condensate within the anvil cloud is not as great as in the midlatitude case, which may indicate that the increased hydrometeor advection compensates somewhat so that diminished or negligible convective heating has less of an effect.

Vertical motion averaged over the stratiform rain region during the 270-360 minute time period (Fig. 9.11) decreases slightly from that in the GATE control run (Fig. 9.6). The decrease in ascent aloft is not as great as that which occurred for the no convective heating simulation of the 11 June system. Peak ascent is only a few cm s^{-1} less than in GATE, with about a 30% decrease in peak descent.

Rear-inflow is slower to develop without convective heating and is less than half the magnitude present in the GATE control run (Fig. 9.12). The rear-inflow is again restricted to the lowest 3km at most times. FTR flow is enhanced at midlevels but the enhancement is much weaker than in the convective heating run. In general, the circulations are restricted to the 50-100 km nearest the convective line and do not expand to cover the entire domain

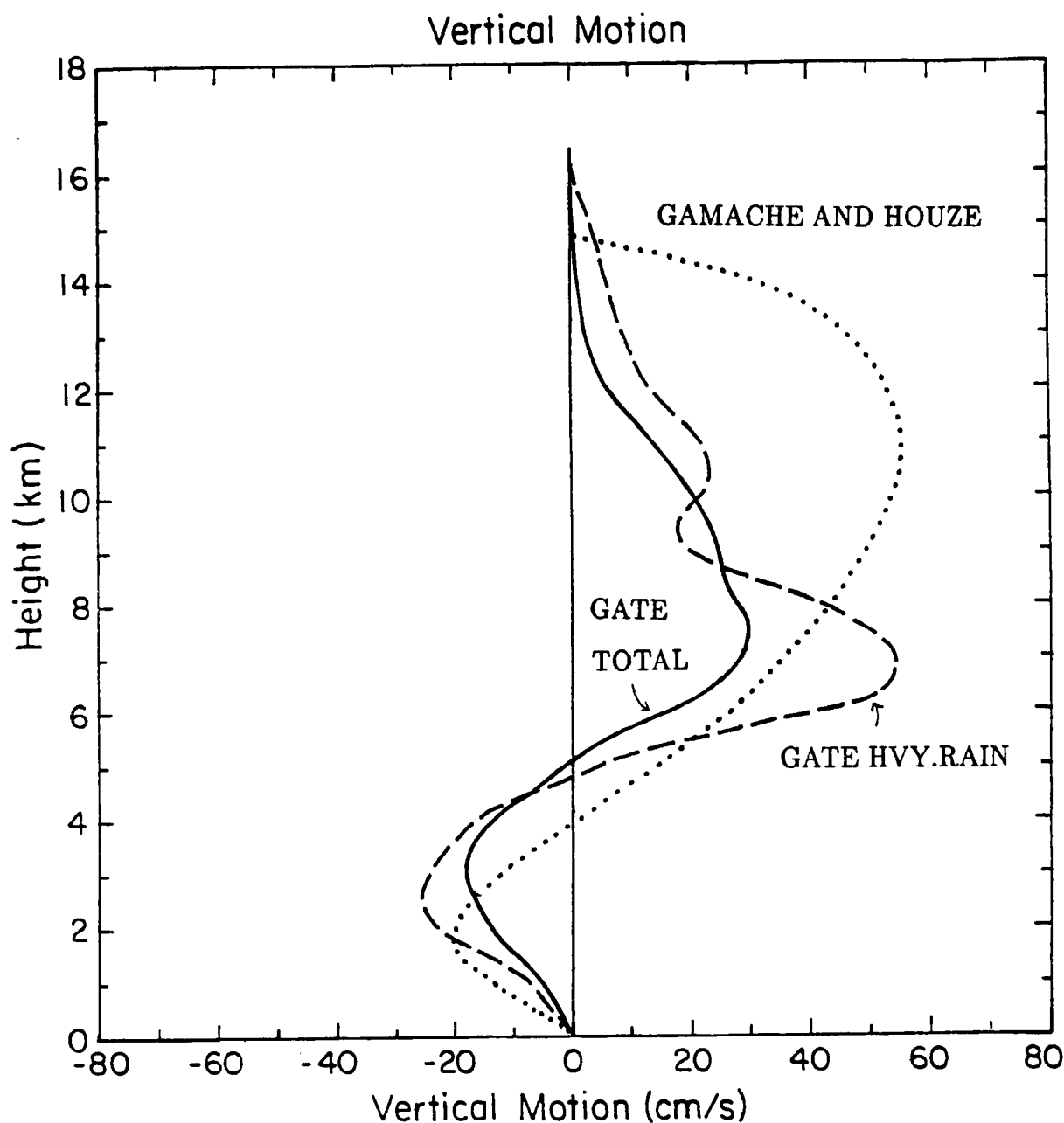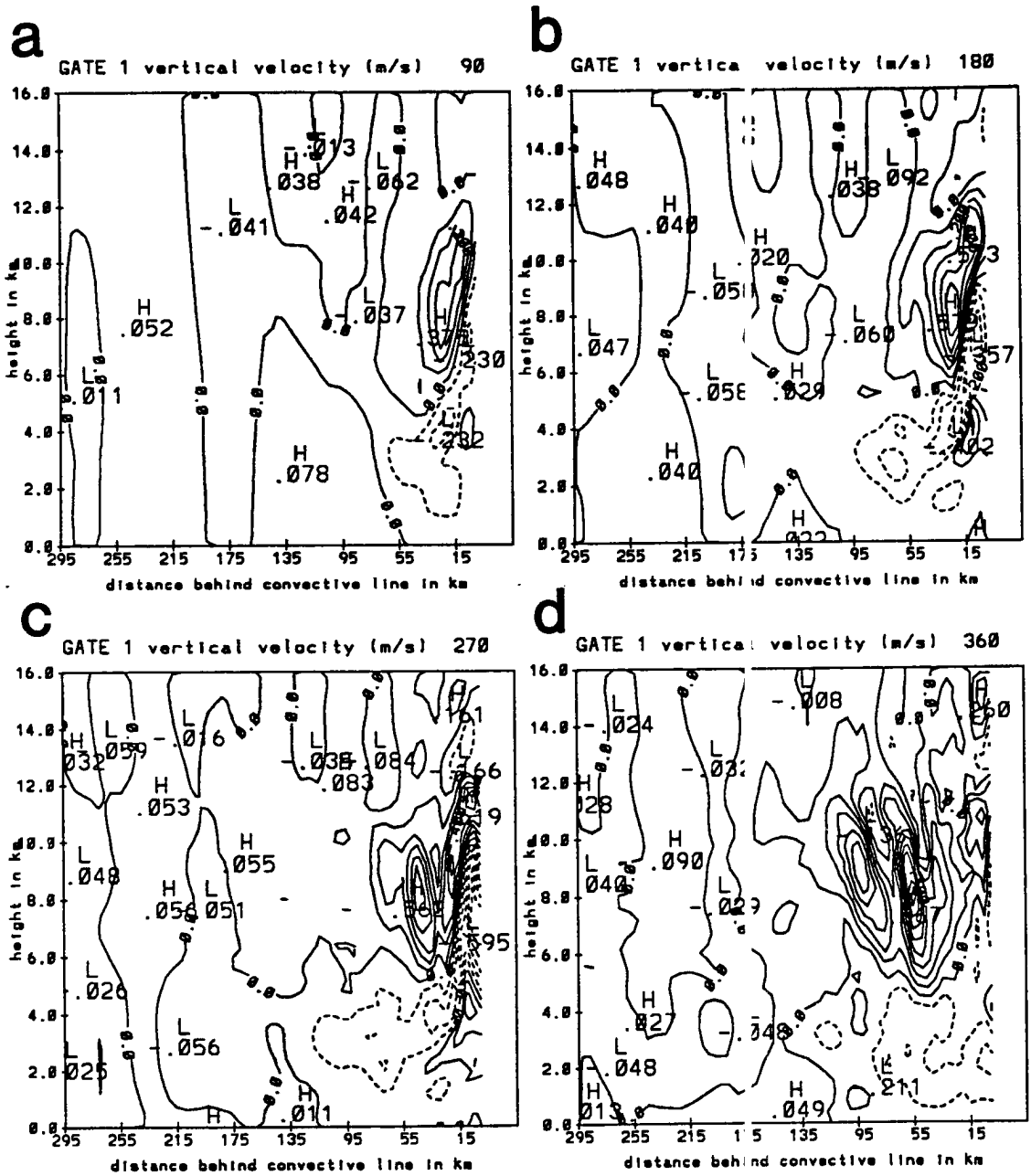Figure 9.10: As in Fig. 5.24 except for the GATE simulation w.thout convective heating.
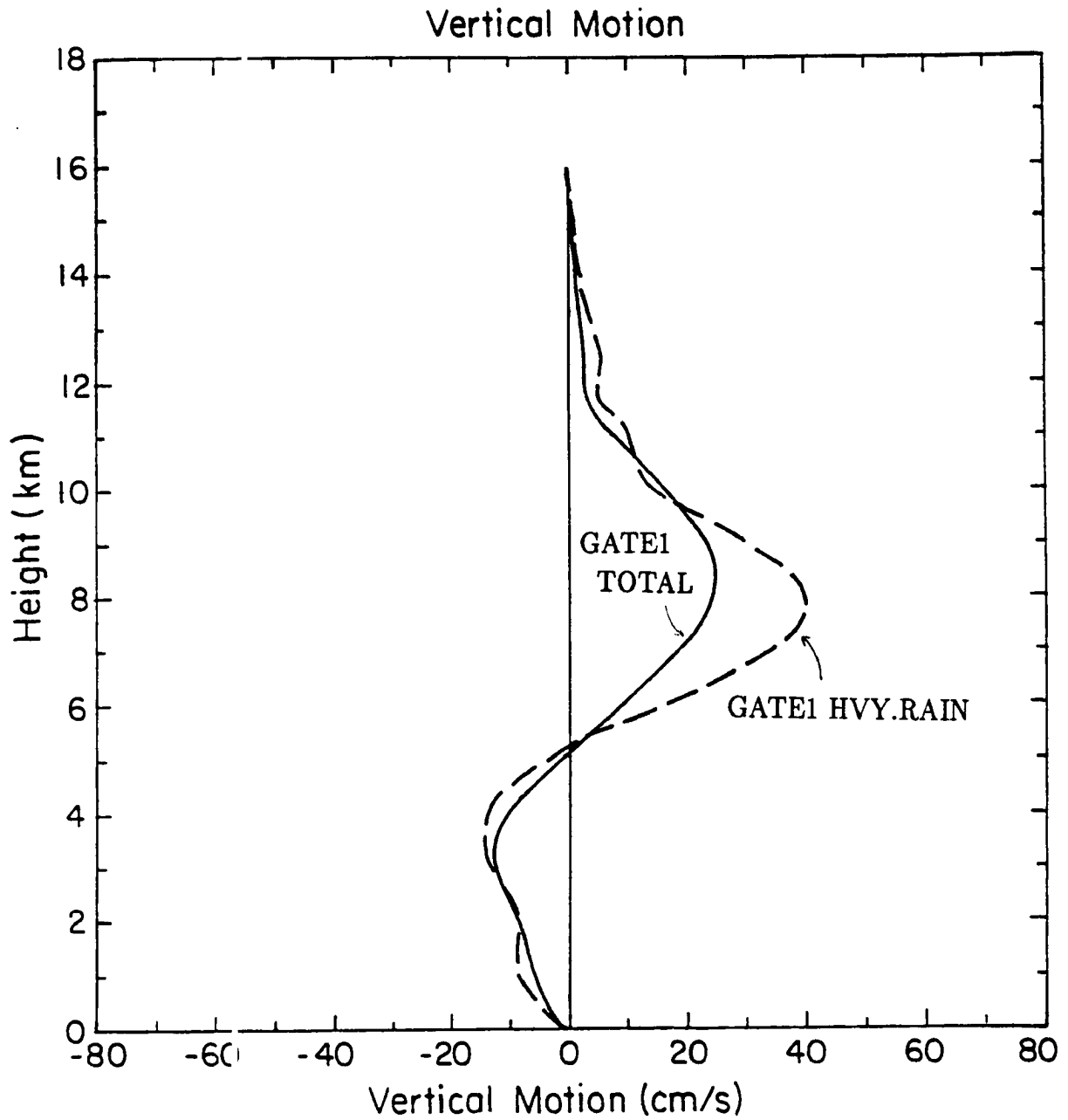
Figure 9.11: Ve tical profiles of vertical motion averaged over the entire stratiform rain region (solid cur /e) and over an EVAD-scale region of heaviest stratiform rainfall (dashed curve) during t ie 270-360 minute time period for the GATE case without convective heating.

Figure 9.12: As in Fig. 5.15 except for the GATE simulation without convective heating.

as in run with convective heating. When combined with the ambient flow, the weakness of the RTF perturbation flow results in only a very gradual descent in the weak rear-inflow jet (Fig. 9.13). Rear-inflow does intensify with time, but the strongest RTF flow generally remains near 3 km. The FTR jet aloft shows little upward slope until 360 minutes (Fig. 9.13d). Peak FTR flow is significantly less than in GATE.

The GATE simulations show that tropical squall lines may behave similarly to midlatitude cases, even in environments not as conducive to evaporation because the convective elments within the systems may contain much larger amounts of condensate, especially graupel. These large amounts of hydrometeors that advect away from the convective line can lead to broad regions of significant stratiform precipitation, even if mesoscale descent is rather weak. The stratiform region appears to be less influenced by the convective heating when supplied with large amounts of condensate from the convective line. In many ways the GATE simulations produced results similar to those from the 11 June midlatitude case, even though graupel was the primary hydrometeor as opposed to snow in the 11 June case. The total quantity of solid hydrometeors is far more important than the relative amounts of each.

247
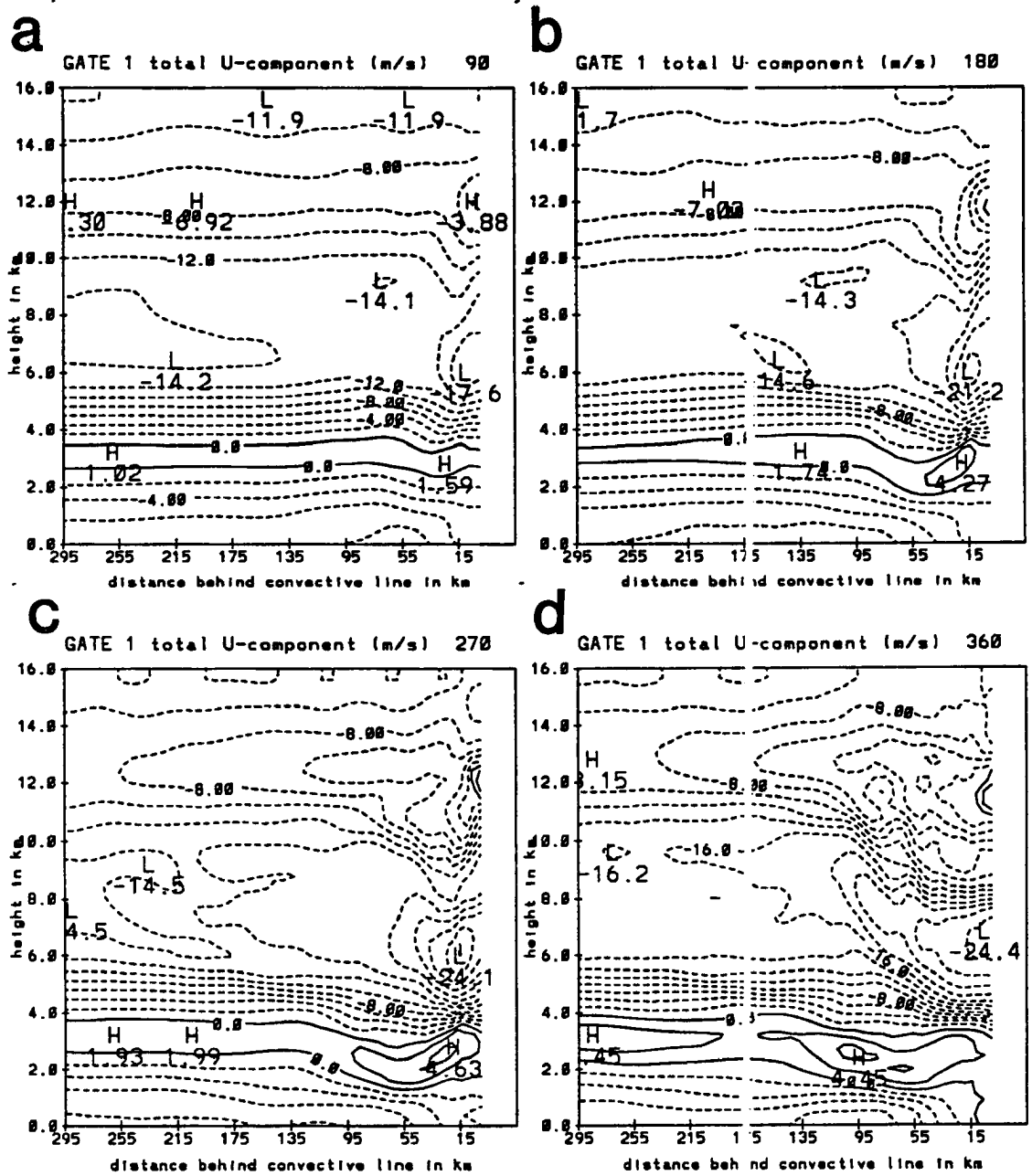
Figure 9.13: As in Fig. 5.16 except for the GATE simulation w.thout convective heating.

Chapter 10

SUMMARY AND CONCLUSIONS

A two-dimensional mesoscale anelastic cloud model has been developed using the bulk microphysical parameterization developed by Rutledge and Hobbs (1983; 1984). The model is somewhat unique in both its intermediate resolution, 5 km, and approach of only simulating the stratiform region of squall lines. The dynamics within the domain are driven by input from the convective line region, and the model moves with the system so that its right boundary is at the rear of the convective line. Similar modeling approaches with less extensive microphysical schemes have been taken by Szeto et al. (1988b) and Stensrud et al. (1991). Initialization of this model relies heavily on actual data from areas just behind newly developed convection. Simulations are run long enough to trace the evolution of the stratiform region from growth through maturity to the beginning of dissipation. The goals of the study are to investigate the role of hydrometeor and heat advection from the convective line on the development and evolution of circulations in the stratiform region, particularly the rear-inflow jet and mesoscale updraft, and to determine the relative importance of different microphysical processes. It is also hoped that the research improves understanding of why rear-inflow jets behave differently within different MCSs.

The 11 June PRE-STORM squall line is simulated rather well by the model. The modeled area of surface rainfall and its expansion rearward agree particularly well with observations. An enhanced band of higher rain rates and reflectivities is produced in the model and it also drifts rearward with time. A transition zone with little or no surface rainfall forms slowly during the period in which convective influences are greatest, and then broadens rapidly, as observed, when the convective line weakens substantially. Surface rain

rates are underestimated by the model, and this appears to be at least partially due to the limitations of a 2D model in resolving the full convergence that forces the mesoscale ascent in the anvil cloud.

The model produces cooling rates from melting that agree with the general range given by Leary and Houze (1979) and the aircraft measurements from this case by Willis and Heymsfield (1989). Although melting induces significant cooling, it is restricted to a narrow layer and does not play as strong role in driving circulations within the stratiform region as evaporation. Evaporative cooling occurs over a large area with magnitudes as large as twice those of melting. It is shown that evaporative cooling itself can drive circulations that are nearly as strong as those in the full microphysical version of the model. Sublimation results in cooling similar to that of melting, and it is also restricted to a narrow layer just above the melting level and somewhat rearward from the main stratiform rain region. Vapor deposition releases latent heat over a broad region in the anvil cloud, with peak heating rates being rather small. Condensation plays a secondary role early in the simulations, but becomes dominant at later times as the mesoscale updraft intensifies. Cloud water produced by the condensation is distributed throughout the anvil cloud primarily in the 6-9 km layer, with mixing ratios generally under 0.1 g kg^{-1}. The presence of small amounts of cloud water in the anvil cloud near these levels is is supported by observations of significant cloud-to-ground lightning (Rutledge and MacGorman, 1988) even though aircraft instruments did not measure appreciable cloud water.

Vertical motions produced in the stratiform region generally agree well with observations, except for an underestimate of ascent at higher levels in the anvil cloud. Peak values of ascent are rather close to those found by both rawinsondes and Doppler radar, although the level of maximum ascent may be a little low in the model. The mesoscale downdraft is simulated accurately, with strongest descent near the 3 km level. The ascent in the anvil cloud over the length of the simulation results in significant amounts of condensate production. The percentage of surface rainfall attributable to the in situ production of condensate increases from around 15% early in the simulation to over 65% late in the simulation with the average value being around 38%. These figures generally fall within

the range given in water budget studies by Gamache and Houze (1983), Rutledge and Houze (1987) and Gallus and Johnson (1991). An increase in the ascent at higher levels to better agree w th observations would result in better agreement of surface rainfall rates with observation, and also in an increased percentage of in situ production so that the ratio might bette · agree with the 50% figure estimated for this case by Gallus and Johnson (1991).

Horizontal perturbation flows are produced agreeing with observations. The rear-inflow jet develops just behind the convective line at early times and extends farther rearward with ti ne. The peak intensity is slightly under the observed values. Rear-to-front flow is strongly underestimated at the rear of the system, and this supports the conclusions of Zhang and Gao (1991) that large scale baroclinicity produced the elevated portion of the rear-inflow jet far from the convective line. Front-to-rear flow is enhanced at mid-levels in the stratiform region by the microphysical processes within the anvil cloud. The axis of strongest front-to-rear flow agrees with observations, but the strength of the jet is overestimated. Some of this overestimate is again due to the two dimensionality of the model (Nicholls and Weissbluth, 1988). In addition, since the domain moves with the speed of the convective line, and observations showed that the stratiform region slowed in relation to the movement of the convective line at later times, some increase in front-to-rear flow above the values in Rutledge et al. (1988) and Gallus and Johnson (1991) might be expected.

Simulations that excluded convective heating produced much weaker ascent in the anvil cloud with greatly decreased production of condensate there. Without the in situ production, rain rates diminished from those of the control run, especially at later times in the simulation. Qualitatively the circulations that evolved agreed with observations but the magnitudes were much weaker than in the simulation where convective heating also affected the domain. A different simulation in which hydrometeor advection was neglected but convective heating continued to affect the domain showed that much of the strong ascent in the anvil cloud was due to the convective heating. In situ production of condensate increased over that in the run with only hydrometeor advection, but almost no

rain reached the surface. This implies that hydrometeor advection is crucial in producing significant stratiform rainfall at the surface.

A series of sensitivity tests examined both the affects of possible errors in initialization of the domain and the role of environmental conditions on features in the stratiform region. In general the tests showed that total surface rainfall is relatively insensitive to many variations in initial conditions since the same factors that increase the in situ production of condensate also increase the strength of the mesoscale downdraft and the associated water sink. Stability of the post-convective line environment proved to be very important with small increases in instability manifesting themselves as large increases in vertical motion, production and destruction of condensate. Increased instability also resulted in significant increases in surface rainfall. The stronger mesoscale downdraft in a more unstable environment resulted in increased low-level drying; which produced "onion" soundings (Zipser, 1977) that more closely matched those observed. Decreased instability weakened the vertical motions and in situ production of condensate. Sensitivity tests also indicated that surface rainfall in the stratiform region was strongly dependent on the amount of hydrometeors advecting into the domain. A positive feedback occurred so that increased hydrometeor advection resulted in an increase in the in situ production of condensate and much larger surface rainfall rates. This result shows that accurate profiles of convective cell hydrometeor contents are necessary for simulations of the stratiform region.

Sensitivity to internal model parameters was also investigated. Domain size was shown to play a relatively minor role in influencing the results. The model was also insensitive to changes in the ice activation scheme and snowflake size distribution. A change in the raindrop size distribution from Marshall-Palmer to gamma most strongly influenced the evaporation term, with a significant increase leading to more water loss and a small but noticeable reduction in surface rainfall. Decreases in mesh size resulted in increased circulations, but the changes were not overly significant.

Specialized simulations of the rear portion of the stratiform region were done using a higher resolution version of the model. The model was initialized to study a case like the

4 June PRE-STORM MCS which had intense, 6 m s^{-1} subsidence and a strong wake low in a 10 km region at the rear of the stratiform rain area. In these simulations a rear-inflow jet was initialized and large amounts of hydrometeors were permitted to come into contact with the very dry air in the jet. Intense sublimational and evaporational cooling resulted which drove a strong downdraft. Peak values of descent reached 3-5 m s^{-1} which are not significantly less than observed values. The strongest descent did occur near the back of the rain region. Because the microphysical cooling was so intense, adiabatic warming was unable to fully counter it in most areas. Most warming occurred in the subsidence above the melting level, with some at low levels in the region of strongest subsidence. In a very small region, roughly 5 km wide, a more well-defined wake low developed.

The intensity of the warming and pressure falls was rather dependent upon the sounding used to initialize the small domain. Although the finer resolution and initial conditions led to stronger dynamics within these simulations, the full intensity of features like those associated with the 4 June system was not simulated with a steady precipitation rate. Increases in adiabatic warming required stronger subsidence that could only come about with increased microphysical cooling so that pressure falls were not increased. Likewise, decreases in microphysical cooling significantly reduced descent and adiabatic warming which generally weakened the wake low. These results may be influenced by deficiencies of a 2D model, along with the idealized initial conditions.

When a collapsing precipitation core was simulated, the pressure falls were significantly greater than in the case of steady heavy precipitation, and the intensity of the wake low was similar to that observed. Downward motion was not as great as in the simulation with a steady heavy rate of precipitation, but microphysical cooling was less intense, and adiabatic warming was therefore able to induce greater pressure falls. Microphysical processes therefore do appear able to explain much of the subsidence and pressure perturbations that occur in cases like the 4 June system. One cannot rule out, however, that some other dynamic factor besides microphysical cooling is responsible for the intense descent and wake low that can sometimes be found at the rear of these systems.

Lastly, a GATE tropical oceanic squall line was simulated with the model. The model produced results again agreeing reasonably well with observations, with the exception,

possibly, of an underestimate of ascent at high levels in the anvil cloud. Even though conditions were less favorable for strong evaporative cooling in this environment, the larger amounts of hydrometeors advecting from the convective line were able to drive circulations similarly strong to those in the 11 June case. Because of the large amount of hydrometeor mass advecting rearward from the convective line the neglect of convective heating had less impact on the simulations than in the mid-latitude case.

In summary, this approach to modeling the stratiform region adequately reproduced observed features even though some simplifications to the interaction between the convective line and stratiform region were necessary. The 5 km resolution appeared to be sufficiently small to accurately simulate many features within the stratiform region, although in some systems where strong dynamics occur in the stratiform region, a smaller mesh size would be necessary. The strong sensitivity to both hydrometeor advection and tropospheric stability indicated by the model suggests that these variations may explain some of the three dimensionality seen in observed stratiform regions. Heaviest stratiform rain should occur rearward of the strongest convective elements. The most intense low-level descent and ascent aloft may occur in regions that were more unstable initially. Because the motions in the stratiform region were significantly affected by the profile of the convective heating and the amount of hydrometeors advected rearward, forecasting of these squall line events with larger meshed models will be highly dependent on the accuracy of the cumulus parameterizations used. Other studies have shown that some sort of ice class is necessary for accurate simulation of the stratiform region. Since most of the dynamics driving this model were due to ice processes, the results support the inclusion of ice into microphysical parameterizations. The total hydrometeor mass exiting the convective line is important for determining the amount and areal coverage of stratiform rain, and to a lesser extent the strength of circulations that develop in the stratiform region.

In the future, this model should be used with an even finer mesh to look at stratiform features of cases that behaved differently from the 11 June PRE-STORM squall line. The 4 June PRE-STORM MCS which was briefly discussed in Chapter 8 had a rear-inflow jet that did not descend gradually as in the 11 June case, but instead descended abruptly.

The 23-24 June MCS (Johnson and Bartels, 1992) exhibited some similarities to the 4 June case. Both of these cases had very small regions, 10 km wide or less, of intense subsidence that might require a much finer mesh to accurately simulate. Carbone et al. (1990) studied one case where this jet actually ascended. Perhaps this ascent could be investigated with his model.

Also in the future, this model should be expanded to three dimensions to enable better simulation of the ascent in the anvil cloud. In three dimensions the model could be applied to asymmetric systems in which the flow parallel to the system plays an important role. The role of the Coriolis force could also be studied.

Finally, the model could also be used to investigate circulations that may occur in winter storm systems near rain/snow boundaries, similar to the study of Lin and Stewart (1986). Radar reflectivity data could be used in the absence of detailed aircraft measurements to provide reasonably accurate estimations of hydrometeor content.

Chapter 11

REFERENCES

Anthes, R. A. and T. T. Warner, 1978: The development of mesoscale models suitable for air pollutioɪ and other meteorological studies. *Mon. Wea. Rev.*, **106**, 1045-1078.

Arakawa, A., 1966 Computational design for long-term numerical integration of the equations of fluɪd motion: Two-dimensional incompressible flow, Part I. *J. Comput. Phys.*, **1**, ː19-143.

Asselin, R., 1972: Frequency filter for time integrations. *Mon. Wea. Rev.*, **100**, 487-490.

Atlas, D., K. R. Hardy, R. Wexler and R. J. Boucher, 1963: On the origin of hurricane spiral rainbands. *Geophys. Int.*, **3**, 123-132.

Atlas, D., R. Tɪtehira, R. C. Srivastava, W. Marker and R. E. Carbone, 1969: Precipitation-induced mesoscale wind perturbations in the melting layer. *Quart. J. Roy. Meteor. Soc.*, **95**, 544-560

Augustine, J. A. and E. J. Zipser, 1987: The use of wind profilers in a mesoscale experiment. *Bull Amer. Meteor. Soc.*, **68**, 4-17.

Barnes, G. M. and K. Sieckman, 1984: The environment of fast- and slow-moving tropical mesoscale ɔonvective cloud lines. *Mon. Wea. Rev.*, **112**, 1782-1794.

Bartels, D. L. and R. A. Maddox, 1991: Midlevel cyclonic vortices generated by mesoscale convective systems. *Mon. Wea. Rev.*, **119**, 104-118.

Bergeron, T., 1950: Uber der mechanismus der ausgiebigan neiderschlage. Ber. Deut. Wetterd., **12**, 225-232.

Biggerstaff, M. I. and R. A. Houze, Jr., 1991a: Kinematic and precipitation structure of the 10-11 June 1985 squall line. *Mon. Wea. Rev.*, **119**, 3034-3065.

Biggerstaff, M. I. and R. A. Houze, Jr., 1991b: Midlevel vorticity structure of the 10-11 June 1985 squall line. *Mon. Wea. Rev.*, **119**, 3066-3079.

Bluestein, H. B. and M. H. Jain, 1985: Formation of mesoscale lines of precipitation: Severe squall lines in Oklahoma during the spring. *J. Atmos. Sci.*, **42**, 1711-1732.

Bosart, L. F. and F. Sanders, 1981: The Johnstown flood of July 1977: A long-lived convective system. *J. Atmos. Sci.*, **38**, 1616-1642.

Bott, A., 1989: A positive definite advection scheme obtained by nonlinear renormalization of the advective fluxes. *Mon. Wea. Rev.*, **117**, 1006-1015.

Brandes, E. A., 1990: Evolution and structure of the 6-7 May 1985 mesoscale convective system and associated vortex. *Mon. Wea. Rev.*, **118**, 109-127.

Brown, J. M., 1979: Mesoscale unsaturated downdrafts driven by rainfall evaporation : A numerical study. *J. Atmos. Sci.*, **36**, 313-338.

Carbone, R. E., J. W. Conway, N. A. Crook and M. W. Moncrieff, 1990: The generation and propagation of a nocturnal squall line. Part I: Observations and implications for mesoscale predictability. *Mon. Wea. Rev.*, **118**, 26-50.

Chen, S. and W. R. Cotton, 1988: The sensitivity of a simulated extratropical mesoscale convective system to longwave radiation and ice-phase microphysics. *J. Atmos. Sci.*, **45**, 3897-3910.

Chen, Y.-L. and E. J. Zipser, 1982: The role of horizontal advection of hydrometeors in the water budget of a large squall line system. *Preprints, 12th Conf. Severe Local Storms*, S; .n Antonio, Amer. Meteor. Soc., 355-358.

Cheng, C.-P. an(R. A. Houze, Jr., 1979: The distribution of convective and mesoscale precipitati ɔn in GATE radar echo patterns. *Mon. Wea. Rev.*, **107**, 1370-1381.

Cheng, C.-P. anć R. A. Houze, Jr., 1981: Inclusion of mesoscale updrafts and downdrafts in compul ations of vertical fluxes by ensembles of tropical clouds. *J. Atmos. Sci.*, **38**, 1751 1770.

Chong, M. and Ɔ. Hauser, 1990: A tropical squall line observed during the COPT 81 experimer t in West Africa. Part III: Heat and moisture budgets. *Mon. Wea. Rev.*, **118**, 16£ 6-1706.

Chong, M., P. A nayenc, G. Scialom and J. Testud, 1987: A tropical squall line observed during th ɔ COPT 81 experiment in West Africa. Part I: Kinematic structure inferred fro n dual Doppler radar data. *Mon. Wea. Rev.*, **115**, 670-694.

Churchill, D. D. ınd R. A. Houze, Jr. 1984: Development and structure of winter monsoon cloud clur ters on 10 December 1978. *J. Atmos. Sci.*, **41**, 933-960.

Churchill, D. D and R. A. Houze, Jr., 1991: Effects of radiation and turbulence on the diaba ɨic heating and water budget of the stratiform region of a tropical cloud cluster. *J Atmos. Sci.*, **48**, 903-922.

Clark, T. L., 1ⁿ77: A small-scale dynamic model using a terrain-following coordinate transforn ation. *J. Comput. Phys.*, **24**, 186-215.

Clark, T. L., 19 ʼ9: Numerical simulations with a three-dimensional cloud model. Lateral boundarȝ condition experiments and multi-cellular severe storm simulations. *J. Atmos. ʃci.*, **36**, 2191-2215.

Cotton, W. R., 1972: Numerical simulation of precipitation de *relopment* in supercooled cumuli–Part II. *Mon. Wea. Rev.*, **100**, 764-784.

Cotton, W.R. and R. A. Anthes, 1989: *Storm and Cloud Dynarics.* Academic Press, 883 pp.

Cotton, W. R., M. A. Stephens, T. Nehrkorn and G. J. Tripoli, 1982: The Colorado State University three dimensional cloud mesoscale model – 1982. Part II: an ice phase parameterization. *J. Rech. Atmos.*, **16**, No. 4, 295-320.

Cox, S. K. and K. T. Griffith, 1979: Estimation of radiation di *rergence* during Phase III of the GARP Atlantic Tropical Experiment. Part II. An *dysis* of Phase III results. *J. Atmos. Sci.*, **36**, 586-601.

Dudhia, J., 1990: Numerical study of convection observed du *ing* the Winter Monsoon Experiment using a mesoscale two-dimensional model. *J Atmos. Sci.*, **46**, 3077-3107.

Dudhia, J., and M.W. Moncrieff, 1989: A three-dimensional nt merical study of an Oklahoma squall line containing right-flank supercells. *J. Atn os. Sci.*, **46**, 3363-3391.

Dudhia, J., M. W. Moncrieff and D. W.K. So, 1987: The tw« -dimensional dynamics of West African squall lines. *Quart. J. Roy. Meteor. Soc.*, .13, 121-146.

Durran, D. R., M.-J. Yang, D. N. Slinn and R. G. Brown, 19! 3: Toward more accurate wave-permeable boundary conditions. *Mon. Wea. Rev.*, **121**, 604-620.

Esbensen, S. K., J.-T. Wang and E. I. Tollerud, 1988: A comp« site life cycle of nonsquall mesoscale convective systems over the tropical ocean. F art II: Heat and moisture budgets. *J. Atmos. Sci.*, **45**, 537-548.

Farley, R. D. and H. D. Orville, 1986: Numerical modeling of hailstorms and hailstone growth. Part I: Preliminary model verification and sensitivity tests. *J. Climate Appl. Meteor.* **25**, 2014-2035.

Ferrier, B. S. and R. A. Houze, Jr., 1989: One-dimensional time-dependent modeling of GATE cumulonimbus convection. *J. Atmos. Sci.*, **46**, 330-352.

Flatau, M. and D E. Stevens, 1987: The effect of horizontal pressure gradients on the momentum transport in tropical convective lines. Part I: The results of the convective parameterization. *J. Atmos. Sci.*, **44**, 2074-2087.

Fletcher, N. H., 1962: *The Physics of Rainclouds*, Cambridge University Press, 386 pp.

Fovell, R. G., 1991: Influence of the Coriolis force on two-dimensional model storms. *Mon. Wea. Rev.*, **119**, 606-630.

Fovell, R. G., and Y. Ogura, 1988: Numerical simulations of a mid-latitude squall line in two dimensions. *J. Atmos. Sci.*, **45**, 3846-3879.

Fovell, R. G., and Y. Ogura, 1989: Effect of vertical wind shear on numerically simulated multicell storm structure. *J. Atmos. Sci.*, **46**, 3144-3176.

Frank, W. M., 1983: The cumulus parameterization problem. *Mon. Wea. Rev.*, **111**, 1859-1871.

Frank, W. M. and C. Cohen, 1985: Properties of tropical cloud ensembles estimated using a cloud model and an observed updraft population. *J. Atmos. Sci.*, **42**, 1911-1928.

Fritsch, J. M. and C. F. Chappell, 1980: Numerical prediction of convectively driven mesoscale pressure systems. Part I: Convective parameterization. *J. Atmos. Sci.*, **37**, 1722-1733.

Fritsch, J. M. and R. A. Maddox, 1981a: Convectively driven mesoscale pressure systems aloft. Part I: Observations. *J. Appl. Meteor.*, **20**, 9-19.

Fritsch, J. M. and R. A. Maddox, 1981b: Convectively driven mesoscale pressure systems aloft. Part II: Numerical simulations. *J. Appl. Meteor.*, **20**, 20-26.

Fritsch, J. M., R. J. Kane and C. R. Chelius, 1986: The contribution of mesoscale convective weather systems to the warm-season precipitation in the United States. *J. Climate Appl. Meteor.*, **25**, 1333-1345.

Fujita, T. T., 1955: Results of detailed synoptic studies of squall lines. *Tellus*, **7**, 405-436.

Gallus, W. A., Jr. and R. H. Johnson, 1991: Heat and moisture budgets of an intense midlatitude squall line. *J. Atmos. Sci.*, **48**, 122-146.

Gallus, W. A., Jr. and R. H. Johnson, 1992: The momentum budget of an intense midlatitude squall line. *J. Atmos. Sci.*, **49**, 422-450.

Gamache, J. F. and R. A. Houze, 1982: Mesoscale air motions associated with a tropical squall line. *Mon. Wea. Rev.*, **110**, 118-135.

Gamache, J. F. and R. A. Houze, 1983: Water budget of a mesoscale convective system in the tropics. *J. Atmos. Sci.*, **40**, 1835-1850.

Gamache, J. F. and R. A. Houze, 1985: Further analysis of the composite wind and thermodynamic structure of the 12 September GATE squall line. *Mon. Wea. Rev.*, **113**, 1241-1259.

Gao, K., D.-L. Zhang, M. W. Moncrieff and H.-R. Cho, 1990: Mesoscale momentum budget in a midlatitude squall line: A numerical case study. *Mon. Wea. Rev.*, **118**, 1011-1028

Grell, G. A., 199? : Prognostic evaluation of assumptions used by cumulus parameterizations. *Mon. Wea. Rev.*, **121**, 764-787.

Gunn, K.L.S., and J. S. Marshall, 1958: The distribution with size of aggregate snowflakes. *J. Meteor.* **15**, 452-461.

Hall, W. D., 1980 A detailed microphysical model with a two-dimensional dynamic framework: model description and preliminary results. *J. Atmos. Sci.*, **37**, 2486-2507.

Hane, C. E., 197?: The squall line thunderstorm: Numerical experimentation. *J. Atmos. Sci.*, **30**, 1672-1690.

Hauser, D. and P Amayenc, 1986: Retrieval of cloud water and water vapor contents from Doppler radar data in a tropical squall line. *J. Atmos. Sci.*, **43**, 823-838.

Hemler, R. S., F. B. Lipps and B. B. Ross, 1991: A simulation of a squall line using a nonhydrostatic cloud model with a 5-km horizontal grid. *Mon. Wea. Rev.*, **119**, 3012-3033

Heymsfield, A. J. and M. R. Hjemfelt, 1984: Processes of hydrometeor development in Oklahoma convective clouds. *J. Atmos. Sci.*, **41**, 2811-2835.

Heymsfield, G. M. and S. Schotz, 1985: Structure and evolution of a severe squall line over Oklahoma. *Mon. Wea. Rev.*, **113**, 1563-1589.

Hjelmfelt, M. R , H.-Y. Chou, R. D. Farley and D. L. Priegnitz, 1992: Organization and development of a squall line in North Dakota as revealed by Doppler radar and numerical simulations. *Preprints, Fifth Conf. on Mesoscale Processes*, Atlanta, Amer. Met. Soc., 221-226.

Houghton, H. G , 1968: On precipitation mechanisms and their artificial modification. *J. Appl. Meteor.* **7**, 851-859.

Houze, R. A., Jr., 1977: Structure and dynamics of a tropical squall-line system observed during GATE. *Mon. Wea. Rev.*, **105**, 1540-1567.

Houze, R. A., Jr., 1981: Structure of atmospheric precipitation systems-a global survey. *Radio Sci.*, **16**, 671-689.

Houze, R. A., Jr., 1982: Cloud clusters and large-scale vertical motions in the tropics. *J. Meteorol. Soc. Jap.* **60**, 396-409.

Houze, R. A., Jr. and A. K. Betts, 1981: Convection in GATE. *Rev. Geoph. Space Phys.*, **19**, 541-576.

Houze, R. A., Jr. and E. N. Rappaport, 1984: Air motions and precipitation structure of an early summer squall line over the eastern tropical Atlantic. *J. Atmos. Sci.*, **41**, 553-574.

Houze, R. A., Jr., P. V. Hobbs, P. H. Herzegh and D. B. Parsons, 1979: Size distributions of precipitation particles in frontal clouds. *J. Atmos. Sci.*, **36**, 156-162.

Houze, R. A., Jr., S. A. Rutledge, M. I. Biggerstaff and B. F. Smull, 1989: Interpretation of Doppler weather radar displays of midlatitude mesoscale convective systems. *Bull. Amer. Meteor. Soc.*, **70**, 608-619.

Houze, R. A., Jr., B. F. Smull and P. Dodge, 1990: Mesoscale organization of springtime rainstorms in Oklahoma. *Mon. Wea. Rev.*, **118**, 613-654.

Hsie, E. and R. A Anthes, 1984: Simulations of frontogenesis in a moist atmosphere using alternative parameterizations of condensation and precipitation. *J. Atmos. Sci.*, **41**, 2701-2716.

Hsie, E.-Y., Anthes, R. A. and D. Keyser, 1984: Numerical simulation of frontogenesis in a moist atmosphere. *J. Atmos. Sci.*, **41**, 2581-2594.

Johnson, B. C., 1983: The heat burst of 29 May 1976. *Mon. Wea. Rev.*, **111**, 1776-1792.

Johnson, R. H., 1982: Vertical motion in near-equatorial winter monsoon convection. *J. Meteor. Soc. Jap.* **60**, 682-690.

Johnson, R. H., 1984: Partitioning tropical heat and moisture budgets into cumulus and mesoscale components: Implications for cumulus parameterization. *Mon. Wea. Rev.*, **112**, 1590-1601.

Johnson, R. H. and D. C. Kriete, 1982: Thermodynamic and circulation characteristics of winter monsoon tropical mesoscale convection. *Mon. Wea. Rev.*, **110**, 1898-1911.

Johnson, R. H. and G. S. Young, 1983: Heat and moisture budgets of tropical mesoscale anvil clouds. *J. Atmos. Sci.*, **40**, 2138-2147.

Johnson, R. H. and D. L. Bartels, 1992: Circulations associated with a mature-to-decaying midlatitude mesoscale convective system. Part II: Upper-level features. *Mon. Wea. Rev.*, **120**, 1301-1320.

Johnson, R. H., and P. J. Hamilton, 1988: The relationship of surface pressure features to the precipitation and air flow structure of an intense midlatitude squall line. *Mon. Wea. Rev.*, **116**, 1444-1472.

Johnson, R. H., S. Chen and J. J. Toth, 1989: Circulations associated with a mature-to-decaying midlatitude mesoscale convective system. Part I: Surface features-Heat bursts and mesolow development. *Mon. Wea. Rev.*, **117**, 942-959.

Johnson, R. H., W. A. Gallus, Jr. and M. D. Vescio, 1990: Near-tropopause vertical motions within the trailing stratiform regions of squall lines. *J. Atmos. Sci.*, **47**, 2200-2210.

Johnston, E. C., 1982: Mesoscale vorticity centers induced by mesoscale convective complexes. *9th Conf. on Wea. Forecasting and Analysis*, Seattle, Amer. Meteor. Soc., 196-200.

Kalb, M. W., 1985: Results from a limited area mesoscale numerical simulation for 10 April 1979. *Mon. Wea. Rev.*, **113**, 1644-1662.

Kalb, M. W., 1987: The role of convective parameterization in the simulation of a Gulf coast precipitation system. *Mon. Wea. Rev.*, **115**, 214-234.

Kasahara, A., 1961: A numerical experiment on the development of a tropical cyclone. *J. Meteorol.*, **18**, 259-282.

Kessinger, C. J., P. S. Ray and C. E. Hane, 1987: The Oklahoma squall line of 19 May 1977. Part I: A multiple Doppler analysis of convective and stratiform structure. *J. Atmos. Sci.*, **44**, 2840-2864.

Kessler, E., 1969: On the distribution and continuity of water substance in atmospheric circulations. *Met. Mon.* **10**, No. 32.

Klemp, J. B. and R. B. Wilhelmson, 1978: The simulation of three-dimensional convective storm dynamics. *J. Atmos. Sci.*, **35**, 1070-1096.

Klimowski, B. A., 1993: The June 28-29 1989 North Dakota meso-convective system: Initiation and development of rear inflow. *Mon. Wea. Rev.*, (**submitted**).

Knupp, K. R. and W. R. Cotton, 1987: Internal structure of a small mesoscale convective system. *Mon. Wea. Rev.*, **115**, 629-645.

Kreitzburg, C. W. and D. J. Perkey, 1977: Release of potential instability: Part II: The mechanism of convective/mesoscale interaction. *J. Atmos. Sci.*, **34**, 1569-1595.

Kuo, Y.-H. and R. A. Anthes, 1984: Mesoscale budgets of heat and moisture in a convective system over the central United States. *Mon. Wea. Rev.*, **112**, 1482-1497.

LaFore, J.-P., and M. W. Moncrieff, 1989: A numerical investigation of the organization and interaction of the convective and stratiform regions of tropical squall lines. *J. Atmos. Sci.*, **46**, 521-524.

Leary, C. A., 1980: Temperature and humidity profiles in mesoscale unsaturated downdrafts. *J. Atmos. Sci.*, **37**, 1005-1012.

Leary, C. A., and R. A. Houze, Jr., 1979: Melting and evaporation of hydrometeors in precipitation from the anvil clouds of deep tropical convection. *J. Atmos. Sci.*, **36**, 669-679.

Leary, C. A., and E. N. Rappaport, 1987: The life cycle and internal structure of a mesoscale convective complex. *Mon. Wea. Rev.*, **115**, 1503-1527.

LeMone, M. A., 1983: Momentum transport by a line of cumulonimbus. *J. Atmos. Sci.*, **40**, 1815-1834.

LeMone, M. A., G. M. Barnes and E. J. Zipser, 1984: Momentum flux by lines of cumulonimbus over the tropical oceans. *J. Atmos. Sci.*, **41**, 1914-1932.

Lewis, J. M, Y. Ogura, and L. Gidel, 1974: Large-scale influences upon the generation of a mesoscale disturbance. *Mon. Wea. Rev.*, **102**, 545-560.

Lin, C. A. and R. E. Stewart, 1986: Mesoscale circulations initiated by melting snow. *J. Geophys. Res.,* **91**, 13299-13302.

Lin, Y.-L., R.D. Farley and H. D. Orville, 1983: Bulk parameterization of the snow field in a cloud model. *J. Climate Appl. Meteor.*, **22**, 1065-1092.

Locatelli, J. D., and P. V. Hobbs, 1974: Fall speeds and masses of solid precipitation particles. *J. Geophys. Res.* **79**, 2185-2197.

Lord, S. J., H. E. Willoughby and J. M. Piotrowicz, 1984: Role of parameterized ice-phase microphysics in an axisymmetric, nonhydrostatic tropical cyclone model. *J. Atmos. Sci.*, **41**, 2836-2848.

Maddox, R. A., 1980: Mesoscale convective complexes. *Bull. Amer. Meteor. Soc.*, **61**, 1374-1387.

Marshall, J. S., and W. McK. Palmer, 1948: The distribution of raindrops with size. *J. Meteor.*, **5**, 165-166.

Matejka, T. and T. J. Schuur, 1991: The relationship between vertical air motions and the precipitation band in the stratiform region of a squall line. *Preprints, 25th International Conf. on Radar Meteor.*, Paris, Amer. Meteor. Soc., 501-504.

McAnelly, R. L. and W. R. Cotton, 1986: Meso-β-scale characteristics of meso-α- scale convective complexes. *Mon. Wea. Rev.*, **114**, 1740-1770.

McCumber, M., W.-K. Tao, J. Simpson, R. Penc and S.-T. Soong, 1991: Comparison of ice-phase microphysical parameterization schemes using numerical simulations of tropical convection. *J. Appl. Meteor.* **30**, 985-1004.

Menard, R. D., D. L. Sims and J. M. Fritsch, 1988: Case example of the effect of a wake low on subsequent convective events. Preprints, *15th Conf. on Severe Local Storms*, Baltimore, Amer. Meteor. Soc., 225-228.

Molinari, J. and M. Dudek, 1986: Implicit versus explicit convective heating in numerical weather prediction models. *Mon. Wea. Rev.*, **114**, 1822-1831.

Moncrieff, M. W., 1978: The dynamical structure of two-dimensional steady convection in constant vertical shear. *Quart. J. Roy. Meteorol. Soc.*, **104**, 543-567.

Moncrieff, M. W., 1981: A theory of organized steady convection and its transport properties. *Quart. J. Roy. Meteorol. Soc.*, **107**, 29-50.

Moncrieff, M. W. and Miller, M. J., 1976: The dynamics and simulation of tropical cumulonimbus and squall lines. *Quart. J. Roy. Meteorol Soc.*, **102**, 373-394.

Myers, M. P., P. J. DeMott and W. R. Cotton, 1992: New primary ice-nucleation parameterization in an explicit cloud model. *J. Appl. Meteor.* **31**, 708-721.

Newton, C. W., 1950: Structure and mechanisms of the prefrontal squall line. *J. Meteor.* **7**, 210-223.

Newton, C. W., 1966: Circulations in large sheared cumulonimbus. *Tellus*, **18**, 699-712.

Newton, C. W. and J. C. Fankhauser, 1964: On the movements of convective storms, with emphasis on size discrimination in relation to water-budget requirements. *J. Appl. Meteor.* **3**, 651-668.

Nicholls, M.E., 1987: A comparison of the results of a two dimensional numerical simulation of a tropical squall line with observations. *Mon. Wea. Rev.*, **115**, 3055-3077.

Nicholls, M.E. and M. J. Weissbluth, 1988: A comparison of two-dimensional and quasi-three dimensional simulations of a tropical squall line. *Mon. Wea. Rev.*, **116**, 2437-2452.

Nicholls, M.E., R. H. Johnson and W. R. Cotton, 1988: The sensitivity of two-dimensional simulations of tropical squall lines to environmental profiles. *J. Atmos. Sci.*, **45**, 3625-3649.

Nickerson, E. C., E. R. Richard, R. Rosset and D. R. Smith, 1986: The numerical simulation of clouds, rain, and airflow over the Vosges and Black Forest Mountains: A meso-beta model with parameterized microphysics. *Mon. Wea. Rev.*, **114**, 398-414.

Ninomiya, K., 1971: Mesoscale modification of synoptical situations from thunderstorm development as revealed by ATS III and aerological data. *J. Appl. Meteor.* **10**, 1103-1121.

Ogura, Y. and N. A. Phillips, 1962: Scale analysis of deep and shallow convection in the atmosphere. *J. Atmos. Sci.*, **19**, 173-179.

Ogura, Y. and T. Takahashi, 1973: The development of warm rain in a cumulus model. *J. Atmos. Sci.*, **30**, 262-277.

Ogura, Y. and M.-T. Liou, 1980: The structure of a midlatitude squall line: a case study. *J. Atmos. Sci.*, **37**, 553-567.

Orlanski, I., 1975: A rational subdivision of scales for atmospheric processes. *Bull. Amer. Meteor. Soc.*, **56**, 527-530.

Orlanski, I., 1976: A simple boundary condition for unbounded hyperbolic flows. *J. Comput. Phys.*, **21**, 251-269.

Orlanski, I. and B. B. Ross, 1973: Numerical simulation of the generation and breaking of internal gravity waves. *J. Geophys. Res.*, **78**, 8808-8826.

Orlanski, I. and B. B. Ross, 1977: The circulation associated with a cold front. Part I: Dry case. *J. Atmos. Sci.*, **33**, 1619-1633.

Orville, H. D. and F. J. Kopp, 1977: Numerical simulation of the life history of a hailstorm. *J. Atmos. Sci.*, **34**, 1596-1618.

Pedgley, D. E., 1962: A meso-synoptic analysis of the thunderstorms on 28 August 1958. *Brit. Meteor. Off., Geophys. Mem.* **106**, 74 pp.

Perkey, D. J. and R. A. Maddox, 1985: A numerical investigation of a mesoscale convective system. *Mon. Wea. Rev.*, **113**, 553-566.

Pointin, Y., 1985: Numerical simulation of organized convection. Part I: Model description and preliminary comparisons with squall line observations. *J. Atmos. Sci.*, **42**, 155-172.

Potter, B. E., 1991: Improvements to a commonly used cloud microphysical bulk parameterization. *J. Appl. Meteor.* **30**, 1040-1042.

Proctor, F.H., 1988: Numerical simulations of an isolated microburst. Part II: Dynamics and structure. *J. Atmos. Sci.*, **45**, 3137-3160.

Rasmussen, E. N. and S. A. Rutledge, 1993: Evolution of quasi-two-dimensional squall lines. Part I: Kinematic and reflectivity structure. *J. Atmos. Sci.*, **50**, 2584-2606.

Raymond, W. H. and H.-L. Kuo, 1981: A radiation boundary condition for multi-dimensional flows. In: Kuo, H.-L., W. H. Raymond and K. L. Seitter, 1981: *Theoretical Studies of Squall-line Type and Tornado-like Disturbances*, AFGL-TR-82-0005, 65-96 [Available through NTIS and DTIC, AD-A113 086/3.]

Redelsberger J. L. and J. P. LaFore, 1988: A three-dimensional simulation of a tropical squall line: Convective organization and thermodynamic vertical transport. *J. Atmos. Sci.*, **45**, 1334-1356.

Rickenbach, T. M., 1990: Precipitation processes and water budget study of the 10-11 June 1985 mesoscale convective system. M. S. thesis, Colorado State University, 180 pp. [Available from Atmos. Sci. Dept., Colorado State University, Ft. Collins, CO, 80523.]

Riehl, H. and J. S. Malkus, 1958: On the heat balance in the equatorial trough zone. *Geophysica* **6**, 503-538.

Rosenthal, S. L., 1978: Numerical simulation of tropical cyclone development with latent heat release by the resolvable scales. I: Model description and preliminary results. *J. Atmos. Sci.*, **35**, 258-271.

Rosenthal, S. L., 1979: The sensitivity of simulated hurricane development to cumulus parameterization details. *Mon. Wea. Rev.*, **107**, 193-197.

Ross, B. B. and I. Orlanski, 1982: The evolution of an observed cold front. Part I: Numerical simulation. *J. Atmos. Sci.*, **39**, 296-327.

Roux, F., 1988: The West African squall line observed on 23 June 1981 during COPT 81: Kinematics and thermodynamics of the convective region. *J. Atmos. Sci.*, **45**, 406-426.

Roux, F., J. Testud, M. Payen and B. Pinty, 1984: West African squall line thermodynamic structure retrieved from dual-Doppler radar observations. *J. Atmos. Sci.*, **41**, 3104-3120.

Rotunno, R. and K. A. Emanuel, 1987: An air-sea interaction theory for tropical cyclones. Part II: Evolutionary study using a nonhydrostatic axisymmetric numerical model. *J. Atmos. Sci.*, **44**, 542-561.

Rutunno, R., J. B. Klemp and M. L. Weisman, 1988: A theory for strong, long-lived squall lines. *J. Atmos. Sci.*, **45**, 463-485.

Rutledge, S. A., 1986: A diagnostic numerical study of the stratiform region associated with a tropical squall line. *J. Atmos. Sci.*, **43**, 1337-1358.

Rutledge, S. A. and P. V. Hobbs, 1983: The mesoscale and microscale structure and organization of clouds and precipitation in midlatitude cyclones. VIII: A model for the "Seeder-Feeder" process in warm-frontal rainbands. *J. Atmos. Sci.*, **40**, 1185-1206.

Rutledge, S. A. and P. V. Hobbs, 1984: The mesoscale and microscale structure and organization of clouds and precipitation in midlatitude cyclones. XII: A diagnostic modeling study of precipitation development in narrow cold-frontal rainbands. *J. Atmos. Sci.*, **41**, 2949-2972.

Rutledge, S. A. and R. A. Houze, Jr. 1987: A diagnostic modeling study of the trailing stratiform region of a midlatitude squall line. *J. Atmos. Sci.*, **44**, 2640-2656.

Rutledge, S. A. and D. R. MacGorman, 1988: Cloud-to-ground lightning activity in the 10-11 June 1985 mesoscale convective system observed during the Oklahoma-Kansas PRE-STORM project. *Mon. Wea. Rev.*, **116**, 1393-1408.

Rutledge, S. A., R. A. Houze, Jr., M. I. Biggerstaff, and T. Matejka, 1988: The Oklahoma-Kansas mesoscale convective system of 10-11 June 1985: precipitation structure and single-Doppler radar analysis. *Mon. Wea. Rev.*, **116**, 1409-1430.

Sanders, F. and R. J. Paine, 1975: The structure and thermodynamics of an intense mesoscale convective storm in Oklahoma. *J. Atmos. Sci.*, **32**, 1563-1579.

Sanders, F. and K. A. Emanuel, 1977: The momentum budget and temporal evolution of a mesoscale convective system. *J. Atmos. Sci.*, **34**, 322-330.

Schmidt, J. M. and W. R. Cotton, 1990: Interactions between upper and lower atmospheric gravity waves on squall line structure and maintenance. *J. Atmos. Sci.*, **47**, 1205-1222.

Schubert, W. H., S. R. Fulton and R. F. A. Hertenstein, 1989: Balanced atmospheric response to squall lines. *J. Atmos. Sci.*, **46**, 2478-2483.

Scott, B. C. and P. V. Hobbs, 1977: A theoretical study of the evolution of mixed phase cumulus clouds. *J. Atmos. Sci.*, **34**, 812-826.

Seitter, K. L., and H.-L. Kuo, 1983: The dynamic structure of squall-line type thunderstorms. *J. Atmos. Sci.*, **40**, 2831-2854.

Smull, B. F. and R. A. Houze, 1985: A midlatitude squall line with a trailing region of stratiform rain: Radar and satellite observations. *Mon. Wea. Rev.*, **113**, 117-133.

Smull, B. F. and R. A. Houze, 1987a: Dual-Doppler radar analysis of a midlatitude squall line with a trailing region of stratiform rain. *J. Atmos. Sci.*, **43**, 356-377.

Smull, B. F. and R. A. Houze, 1987b: Rear inflow in squall lines with trailing stratiform precipitation. *Mon. Wea. Rev.*, **115**, 2869-2889.

Smull, B. F. and J. A. Augustine, 1993: Multiscale analysis of a mature mesoscale convective complex. *Mon. Wea. Rev.*, **121**, 103-132.

Sommeria, G. and J. Testud, 1984: COPT 81: a field experiment designed for the study of dynamics and electrical activity of deep convection in continental tropical regions. *Bull. Amer. Meteor. Soc.*, **65**, 4-10.

Soong, S. T. and Y. Ogura, 1980: Response of trade-wind cumuli to large-scale processes. *J. Atmos. Sci.*, **37**, 2035-2050.

Srivastava, R. C., 1987: A model of intense downdrafts driven by the melting and evaporation of precipitation. *J. Atmos. Sci.*, **44**, 1752-1773.

Srivastava, R. C., T. J. Matejka, and T. J. Lorello, 1986: Doppler radar study of the trailing anvil region associated with a squall line. *J. Atmos. Sci.*, **43**, 356-377.

Stensrud, D. J., R. A. Maddox and C. L. Ziegler, 1991: A sublimation-initiated mesoscale downdraft and its relation to the wind field below a precipitating anvil cloud. *Mon. Wea. Rev.*, **119**, 2124-2139.

Stephens, G. L., 1983: The influence of radiative transfer on the mass and heat budgets of ice crystals falling in the atmosphere. *J. Atmos. Sci.*, **40**, 1729-1739.

Stewart, R. E., J. D. Marwitz, J. C. Pace and R. E. Carbone, 1984: Characteristics through the melting layer of stratiform cloud. *J. Atmos. Sci.*, **41**, 3227-3237.

Stumpf, G. J., R. H. Johnson and B. F. Smull, 1991: The wake low in a midlatitude mesoscale convective system having complex convective organization. *Mon. Wea. Rev.*, **119**, 134-158.

Szeto, K. K., C. A. Lin and R. E. Stewart, 1988a: Mesoscale circulations forced by melting snow. Part I: Basic simulations and dynamics. *J. Atmos. Sci.*, **45**, 1629-1641.

Szeto, K. K., R. E. Stewart and C. A. Lin, 1988b: Mesoscale circulations forced by melting snow. Part II: Application to meteorological features. *J. Atmos. Sci.*, **45**, 1642-1650.

Takahashi, T., 1976: Hail in an axisymmetric cloud model. *J. Atmos. Sci.*, **33**, 1579-1601.

Takeda, T., 1965: The downdraft in convective showercloud under the vertical wind shear and its significance for the maintenance of convective systems. *J. Meteor. Soc. Jap* **43**, 302-309.

Takeda, T., 1971: Numerical simulation of a precipitating cloud: The formation of a "long-lasting" cloud. *J. Atmos. Sci.*, **28**, 350-376.

Tao, W.-K. and J. Simpson, 1989: Modeling study of a tropical squall-type convective line. *J. Atmos. Sci.*, **46**, 177-202.

Tao, W.-K. J. Simpson and S.-T. Soong, 1991: Numerical simulation of a subtropical squall line over the Taiwan Strait. *Mon. Wea. Rev.*, **119**, 2699-2723.

Tao, W.-K. J. Simpson, C.-H. Sui, B. Ferrier, S. Lang, J. Scala, M.-D. Chou and K. Pickering , 1993: Heating, moisture and water budgets of tropical and midlatitude squall lines: Comparison and sensitivity to longwave radiation. *J. Atmos. Sci.*, **50**, 673-690.

Thorpe, A. J., M. J. Miller and M. W. Moncrieff, 1982: Two-dimensional convection in nonconstant shear: a model of midlatitude squall lines. *Quart. J. Roy. Meteorol. Soc.*, , **108**, 739-762.

Tripoli, G. J. and W. R. Cotton, 1978: Cumulus convection in shear flow - three dimensional numerical experiments. *J. Atmos. Sci.*, **35**, 1503-1521.

Tripoli, G. J. and W. R. Cotton, 1982: The Colorado State University three-dimensional cloud/ mesoscale model - 1982. Part I: General theoretical framework and sensitivity experiments. *J. de. Rech. Atmos.*, **16**, 185-200.

Verlinde, J. and W. R. Cotton, 1990: A mesoscale vortex couplet observed in the trailing anvil of a multicellular convective complex. *Mon. Wea. Rev.*, **118**, 993-1010.

Webster, P. J. and G. L. Stephens, 1980: Tropical upper-tropospheric extended clouds: Inferences from winter MONEX. *J. Atmos. Sci.*, **37**, 1521-1541.

Weisman, M. L., 1992: The role of convectively generated rear-inflow jets in the evolution of long-lived meso-convective systems. *J. Atmos. Sci.*, **49**, 1826-1847.

Weisman, M. L., and J. B. Klemp, 1982: The dependence of numerically simulated convective storms on wind shear and buoyancy. *Mon. Wea. Rev.*, **110**, 504-520.

Weisman, M. L., J. B. Klemp and R. Rotunno, 1988: Structure and evolution of numerically simulated squall lines. *J. Atmos. Sci.*, **45**, 1990-2013.

Willis, P. T., 1984: Functional fits to some observed drop size distributions and parameterization of rain. *J. Atmos. Sci.*, **41**, 1648-1661.

Willis, P. T. and A. J. Heymsfield, 1989: Structure of the melting layer in mesoscale convective system stratiform precipitation. *J. Atmos. Sci.*, **46**, 2008-2025.

Willoughby, H. E., H. Jin, S. J. Lord and J. M. Piotrowicz, 1984: Hurricane structure and evolution as simulated by an axisymmetric, nonhydrostatic numerical model. *J. Atmos. Sci.*, **41**, 1169-1186.

Yamasaki, M., 1977: A preliminary experiment of the tropical cyclone without parameterizing the effects of cumulus convection. *J. Meteorol. Soc. Jap.*, **55**, 11-30.

Yoshizaki, M., 1986: Numerical simulations of tropical squall-line clusters: Two-dimensional model. *J. Meteorol. Soc. Jpn.* **64**, 469-491.

Zhang, D. -L., 1992: The formation of a cooling-induced mesovortex in the trailing stratiform region of a midlatitude squall line. *Mon. Wea. Rev.*, **120**, 2763-2785.

Zhang, D.-L. and J.M.Fritsch, 1986: Numerical simulation of the mesoβ scale structure and evolution of the 1977 Johnstown flood. Part I: Model description and verification. *J. Atmos. Sci.*, **43**, 1913-1943

Zhang, D.-L. and J.M.Fritsch, 1987: Numerical simulation of the mesoβ scale structure and evolution of the 1977 Johnstown flood. Part II: Inertially stable warm core vortex and the mesoscale convective complex. *J. Atmos. Sci.*, **44**, 2593-2612.

Zhang, D.-L. and J. M. Fritsch, 1988a: Numerical sensitivity experiments of varying model physics on the structure, evolution and dynamics of two mesoscale convective systems. *J. Atmos. Sci.*, **45**, 261-293.

Zhang, D.-L. and J. M. Fritsch, 1988b: A numerical investigation of a convectively generated, inertially stable, extratropical warm-core mesovortex over land. Part I: Structure and evolution. *Mon. Wea. Rev.*, **116**, 2660-2687.

Zhang, D.-L. and K. Gao, 1989: Numerical simulation of an intense squall line during 10-11 June 1985 PRE-STORM. Part II: Rear inflow, surface pressure perturbations and stratiform precipitation. *Mon. Wea. Rev.*, **117**, 2067-2094.

Zhang, D.-L. and H.-R. Cho, 1992: The development of negative moist potential vorticity in the stratiform region of a simulated squall line. *Mon. Wea. Rev.*, **120**, 1322-1341.

Zhang, D.-L., E.-Y. Hsie and M. W. Moncrieff, 1988: A comparison of explicit and implicit predictions of convective and stratiform precipitating weather systems with a mesoβ-scale numerical model. *Quart. J. Roy. Meteorol. Soc.*, **114**, 31-60.

Zhang, D.-L., K. Gao and D. B. Parsons, 1989: Numerical simulation of an intense squall line during 10-11 June 1985 PRE-STORM. Part I: Model verification. *Mon. Wea. Rev.*, **117**, 960-994.

Ziegler, C. L., 1985: Retrieval of thermal and microphysical variables in observed convective storms. Part I: Model development and preliminary testing. *J. Atmos. Sci.*, **42**, 1487-1509.

Ziegler, C. L., P. S. Ray and D. R. MacGorman, 1986: Relations of kinematics, microphysics and electrification in an isolated mountain thunderstorm. *J. Atmos. Sci.*, **43**, 2098-2114.

Zipser, E. J., 1969: The role of organized unsaturated convective downdrafts in the structure and rapid decay of an equitorial disturbance. *J. Appl. Meteor.* **8**, 799-814.

Zipser, E. J., 1977: Mesoscale and convective-scale downdrafts as distinct components of squall-line structure. *Mon. Wea. Rev.*, **105**, 1568-1589.

Appendix A

MICROPHYSICAL PARAMETERIZATION

The microphysical parameterization used in this model is the six water class scheme used by Rutledge and Hobbs (1983, 1984) which is similar to the parameterization described in Lin et al. (1983). Minor modifications have been made to these schemes, including the corrections to the snow and graupel fallspeeds discussed in Potter (1991). The equations are shown here with little detail. A more comprehensive description can be found in Rutledge and Hobbs (1983, 1984).

A.1 *Size distributions*

For rain, a Marshall and Palmer (1948) size distribution is assumed as given by:

$$N_{DR} = N_{0R}exp(-\lambda_R D_R)dD_R \qquad (A1a)$$

where $N_{DR}[m^{-3}]$ is the number of raindrops per cubic meter with diameters between D_R and $D_R + dD_R$. The coefficient $N_{0R}[m^{-4}]$ is the constant slope intercept with a value of $8 \times 10^6 \ m^{-4}$, and $\lambda_R[m^{-1}]$ is the distribution slope.

For the gamma distribution used in one sensitivity test, the raindrop size distribution is given by

$$N'_{DR} = N'_{0R}D_R^{\alpha}exp(-\lambda'_R D_R)dD_R, \qquad (A1b)$$

where most of the notation is similar to the Marshall-Palmer distribution, and α is a constant curvature parameter for the size distribution set equal to 2.5 (Willis, 1984). With the gamma distribution, N'$_{0R}$ is not a constant, and varies with rainwater concentration as

$$N'_{0R} = \frac{6.36 \times 10^{-4} M}{D_0{}^4} \left(\frac{1}{D_0}\right)^{2.5}, \qquad (A1c)$$

with D_0[cm] the median volume diameter calculated empirically from the relation

$$D_0 = 0.157 M^{0.168}, \qquad (A1d)$$

where $M = \rho q_R$[g m^{-3}]. In the gamma distribution, the slope is given by

$$\lambda'_R = \frac{5.57}{D_0}. \qquad (A1e)$$

For snow, the size distribution is assumed to be that given by Gunn and Marshall (1958):

$$N_{DS} = N_{0S} exp(-\lambda_S D_S) dD_S \qquad (A2)$$

where N_{DS} and λ_S are defined similarly as above. The slope intercept coefficient N_{0S} is taken from Rutledge and Hobbs (1984) to be $4 \times 10^6 m^{-4}$.

The graupel size distribution is defined as in Rutledge and Hobbs (1984) as:

$$N_{DG} = N_{0G} exp(-\lambda_G D_G) dD_G \qquad (A3)$$

where N_{DG} and λ_G are defined similarly as above. The slope intercept coefficient N_{0G} is equal to N_{0S} based on the study of Houze et al. (1979).

A.2   Mass-weighted fallspeeds

All hydrometeors in the precipitating fields are assumed to fall at their mass-weighted fallspeeds. For rain, the polynomial fit used in Rutledge and Hobbs (1983),

$$V_R(D_R) = -0.267 + 51.5 D_R - 102.25 D_R^2 + 75.5 D_R^3, \qquad (A4)$$

determines the fallspeed, where D_R is in cm and V_R is in ms^{-1}. Making appropriate substitutions, the equation becomes:

$$\overline{V}_R = (-0.267 + 206\lambda_R^{-1} - 2.045 \times 10^3\lambda_R^{-2} + 9.06 \times 10^3\lambda_R^{-3})\left(\frac{p_0}{p}\right)^{0.4}, \qquad (A5a)$$

where $\lambda_R(cm^{-1})$ is given by Eq. 3.7a. In a sensitivity test in which the Marshall-Palmer distribution was replaced by the gamma distribution, integrations of equations were simplified by using a fall speed equation for rain of the form

$$V_R(D_R) = 3000s^{-1}D_R. \qquad (A5b)$$

The fallspeed equation for snow is derived similarly to Rutledge and Hobbs (1983) and is

$$\overline{V}_S = a''\frac{\Gamma(4 + b)}{6}\lambda_S^{-b}\left(\frac{p_0}{p}\right)^{0.4}, \qquad (A6)$$

where λ_S is given by Eq. 3.7b, and the values of a" and b as shown in Appendix B differ from those previously used by Lin et al. (1983), and Rutledge and Hobbs (1983) because of corrections suggested by Potter (1991).

The fallspeed equation for graupel is derived as in Rutledge and Hobbs (1984) and is

$$\overline{V}_G = a'''\frac{\Gamma(4 + b')}{6}\lambda_G^{-b'}\left(\frac{p_0}{p}\right)^{0.4}, \qquad (A7)$$

where λ_G is given by Eq. 2.7c, and a"' and b' (see Appendix B) are adjusted (Potter, 1991) from the values used in Rutledge and Hobbs (1984).

A.3   Sources and sinks of water continuity variables

1) CONDENSATION AND EVAPORATION OF CLOUD WATER (PCOND)

$$PCOND = \rho(q_v - q_{sw})\left[\Delta t\left(1 + \frac{L_v^2 q_{sw}}{c_p R_w T^2}\right)\right]^{-1} \qquad (A8)$$

2) AUTOCONVERSION OF CLOUD WATER (PRAUT)

$$PRAUT = \alpha'\rho(q_c - q_o) \qquad (A9)$$

3) COLLECTION OF CLOUD WATER BY RAINWATER (PRACW)

$$PRACW = \frac{\pi}{4}\rho q_c E_{RC} N_{0R} \left(\frac{p_0}{p}\right)^{0.4} \times \left[\frac{a_0\Gamma(3)}{\lambda_R{}^3} + \frac{a_1\Gamma(4)}{\lambda_R{}^4} + \frac{a_2\Gamma(5)}{\lambda_R{}^5} + \frac{a_3\Gamma(6)}{\lambda_R{}^6}\right] \quad (A10)$$

4) EVAPORATION OF RAINWATER (PREVP)

$$PREVP = \frac{2\pi N_{0R}(S-1)}{A'+B'} \times \left[\frac{0.78}{\lambda_R{}^2} + 0.31 S_c{}^{1/3}\frac{(a'\rho/\mu)^{.5}}{\lambda_R{}^3}\Gamma(3)\left(\frac{p_0}{p}\right)^{0.2}\right] \quad (A11)$$

with

$$A' = \frac{L_v}{K_a T}\left(\frac{L_v M_w}{R^* T} - 1\right)$$

and

$$B' = R^* T / \chi M_w e_{sw}$$

For the sensitivity test in which the Marshall-Palmer size distribution was replaced by the gamma distribution, the equation for evaporation of rainfall becomes:

$$PREVP = \frac{2\pi N'_{0R}(S-1)}{A'+B'} \times \left[\frac{0.78\Gamma(2+\alpha)}{\lambda'_R{}^{(2+\alpha)}} + 0.31 S_c{}^{1/3}\frac{(a'\rho_L/\mu)}{\lambda'_R{}^{(3+\alpha)}}\Gamma(3+\alpha)\left(\frac{p_0}{p}\right)^{0.2}\right] \quad (A11')$$

5) INITIATION OF CLOUD ICE (PINT)

The concentration of ice crystals existing when T < 0°C and the air is saturated with respect to ice is assumed to be given by the Fletcher (1962) formula,

$$n_{ci} = n_0 exp[\beta(T_0 - T)], \quad (A12a)$$

for the dependence of activated ice nuclei on temperature. The Myers et al. (1992) formula for ice nuclei activation, which is dependent on moisture content and may be better at temperatures warmer than -25° C, was used in a sensitivity test (discussed in

Chapter 7), and did not lead to significant changes. Therefore, the Fletcher formulation and the same procedure of Rutledge and Hobbs (1983) was again used here.

$$PINT = MIN \left\{ \begin{array}{l} M_0 n_{ci}/\Delta t \\ \rho(q_v - q_{si})/\Delta t \end{array} \right. \tag{A12b}$$

6) DEPOSITIONAL GROWTH OF CLOUD ICE (PDEPI)

$$PDEPI = \frac{65.2 M_I^{.5}(S_i - 1)n_{ci}}{A'' + B''} \tag{A13}$$

with

$$A'' = \frac{L_v}{K_a T}\left(\frac{L_s M_w}{R^* T} - 1\right)$$

and

$$B'' = R^* T/\chi M_w e_{si}$$

7) CONVERSION OF CLOUD ICE TO SNOW (PCONV)

$$PCONV = \rho(q_i - M_{max} n_{ci}/\rho) \tag{A14}$$

8) COLLECTION OF CLOUD ICE BY SNOW (PSACI)

$$PSACI = \frac{\rho \pi a'' q_i E_{SI} N_{0S}}{4}\left(\frac{po}{p}\right)^{0.4}\frac{\Gamma(b+3)}{\lambda_S^{b+3}} \tag{A15}$$

9) COLLECTION OF CLOUD WATER BY SNOW (PSACW)

$$PSACW = \frac{\rho \pi a'' q_c E_{SC} N_{0S}}{4}\left(\frac{po}{p}\right)^{0.4}\frac{\Gamma(b+3)}{\lambda_S^{b+3}} \tag{A16}$$

10) MELTING OF SNOW (PSMLT)

$$PSMLT = -\frac{2\pi N_{0S}}{L_f}K_a(T - T_0) \times \left[\frac{0.65}{\lambda_S^2}\right.$$

$$\left. +0.44 S_c^{1/3}(a''\rho/\mu)^{.5}\left(\frac{po}{p}\right)^{0.2}\frac{\Gamma\left(\frac{b}{2}+\frac{5}{2}\right)}{\lambda_S^{b/2+5/2}}\right] \tag{A17}$$

11) DEPOSITIONAL GROWTH OF SNOW (PSDEP)

$$PSDEP = \frac{4(S_i - 1)N_{0S}}{A'' + B''} \times \left[\frac{0.65}{\lambda_S^2} + 0.44S_c^{1/3}(a''\rho/\mu)^{.5}\left(\frac{p_0}{p}\right)^{0.2}\frac{\Gamma\left(\frac{b}{2} + \frac{5}{2}\right)}{\lambda_S^{b/2+5/2}}\right] \quad (A18)$$

12) EVAPORATION OF MELTING SNOW (PMLTEV)

$$PSMLTEV = \frac{4(S - 1)N_{0S}}{A' + B'} \times \left[\frac{0.65}{\lambda_S^2}\right.$$

$$\left. +0.44S_c^{1/3}(a''\rho/\mu)^{.5}\left(\frac{p_0}{p}\right)^{0.2}\frac{\Gamma\left(\frac{b}{2} + \frac{5}{2}\right)}{\lambda_S^{b/2+5/2}}\right] \quad (A19)$$

13) MELTING OF CLOUD ICE (PSMLTI)

$$PSMLTI = \rho q_i/\Delta t \quad (A20)$$

14) GRAUPEL INITIATION BY RAIN-CLOUD ICE COLLISIONS (PRACI, PI-ACR)

$$PRACI = \frac{\pi}{4}\rho q_i E_{RI} N_{0R}\left(\frac{p_0}{p}\right)^{0.4} \times \left[\frac{a_0\Gamma(3)}{\lambda_R^3} + \frac{a_1\Gamma(4)}{\lambda_R^4} + \frac{a_2\Gamma(5)}{\lambda_R^5} + \frac{a_3\Gamma(6)}{\lambda_R^6}\right] \quad (A21)$$

$$PIACR = n_{ci}E_{RI}\frac{\pi^2}{24}\rho_L N_{0R}\left(\frac{p_0}{p}\right)^{0.4} \times \left[\frac{a_0\Gamma(6)}{\lambda_R^6} + \frac{a_1\Gamma(7)}{\lambda_R^7} + \frac{a_2\Gamma(8)}{\lambda_R^8} + \frac{a_3\Gamma(9)}{\lambda_R^9}\right] \quad (A22)$$

15) GRAUPEL INITIATION BY COLLISIONS BETWEEN RAIN AND SNOW (PSACR, PRACS)

$$PSACR = E_{SR}\pi^2\rho_L N_{0R}N_{0S}\left|\overline{V}_S - \overline{V}_R\right|\left(\frac{p_0}{p}\right)^{0.4} \times$$

$$\left[\frac{5}{\lambda_R^6\lambda_S} + \frac{2}{\lambda_R^5\lambda_S^2} + \frac{0.5}{\lambda_R^4\lambda_S^3}\right] \quad (A23)$$

$$PRACS = E_{SR}\pi^2\rho_S N_{0R}N_{0S}\left|\overline{V}_R - \overline{V}_S\right|\left(\frac{p_0}{p}\right)^{0.4} \times$$

$$\left[\frac{5}{\lambda_S^6\lambda_R} + \frac{2}{\lambda_S^5\lambda_R^2} + \frac{0.5}{\lambda_S^4\lambda_R^3}\right] \quad (A24)$$

16) GRAUPEL INITIATION BY SNOW-CLOUD WATER COLLISIONS (PWACS)

$$PWACS = n_c E_{SC} \frac{\pi^2}{24} a'' \rho_S N_{0S} \left(\frac{p_0}{p}\right)^{0.4} \frac{\Gamma(b+6)}{\lambda_S^{b+6}} \qquad (A25)$$

17) COLLECTION OF CLOUD WATER BY GRAUPEL (PGACW)

$$PSACW = \frac{\rho \pi a''' q_c E_{GC} N_{0G}}{4} \left(\frac{p_0}{p}\right)^{0.4} \frac{\Gamma(b'+3)}{\lambda_G^{b'+3}} \qquad (A26)$$

18) COLLECTION OF RAIN BY GRAUPEL (PGACR)

$$PGACR = E_{GR} \pi^2 \rho_L N_{0R} N_{0G} \left|V_G - V_R\right| \left(\frac{p_0}{p}\right)^{0.4} \times$$
$$\left[\frac{5}{\lambda_R^6 \lambda_G} + \frac{2}{\lambda_R^5 \lambda_G^2} + \frac{0.5}{\lambda_R^4 \lambda_G^3}\right] \qquad (A27)$$

19) DEPOSITIONAL GROWTH OF GRAUPEL (PGDEP)

$$PGDEP = \frac{2\pi(S_i - 1)N_{0G}}{A'' + B''} \times \left[\frac{0.78}{\lambda_G^2} + 0.31 S_c^{1/3}(a''' \rho/\mu)^{.5} \left(\frac{p_0}{p}\right)^{0.2} \frac{\Gamma\left(\frac{b'}{2} + \frac{5}{2}\right)}{\lambda_G^{b'/2+5/2}}\right] \qquad (A28)$$

20) MELTING OF GRAUPEL (PGMLT)

$$PGMLT = -\frac{2\pi N_{0G}}{L_f} K_a(T - T_0) \times \left[\frac{0.78}{\lambda_G^2}\right.$$
$$\left. +0.31 S_c^{1/3}(a''' \rho/\mu)^{.5} \left(\frac{p_0}{p}\right)^{0.2} \frac{\Gamma\left(\frac{b'}{2} + \frac{5}{2}\right)}{\lambda_G^{b'/2+5/2}}\right] \qquad (A29)$$

21) EVAPORATION OF MELTING GRAUPEL (PMLTGE)

$$PSMLTGE = \frac{2\pi(S - 1)N_{0G}}{A' + B'} \times \left[\frac{0.78}{\lambda_G^2}\right.$$
$$\left. +0.31 S_c^{1/3}(a''' \rho/\mu)^{.5} \left(\frac{p_0}{p}\right)^{0.2} \frac{\Gamma\left(\frac{b'}{2} + \frac{5}{2}\right)}{\lambda_G^{b'/2+5/2}}\right] \qquad (A30)$$

22) SHEDDING OF ACCRETED WATER (PGSHR)

$$PGSHR = PGACR + PGACW \qquad (A31)$$

23) ENHANCEMENT OF THE MELTING OF GRAUPEL BY THE ACCRETION OF WATER (PGACWM, PGACRM)

$$PGACRM = \frac{-c_w}{L_f}(T - T_0)(PGACR) \tag{A32}$$

$$PGACWM = \frac{-c_w}{L_f}(T - T_0)(PGACW) \tag{A33}$$

A.4 *Source terms for the water continuity variables*

For water vapor q_v:

$$S_v = -[PCOND + PREVP + PSDEP + PGDEP+$$

$$(PMLTEV + PMLTGE)(T \geq 0^oC) + PDEPI + PINT]. \tag{A34}$$

For cloud water q_c:

$$S_c = PCOND + PSMLTI(T \geq 0^oC) - PRAUT - PRACW$$

$$-PSACW - PGACW. \tag{A35}$$

For cloud ice q_i:

$$S_i = PDEPI + PINT - PSMLTI(T \geq 0^oC) - PSACI - PCONV$$

$$-PGACI - PRACI. \tag{A36}$$

For rain, q_r, in regions where $T \geq 0^oC$:

$$S_r = PRAUT + PRACW + PREVP - PGMLT - PSMLT - PGACRM - PGACWM$$

$$+PSACW + PRACS + PGSHR - PGACR. \tag{A37}$$

For rain in regions where T < 0°C:

$$S_r = PRAUT + PRACW + PREVP - PGACR - PSACR - PIACR. \tag{A38}$$

For snow, q_s, in regions where T $\geq$ 0°C:

$$S_s = PSMLT - PRACS - PGACS + PMLTEV. \tag{A39}$$

For snow in regions where T < 0°C:

$$S_s = PCONV + PSACI + PSDEP - PGACS + PRACI(\delta_1) + PIACR(\delta_1) +$$

$$PSACR(\delta_2) - PRACS(1 - \delta_2) + PSACW(\delta_3) - PWACS(1 - \delta_3), \tag{A40}$$

where the deltas have the following meanings:

$$\delta 1 = \begin{cases} 0 & if\ q_r > 0.1\ g\ kg^{-1} \\ 1 & otherwise \end{cases} \tag{A41}$$

$$\delta 2 = \begin{cases} 0 & if\ q_r\ and\ q_s > 0.1\ g\ kg^{-1} \\ 1 & otherwise \end{cases} \tag{A42}$$

$$\delta 3 = \begin{cases} 0 & if\ q_s > 0.1\ g\ kg^{-1}\ and\ q_c > 0.5\ gkg^{-1} \\ 1 & otherwise \end{cases} \tag{A43}$$

For graupel, q_g, in regions where T $\geq$ 0°C:

$$S_g = PGMLT + PGACRM + PGACWM + PGACS + PMLTGE. \tag{A44}$$

For graupel in regions where T < 0°C:

$$S_g = PGACW + PGACR + PGACI + PGACS + PGDEP + PRACI(1-\delta1) + PIACR(1-\delta1)$$

$$+PSACR(1 - \delta2) + PRACS(1 - \delta2) + PSACW(1 - \delta3) + PWACS(1 - \delta3). \quad (A45)$$

The total microphysical diabatic heating terms used in the thermodynamic energy equation (2.3) are for T < 0°C:

$$Q^* = \frac{L_f}{c_p}[PSACW + PIACR + PSACR + PGACR + PGACW] + \frac{L_c}{c_p}[PCOND + PREVP]$$

$$+\frac{L_s}{c_p}[PGDEP + PSDEP + PDEPI + PINT]. \quad (A46)$$

For T ≥ 0°C:

$$Q^* = \frac{L_f}{c_p}[PGMLT + PSMLT + PGACWM + PGACRM - PSMLTI - PRACS]+$$

$$\frac{L_c}{c_p}[PCOND + PREVP + PMLTEV + PMLTGE]. \quad (A47)$$

Appendix B

LIST OF SYMBOLS

Symbols	Description	Value	SI units
A'	Thermodynamic term		$m\ s\ kg^{-1}$
A''	Thermodynamic term		$m\ s\ kg^{-1}$
a''	constant in fallspeed relation for snow	12.37	$m^{(1-b)}\ s^{-1}$
a'''	constant in fallspeed relation for graupel	8.73	$m^{(1-b')}\ s^{-1}$
a_0	Coefficient in polynomial fallspeed relation for rain	-0.267	$m\ s^{-1}$
a_1	Coefficient in polynomial fallspeed relation for rain	5.15×10^3	s^{-1}
a_2	Coefficient in polynomial fallspeed relation for rain	-1.0225×10^6	$m^{-1}\ s^{-1}$
a_3	Coefficient in polynomial fallspeed relation for rain	7.55×10^7	$m^{-2}\ s^{-1}$
B'	Thermodynamic term		$m\ s\ kg^{-1}$
B''	Thermodynamic terma		$m\ s\ kg^{-1}$
b	Fallspeed exponent for snow	0.42	
b'	Fallspeed exponent for graupel	0.36	
c	Constant used in turbulence parameterization	0.5	
c_p	Specific heat of air at constant pressure	1004.	$J\ kg^{-1}\ K^{-1}$
c_w	Specific heat of liquid water at $0°C$	4218.	$J\ kg^{-1}\ K^{-1}$
D	Constant used for horizontal exchange coefficient	5.0	
D_G	Graupel diameter		m
D_R	Raindrop diameter		m
D_S	Snowflake diameter		m
E_{GC}	Graupel/cloud water collection efficiency	1.	
E_{GI}	Graupel/cloud ice collection efficiency	0.1	
E_{GR}	Graupel/rain collection efficiency	1.	
E_{GS}	Graupel/snow collection efficiency	0.1	
E_{RI}	Rain/cloud ice collection efficiency	1.	
E_{SR}	Snow/rain collection efficiency	1.	
e_{si}	Saturation vapor pressure for ice		$N\ m^{-2}$
e_{sw}	Saturation vapor pressure for water		$N\ m^{-2}$
f	Coriolis parameter		s^{-1}
g	Gravitational constant	9.8	$m\ s^{-2}$
J	Jacobian operator		
K_a	Thermal conductivity of air	2.43×10^{-2}	$J\ m^{-1}\ s^{-1}\ K^{-1}$

Symbols	Description	Value	SI units
K_H	Horizontal eddy diffusivity of heat		$m^2\ s^{-1}$
K_Z	Vertical eddy diffusivity of heat		$m^2\ s^{-1}$
K_{Z0}	Constant background vertical eddy diffusivity of heat	0.6	$m^2\ s^{-1}$
L_f	Latent heat of fusion	3.337×10^5	$J\ kg^{-1}$
L_s	Latent heat of sublimation	2.834×10^6	$J\ kg^{-1}$
L_v	Latent heat of vaporization	2.5×10^6	$J\ kg^{-1}$
M_c	Average mass of cloud droplet	$4. \times 10^{-12}$	kg
M_I	Average mass of cloud ice particle	$6. \times 10^{-12}$	kg
M_w	Molecular weight of water	18.0160	
N_{0G}	Intercept value in graupel size distribution	4×10^6	m^{-4}
N_{0R}	Intercept value in raindrop size distribution	8×10^6	m^{-4}
N_{0S}	Intercept value in snowflake size distribution	4×10^6	m^{-4}
n_{ci}	Number concentration of cloud ice crystals		m^{-3}
n_c	Number concentration of cloud water droplets		m^{-3}
n_i	Number concentration of ice nuclei		m^{-3}
n_0	Constant in expression for ice nuclei concentration	variable	m^{-3}
p	Pressure		$N\ m^{-2}$
p_0	Constant in empirical relation	10^5	$N\ m^{-2}$
$PCOND$	Condensation of water vapor		$kg\ m^{-3}\ s^{-1}$
$PCONV$	Conversion of cloud ice to snow		$kg\ m^{-3}\ s^{-1}$
$PDEPI$	Depositional growth of ice		$kg\ m^{-3}\ s^{-1}$
$PGACI$	Collection of cloud ice by graupel		$kg\ m^{-3}\ s^{-1}$
$PGACR$	Collection of rain by graupel		$kg\ m^{-3}\ s^{-1}$
$PGACRM$	Enhanced melting of graupel due to accretion of rain		$kg\ m^{-3}\ s^{-1}$
$PGACS$	Collection of snow by graupel		$kg\ m^{-3}\ s^{-1}$
$PGACW$	Collection of cloud water by graupel		$kg\ m^{-3}\ s^{-1}$
$PGACWM$	Enhanced melting of graupel due to accretion of cloud water		$kg\ m^{-3}\ s^{-1}$
$PGDEP$	Depositional growth of graupel		$kg\ m^{-3}\ s^{-1}$
$PGMLT$	Melting of graupel		$kg\ m^{-3}\ s^{-1}$
$PGSHR$	Shedding of accreted water by graupel		$kg\ m^{-3}\ s^{-1}$
$PIACR$	Collection of rain by cloud ice		$kg\ m^{-3}\ s^{-1}$
$PINT$	Initiation of cloud ice		$kg\ m^{-3}\ s^{-1}$
$PMLTEV$	Evaporation of melting snow		$kg\ m^{-3}\ s^{-1}$
$PMLTGE$	Evaporation of melting graupel		$kg\ m^{-3}\ s^{-1}$
$PRACI$	Collection of cloud ice by rain		$kg\ m^{-3}\ s^{-1}$
$PRACS$	Collection of snow by rain		$kg\ m^{-3}\ s^{-1}$
$PRACW$	Collection of cloud water by rain		$kg\ m^{-3}\ s^{-1}$
$PRAUT$	Autoconversion of cloud water		$kg\ m^{-3}\ s^{-1}$
$PREVP$	Evaporation of rainwater		$kg\ m^{-3}\ s^{-1}$
$PSACI$	Collection of cloud ice by snow		$kg\ m^{-3}\ s^{-1}$
$PSACR$	Collection of rain by snow		$kg\ m^{-3}\ s^{-1}$
$PSACW$	Collection of cloud water by snow		$kg\ m^{-3}\ s^{-1}$
$PSDEP$	Depositional growth of snow		$kg\ m^{-3}\ s^{-1}$

Symbols	Description	Value	SI units
$PSMLT$	Melting of snow		kg m^{-3} s^{-1}
$PSMLTI$	Melting of cloud ice		kg m^{-3} s^{-1}
$PWACS$	Collection of snow by cloud water		kg m^{-3} s^{-1}
Q^*	Diabatic heating term		K kg m^{-3} s^{-1}
q_c	Mixing ratio of cloud water		kg kg^{-1}
q_g	Mixing ratio of graupel		kg kg^{-1}
q_i	Mixing ratio of cloud ice		kg kg^{-1}
q_r	Mixing ratio of rain water		kg kg^{-1}
q_s	Mixing ratio of snow		kg kg^{-1}
q_v	Mixing ratio of water vapor		kg kg^{-1}
R^*	Universal gas constant 8314.	J kmol^{-1} K^{-1}	
R_w	Gas constant for water vapor	461.	J kg^{-1} K^{-1}
S	Saturation ratio with respect to water		
S_c	Schmidt number	0.6	
S_e	Source term for cloud water		kg m^{-3} s^{-1}
S_g	Source term for graupel		kg m^{-3} s^{-1}
S_h	Source term for cloud ice		kg m^{-3} s^{-1}
S_i	Saturation ratio with respect to ice		kg m^{-3} s^{-1}
S_o	Represents sources and sinks for q		kg m^{-3} s^{-1}
S_r	Source term for rain		kg m^{-3} s^{-1}
S_s	Source term for snow		kg m^{-3} s^{-1}
S_v	Source term for water vapor		kg m^{-3} s^{-1}
T	Temperature		K
T_0	Reference temperature	273.16	K
t	Time		s
u	Horizontal x-velocity perturbation		m s^{-1}
$U(z)$	Basic x-velocity		m s^{-1}
v	y-velocity		m s^{-1}
$\overline{V}$	Mass-weighted fallspeed of precipitation		m s^{-1}
$\overline{V}_G$	Mass-weighted fallspeed for graupel		m s^{-1}
$\overline{V}_R$	Mass-weighted fallspeed for rain		m s^{-1}
$\overline{V}_S$	Mass-weighted fallspeed for snow		m s^{-1}
w	Vertical air velocity		m s^{-1}
x	Horizontal distance		m
z	Vertical distance		m
α	Specific volume of air		m^3 kg^{-1}
α_0	Reference specific volume		m^3 kg^{-1}
β	Constant in ice crystal concentration	0.4	K^{-1}
Γ	Gamma function		
ρ	Air density		kg m^{-3}

Symbols	Description	Value	SI units
ρ_G	Density of graupel	400.	kg m^{-3}
ρ_L	Density of water	1000.	kg m^{-3}
ρ_S	Density of snow	100.	kg m^{-3}
λ_G	Slope of graupel size distribution		m^{-1}
λ_R	Slope of raindrop size distribution		m^{-1}
λ_S	Slope of snow size distribution		m^{-1}
η	Vorticity in the x-z plane		s^{-2}
χ	Diffusivity of water vapor in air	2.26×10^{-5}	m^2 s^{-1}
μ	Dynamic viscosity of air	1.718×10^{-5}	kg m^{-1} s^{-1}
ν_H	Horizontal eddy viscosity		m^2 s^{-1}
ν_Z	Vertical eddy viscosity		m^2 s^{-1}
ν_{Z0}	Constant background vertical eddy viscosity		m^2 s^{-1}
ψ	Streamfunction in the x-z plane		kg s^{-1} m^{-1}
θ	Potential temperature		K
θ_0	Reference potential temperature		K
Δt	Time increment	15	s
Δx	Horizontal spatial increment	5000	m
Δz	Vertical spatial increment	400	m